Higher Order Finite Elements for Relaxed Micromorphic Continua

M.Eng. Adam Sky

Dissertation
to attain the academic degree

Doctor of Engineering (Dr.-Ing.)

at the
Institute of Statics, Dynamics and Structural Mechanics,
Technical University of Dortmund

Supervisors:

Prof.Dr.-Ing. Ingo Muench

Prof.Dr.rer.nat.habil. Patrizio Neff

08.09.2022

”The most important step a man can take. It’s not the first one, is it? It’s the next one. Always the next step.”

- Brandon Sanderson

Abstract

Metamaterials, being materials with exotic properties due to their artificially designed micro-structure, are gaining popularity in the engineering community. The ability to design the micro-structure in order to induce specific material properties is extremely useful and finds its applications in a variety of fields. For example, band-gap metamaterials can be used to both isolate sounds as well as for seismic shielding. However, the process of designing metamaterials is no easy task and usually met with computational constraints. Due to the complex geometry of the micro-structure, viable solutions require extremely fine discretizations of the displacement field when Cauchy continuum models are employed. Alternative methods such as multi-scale computations are met with the same limitations if the micro-structure is either non-periodic or if the computation is non-linear.

An alternative approach can be derived by using enriched continuum models. These theories extend the kinematics of the material point by adding additional degrees of freedom, thus accounting for perturbations stemming from the micro-structure. One such model is the relaxed micromorphic continuum. The model introduces the microdistortion $\boldsymbol{P}$ for each material point, being an affine deformation field, thus extending the kinematics of the material point with nine additional degrees of freedom. Consequently, each material point is regarded as an affine deformable micro-body. The model is unique in its definition of a free energy functional, where the Curl of the microdistortion $\operatorname{Curl}\boldsymbol{P}$ rather than its full gradient $\mathrm{D}\boldsymbol{P}$ is applied. A direct consequence of the latter is the reduced continuity of the microdistortion as well as its compatibility with the space of the deformation gradient, namely $H(\mathrm{Curl})$. Further, the micro-dislocation, being the Curl of the microdistortion, remains a second order tensor, whereas $\mathrm{D}\boldsymbol{P}$ is represented by a third order tensor. Another consequence is that on the boundary, only the tangential component of the microdistortion can be controlled. As such, the theory introduces the consistent coupling condition, which is energetically consistent with the lower and upper bounds given by equivalent Cauchy continua. The ability of the theory to capture the behaviour of meta band-gap materials has been shown in multiple works, thus making it an excellent candidate for the computation of materials with a pronounced microstructure.

The challenge of the relaxed micromorphic model stems from its application of the Curl operator, which is rather uncommon in the field of structural mechanics. A consequence of the operator is the definition of the microdistortion in the Hilbert space $H(\mathrm{Curl})$ of tangentially continuous fields. While the construction of low order conforming subspaces for the Hilbert space $H(\mathrm{curl})$ is well known, the definition of higher order finite elements remains quite complex. The construction of higher order finite elements is required in the framework of hp-finite element methods, where both the element size as well as its polynomial order can be refined in order to obtain exponential convergence of the error with respect to an analytical solution over the domain.

This dissertation discusses the relaxed micromorphic model, its kinematical reduction to plane strain and antiplane shear, and its existence and uniqueness in the context of the Lax-Milgram theorem. Further, several a priori error estimates using Cea's lemma are derived and subsequently improved for s-regular problems by the Aubin-Nitsche technique. The thesis also examines the implementation aspects of low order finite elements and proposes simple solutions to both the orientation problem as well as for the discrete consistent coupling condition. However, the main novelty of this work lies in its conception of a new construction methodology for arbitrary order $H(\mathrm{curl})$-conforming finite elements for a variety of polynomial bases. A short description of the methodology is as follows: the reference element is equipped with a polytopal template respecting its geometry. The tensor product of the template with an H^1-conforming polynomial basis, where the base functions are clearly associated with the polytopes of the reference element, yields an $H(\mathrm{curl})$-conforming element, such that the base functions have a clear association with their polytopes. The biggest advantage of this approach is that the $H(\mathrm{curl})$-formulation inherits many of the properties of the underlying H^1-conforming polynomial basis. In this work, we rely on Bernstein polynomials yielding optimal complexity through sum factorization. Thus, we introduce an optimal basis for assembly in hp-finite element analysis. Further, we discuss efficient methods for computing the base functions and their derivatives by means of automatic forward differentiation via dual numbers. The newly defined finite elements are used to investigate the behaviour of the relaxed micromorphic model, find viable approximations, and explore its relation to micro-structured materials.

Acknowledgements

I wish to begin by expressing my utmost gratitude to my supervisors, Prof. Ingo Muench and Prof. Patrizio Neff for their support, inspiration, and insight throughout these last few years. Through their knowledge and interest, I received the opportunity to expand my own and explore exciting fields of research. I am very grateful for the many profound discussions and their unyielding patience.

Secondly, I would like to thank Dr. Michael Neunteufel for the countless talks that greatly extended my understanding of numerics and for graciously accepting to proof-read this work.

Special thanks go out to Prof. Roman Kemmler and Prof. Silke Michaelsen for opening my eyes to the vastness of mechanics and mathematics and recommending me for a PhD candidature.

Lastly, I wish to thank my family; my loving parents, Nor and Raquel, my beloved wife, Annina, and my cherished brothers, Itai and Nathan. This thesis is the result of your love and support throughout the years and is thus dedicated to you!

Eidesstattliche Erklärung

Ich erkläre an Eides statt, dass ich die vorliegende Dissertation selbstständig und ohne fremde Hilfe verfasst, andere als die angegebenen Quellen und Hilfsmittel nicht benutzt bzw. die wörtlich oder sinngemäß entnommenen Stellen als solche kenntlich gemacht habe.

Dortmund, am 08. September 2022

____
Adam Sky

Contents

1 Introduction

A continuum theory emerges under the assumption that a medium can be mathematically treated as a continuum rather than a discrete set. In practice, this approach is feasible down to a certain scale, where the effects of the micro-structure become too dominant to neglect. Since the structural engineering community is mostly interested in the description of phenomena at the higher scales, continuum theories have been prevalent and successfully applied to the design of machines and structures. Perhaps the most prominent theory of them all is the classical Cauchy continuum theory, where the assumption of material points with three translational degrees of freedom is made. The continuum is therefore a collection of an infinite amount of simple material points. While the Cauchy model is still the dominant model in computational mechanics today, it is reaching its limits when materials with exotic properties are considered. The exotic properties mentioned are, for example, negative Poisson ratios [21, 104], band-gaps [28], and solids with zero shear moduli [94]. The common denominator of such materials is an underlying complex micro-structure arising either naturally or artificially with specific intent. Examples of natural materials with a micro-structure are porous media, whereas for artificial ones, namely metamaterials, the possibilities for the geometry of the micro-structure are limitless.

Attempts to alleviate the modelling limits within the confines of the Cauchy theory can be divided into two methodologies. The first and most straight-forward one is to fully resolve the underlying micro-structure in the computational model. This means that each pore and complex geometry in the model must be fully captured by the geometrical model. In terms of finite element methods, this can only be done by using extremely fine meshes. As such, it is clear that the latter approach is bound by computational capacity. The second approach splits the model into a macro and a micro scale. The different scales are computed separately but are coupled by their respective results. For example, the effect of the micro-structure can be considered by a separate computational model on each integration point of the macro-model. In terms of finite element computations, this implies the existence of two simultaneous discretizations, one for the macro-model and one for the micro-structure. The latter methodology is commonly known under the name multi-scale methods [1, 36, 37, 43].

An alternative technique reconsiders the underlying mathematical application of solely the deformation gradient, which restricts the material point to affine deformations. Higher gradient continuum theories [11, 67, 76] challenge this approach by taking higher order gradients of the displacement field into account when computing the work of a system. This results in a more complex mathematical model and higher restrictions on the continuity of the displacement field. In comparison to Cauchy models where C^0-continuity is required for the displacement field, gradient elasticity for example, necessitates C^1-continuity. While the development of C^1-continuous computational methods has gained popularity with the rise of the isogeometrical analysis method (IGA) [48, 49], the problem of addressing volumetric geometries has not been fully resolved as of yet [22]. Further, the assumption of higher continuity on the displacement field might be counter-productive when considering materials with a pronounced micro-structure, as the micro-structure may often induce perturbations, implying the possibility of partially discontinuous solutions in the gradient of the displacement field.

It is to be noted that the main assumption of translational material points in the Cauchy model also incorporates two major restrictions. Firstly, each material point is irrotational. Secondly, each material point is non-deformable. Considering the limitations of the discussed approaches it is logical to introduce new continuum theories, where the continuity of the displacement gradient is preserved (C^0) and still a more complex mathematical model arises, allowing for intricate kinematical behaviour. The collection of such models is known under the name generalized continua. The first notable attempt to alleviate these restrictions is due to the Cosserat brothers [25], who introduced the so-called micropolar model [38, 52, 53, 72]. By equipping each material point with non-deformable directors, it was possible to attach orientational information to each material point. Effectively, the micro-polar theory turned each material point into a non-deformable solid sphere, implying the existence of a local moment of inertia. Another consequence is the introduction of couple tractions, being higher order tractions on the material point. Today the Cosserat theory is applied in the simulation of granular materials [107] due to its obvious affinity to the natural behaviour of such media. In terms of energy, it is shown in [78] that the latter allows for non-conventional displacement modes with lower energies than those achieved by a straight line during simple shear. Clearly, this indicates the ability of the model to capture certain micro-effects unaccounted for in Cauchy continua.

The next prominent step in the development of generalized continua is due to Eringen and Mindlin [39, 68], who removed the second restriction on Cauchy continua, namely the non-deformability of the material point. This was achieved by making the accompanying directors of the Cosserat theory deformable. The resulting theory is known as the full micromorphic theory. Essentially, the theory implies that each material point is an affine deformable micro-structure with its own micro-stiffness. The full micromorphic theory can be seen as a superset of the micro-polar theory and in fact, many other subsets of micromorphic continua exist, where restrictions are imposed on the deformation modes of the material point. Common examples are micro-stretch [57, 93] and micro-strain [41, 50]. In the full micromorphic continuum theory the transformation of an infinitesimal body from the reference to the current configuration is governed by the deformation gradient as well as by an independent tensor field called the microdistortion. In energy formulations of the full micromorphic model, the gradient of the microdistortion is taken into account, implying a minimal C^0-continuity of the microdistortion. Due to the strong interaction with the gradient of the displacement field and since the effective strain on the infinitesimal element is defined to be a function of the gradient and of the microdistortion, it becomes clear that the continuity of the strain is governed by a mixture of both. Observing that the continuity of the deformation tensor is only tangential implies an increased continuity of the strain due to the microdistortion. In [101] it is observed that the latter limits the ability of the formulation to optimally capture C^0-continuous displacement fields. Since the microdistortion is a second order tensor, its gradient yields a third order tensor, making its implementation and interpretation more challenging, as for example, a linear constitutive relation to it is given by sixth order tensors, implying the more material parameters. The influence of the micro-stiffness is usually governed by a parameter (or multiple parameters) called the characteristic length scale. Taking the upper limit of the characteristic length in the full micromorphic theory reduces the microdistortion to a constant field. As shown in [101] this leads to boundary layers if non-constant boundary values are imposed for the microdistortion.

A remedy to the continuity problem of the strain is proposed in [75] where instead of the full gradient of the microdistortion, only its skew-symmetric part, being equivalent to its Curl, is assumed to produce non-negligible energies. Consequently, the regularity assumptions of the microdistortion are reduced to tangential continuity and are compatible with the deformation gradient. The model is dubbed the relaxed micromorphic continuum theory [46, 74]. A result of the tangential continuity of the microdistortion is that only its tangential projection can be controlled on the boundary [99]. Consequently, the theory introduces the so-called consistent coupling condition [27], where the tangential projection of the gradient of the displacement field and the tangential projection of the microdistortion are set to be equal. The consistent coupling condition is energetically consistent with lower and upper bounds on the energy of the system given by equivalent macro and micro Cauchy continuum models. We note that the Curl of the microdistortion remains a second order tensor. Further, taking the upper limit of the characteristic length scale reduces the microdistortion to a gradient field, thus circumventing the problem of boundary layers for non-constant boundary conditions on the microdistortion [101]. The relaxed micromorphic model incorporates the Cosserat model by allowing for a skew-symmetric stress tensor governed by a rotational coupling modulus [75]. In fact, under the assumption of an infinite micro-stiffness the relaxed micromorphic model reduces to a micro-polar continuum. However, by setting the rotational coupling modulus to zero the relaxed micromorphic model retrieves a symmetric stress tensor while remaining well-posed [45,100]. Furthermore, analytical solutions of the model for uniaxial extension [91], cylindrical bending [89], torsion [88], and shear [90] have been derived, revealing the intrinsic behaviour of the model for boundary value problems. The theory has been successfully applied in the modelling of acoustic metamaterials for band-gap materials [6, 7, 14, 15, 26, 64, 65, 77] and seismic shielding [92] and such, represents a promising approach for the computation of micro-structured materials.

Analytical solutions of the relaxed micromorphic model can only be derived for special cases. Consequently, the need for numerical discretization techniques for the solution of general geometries and boundary conditions is evident. Amongst a multitude of numerical approximation schemes, the finite element method (FEM) [16,18,19,23,111] remains the most prominent. The main advantages of the method are its flexible application to a variety of variational problems, geometries, and boundary conditions. Further, the method is based on a strong foundation of functional analysis, allowing for mathematical proof of its effectiveness. The standard low order finite element method (h-FEM) relies on so called h-refinement in order to approach the analytical solution. This refers to the decrease in element size, thus yielding a finer discretization of the domain. Commonly, either linear or quadratic polynomials underline the approximation capacity of each finite element in the mesh. One can show that h-refinement leads to an algebraic decline in the error over the domain. An alternative approach to h-refinement is the so-called p-refinement, leading to the so called p-Finite-Element-Method (p-FEM) [12, 13]. In p-refinement, the elements do not change their size but rather their polynomial order. In the case of highly smooth solutions, p-refinement leads to exponential convergence with respect to the error over the domain. However, if the solution is of low regularity the convergence of p-refinement reduces to an algebraic rate. Consequently, singularities over the domain lead to a decay of the convergence rate, thus offering no advantage over h-refinement. However, by combining both h- and p-refinement, such that the area of a singularity is localized by h-refinement, one can retrieve exponential convergence. This gives rise to the so called hp-Finite-Element-Method (hp-FEM) [29, 31, 103, 105].

Since the relaxed micromorphic theory introduces the Curl of the microdistortion in its energy functional, the variational problem is well-posed for $\boldsymbol{P} \in H(\mathrm{Curl})$. The development of $H(\mathrm{curl})$-conforming finite elements with minimal regularity assumptions is due to Nédélec [70, 71] and as such, they are named after him. Their necessity in allowing to capture C^0-continuous solutions of the displacement field and the suboptimal convergence obtained by using Lagrangian (C^0) elements in their place is shown in [97, 98, 101]. The application of $H(\mathrm{curl})$-conforming subspaces in finite element computations is usually found for Maxwell's equations [69, 96, 110] and is not common in structural mechanics. However, the appearance of the Curl operator in related works, such as plasticity with dislocations [24] and micro-curl [35] continua or the novel TDNNS-formulation in elasticity [82, 86] makes their usage relevant for structural mechanics as well.

The investigation of efficient finite element methods for the relaxed micromorphic model is the focus of this work and is outlined as follows:

1. First, we introduce classical linear elasticity and its kinematically reduced models. Linear elasticity represents the limit cases for the relaxed micromorphic model and is a crucial component in the comparison to fully resolved geometries with micro-structures.

2. Secondly, the relaxed micromorphic model is introduced along with comparably reduced kinematics to the ones introduced for linear elasticity. We derive the variational and strong form and discuss limit cases.

3. Next we show proofs of existence and uniqueness of the relaxed micromorphic model in the context of the Lax-Milgram theorem.

4. Using the latter proofs we apply Cea's lemma in order to present a priori error estimates of the model.

5. This is followed by an introduction of low order Lagrangian and Nédélec elements of the first and second type on triangles and tetrahedra. The construction along with solutions to the orientation problem and the discrete consistent coupling condition are demonstrated.

6. Chapter six presents a new methodology for the construction of $H(\mathrm{curl})$-conforming finite elements, being the main novelty of this work. The method allows for a simple construction of vectorial finite elements independently of the choice of a polynomial basis. Here we make use of Bernstein polynomials, thus leading to optimal complexity in the assembly process. Further, we discuss an efficient approach of computing derivatives of the base functions and explore methods of applying boundary conditions.

7. In chapter seven we test both the low and higher order finite element formulations for convergence and accuracy and discuss their behaviour over a variety of examples. A special emphasis is put on the efficiency of the methods to correctly capture the intrinsic behaviour of the relaxed micromorphic model and reproduce its ability to interpolate between micro- and macro reactions.

8. Lastly, we draw our conclusions and discuss possibilities of further development.

The culmination of this work is the hp-finite element analysis software Rayse, which is freely available for Windows 64-bit computers on the PyPi-repository. The computational kernel of the program is written in the Rust programming language for high performance and implements the CRAC sparse matrix format [102] for parallel assembly and solution. For convenience and simplicity of use, the program is controlled through a Python user interface.

1.1 Notation

The following notation is used throughout this work:

- Simple lower case letters are scalars a, λ. Vectors are denoted with bold lower case letters $\mathbf{v}$, $\boldsymbol{\phi}$. Matrices and second order tensors are indicated by bold capital letters $\boldsymbol{P}$, $\boldsymbol{\Theta}$. Fourth order tensors are identified by the blackboard-bold format $\mathbb{C}$, $\mathbb{J}$. Exceptions to this rule, such as the linear strain tensor $\boldsymbol{\varepsilon}$, are clear from context.

- The symbol $\mathbb{1} \in \mathbb{R}^{3\times3}$ represents the second order identity tensor. The fourth order identity tensor is designated by $\mathbb{J} \in \mathbb{R}^{3\times3\times3\times3}$.

- The physical domain is denoted by $V \subset \mathbb{R}^3$ for three-dimensional bodies. Two dimensional physical domains are given by $A \subset \mathbb{R}^2$, and one dimensional curves in the physical space by $s \subset \mathbb{R}$. Their respective counterparts on reference domains are $\Omega \subset \mathbb{R}^3$, $\Gamma \subset \mathbb{R}^2$ and $\mu \subset \mathbb{R}$.

- The normal vector on boundaries of physical domains $\partial V \subset \mathbb{R}^2$ or $\partial A \subset \mathbb{R}$, is indicated by $\mathbf{n}$. On the reference domain $\boldsymbol{\nu}$ is used in its stead. Tangent vectors on the physical and reference domains are denoted by $\mathbf{t}$ and $\boldsymbol{\tau}$, respectively.

- The scalar product operation is denoted by $\langle \cdot, \cdot \rangle$. The operation represents either single contraction or higher contraction, in accordance with its argument. The single contraction between vectors and second order tensors is written without an operator $\boldsymbol{A}\mathbf{v} \in \mathbb{R}^3$, $\boldsymbol{A} \in \mathbb{R}^{3\times3}$, $\mathbf{v} \in \mathbb{R}^3$. Likewise, the double contraction between fourth order tensors and second order tensors is implied as $\mathbb{C}\boldsymbol{P} \in \mathbb{R}^{3\times3}$, $\mathbb{C} \in \mathbb{R}^{3\times3\times3\times3}$, $\boldsymbol{P} \in \mathbb{R}^{3\times3}$.

- Norms are indicated by the $\| \cdot \|$ operator, whereas $| \cdot |$ stands for the absolute value, and $[\![\cdot]\!]$ represents the jump operator.

- The gradient operator for scalars is implied by $\nabla\lambda$, the curl operator by $\operatorname{curl}\mathbf{v} = \nabla \times \mathbf{v}$, and the divergence by $\operatorname{div}\mathbf{v} = \langle \nabla, \mathbf{v} \rangle$. The operator D defines the right-gradient for vectors, and the Curl-operator applies the vector curl operator row-wise on second order tensors. Analogously, the Div-operator applies the vector divergence operator row-wise on second order tensors.

- **For the remainder of this work, unless stated otherwise, vectors and higher order tensors are defined using the Cartesian basis** $\{\mathbf{e}_1, \mathbf{e}_2, \mathbf{e}_3\}$.

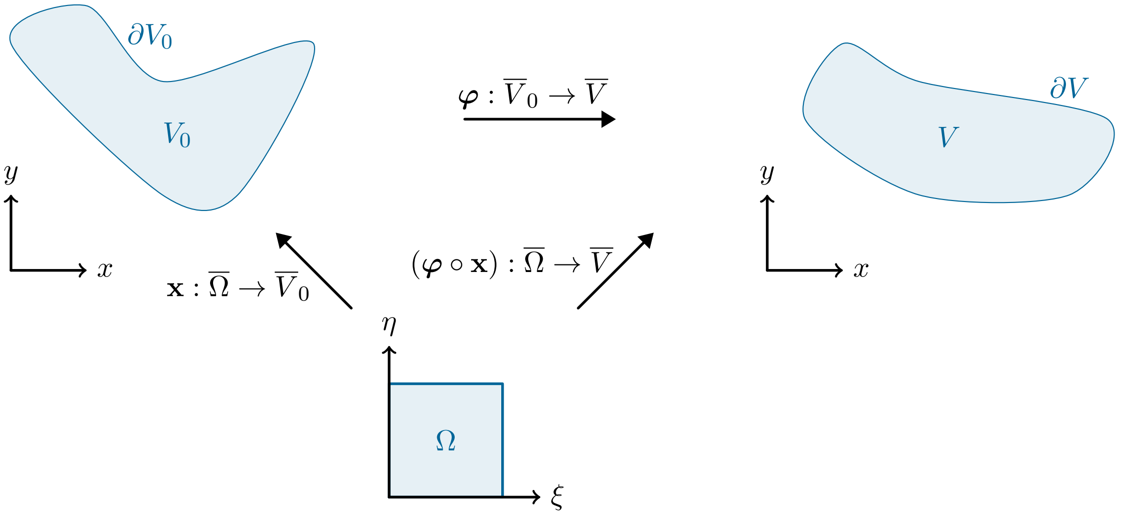

Figure 2.1: The parametric domain, reference configuration and current configuration connected by their respective mappings.

2 Linear Elasticity

This section is devoted to the introduction of the theory of linear elasticity [8, 56]. The theory can be considered as a subclass of the relaxed micromorphic continuum and is retrieved for certain limit cases of the relaxed micromorphic model. Further, we employ the theory for comparisons with discrete micro-structured geometries.

2.1 Kinematics

Let $V_0 \subset \mathbb{R}^3$ be an open and bounded domain with a sufficiently smooth boundary ∂V_0, then the reference configuration of a body can be defined by $\overline{V}_0 = V_0 \cup \partial V_0$. Further, for computational purposes we assume that the reference configuration is mapped from some parametric space $\overline{\Omega}$ with $\Omega \subset \mathbb{R}^3$ such that

$$\mathbf{x} : \overline{\Omega} \to \overline{V}_0 \, . \tag{2.1}$$

The current configuration of the body $\overline{V}$ is given by the vector field (see Fig. 2.1)

$$\boldsymbol{\varphi} : \overline{V}_0 \to \overline{V} \subset \mathbb{R}^3 \, , \tag{2.2}$$

and consequently, the displacement field is extracted from the difference

$$\mathbf{u}(\mathbf{x}) = \boldsymbol{\varphi}(\mathbf{x}) - \mathbf{x} \, . \tag{2.3}$$

At each material point, the deformation gradient $\boldsymbol{F}$ is given by the displacement field

$$\boldsymbol{F} = \mathrm{D}\boldsymbol{\varphi} = \mathbb{1} + \mathrm{D}\mathbf{u} \, , \qquad \mathrm{D}\mathbf{u} = \begin{bmatrix} \nabla u_1 \\ \nabla u_2 \\ \nabla u_3 \end{bmatrix} = \begin{bmatrix} u_{1,x} & u_{1,y} & u_{1,z} \\ u_{2,x} & u_{2,y} & u_{2,z} \\ u_{3,x} & u_{3,y} & u_{3,z} \end{bmatrix} \, , \qquad \nabla u = \begin{bmatrix} u_{,x} \\ u_{,y} \\ u_{,z} \end{bmatrix} \, , \tag{2.4}$$

where $\mathrm{D}(\cdot)$ and $\nabla(\cdot)$ define the gradient operator for vectors and scalars, respectively. The deformation gradient contains both deformations and rigid body motions. The metric of the current configuration is represented by the Cauchy-Green strain tensor

$$\boldsymbol{C} = \boldsymbol{F}^T \boldsymbol{F} \,, \qquad \|\mathrm{d}\boldsymbol{\varphi}\|^2 = \langle \boldsymbol{F}\,\mathrm{d}\mathbf{x},\, \boldsymbol{F}\,\mathrm{d}\mathbf{x} \rangle = \langle \mathrm{d}\mathbf{x},\, \boldsymbol{C}\,\mathrm{d}\mathbf{x} \rangle \,, \tag{2.5}$$

and does not capture rigid body motions since

$$\boldsymbol{C} = \mathbb{1} \quad \iff \quad \boldsymbol{\varphi} = \mathbf{a} + \boldsymbol{Q}\mathbf{x} \,, \qquad \mathbf{a} \in \mathbb{R}^3 \,, \boldsymbol{Q} \in \mathrm{SO}(3) \,, \tag{2.6}$$

where $\mathrm{SO}(3)$ is the space of special orthogonal second order tensors. As such, the strain can be measured by taking the difference between the metric of the current and reference configurations

$$\begin{aligned} \|\mathrm{d}\boldsymbol{\varphi}\|^2 - \|\mathrm{d}\mathbf{x}\|^2 = \langle \mathrm{d}\mathbf{x},\, \boldsymbol{C}\,\mathrm{d}\mathbf{x} \rangle - \langle \mathrm{d}\mathbf{x},\, \boldsymbol{I}\,\mathrm{d}\mathbf{x} \rangle = \langle \mathrm{d}\mathbf{x},\, (\boldsymbol{C} - \boldsymbol{I})\,\mathrm{d}\mathbf{x} \rangle = \langle \mathrm{d}\mathbf{x},\, 2\boldsymbol{E}\,\mathrm{d}\mathbf{x} \rangle \,, \\ \boldsymbol{E} = \frac{1}{2}(\boldsymbol{C} - \mathbb{1}) = \frac{1}{2}(\boldsymbol{F}^T\boldsymbol{F} - \mathbb{1}) = \frac{1}{2}([\mathrm{D}\mathbf{u}]^T \mathrm{D}\mathbf{u} + [\mathrm{D}\mathbf{u}]^T + \mathrm{D}\mathbf{u}) \,, \end{aligned} \tag{2.7}$$

which is represented by the Green-Lagrange strain tensor $\boldsymbol{E}$. Linearisation of the Green-Lagrange strain tensor with respect to $\mathbf{u}$ results in

$$\boldsymbol{\varepsilon} = \operatorname{sym} \mathrm{D}\mathbf{u} = \frac{1}{2}([\mathrm{D}\mathbf{u}]^T + \mathrm{D}\mathbf{u}) \,, \qquad \mathrm{D}\mathbf{u} = \operatorname{sym} \mathrm{D}\mathbf{u} + \operatorname{skew} \mathrm{D}\mathbf{u} \,, \tag{2.8}$$

being the so called engineering strains that are applicable to problems with small strains $\|\boldsymbol{\varepsilon}\|_F \ll 1$ and small rotations $\|\operatorname{skew} \mathrm{D}\mathbf{u}\|_F \ll 1$. Here $\|\cdot\|_F$ denotes the matrix Frobenius norm and $\operatorname{skew}(\cdot)$ the extraction of a skew symmetric matrix

$$\|\boldsymbol{P}\|_F = \sqrt{\langle \boldsymbol{P},\, \boldsymbol{P} \rangle} \,, \qquad \operatorname{skew} \boldsymbol{P} = \frac{1}{2}(\boldsymbol{P} - \boldsymbol{P}^T) \,. \tag{2.9}$$

2.2 Constitutive equations

The relation between stresses and strains is given by constitutive equations. Deformation stems from mechanical loads acting on the body. Elastic bodies return to their undeformed state after load removal. Therefore, an hyperelastic material law can be defined by considering an energy density function W of strains

$$E = \int_V W(\boldsymbol{E})\,\mathrm{d}V \,, \tag{2.10}$$

where E represents the total elastic energy of the body. A material is called isotropic if it exhibits the same stress-strain relation in all directions. The latter implies that the energy density function is invariant to rotations of its argument such that

$$W(\boldsymbol{E}) = W(\boldsymbol{Q}^T \boldsymbol{E} \boldsymbol{Q}) \,, \qquad \boldsymbol{Q} \in \mathrm{SO}(3) \,. \tag{2.11}$$

Since $\boldsymbol{F}$ is assumed to be invertible (to prevent self-intersection of material points during deformation) and real, the strain tensor $\boldsymbol{E}$ is symmetric positive definite and the energy density can be described using solely its eigenvalues $\boldsymbol{\Lambda}$

$$W(\boldsymbol{E}) = W(\boldsymbol{V}\boldsymbol{\Lambda}\boldsymbol{V}^T) = W(\boldsymbol{\Lambda}) \,, \qquad \boldsymbol{V} \in \mathrm{SO}(3) \,, \tag{2.12}$$

where $\boldsymbol{E} = \boldsymbol{V}\boldsymbol{\Lambda}\boldsymbol{V}^T$ is the spectral decomposition. Commonly, the main invariants are used instead of directly acting on each eigenvalue

$$W(\boldsymbol{E}) = W(I, II, III) = W(\operatorname{tr}\boldsymbol{E}, (1/2)[(\operatorname{tr}\boldsymbol{E})^2 - \operatorname{tr}(\boldsymbol{E}^2)], \det\boldsymbol{E})\,. \tag{2.13}$$

Development of the energy density functional into a Taylor series yields

$$W(\boldsymbol{E}) = W_0 + \langle\nabla W,\, \Delta\mathbf{I}\rangle + \frac{1}{2}\langle \mathrm{D}\nabla W,\, \Delta\mathbf{I}\otimes\Delta\mathbf{I}\rangle + \mathcal{O}(\|\boldsymbol{I}\|^3)\,, \qquad \mathbf{I} = \begin{bmatrix} I & II & III\end{bmatrix}^T\,. \tag{2.14}$$

Since $W(\boldsymbol{E})$ describes an hyperelastic material we assume the global minimum $W = 0$ at $\boldsymbol{E} = 0$ while dropping higher order terms, such that the Taylor series reduces to

$$\widehat{W}(\boldsymbol{E}) = \frac{1}{2}\frac{\partial^2 W}{\partial I^2}(\operatorname{tr}\boldsymbol{E})^2 + \frac{\partial W}{\partial II}\operatorname{tr}\boldsymbol{E}^2\,. \tag{2.15}$$

Setting the Lamé constants

$$\frac{\partial^2 W}{\partial I^2} = \lambda\,, \qquad\qquad \frac{\partial W}{\partial II} = \mu\,, \tag{2.16}$$

yields Hooke's law

$$\widehat{W}(\boldsymbol{E}) = \frac{\lambda}{2}(\operatorname{tr}\boldsymbol{E})^2 + \mu\|\boldsymbol{E}\|_F^2\,, \qquad\qquad \boldsymbol{\sigma} = \frac{\partial\widehat{W}}{\partial\boldsymbol{E}} = \lambda(\operatorname{tr}\boldsymbol{E})\mathbb{1} + 2\mu\boldsymbol{E}\,. \tag{2.17}$$

The constitutive equation can also be described using higher dimensional tensors

$$\boldsymbol{\sigma} = \mathbb{C}\,\boldsymbol{E}\,, \qquad\qquad \mathbb{C} = \lambda\mathbb{1}\otimes\mathbb{1} + 2\mu\,\mathbb{J} \in \mathbb{R}^{3\times3\times3\times3}\,, \tag{2.18}$$

where $\mathbb{J}$ is the fourth-order identity tensor. In the linear theory of elasticity the material tensor $\mathbb{C}$ is applied to the engineering strains $\boldsymbol{\sigma} = \mathbb{C}\,\boldsymbol{\varepsilon}$.

2.3 Variational formulation

In the following we consider only the geometrically linear theory of elasticity, i.e., engineering strains are employed and integration is performed over the reference configuration. The total energy of the system is determined by the deformation energy and the work performed by volume forces

$$I(\mathbf{u}) = \int_V W(\mathrm{D}\mathbf{u})\,\mathrm{d}V - \int_V \langle\mathbf{u},\, \mathbf{f}\rangle\,\mathrm{d}V \to \min \quad \text{w.r.t.} \quad \mathbf{u}\,, \tag{2.19}$$

where equilibrium is defined as a minimizer with respect to the displacement field $\mathbf{u}$, since it asserts the equality of internal and external work. Taking variations with respect to the displacement field $\mathbf{u}$ yields

$$\delta I(\mathbf{u}) = \int_V \langle \operatorname{sym}(\mathrm{D}\delta\mathbf{u}),\, \mathbb{C}\operatorname{sym}(\mathrm{D}\mathbf{u})\rangle\,\mathrm{d}V - \int_V \langle\delta\mathbf{u},\, \mathbf{f}\rangle\,\mathrm{d}V = 0\,. \tag{2.20}$$

Using the Green-type formula

$$\int_V \langle\mathrm{D}\mathbf{v},\, \boldsymbol{T}\rangle\,\mathrm{d}V = \int_{\partial V}\langle\mathbf{v},\, \boldsymbol{T}\mathbf{n}\rangle\,\mathrm{d}A - \int_V\langle\mathbf{v},\, \operatorname{Div}\boldsymbol{T}\rangle\,\mathrm{d}V \qquad \mathbf{v}\in[C^\infty(\overline{V})]^3\,, \quad \boldsymbol{T}\in[C^\infty(\overline{V})]^{3\times3}\,, \tag{2.21}$$

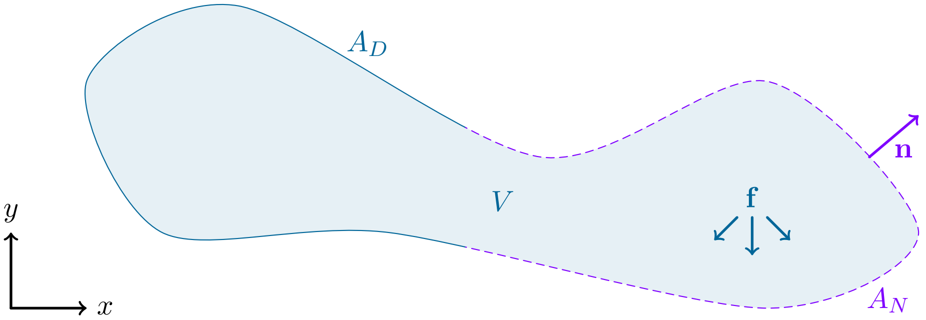

Figure 2.2: The domain with Dirichlet and Neumann boundaries under internal forces.

partial integration of Eq. (2.20) results in

$$-\int_V \langle \delta\mathbf{u},\, \mathrm{Div}[\mathbb{C}\,\mathrm{sym}(\mathrm{D}\mathbf{u})]\rangle \mathrm{d}V + \int_{\partial V} \langle \delta\mathbf{u},\, [\mathbb{C}\,\mathrm{sym}(\mathrm{D}\mathbf{u})]\,\mathbf{n}\rangle\,\mathrm{d}A - \int_V \langle \delta\mathbf{u},\, \mathbf{f}\rangle\,\mathrm{d}V = 0\,, \tag{2.22}$$

from which we extract the elastostatic Navier-Cauchy equations and the boundary conditions

$$-\,\mathrm{Div}[\mathbb{C}\,\mathrm{sym}(\mathrm{D}\mathbf{u})] = \mathbf{f} \qquad \text{in} \quad V\,, \tag{2.23a}$$

$$[\mathbb{C}\,\mathrm{sym}(\mathrm{D}\mathbf{u})]\,\mathbf{n} = 0 \qquad \text{on} \quad A_N\,, \tag{2.23b}$$

$$\mathbf{u} = \widetilde{\mathbf{u}} \qquad \text{on} \quad A_D\,, \tag{2.23c}$$

where the boundary has been split to $\partial V = A_N \cup A_D$ and $A_N \cap A_D = \emptyset$ (see Fig. 2.2) and the divergence operator for second order tensors reads

$$\mathrm{Div}\,\boldsymbol{P} = \begin{bmatrix} \mathrm{div}(\begin{bmatrix} P_{11} & P_{12} & P_{13}\end{bmatrix}) \\ \mathrm{div}(\begin{bmatrix} P_{21} & P_{22} & P_{23}\end{bmatrix}) \\ \mathrm{div}(\begin{bmatrix} P_{31} & P_{32} & P_{33}\end{bmatrix}) \end{bmatrix}\,, \qquad \mathrm{div}\,\mathbf{p} = \langle \nabla,\, \mathbf{p}\rangle\,. \tag{2.24}$$

Here, $\mathrm{div}(\cdot)$ defines the divergence operator for vectors. The prescribed displacement $\widetilde{\mathbf{u}}$ is set on the Dirichlet boundary A_D and the natural Neumann boundary condition of zero tractions is employed on A_N. From Eq. (2.20) one extracts the bilinear and linear forms

$$a(\delta\mathbf{u}, \mathbf{u}) = \int_V \langle \mathrm{sym}(\mathrm{D}\delta\mathbf{u}),\, \mathbb{C}\,\mathrm{sym}(\mathrm{D}\mathbf{u})\rangle\,\mathrm{d}V\,, \tag{2.25a}$$

$$l(\delta\mathbf{u}) = \int_V \langle \delta\mathbf{u},\, \mathbf{f}\rangle\,\mathrm{d}V\,. \tag{2.25b}$$

2.4 Reduced kinematics

The three-dimensional variational formulation introduced in Eq. (2.25) can be reduced to two-dimensional formulations by making some assumptions regarding the kinematics of the model. In the following we reduce the model to models of plane strain and antiplane shear.

2.4.1 Plane strain

In the plane strain model we assume a two-dimensional domain $A \subset \mathbb{R}^2$ where the strain in the third direction is set to zero. This implies no deformation can take place outside the plane

$$\mathbf{u} = \begin{bmatrix} u \\ v \end{bmatrix} , \qquad \boldsymbol{\varepsilon} = \begin{bmatrix} u_{,x} & 1/2(u_{,y} + v_{,x}) \\ 1/2(u_{,y} + v_{,x}) & v_{,y} \end{bmatrix} . \tag{2.26}$$

Although the stress tensor does contain out-of-plane components, they do not produce work as their strain counterparts are set to zero. Consequently, the material tensor can be reduced to $\mathbb{C} \in \mathbb{R}^{2\times2\times2\times2}$.

Remark 2.1
The reduction of the material tensor in the latter case applies only to the energy functional and the bilinear form. Computation of the stress tensor requires a different approach where the out-of-plane components are considered.

As such, one can formulate the reduced problem as

$$- \operatorname{Div}[\mathbb{C} \operatorname{sym}(\mathrm{D}\mathbf{u})] = \mathbf{f} \qquad \text{in} \quad A , \tag{2.27a}$$

$$[\mathbb{C} \operatorname{sym}(\mathrm{D}\mathbf{u})]\, \mathbf{n} = 0 \qquad \text{on} \quad s_N , \tag{2.27b}$$

$$\mathbf{u} = \widetilde{\mathbf{u}} \qquad \text{on} \quad s_D , \tag{2.27c}$$

where the boundary is reduced to the curve $\partial A = s = s_D \cup s_N$. The corresponding energy functional reads

$$I(\mathbf{u}) = \frac{1}{2} \int_A \langle \operatorname{sym} \mathrm{D}\mathbf{u},\, \mathbb{C}(\operatorname{sym} \mathrm{D}\mathbf{u}) \rangle \,\mathrm{d}A - \int_A \langle \mathbf{u},\, \mathbf{f} \rangle \,\mathrm{d}A \to \min \quad \text{w.r.t.} \quad \mathbf{u} , \tag{2.28}$$

and the bi-/ linear forms are given by

$$a(\delta\mathbf{u}, \mathbf{u}) = \int_A \langle \operatorname{sym}(\mathrm{D}\delta\mathbf{u}),\, \mathbb{C} \operatorname{sym}(\mathrm{D}\mathbf{u}) \rangle \,\mathrm{d}A , \tag{2.29a}$$

$$l(\delta\mathbf{u}) = \int_A \langle \delta\mathbf{u},\, \mathbf{f} \rangle \,\mathrm{d}A . \tag{2.29b}$$

2.4.2 Antiplane shear

An alternative reduction of the model is achieved when considering antiplane shear [106]. In this case, only out-of-plane displacements can occur. Consequently, the displacement vector is reduced to a scalar and the strain tensor is given by a two-dimensional vector $\boldsymbol{\varepsilon} = \nabla u$. Further, the material tensor is reduced to the shear modulus constant μ. The energy functional takes the form

$$I(u) = \frac{1}{2} \int_A \mu \| \nabla u \|^2 \,\mathrm{d}A - \int_A u\, f \,\mathrm{d}A \to \min \quad \text{w.r.t.} \quad u . \tag{2.30}$$

Variation leads to the bilinear and linear forms

$$a(\delta u, u) = \int_A \langle \nabla \delta u,\, \mu \nabla u \rangle \,\mathrm{d}A , \tag{2.31a}$$

$$l(\delta u) = \int_A \delta u\, f \,\mathrm{d}A . \tag{2.31b}$$

Partial integration with the Green-type formula

$$\int_A \langle \nabla q,\, \mathbf{v} \rangle \,\mathrm{d}A = \int_{\partial A} q \,\langle \mathbf{v},\, \mathbf{n} \rangle \,\mathrm{d}s - \int_A q \,\operatorname{div} \mathbf{v} \,\mathrm{d}A\,, \qquad q \in C^\infty(\overline{A}),\, \mathbf{v} \in [C^\infty(\overline{A})]^2\,, \tag{2.32}$$

yields

$$\int_{\partial A} \mu \,\delta u \,\langle \nabla u,\, \mathbf{n} \rangle \,\mathrm{d}s - \int_A (\delta u)\, \mu \,\Delta u \,\mathrm{d}A - \int_A \delta u \, f \,\mathrm{d}A = 0\,, \tag{2.33}$$

from which one extracts the strong form

$$-\mu \,\Delta u = f \qquad \text{in} \quad A\,, \tag{2.34a}$$

$$\langle \nabla u,\, \mathbf{n} \rangle = 0 \qquad \text{on} \quad s_N\,, \tag{2.34b}$$

$$u = \widetilde{u} \qquad \text{on} \quad s_D\,, \tag{2.34c}$$

representing a classical Poisson problem. The boundary of the domain is split into Dirichlet and Neumann boundaries $\partial A = s_D \cup s_N$.

3 Relaxed Micromorphic Continua

This chapter is dedicated to the introduction of the relaxed micromorphic model [75]. The full three-dimensional model is introduced and subsequently reduced to models of plane strain and antiplane shear. Further, edge cases with respect to the characteristic length L_c are expanded upon.

3.1 The relaxed micromorphic model

The relaxed micromorphic continuum is governed by a free energy functional, incorporating the gradient of the displacement field $\mathrm{D}\mathbf{u}$, the microdistortion $\boldsymbol{P}$ and the Curl of the microdistortion, namely the micro-dislocation

$$\begin{aligned} I(\mathbf{u}, \boldsymbol{P}) = \frac{1}{2} \int_V & \langle \operatorname{sym}(\mathrm{D}\mathbf{u} - \boldsymbol{P}),\, \mathbb{C}_\mathrm{e} \operatorname{sym}(\mathrm{D}\mathbf{u} - \boldsymbol{P}) \rangle + \langle \operatorname{sym} \boldsymbol{P},\, \mathbb{C}_\mathrm{micro} \operatorname{sym} \boldsymbol{P} \rangle \\ & + \langle \operatorname{skew}(\mathrm{D}\mathbf{u} - \boldsymbol{P}),\, \mathbb{C}_\mathrm{c} \operatorname{skew}(\mathrm{D}\mathbf{u} - \boldsymbol{P}) \rangle + \mu_\mathrm{macro} L_\mathrm{c}^2 \| \operatorname{Curl} \boldsymbol{P} \|^2 \, \mathrm{d}V \\ & - \int_V \langle \mathbf{u},\, \mathbf{f} \rangle + \langle \boldsymbol{P},\, \boldsymbol{M} \rangle \, \mathrm{d}V \to \min \quad \text{w.r.t.} \quad \{\mathbf{u}, \boldsymbol{P}\} \,, \end{aligned} \tag{3.1}$$

where the Curl operator for second order tensors is defined row-wise as

$$\begin{aligned} \operatorname{Curl} \boldsymbol{P} &= \begin{bmatrix} \operatorname{curl}(\begin{bmatrix} P_{11} & P_{12} & P_{13} \end{bmatrix}) \\ \operatorname{curl}(\begin{bmatrix} P_{21} & P_{22} & P_{23} \end{bmatrix}) \\ \operatorname{curl}(\begin{bmatrix} P_{31} & P_{32} & P_{33} \end{bmatrix}) \end{bmatrix} = \begin{bmatrix} P_{13,y} - P_{12,z} & P_{11,z} - P_{13,x} & P_{12,x} - P_{11,y} \\ P_{23,y} - P_{22,z} & P_{21,z} - P_{23,x} & P_{22,x} - P_{21,y} \\ P_{33,y} - P_{32,z} & P_{31,z} - P_{33,x} & P_{32,x} - P_{31,y} \end{bmatrix} \,, \\ \operatorname{curl} \mathbf{p} &= \nabla \times \mathbf{p} \,, \qquad \mathbf{p} : \overline{V} \subset \mathbb{R}^3 \to \mathbb{R}^3 \,, \end{aligned} \tag{3.2}$$

and $\operatorname{curl}(\cdot)$ is the vectorial curl operator. The displacement field and the microdistortion field are functions of the reference domain

$$\mathbf{u} : \overline{V} \subset \mathbb{R}^3 \to \mathbb{R}^3 \,, \qquad \boldsymbol{P} : \overline{V} \subset \mathbb{R}^3 \to \mathbb{R}^{3\times 3} \,. \tag{3.3}$$

The tensors $\mathbb{C}_\mathrm{e}, \mathbb{C}_\mathrm{micro} \in \mathbb{R}^{3\times3\times3\times3}$ are standard fourth order material tensors. For isotropic materials they take the same form as Eq. (2.18)

$$\mathbb{C}_\mathrm{e} = \lambda_\mathrm{e} \mathbb{1} \otimes \mathbb{1} + 2\mu_\mathrm{e} \, \mathbb{J} \,, \qquad \mathbb{C}_\mathrm{micro} = \lambda_\mathrm{micro} \mathbb{1} \otimes \mathbb{1} + 2\mu_\mathrm{micro} \, \mathbb{J} \,. \tag{3.4}$$

The fourth order tensor $\mathbb{C}_\mathrm{c} \in \mathbb{R}^{3\times3\times3\times3}$ is a positive semi-definite material tensor related to Cosserat micro-polar continua and accounts for infinitesimal rotations $\mathbb{C}_\mathrm{c} : \mathfrak{so}(3) \to \mathfrak{so}(3)$, where $\mathfrak{so}(3)$ is the space of skew-symmetric matrices. Consequently, one way to define the tensor for isotropic materials is by using the fourth order anti-symmetry tensor (see Appendix A)

$$\mathbb{C}_\mathrm{c} = 2\mu_\mathrm{c} \mathbb{A} \in \mathbb{R}^{3\times3\times3\times3} \,, \qquad \mathbb{A} : \mathbb{R}^{3\times3} \to \mathfrak{so}(3) \,. \tag{3.5}$$

The macroscopic shear modulus is denoted by μ_macro and L_c represents the characteristic length scale motivated by the geometry of the microstructure. The forces and micro-moments are given by $\mathbf{f}$ and $\boldsymbol{M}$, respectively.

Equilibria are found at minima of the energy functional. As such, we consider variations with respect to its parameters, namely the displacement and the microdistortion. Taking variations of the energy functional with respect to the displacement field $\mathbf{u}$ yields

$$\delta_u I = \int_V \langle \operatorname{sym} \mathrm{D}\delta\mathbf{u},\, \mathbb{C}_\mathrm{e} \operatorname{sym}(\mathrm{D}\mathbf{u} - \boldsymbol{P}) \rangle + \langle \operatorname{skew} \mathrm{D}\delta\mathbf{u},\, \mathbb{C}_\mathrm{c} \operatorname{skew}(\mathrm{D}\mathbf{u} - \boldsymbol{P}) \rangle - \langle \delta\mathbf{u},\, \mathbf{f} \rangle \, \mathrm{d}V = 0 \,. \tag{3.6}$$

The variation with respect to the microdistortion $\boldsymbol{P}$ results in

$$\begin{aligned}\delta_P I = \int_V &\langle \operatorname{sym}\delta\boldsymbol{P},\, \mathbb{C}_{\mathrm{e}} \operatorname{sym}(\mathrm{D}\mathbf{u} - \boldsymbol{P})\rangle + \langle \operatorname{skew}\delta\boldsymbol{P},\, \mathbb{C}_{\mathrm{c}} \operatorname{skew}(\mathrm{D}\mathbf{u} - \boldsymbol{P})\rangle \\ &- \langle \operatorname{sym}\delta\boldsymbol{P},\, \mathbb{C}_{\mathrm{micro}} \operatorname{sym}\boldsymbol{P}\rangle - \mu_{\mathrm{macro}} L_{\mathrm{c}}^2 \langle \operatorname{Curl}\delta\boldsymbol{P},\, \operatorname{Curl}\boldsymbol{P}\rangle + \langle \delta\boldsymbol{P},\, \boldsymbol{M}\rangle \,\mathrm{d}V = 0\,. \end{aligned} \tag{3.7}$$

From the total variation we extract the bilinear form

$$\begin{aligned} a(\{\delta\mathbf{u},\delta\boldsymbol{P}\},\{\mathbf{u},\boldsymbol{P}\}) = \int_V &\langle \operatorname{sym}(\mathrm{D}\delta\mathbf{u} - \delta\boldsymbol{P}),\, \mathbb{C}_{\mathrm{e}} \operatorname{sym}(\mathrm{D}\mathbf{u} - \boldsymbol{P})\rangle + \langle \operatorname{sym}\delta\boldsymbol{P},\, \mathbb{C}_{\mathrm{micro}} \operatorname{sym}\boldsymbol{P}\rangle \\ &+ \langle \operatorname{skew}(\mathrm{D}\delta\mathbf{u} - \delta\boldsymbol{P}),\, \mathbb{C}_{\mathrm{c}} \operatorname{skew}(\mathrm{D}\mathbf{u} - \boldsymbol{P})\rangle + \mu_{\mathrm{macro}} L_{\mathrm{c}}^2 \langle \operatorname{Curl}\delta\boldsymbol{P},\, \operatorname{Curl}\boldsymbol{P}\rangle \,\mathrm{d}V\,, \end{aligned} \tag{3.8}$$

and linear form of the loads

$$l(\{\delta\mathbf{u},\delta\boldsymbol{P}\}) = \int_V \langle \delta\mathbf{u},\, \mathbf{f}\rangle + \langle \delta\boldsymbol{P},\, \boldsymbol{M}\rangle \,\mathrm{d}V\,. \tag{3.9}$$

Applying integration by parts to Eq. (3.6) using Eq. (2.21) yields

$$\begin{aligned} &\int_{\partial V} \langle \delta\mathbf{u}\,, [\mathbb{C}_{\mathrm{e}} \operatorname{sym}(\mathrm{D}\mathbf{u} - \boldsymbol{P}) + \mathbb{C}_{\mathrm{c}} \operatorname{skew}(\mathrm{D}\mathbf{u} - \boldsymbol{P})]\,\mathbf{n}\rangle \,\mathrm{d}A \\ &\quad - \int_V \langle \delta\mathbf{u}\,, \operatorname{Div}[\mathbb{C}_{\mathrm{e}} \operatorname{sym}(\mathrm{D}\mathbf{u} - \boldsymbol{P}) + \mathbb{C}_{\mathrm{c}} \operatorname{skew}(\mathrm{D}\mathbf{u} - \boldsymbol{P})] - \mathbf{f}\rangle \,\mathrm{d}V = 0\,. \end{aligned} \tag{3.10}$$

Likewise, integration by parts of Eq. (3.7) using the Green-type formula

$$\int_V \langle \operatorname{Curl}\boldsymbol{T},\, \boldsymbol{Q}\rangle \,\mathrm{d}V = \int_{\partial V} \langle \boldsymbol{T},\, \boldsymbol{Q} \times \mathbf{n}\rangle \,\mathrm{d}A + \int_V \langle \boldsymbol{T},\, \operatorname{Curl}\boldsymbol{Q}\rangle \,\mathrm{d}V\,, \qquad \boldsymbol{T},\boldsymbol{Q} \in [C^\infty(\overline{V})]^{3\times 3}\,, \tag{3.11}$$

results in

$$\begin{aligned} &\int_V \langle \delta\boldsymbol{P},\, \mathbb{C}_{\mathrm{e}} \operatorname{sym}(\mathrm{D}\mathbf{u} - \boldsymbol{P}) + \mathbb{C}_{\mathrm{c}} \operatorname{skew}(\mathrm{D}\mathbf{u} - \boldsymbol{P}) - \mathbb{C}_{\mathrm{micro}} \operatorname{sym}\boldsymbol{P} - \mu_{\mathrm{macro}} L_{\mathrm{c}}^2 \operatorname{Curl}\operatorname{Curl}\boldsymbol{P} + \boldsymbol{M}\rangle \,\mathrm{d}V \\ &\quad - \mu_{\mathrm{macro}} L_{\mathrm{c}}^2 \int_{\partial V} \langle \delta\boldsymbol{P},\, \operatorname{Curl}\boldsymbol{P} \times \mathbf{n}\rangle \,\mathrm{d}A = 0\,. \end{aligned} \tag{3.12}$$

The strong form is extracted from Eq. (3.10) and Eq. (3.12) by splitting the boundary

$$A = A_D \cup A_N\,, \qquad\qquad A_D \cap A_N = \emptyset\,, \tag{3.13}$$

into a Dirichlet boundary with embedded boundary conditions and a Neumann boundary with natural

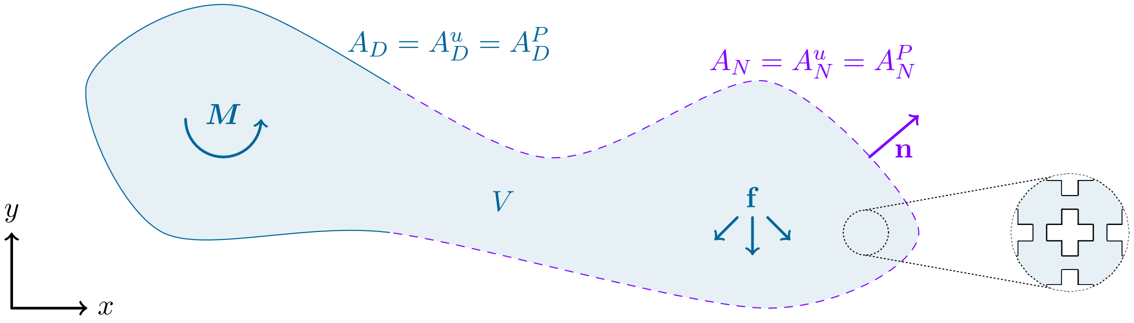

Figure 3.1: The domain in the relaxed micromorphic model with Dirichlet and Neumann boundaries under internal forces and micro-moments. The Dirichlet boundary of the microdistortion is given by the consistent coupling condition. The model can capture the complex kinematics of an underlying micro-structure.

boundary conditions, such that no tractions are defined on the Neumann boundary

$$-\operatorname{Div}[\mathbb{C}_{\mathrm{e}}\operatorname{sym}(\mathrm{D}\mathbf{u}-\boldsymbol{P})+\mathbb{C}_{\mathrm{c}}\operatorname{skew}(\mathrm{D}\mathbf{u}-\boldsymbol{P})]=\mathbf{f} \quad \text{in} \quad V\,, \tag{3.14a}$$

$$-\mathbb{C}_{\mathrm{e}}\operatorname{sym}(\mathrm{D}\mathbf{u}-\boldsymbol{P})-\mathbb{C}_{\mathrm{c}}\operatorname{skew}(\mathrm{D}\mathbf{u}-\boldsymbol{P})+\mathbb{C}_{\mathrm{micro}}\operatorname{sym}\boldsymbol{P}+\mu_{\mathrm{macro}}\,L_{\mathrm{c}}^2\operatorname{Curl}\operatorname{Curl}\boldsymbol{P}=\boldsymbol{M} \quad \text{in} \quad V\,, \tag{3.14b}$$

$$\mathbf{u}=\widetilde{\mathbf{u}} \quad \text{on} \quad A_D^u\,, \tag{3.14c}$$

$$\boldsymbol{P}\times\mathbf{n}=\widetilde{\boldsymbol{P}}\times\mathbf{n} \quad \text{on} \quad A_D^P\,, \tag{3.14d}$$

$$[\mathbb{C}_{\mathrm{e}}\operatorname{sym}(\mathrm{D}\mathbf{u}-\boldsymbol{P})+\mathbb{C}_{\mathrm{c}}\operatorname{skew}(\mathrm{D}\mathbf{u}-\boldsymbol{P})]\,\mathbf{n}=0 \quad \text{on} \quad A_N^u\,, \tag{3.14e}$$

$$\operatorname{Curl}\boldsymbol{P}\times\mathbf{n}=0 \quad \text{on} \quad A_N^P\,. \tag{3.14f}$$

We observe that the Dirichlet boundary condition for the microdistortion controls only its tangential components. It is unclear, how to to control the micro-movements of a material point without also affecting the displacement. As such, the relaxed micromorphic model introduces the so called consistent coupling condition [27]

$$\boldsymbol{P}\times\mathbf{n}=\mathrm{D}\widetilde{\mathbf{u}}\times\mathbf{n} \quad \text{on} \quad A_D^P\,, \tag{3.15}$$

where the prescribed displacement on the Dirichlet boundary $\widetilde{\mathbf{u}}$ automatically dictates the tangential component of the microdistortion on that same boundary. Consequently, the consistent coupling condition enforces the definitions $A_D = A_D^u = A_D^P$ and $A_N = A_N^u = A_N^P$ (see Fig. 3.1). Further, the consistent coupling condition substitutes Eq. (3.14d).

3.1.1 Lower limit of the characteristic length scale parameter $L_{\mathrm{c}} \to 0$

In the relaxed micromorphic model the characteristic length L_{c} takes the form of a scaling parameter between the macro and the micro scales. This characteristic allows the theory to iterate between materials with a pronounced micro-structure and fully homogeneous materials, thus relating the characteristic length scale parameter L_c to the size of the micro-structure in metamaterials. In the lower limit $L_\mathrm{c} \to 0$ the continuum is fully homogeneous and the solution of the classical Cauchy continuum theory is retrieved [7, 73]. This can be observed by reconsidering Eq. (3.14b)

$$-\mathbb{C}_\mathrm{e}\,\mathrm{sym}(\mathrm{D}\mathbf{u} - \boldsymbol{P}) - \mathbb{C}_\mathrm{c}\,\mathrm{skew}(\mathrm{D}\mathbf{u} - \boldsymbol{P}) + \mathbb{C}_\mathrm{micro}\,\mathrm{sym}\,\boldsymbol{P} = \boldsymbol{M}\,, \tag{3.16}$$

which can now be used to express the microdistortion $\boldsymbol{P}$ algebraically

$$\mathrm{sym}\,\boldsymbol{P} = (\mathbb{C}_\mathrm{e} + \mathbb{C}_\mathrm{micro})^{-1}(\mathrm{sym}\,\boldsymbol{M} + \mathbb{C}_\mathrm{e}\,\mathrm{sym}\,\mathrm{D}\mathbf{u})\,, \tag{3.17a}$$

$$\mathrm{skew}\,\boldsymbol{P} = \mathbb{C}_\mathrm{c}^{-1}\,\mathrm{skew}\,\boldsymbol{M} + \mathrm{skew}\,\mathrm{D}\mathbf{u}\,. \tag{3.17b}$$

Setting $\boldsymbol{M} = 0$ corresponds to Cauchy continua, where micro-moments are not accounted for. Thus, one finds

$$\mathbb{C}_\mathrm{c}\,\mathrm{skew}(\mathrm{D}\mathbf{u} - \boldsymbol{P}) = 0\,, \quad \mathbb{C}_\mathrm{e}\,\mathrm{sym}(\mathrm{D}\mathbf{u} - \boldsymbol{P}) = \mathbb{C}_\mathrm{micro}\,\mathrm{sym}\,\boldsymbol{P}\,, \quad \mathrm{sym}\,\boldsymbol{P} = (\mathbb{C}_\mathrm{e} + \mathbb{C}_\mathrm{micro})^{-1}\mathbb{C}_\mathrm{e}\,\mathrm{sym}\,\mathrm{D}\mathbf{u}\,. \tag{3.18}$$

Applying the upper results to Eq. (3.14a) yields

$$-\,\mathrm{Div}[\mathbb{C}_\mathrm{e}\,\mathrm{sym}(\mathrm{D}\mathbf{u} - \boldsymbol{P})] = -\,\mathrm{Div}[\mathbb{C}_\mathrm{micro}(\mathbb{C}_\mathrm{e} + \mathbb{C}_\mathrm{micro})^{-1}\mathbb{C}_\mathrm{e}\,\mathrm{sym}\,\mathrm{D}\mathbf{u}] = -\,\mathrm{Div}[\mathbb{C}_\mathrm{macro}\,\mathrm{sym}\,\mathrm{D}\mathbf{u}] = \mathbf{f}\,, \tag{3.19}$$

where the definition $\mathbb{C}_\mathrm{macro} = \mathbb{C}_\mathrm{micro}(\mathbb{C}_\mathrm{e} + \mathbb{C}_\mathrm{micro})^{-1}\mathbb{C}_\mathrm{e}$ relates the meso- and micro-elasticity tensors to the classical macro-elasticity tensor of the Cauchy continuum. In fact, $\mathbb{C}_\mathrm{macro}$ contains the material constants that arise from standard homogenization for large periodic structures [7, 73] and Eq. (3.19) is equivalent to Eq. (2.23). For isotropic materials one can directly compute the macro parameters

$$\mu_\mathrm{macro} = \frac{\mu_\mathrm{e}\,\mu_\mathrm{micro}}{\mu_\mathrm{e} + \mu_\mathrm{micro}}\,, \qquad 2\mu_\mathrm{macro} + 3\lambda_\mathrm{macro} = \frac{(2\mu_\mathrm{e} + 3\lambda_\mathrm{e})(2\mu_\mathrm{micro} + 3\lambda_\mathrm{micro})}{(2\mu_\mathrm{e} + 3\lambda_\mathrm{e}) + (2\mu_\mathrm{micro} + 3\lambda_\mathrm{micro})}\,. \tag{3.20}$$

We note that by Eq. (3.17) even if the micro-moments are given by a gradient field $\boldsymbol{M} = \mathrm{D}\mathbf{m}$ for some vector $\mathbf{m}$, it does **not** imply $\boldsymbol{P} = \mathrm{D}\mathbf{v}$ for some vector $\mathbf{v}$. In other words, in the general case the microdistortion field is not a gradient.

3.1.2 Upper limit of the characteristic length scale parameter $L_\mathrm{c} \to +\infty$

In the upper limit $L_\mathrm{c} \to +\infty$, the stiffness of the micro-body becomes dominant. As the characteristic length L_c can be viewed as a zoom-factor into the microstructure, the state $L_\mathrm{c} \to +\infty$ can be interpreted as the entire domain being the micro-body itself. However, this is only theoretically possible as in practice, the limit is given by the size of one unit cell. Since the energy functional is being minimized, on contractible domains this implies the reduction of the microdistortion to a gradient field $\boldsymbol{P} \to \mathrm{D}\mathbf{v}$ due to the classical identity

$$\mathrm{Curl}\,\mathrm{D}\mathbf{v} = 0 \quad \forall\,\mathbf{v} \in [C^\infty(V)]^3\,, \tag{3.21}$$

thus asserting finite energies of the relaxed micromorphic model for large characteristic length values. Since only the micro-body is considered, one sets $\mathbf{f} = 0$ to find

$$-\,\mathrm{Div}[\mathbb{C}_\mathrm{e}\,\mathrm{sym}(\mathrm{D}\mathbf{u} - \boldsymbol{P}) + \mathbb{C}_\mathrm{c}\,\mathrm{skew}(\mathrm{D}\mathbf{u} - \boldsymbol{P})] = 0\,, \tag{3.22}$$

for Eq. (3.14a). As such, taking the divergence of Eq. (3.14b) yields

$$\operatorname{Div}(\mathbb{C}_{\text{micro}} \operatorname{sym} \mathrm{D}\mathbf{v}) = \operatorname{Div} \boldsymbol{M} \,. \tag{3.23}$$

The divergence of the micro-moments $\operatorname{Div} \boldsymbol{M}$ can be interpreted as the micro body-forces. The latter implies that the limit $L_{\text{c}} \to +\infty$ defines a classical Cauchy continuum with a finite stiffness governed by $\mathbb{C}_{\text{micro}}$, representing the upper limit of the stiffness for the relaxed micromorphic continuum. Further, note that due to Eq. (3.22) and the consistent coupling condition Eq. (3.15) there holds $\mathbf{v} = \mathbf{u}$ since the solution is unique.

Remark 3.1
If we assume $\mathbb{C}_{\text{micro}} \to \infty$ then there follows $\boldsymbol{P} \in \mathfrak{so}(3)$ for finite energies such that the material point becomes non-deformable and the relaxed micromorphic model reduces to an equivalent Cosserat micro-polar model [75].

3.2 Reduced kinematics

In the following we introduce analogues to the plane strain and antiplane shear models of linear elasticity for the relaxed micromorphic model. The reduction follows the assertion that the microdistortion field has as many components as the gradient of the displacement field. Further, the reduction makes use of the two-dimensional versions of the curl operator

$$\operatorname{div}(\boldsymbol{R}\mathbf{p}) = p_{2,x} - p_{1,y} \,, \qquad \boldsymbol{R}\nabla p = \begin{bmatrix} p_{,y} \\ -p_{,x} \end{bmatrix} , \qquad \boldsymbol{R} = \begin{bmatrix} 0 & 1 \\ -1 & 0 \end{bmatrix} , \tag{3.24}$$

for vectorial and scalar fields, respectively. The operators arise by considering bivariate fields on a the (x, y)-plane in the $\mathbb{R}^3$-space, where vectors are written using the first and second components, and scalars are in the third position of a vector.

3.2.1 Plane strain

Analogous to Section 2.4.1 plane strain assumes the displacement field $\mathbf{u} = \begin{bmatrix} u & v \end{bmatrix}^T$, such that the gradient and the microdistortion read

$$\mathrm{D}\mathbf{u} = \begin{bmatrix} u_{,x} & u_{,y} \\ v_{,x} & v_{,y} \end{bmatrix} , \qquad \boldsymbol{P} = \begin{bmatrix} P_{11} & P_{12} \\ P_{21} & P_{22} \end{bmatrix} . \tag{3.25}$$

The material tensors are reduced to $\mathbb{C}_{\text{e}}, \mathbb{C}_{\text{c}}, \mathbb{C}_{\text{micro}} \in \mathbb{R}^{2\times2\times2\times2}$.

Remark 3.2
Note that the material tensors are only used in the energy functional and the bilinear form. Computation of out-of-plane stress components requires a different approach.

While the energy functional

$$\begin{aligned} I(\mathbf{u}, \boldsymbol{P}) = \frac{1}{2} \int_A & \langle \operatorname{sym}(\mathrm{D}\mathbf{u} - \boldsymbol{P}),\, \mathbb{C}_{\text{e}} \operatorname{sym}(\mathrm{D}\mathbf{u} - \boldsymbol{P}) \rangle + \langle \operatorname{sym} \boldsymbol{P},\, \mathbb{C}_{\text{micro}} \operatorname{sym} \boldsymbol{P} \rangle \\ & + \langle \operatorname{skew}(\mathrm{D}\mathbf{u} - \boldsymbol{P}),\, \mathbb{C}_{\text{c}} \operatorname{skew}(\mathrm{D}\mathbf{u} - \boldsymbol{P}) \rangle + \mu_{\text{macro}} L_{\text{c}}^2 \| \operatorname{Curl} \boldsymbol{P} \|^2 \, \mathrm{d}A \\ & - \int_A \langle \mathbf{u},\, \mathbf{f} \rangle + \langle \boldsymbol{P},\, \boldsymbol{M} \rangle \, \mathrm{d}A \to \min \quad \text{w.r.t.} \quad \{\mathbf{u}, \boldsymbol{P}\} \,. \end{aligned} \tag{3.26}$$

and the (bi)linear forms

$$a(\{\delta\mathbf{u},\delta\boldsymbol{P}\},\{\mathbf{u},\boldsymbol{P}\}) = \int_A \langle \operatorname{sym}(\mathrm{D}\delta\mathbf{u}-\delta\boldsymbol{P}),\, \mathbb{C}_{\mathrm{e}}\operatorname{sym}(\mathrm{D}\mathbf{u}-\boldsymbol{P})\rangle + \langle \operatorname{sym}\delta\boldsymbol{P},\, \mathbb{C}_{\mathrm{micro}}\operatorname{sym}\boldsymbol{P}\rangle \tag{3.27a}$$

$$+ \langle \operatorname{skew}(\mathrm{D}\delta\mathbf{u}-\delta\boldsymbol{P}),\, \mathbb{C}_{\mathrm{c}}\operatorname{skew}(\mathrm{D}\mathbf{u}-\boldsymbol{P})\rangle + \mu_{\mathrm{macro}}L_{\mathrm{c}}^2\langle \operatorname{Curl}\delta\boldsymbol{P},\, \operatorname{Curl}\boldsymbol{P}\rangle\,\mathrm{d}A\,,$$

$$l(\{\delta\mathbf{u},\delta\boldsymbol{P}\}) = \int_A \langle\delta\mathbf{u},\,\mathbf{f}\rangle + \langle\delta\boldsymbol{P},\,\boldsymbol{M}\rangle\,\mathrm{d}A\,, \tag{3.27b}$$

maintain their notation with the exception of the adaption to a two dimensional domain, we note that by Eq. (3.24) $\operatorname{Curl}\boldsymbol{P}$ now reads

$$\operatorname{Curl}\boldsymbol{P} = \begin{bmatrix}\operatorname{div}(\boldsymbol{R}\begin{bmatrix}P_{11} & P_{12}\end{bmatrix}) \\ \operatorname{div}(\boldsymbol{R}\begin{bmatrix}P_{21} & P_{22}\end{bmatrix})\end{bmatrix} = \begin{bmatrix}P_{12,x}-P_{11,y} \\ P_{22,x}-P_{21,y}\end{bmatrix}\,, \tag{3.28}$$

such that a vector is produced by the operator. Furthermore, in two dimensions the Curl-Curl operation is a combination of the two two-dimensional curl operators (see Eq. (3.24)) and yields

$$\operatorname{Curl}\operatorname{Curl}\boldsymbol{P} = \begin{bmatrix}\boldsymbol{R}\nabla\operatorname{div}(\boldsymbol{R}\mathbf{p}_1) \\ \boldsymbol{R}\nabla\operatorname{div}(\boldsymbol{R}\mathbf{p}_2)\end{bmatrix} = \begin{bmatrix}P_{12,xy}-P_{11,yy} & P_{11,yx}-P_{12,xx} \\ P_{22,xy}-P_{21,yy} & P_{21,yx}-P_{22,xx}\end{bmatrix}\,, \tag{3.29}$$

such that the strong form with boundary conditions adapted to two dimensions reads

$$-\operatorname{Div}[\mathbb{C}_{\mathrm{e}}\operatorname{sym}(\mathrm{D}\mathbf{u}-\boldsymbol{P}) + \mathbb{C}_{\mathrm{c}}\operatorname{skew}(\mathrm{D}\mathbf{u}-\boldsymbol{P})] = \mathbf{f} \quad \text{in} \quad A\,, \tag{3.30a}$$

$$-\mathbb{C}_{\mathrm{e}}\operatorname{sym}(\mathrm{D}\mathbf{u}-\boldsymbol{P}) - \mathbb{C}_{\mathrm{c}}\operatorname{skew}(\mathrm{D}\mathbf{u}-\boldsymbol{P}) + \mathbb{C}_{\mathrm{micro}}\operatorname{sym}\boldsymbol{P} + \mu_{\mathrm{macro}}\,L_{\mathrm{c}}^2\operatorname{Curl}\operatorname{Curl}\boldsymbol{P} = \boldsymbol{M} \quad \text{in} \quad A\,, \tag{3.30b}$$

$$\mathbf{u} = \widetilde{\mathbf{u}} \quad \text{on} \quad s_D^u\,, \tag{3.30c}$$

$$\boldsymbol{P}\,\mathbf{t} = \widetilde{\boldsymbol{P}}\,\mathbf{t} \quad \text{on} \quad s_D^P\,, \tag{3.30d}$$

$$[\mathbb{C}_{\mathrm{e}}\operatorname{sym}(\mathrm{D}\mathbf{u}-\boldsymbol{P}) + \mathbb{C}_{\mathrm{c}}\operatorname{skew}(\mathrm{D}\mathbf{u}-\boldsymbol{P})]\,\mathbf{n} = 0 \quad \text{on} \quad s_N^u\,, \tag{3.30e}$$

$$\langle\operatorname{Curl}\boldsymbol{P},\,\mathbf{t}\rangle = 0 \quad \text{on} \quad s_N^P\,. \tag{3.30f}$$

Here the boundary is reduced to the curve $\partial A = s = s_D \cup s_N$.

3.2.2 Antiplane shear

We introduce the relaxed micromorphic model of antiplane shear by reducing the displacement field to

$$\mathbf{u} = \begin{bmatrix}0\\0\\u\end{bmatrix}\,, \tag{3.31}$$

such that $\mathbf{u} = \mathbf{u}(x, y)$ is a function of the $x - y$-plane. Consequently, its gradient reads

$$\mathrm{D}\mathbf{u} = \begin{bmatrix} 0 & 0 & 0 \\ 0 & 0 & 0 \\ u_{,x} & u_{,y} & 0 \end{bmatrix} . \tag{3.32}$$

The structure of the microdistortion tensor is chosen accordingly

$$\boldsymbol{P} = \begin{bmatrix} 0 & 0 & 0 \\ 0 & 0 & 0 \\ p_1 & p_2 & 0 \end{bmatrix} . \tag{3.33}$$

Analogously to the displacement field $\mathbf{u}$, the microdistortion $\boldsymbol{P}$ is also set to be a function of the $\{x, y\}$-variables $\boldsymbol{P} = \boldsymbol{P}(x, y)$. We observe the following sym-skew decompositions of the gradient and microdistortion tensors

$$\begin{aligned} \operatorname{sym} \boldsymbol{P} &= \frac{1}{2} \begin{bmatrix} 0 & 0 & p_1 \\ 0 & 0 & p_2 \\ p_1 & p_2 & 0 \end{bmatrix} , \qquad \operatorname{sym}(\mathrm{D}\mathbf{u} - \boldsymbol{P}) = \frac{1}{2} \begin{bmatrix} 0 & 0 & u_{,x} - p_1 \\ 0 & 0 & u_{,y} - p_2 \\ u_{,x} - p_1 & u_{,y} - p_2 & 0 \end{bmatrix} , \\ \operatorname{skew}(\mathrm{D}\mathbf{u} - \boldsymbol{P}) &= \frac{1}{2} \begin{bmatrix} 0 & 0 & p_1 - u_{,x} \\ 0 & 0 & p_2 - u_{,y} \\ u_{,x} - p_1 & u_{,y} - p_2 & 0 \end{bmatrix} . \end{aligned} \tag{3.34}$$

Clearly, there holds

$$\operatorname{tr}[\operatorname{sym} \boldsymbol{P}] = \operatorname{tr}[\operatorname{sym}(\mathrm{D}\mathbf{u} - \boldsymbol{P})] = \operatorname{tr}[\operatorname{skew}(\mathrm{D}\mathbf{u} - \boldsymbol{P})] = 0 , \tag{3.35}$$

such that the contraction with the material tensors reduces to

$$\begin{aligned} &\mathbb{C}_{\mathrm{e}} \operatorname{sym}(\mathrm{D}\mathbf{u} - \boldsymbol{P}) = 2\mu_{\mathrm{e}} \operatorname{sym}(\mathrm{D}\mathbf{u} - \boldsymbol{P}) , \qquad \mathbb{C}_{\mathrm{micro}} \operatorname{sym}(\mathrm{D}\mathbf{u} - \boldsymbol{P}) = 2\mu_{\mathrm{micro}} \operatorname{sym} \boldsymbol{P} , \\ &\mathbb{C}_{\mathrm{c}} \operatorname{skew}(\mathrm{D}\mathbf{u} - \boldsymbol{P}) = 2\mu_{\mathrm{c}} \operatorname{skew}(\mathrm{D}\mathbf{u} - \boldsymbol{P}) . \end{aligned} \tag{3.36}$$

As such, the quadratic forms of the energy functional are given by

$$\begin{aligned} \langle \operatorname{sym}(\mathrm{D}\mathbf{u} - \boldsymbol{P}), \, \mathbb{C}_{\mathrm{e}} \operatorname{sym}(\mathrm{D}\mathbf{u} - \boldsymbol{P}) \rangle &= 2\mu_{\mathrm{e}} \langle \operatorname{sym}(\mathrm{D}\mathbf{u} - \boldsymbol{P}), \, \operatorname{sym}(\mathrm{D}\mathbf{u} - \boldsymbol{P}) \rangle \\ &= \frac{2\mu_{\mathrm{e}}}{4} ([u_{,x} - p_1]^2 + [u_{,y} - p_2]^2 + [u_{,x} - p_1]^2 + [u_{,y} - p_2]^2) \\ &= \mu_{\mathrm{e}} \|\nabla u - \mathbf{p}\|^2 , \end{aligned} \tag{3.37a}$$

$$\begin{aligned} \langle \operatorname{skew}(\mathrm{D}\mathbf{u} - \boldsymbol{P}), \, \mathbb{C}_{\mathrm{c}} \operatorname{skew}(\mathrm{D}\mathbf{u} - \boldsymbol{P}) \rangle &= 2\mu_{\mathrm{c}} \langle \operatorname{skew}(\mathrm{D}\mathbf{u} - \boldsymbol{P}), \, \operatorname{skew}(\mathrm{D}\mathbf{u} - \boldsymbol{P}) \rangle \\ &= \frac{2\mu_{\mathrm{c}}}{4} ([p_1 - u_{,x}]^2 + [p_2 - u_{,y}]^2 + [u_{,x} - p_1]^2 + [u_{,y} - p_2]^2) \\ &= \mu_{\mathrm{c}} \|\nabla u - \mathbf{p}\|^2 , \end{aligned} \tag{3.37b}$$

$$\begin{aligned} \langle \operatorname{sym} \boldsymbol{P}, \, \mathbb{C}_{\mathrm{micro}} \operatorname{sym} \boldsymbol{P} \rangle &= 2\mu_{\mathrm{micro}} \langle \operatorname{sym} \boldsymbol{P}, \, \operatorname{sym} \boldsymbol{P} \rangle \\ &= \frac{2\mu_{\mathrm{micro}}}{4} (p_1^2 + p_2^2 + p_1^2 + p_2]^2 \\ &= \mu_{\mathrm{micro}} \|\mathbf{p}\|^2 , \end{aligned} \tag{3.37c}$$

with the definitions

$$\nabla u = \begin{bmatrix} u_{,x} \\ u_{,y} \end{bmatrix} \,, \qquad\qquad \mathbf{p} = \begin{bmatrix} p_1 \\ p_2 \end{bmatrix} \,. \tag{3.38}$$

The resulting energy functional for antiplane shear reads

$$I(u,\mathbf{p}) = \frac{1}{2}\int_A (\mu_{\mathrm{e}}+\mu_{\mathrm{c}})\|\nabla u - \mathbf{p}\|^2 + \mu_{\mathrm{micro}}\|\mathbf{p}\|^2 + \mu_{\mathrm{macro}} L_{\mathrm{c}}^2 \|\mathrm{div}(\boldsymbol{R}\mathbf{p})\|^2 \,\mathrm{d}A - \int_A u\, f + \langle \mathbf{p},\, \mathbf{m}\rangle \,\mathrm{d}A \,. \tag{3.39}$$

In order to maintain consistency with the three-dimensional model we must choose $\mu_{\mathrm{c}} = 0$. The reasoning for this choice is explained upon in Remark 3.3. Consequently, the energy functional is given by

$$\begin{aligned} I(u,\mathbf{p}) = \frac{1}{2}\int_A &\mu_{\mathrm{e}}\|\nabla u - \mathbf{p}\|^2 + \mu_{\mathrm{micro}}\|\mathbf{p}\|^2 + \mu_{\mathrm{macro}} L_{\mathrm{c}}^2 \|\mathrm{div}(\boldsymbol{R}\mathbf{p})\|^2 \,\mathrm{d}A \\ &- \int_A u\, f \; + \langle \mathbf{p},\, \mathbf{m}\rangle \,\mathrm{d}A \to \min \quad \text{w.r.t.} \quad \{u, \mathbf{p}\} \,. \end{aligned} \tag{3.40}$$

Taking variations with respect to the displacement field results in

$$\delta_u I = \int_A \mu_{\mathrm{e}} \langle \nabla \delta u,\, \nabla u - \mathbf{p}\rangle - \delta u\, f \,\mathrm{d}A = 0 \,, \tag{3.41}$$

and variation with respect to the microdistortion yields

$$\delta_p I = \int_A \mu_{\mathrm{e}} \langle \delta\mathbf{p},\, \nabla u - \mathbf{p}\rangle - \mu_{\mathrm{micro}}\langle \delta\mathbf{p},\, \mathbf{p}\rangle - \mu_{\mathrm{macro}} L_{\mathrm{c}}^2 \mathrm{div}(\boldsymbol{R}\delta\mathbf{p})\mathrm{div}(\boldsymbol{R}\mathbf{p}) + \langle \delta\mathbf{p},\, \mathbf{m}\rangle \,\mathrm{d}A = 0 \,. \tag{3.42}$$

Consequently, one finds the bilinear and linear forms

$$a(\{\delta u, \delta\mathbf{p}\}, \{u, \mathbf{p}\}) = \int_A \mu_{\mathrm{e}} \langle \nabla \delta u - \delta\mathbf{p},\, \nabla u - \mathbf{p}\rangle + \mu_{\mathrm{micro}}\langle \delta\mathbf{p},\, \mathbf{p}\rangle + \mu_{\mathrm{macro}} L_{\mathrm{c}}^2 \mathrm{div}(\boldsymbol{R}\delta\mathbf{p})\mathrm{div}(\boldsymbol{R}\mathbf{p}) \,\mathrm{d}A \,, \tag{3.43a}$$

$$l(\{\delta u, \delta\mathbf{p}\}) = \int_A \delta u\, f + \langle \delta\mathbf{p},\, \mathbf{m}\rangle \,\mathrm{d}A \,. \tag{3.43b}$$

Partial integration of Eq. (3.41) using Eq. (2.32) results in

$$\int_{\partial A} \delta u\, \langle \mu_{\mathrm{e}}(\nabla u - \mathbf{p}),\, \mathbf{n}\rangle \,\mathrm{d}s - \int_A \delta u\, [\mu_{\mathrm{e}}\, \mathrm{div}(\nabla u - \mathbf{p}) + f] \,\mathrm{d}A = 0 \,. \tag{3.44}$$

Applying the Green-type formula

$$\int_A \mathrm{div}(\boldsymbol{R}\mathbf{v})\, q \,\mathrm{d}A = \int_{\partial A} \langle \mathbf{v},\, \mathbf{t}\rangle\, q \,\mathrm{d}s + \int_A \langle \mathbf{v},\, \boldsymbol{R}\nabla q\rangle \,\mathrm{d}A \,, \qquad \mathbf{v} \in [C^\infty(\overline{A})]^2,\, q \in C^\infty(\overline{A}) \,, \tag{3.45}$$

to Eq. (3.42) yields

$$\int_A \langle \delta\mathbf{p},\, \mu_{\mathrm{e}}(\nabla u - \mathbf{p}) - \mu_{\mathrm{micro}}\,\mathbf{p} - \mu_{\mathrm{macro}} L_{\mathrm{c}}^2 \boldsymbol{R}\nabla\mathrm{div}(\boldsymbol{R}\mathbf{p}) + \mathbf{m}\rangle \,\mathrm{d}A - \int_{\partial A} \langle \delta\mathbf{p},\, \mu_{\mathrm{macro}} L_{\mathrm{c}}^2 \mathrm{div}(\boldsymbol{R}\mathbf{p})\, \mathbf{t}\rangle \,\mathrm{d}s = 0 \,. \tag{3.46}$$

Consequently, the strong form reads

$$-\mu_{\mathrm{e}}\,\mathrm{div}(\nabla u-\mathbf{p})=f \qquad \text{in} \quad A\,, \tag{3.47a}$$

$$-\mu_{\mathrm{e}}(\nabla u-\mathbf{p})+\mu_{\mathrm{micro}}\,\mathbf{p}+\mu_{\mathrm{macro}}L_{\mathrm{c}}^2\boldsymbol{R}\nabla\mathrm{div}(\boldsymbol{R}\mathbf{p})=\mathbf{m} \qquad \text{in} \quad A\,, \tag{3.47b}$$

$$u=\widetilde{u} \qquad \text{on} \quad s_D^u\,, \tag{3.47c}$$

$$\langle\mathbf{p},\,\mathbf{t}\rangle=\langle\widetilde{\mathbf{p}},\,\mathbf{t}\rangle \qquad \text{on} \quad s_D^P\,, \tag{3.47d}$$

$$\langle\nabla u,\,\mathbf{n}\rangle=\langle\mathbf{p},\,\mathbf{n}\rangle \qquad \text{on} \quad s_N^u\,, \tag{3.47e}$$

$$\mathrm{div}(\boldsymbol{R}\mathbf{p})=0 \qquad \text{on} \quad s_N^P\,. \tag{3.47f}$$

3.2.3 Limits of the characteristic length scale parameter L_{c} in antiplane shear

We reconsider the case of a homogeneous material by setting $L_{\mathrm{c}}\to 0$ in the reduced model for antiplane shear. Thus, we find the algebraic identity

$$-\mu_{\mathrm{e}}(\nabla u-\mathbf{p})+\mu_{\mathrm{micro}}\,\mathbf{p}=\mathbf{m}\,, \tag{3.48}$$

derived by using Eq. (3.47a) and Eq. (3.47b). Note that if $\mathbf{m}=\nabla m$ for some scalar field m one finds

$$\mathbf{p}=\nabla\left(\frac{m+\mu_{\mathrm{e}}\,u}{\mu_{\mathrm{e}}+\mu_{\mathrm{micro}}}\right)\,. \tag{3.49}$$

In other words, the microdistortion is reduced to a gradient field if the right hand side given by the micro-moment has a scalar potential and the characteristic length vanishes. Setting $m=0$ leads to the Poisson equation

$$-\,\mathrm{div}\left(\frac{\mu_{\mathrm{e}}\mu_{\mathrm{micro}}}{\mu_{\mathrm{e}}+\mu_{\mathrm{micro}}}\nabla u\right)=-\left(\frac{\mu_{\mathrm{e}}\mu_{\mathrm{micro}}}{\mu_{\mathrm{e}}+\mu_{\mathrm{micro}}}\right)\Delta u=-\mu_{\mathrm{macro}}\Delta u=f\,, \tag{3.50}$$

where the first identity in Eq. (3.20) is used for the definition of the macro parameter.

Remark 3.3
The latter identity forces to choose $\mu_{\mathrm{c}}=0$ in the antiplane shear model, since otherwise the result would read

$$-\left(\frac{\mu_{\mathrm{micro}}[\mu_{\mathrm{e}}+\mu_{\mathrm{c}}]}{\mu_{\mathrm{e}}+\mu_{\mathrm{c}}+\mu_{\mathrm{micro}}}\right)\Delta u=f\,, \tag{3.51}$$

where the relation to the macro parameter μ_{macro} in Eq. (3.20) is lost. Further, the limit defined in Eq. (3.17) with $\boldsymbol{M}=0$ yields the contradiction

$$\mathrm{sym}\,\boldsymbol{P}=(\mathbb{C}_{\mathrm{e}}+\mathbb{C}_{\mathrm{micro}})^{-1}\mathbb{C}_{\mathrm{e}}\,\mathrm{sym}\,\mathrm{D}\mathbf{u}\,, \qquad \mathbb{C}_{\mathrm{c}}\,\mathrm{skew}\,\boldsymbol{P}=\mathbb{C}_{\mathrm{c}}\,\mathrm{skew}\,\mathrm{D}\mathbf{u}\,, \tag{3.52}$$

since the equations degenerate to

$$\mathbf{p}=\frac{\mu_{\mathrm{e}}}{\mu_{\mathrm{e}}+\mu_{\mathrm{micro}}}\nabla u\,, \qquad \mu_{\mathrm{c}}\mathbf{p}=\mu_{\mathrm{c}}\nabla u\,. \tag{3.53}$$

Choosing $\mu_{\mathrm{micro}} = 0$ *leads to a loss of structure in the strong form Eq.* (2.34)*, while satisfying Eq.* (3.53)*. As such, we choose* $\mu_{\mathrm{c}} = 0$*, thus preserving the structure of the equations and satisfying both Eq.* (3.20) *and Eq.* (3.53)*.*

Although the relaxed micromorphic model includes the Cosserat model as a singular limit for $\mu_{\mathrm{micro}} \to \infty$*, it is impossible to deduce the Cosserat model of antiplane shear as a limit of the relaxed micromorphic model, since one needs to satisfy Eq.* (3.53) *for* $\mu_{\mathrm{c}} > 0$ *and* $\mu_{\mathrm{micro}} \to \infty$*, which is impossible.*

Taking the upper limit of the characteristic length $L_{\mathrm{c}} \to \infty$ implies

$$\mathbf{p} = \nabla p \,, \tag{3.54}$$

on contractible domains, thus ensuring finite energies. By setting $f = 0$ in Eq. (3.47b) and taking the divergence of Eq. (3.47a) one finds the Poisson equation

$$\mu_{\mathrm{micro}} \Delta p = \operatorname{div} \mathbf{m} \,, \tag{3.55}$$

where $\operatorname{div} \mathbf{m}$ can be interpreted as the volume force acting on the micro-body.

4 Variational Framework

This chapter is dedicated to the introduction of the natural function spaces [69] for the variational formulation of relaxed micromorphic models, and the demonstration of the well-posedness of the models via classical existence and uniqueness theorems.

4.1 Hilbert spaces

The common differential operators are usually not defined for finite elements due to jumps in the continuity of piece-wise approximations. As such, we introduce the generalized differential operators [110] by using test functions on elements of the Lebesgue space

$$L^2(V) = \{u : V \to \mathbb{R} \mid \|u\|_{L^2(V)} < \infty\} \, , \qquad \|u\|^2_{L^2(V)} = \langle u, \, u \rangle_{L^2(V)} = \int_V u^2 \, \mathrm{d}V \, , \tag{4.1}$$

denoting finite square integrable functions on the domain. The operators are defined using continuous test functions with compact support

$$C_0^\infty(\overline{V}) = \left\{ q \in C^\infty(\overline{V}) \mid q \bigg|_{\partial V} = 0 \right\} . \tag{4.2}$$

Definition 4.1 (Generalized differential operators)
The generalized differential operators are defined as follows:

1. *Let $u \in L^2(V)$, we define $\mathbf{v} = \nabla u$ to be its generalized gradient if there holds*

$$- \int_V u \operatorname{div} \mathbf{q} \, \mathrm{d}V = \int_V \langle \mathbf{v}, \, \mathbf{q} \rangle \, \mathrm{d}V \quad \forall \, \mathbf{q} \in [C_0^\infty(\overline{V})]^d \, ,$$

   where $d \in \{2, 3\}$ is according to the dimensionality of $\mathbf{v}$.

2. *Let $\mathbf{u} \in [L^2(A)]^2$, its generalized two-dimensional curl, $v = \operatorname{div}(\boldsymbol{R}\mathbf{u})$, is defined if there holds*

$$\int_A \langle \mathbf{u}, \, \boldsymbol{R} \nabla q \rangle \, \mathrm{d}A = \int_A v \, q \, \mathrm{d}A \quad \forall \, q \in C_0^\infty(\overline{A}) \, ,$$

3. *Let $\mathbf{u} \in [L^2(V)]^3$, its generalized curl is given by $\mathbf{v} = \operatorname{curl} \mathbf{u}$ if there holds*

$$\int_V \langle \mathbf{u}, \, \operatorname{curl} \mathbf{q} \rangle \, \mathrm{d}V = \int_V \langle \mathbf{v}, \, \mathbf{q} \rangle \, \mathrm{d}V \quad \forall \, \mathbf{q} \in [C_0^\infty(\overline{V})]^3 \, .$$

4. *Let $\mathbf{u} \in [L^2(V)]^3$, one can define its generalized divergence with $v = \operatorname{div} \mathbf{u}$ if there holds*

$$- \int_V \langle \mathbf{u}, \, \nabla q \rangle \, \mathrm{d}V = \int_V v \, q \, \mathrm{d}V \quad \forall \, q \in C_0^\infty(\overline{V}) \, .$$

Next we define Hilbert spaces with norms based on scalar products, where the differential operators are understood in the generalized sense. The following Hilbert spaces are based on the Lebesgue space and define scalar products and norms derived from it

$$H^1(V) = \{u \in L^2(V) \mid \nabla u \in [L^2(V)]^d\} \, , \qquad \|u\|^2_{H^1(V)} = \|u\|^2_{L^2} + \|\nabla u\|^2_{L^2} \, , \tag{4.3a}$$

$$H(\operatorname{div}\boldsymbol{R}, A) = \{\mathbf{u} \in [L^2(A)]^2 \mid \operatorname{div}(\boldsymbol{R}\mathbf{u}) \in L^2(A)\} \, , \quad \|u\|^2_{H(\operatorname{div}\boldsymbol{R}, A)} = \|\mathbf{u}\|^2_{L^2} + \|\operatorname{div}(\boldsymbol{R}\mathbf{u})\|^2_{L^2} \, , \tag{4.3b}$$

$$H(\operatorname{curl}, V) = \{\mathbf{u} \in [L^2(V)]^3 \mid \operatorname{curl} \mathbf{u} \in [L^2(V)]^3\} \, , \quad \|u\|^2_{H(\operatorname{curl}, V)} = \|\mathbf{u}\|^2_{L^2} + \|\operatorname{curl} \mathbf{u}\|^2_{L^2} \, , \tag{4.3c}$$

$$H(\operatorname{div}, V) = \{\mathbf{u} \in [L^2(V)]^3 \mid \operatorname{div} \mathbf{u} \in L^2(V)\} \, , \qquad \|u\|^2_{H(\operatorname{div}, V)} = \|\mathbf{u}\|^2_{L^2} + \|\operatorname{div} \mathbf{u}\|^2_{L^2} \, . \tag{4.3d}$$

$$\begin{tikzcd}
\mathbb{R} \arrow[r, "\mathrm{id}"] & H^1(V) \arrow[r, "\nabla"] & H(\mathrm{curl}, V) \arrow[r, "\mathrm{curl}"] & H(\mathrm{div}, V) \arrow[r, "\mathrm{div}"] & L^2(V)
\end{tikzcd}$$

$$\begin{tikzcd}
\mathbb{R} \arrow[r, "\mathrm{id}"] & H^1(A) \arrow[r, "\nabla"] & H(\mathrm{div}\boldsymbol{R}, A) \arrow[r, "\mathrm{div}\boldsymbol{R}"] & L^2(A)
\end{tikzcd}$$

Figure 4.1: Classical de Rham exact sequences for three- and two-dimensional contractible domains. The range of each operator is exactly the kernel of the next operator in the sequence.

Using the vectorial space $H(\mathrm{curl}, V)$ we also introduce the tensor-valued $H(\mathrm{Curl}, V)$ space

$$H(\mathrm{Curl}, V) = \{\boldsymbol{P} \in [L^2(V)]^{3\times 3} \mid \mathrm{Curl}\,\boldsymbol{P} \in [L^2(V)]^{3\times 3}\}\,, \tag{4.4}$$

where each row of $\boldsymbol{P}$ is an element of $H(\mathrm{curl}, V)$. On contractible domains the Hilbert spaces are connected by exact de Rham sequences [32,85], see Fig. 4.1. The exact de Rham sequence compactly portrays the following relations

$$\nabla H^1(V) = \ker(\mathrm{curl}) \cap H(\mathrm{curl}, V)\,, \tag{4.5a}$$

$$\mathrm{curl}[H(\mathrm{curl}, V)] = \ker(\mathrm{div}) \cap H(\mathrm{div}, V)\,, \tag{4.5b}$$

$$\mathrm{div}[H(\mathrm{div}, V)] = L^2(V)\,, \tag{4.5c}$$

for the three-dimensional case. In two dimensions there holds

$$\nabla H^1(A) = \ker(\mathrm{div}\boldsymbol{R}) \cap H(\mathrm{div}\boldsymbol{R}, A)\,, \tag{4.6a}$$

$$\mathrm{div}[\boldsymbol{R}\, H(\mathrm{div}\boldsymbol{R}, A)] = L^2(A)\,. \tag{4.6b}$$

In this work, the sequence is used in the embedding of appropriate boundary conditions and the construction of conforming finite elements.

For the following results, a restriction of the domain to a Lipschitz domain is required.

Definition 4.2 (Lipschitz domain)
A domain V is called Lipschitz if its boundary ∂V is given by a Lipschitz continuous function or by the finite union of piece-wise Lipschitz continuous functions $\partial V = \bigcup_i \overline{A}_i$ with $A_i \cap A_j = \emptyset$ for $i \neq j$, where a Lipschitz continuous function is defined as

$$\exists\, k > 0 : \quad |f(x_2) - f(x_1)| \leq k|x_2 - x_1| \quad \forall\, x_1, x_2 \in \mathbb{R}\,. \tag{4.7}$$

The usage of a Lipschitz boundary allows for the definition of the outer surface normal almost everywhere on the boundary ∂V. Further, for Lipschitz domains one can define the Hilbert spaces by density as

$$\begin{aligned}
H^1(V) &= \overline{C^\infty(\overline{V})}^{\|\cdot\|_{H^1}}\,, & H(\mathrm{div}\boldsymbol{R}, A) &= \overline{[C^\infty(\overline{A})]^2}^{\|\cdot\|_{H(\mathrm{div}\boldsymbol{R})}}\,, \\
H(\mathrm{curl}, V) &= \overline{[C^\infty(\overline{V})]^3}^{\|\cdot\|_{H(\mathrm{curl})}}\,, & H(\mathrm{div}, V) &= \overline{[C^\infty(\overline{V})]^3}^{\|\cdot\|_{H(\mathrm{div})}}\,,
\end{aligned} \tag{4.8}$$

thus allowing to extend properties of the continuous spaces onto the Hilbert spaces.

4.2 Trace theorems

The embedding of boundary conditions into variational problems depends on so called trace theorems [47]. The latter extend the well known Green type formulas to Hilbert spaces. The following traces are defined for a Lipschitz domain with $V \subset \mathbb{R}^d$ where $d \in \{2,3\}$.

Theorem 4.1 (Traces)
The traces are defined for each Hilbert space as follows:

1. *The trace of the function $u \in H^1(V)$ is defined by the linear bounded operator*

$$\operatorname{tr}_{\partial \mathrm{V}} u = u \bigg|_{\partial V} \in H^{1/2}(\partial V)\,, \quad \exists\, c > 0: \quad \| \operatorname{tr}_{\partial \mathrm{V}} u \|_{H^{1/2}(\partial V)} \leq c \|u\|_{H^1(V)} \quad \forall\, u \in H^1(V)\,. \tag{4.9}$$

   Thus, the trace of the field $\operatorname{tr}_{\partial \mathrm{V}} u$ considers its values only on the boundary of the domain.

2. *The trace of the $H(\mathrm{div}\boldsymbol{R}, A)$ space is given by the restriction of a function to the boundary while considering solely its tangential projection*

$$\operatorname{tr}^{\mathrm{t}}_{\partial \mathrm{A}} \mathbf{u} = \langle \mathbf{t},\, \mathbf{u} \rangle \bigg|_{\partial A} \in H^{-1/2}(\partial A)\,,$$

$$\exists\, c > 0: \quad \| \operatorname{tr}^{\mathrm{t}}_{\partial \mathrm{A}} \mathbf{u} \|_{H^{-1/2}(\partial A)} \leq c \|\mathbf{u}\|_{H(\mathrm{div}\boldsymbol{R}, A)} \quad \forall\, \mathbf{u} \in H(\mathrm{div}\boldsymbol{R}, A)\,. \tag{4.10}$$

3. *The trace of the $H(\mathrm{curl}, V)$ space is similar to the previous trace. However, on a surface the tangent vector is not unique, and as such the projection is defined using the normal vector and the cross product*

$$\operatorname{tr}^{\mathrm{t}}_{\partial \mathrm{V}} \mathbf{u} = \mathbf{n} \times \mathbf{u} \bigg|_{\partial V} \in [H^{-1/2}(\partial V)]^3\,,$$

$$\exists\, c > 0: \quad \| \operatorname{tr}^{\mathrm{t}}_{\partial \mathrm{V}} \mathbf{u} \|_{H^{-1/2}(\partial V)} \leq c \|\mathbf{u}\|_{H(\mathrm{curl}, V)} \quad \forall\, \mathbf{u} \in H(\mathrm{curl}, V)\,. \tag{4.11}$$

4. *Lastly, the trace of the $H(\mathrm{div}, V)$ space is defined by the normal projection at the boundary*

$$\operatorname{tr}^{\mathrm{n}}_{\partial \mathrm{V}} \mathbf{u} = \langle \mathbf{n},\, \mathbf{u} \rangle \bigg|_{\partial V} \in H^{-1/2}(\partial V)\,,$$

$$\exists\, c > 0: \quad \| \operatorname{tr}^{\mathrm{n}}_{\partial \mathrm{V}} \mathbf{u} \|_{H^{-1/2}(\partial V)} \leq c \|\mathbf{u}\|_{H(\mathrm{div}, V)} \quad \forall\, \mathbf{u} \in H(\mathrm{div}, V)\,. \tag{4.12}$$

The positive fractional Hilbert space is given by

$$H^{1/2}(\partial V) = \{ v \in L^2(\partial V) \mid \exists\, u \in H^1(V) : \ \operatorname{tr}_{\partial \mathrm{V}} u = v \}\,, \tag{4.13}$$

and the negative fractional Hilbert space is its dual. A general derivation of fractional Sobolev spaces is given in [33].

With the latter traces at hand one can define the classical Green-type formulas for Hilbert spaces.

$$\begin{tikzcd}
\mathbb{R} \arrow[r, "\mathrm{id}"] & H_0^1(V) \arrow[r, "\nabla"] & H_0(\mathrm{curl}, V) \arrow[r, "\mathrm{curl}"] & H_0(\mathrm{div}, V) \arrow[r, "\mathrm{div}"] & L_0^2(V)
\end{tikzcd}$$

$$\begin{tikzcd}
\mathbb{R} \arrow[r, "\mathrm{id}"] & H_0^1(A) \arrow[r, "\nabla"] & H_0(\mathrm{div}\boldsymbol{R}, A) \arrow[r, "\mathrm{div}\boldsymbol{R}"] & L_0^2(A)
\end{tikzcd}$$

Figure 4.2: De Rham exact sequences for Hilbert spaces with vanishing traces. The Lebesgue zero-space is characterized by functions with a vanishing integral over the domain.

Theorem 4.2 (Integration by parts)
The following integration by parts formula hold with the trace operators defined in Theorem 4.1 for Lipschitz domains

$$\int_V \langle \nabla u, \, \mathbf{q} \rangle \, \mathrm{d}V = \int_{\partial V} (\mathrm{tr}_{\partial \mathrm{V}} \, u) \, \mathrm{tr}^{\mathrm{n}}_{\partial \mathrm{V}} \, \mathbf{q} \, \mathrm{d}A - \int_V u \, \mathrm{div} \, \mathbf{v} \, \mathrm{d}V \qquad \forall \, u \in H^1(V), \, \forall \, \mathbf{v} \in H(\mathrm{div}, V) \, , \tag{4.14a}$$

$$\int_A \mathrm{div}(\boldsymbol{R}\mathbf{u}) \, q \, \mathrm{d}A = \int_{\partial A} (\mathrm{tr}^{\mathrm{t}}_{\partial \mathrm{A}} \, \mathbf{u}) \, \mathrm{tr}_{\partial \mathrm{V}} \, q \, \mathrm{d}s + \int_A \langle \mathbf{u}, \, \boldsymbol{R} \nabla \mathbf{q} \rangle \, \mathrm{d}A \qquad \forall \, \mathbf{u} \in H(\mathrm{div}\boldsymbol{R}, A), \, \forall \, q \in H^1(A) \, , \tag{4.14b}$$

$$\int_V \langle \mathrm{curl} \, \mathbf{u}, \, \mathbf{q} \rangle \, \mathrm{d}V = \int_{\partial V} \langle \mathrm{tr}^{\mathrm{t}}_{\partial \mathrm{V}} \, \mathbf{u}, \, \mathrm{tr}_{\partial \mathrm{V}} \, \mathbf{q} \rangle \, \mathrm{d}A + \int_V \langle \mathbf{u}, \, \mathrm{curl} \, \mathbf{q} \rangle \, \mathrm{d}V \quad \forall \, \mathbf{u} \in H(\mathrm{curl}, V), \, \forall \, \mathbf{q} \in [H^1(V)]^3 \, . \tag{4.14c}$$

Furthermore, using the trace operators one can define Hilbert spaces with vanishing traces

$$L_0^2(V) = \{ u \in L^2(V) \mid \int_V u \, \mathrm{d}V = 0 \} \, , \tag{4.15a}$$

$$H_0^1(V) = \{ u \in H^1(V) \mid \mathrm{tr}_{\partial \mathrm{V}} \, u = 0 \} \, , \tag{4.15b}$$

$$H_0(\mathrm{div}\boldsymbol{R}, A) = \{ \mathbf{u} \in H(\mathrm{div}\boldsymbol{R}, A) \mid \mathrm{tr}^{\mathrm{t}}_{\partial \mathrm{A}} \, \mathbf{u} = 0 \} \, , \tag{4.15c}$$

$$H_0(\mathrm{curl}, V) = \{ \mathbf{u} \in H(\mathrm{curl}, V) \mid \mathrm{tr}^{\mathrm{t}}_{\partial \mathrm{V}} \, \mathbf{u} = 0 \} \, , \tag{4.15d}$$

$$H_0(\mathrm{div}, V) = \{ \mathbf{u} \in H(\mathrm{div}, V) \mid \mathrm{tr}^{\mathrm{n}}_{\partial \mathrm{V}} \, \mathbf{u} = 0 \} \, . \tag{4.15e}$$

Subsequentially, these spaces are used to define Dirichlet boundary conditions. The spaces with vanishing traces are also connected by a de Rham complex, see Fig. 4.2. In other words, applying the differential operator on a function with a vanishing trace in one Hilbert space leads to a function with a vanishing trace in the kernel of the next space, as defined by the differential operator. Finally, the traces are used to identify finite element spaces by interface conditions [81, 103].

Theorem 4.3 (Interface conditions)
A finite element space is a conforming subspace of a Hilbert space if and only if the jump of the trace of its elements vanishes for all arbitrarily defined interfaces $\Xi_{ij} = V_i \cap V_j \, , i \neq j$ where $V = V_i \cup V_j \subset \mathbb{R}^3$ and $\Xi_{ij} \subset \mathbb{R}^2$ (and analogously for two-dimensional domains)

$$u \in H^1(V) \qquad \iff \qquad [\![\mathrm{tr}_{\partial \mathrm{V}} \, u]\!] \Big|_{\Xi_{ij}} = 0 \quad \forall \, \Xi_{ij} = V_i \cap V_j \, , \tag{4.16a}$$

$$\mathbf{u} \in H(\mathrm{div}\boldsymbol{R}, A) \qquad \iff \qquad [\![\mathrm{tr}^{\mathrm{t}}_{\partial \mathrm{A}} \, \mathbf{u}]\!] \Big|_{\Xi_{ij}} = 0 \quad \forall \, \Xi_{ij} = A_i \cap A_j \, , \tag{4.16b}$$

$$\mathbf{u} \in H(\mathrm{curl}, V) \qquad \iff \qquad [\![\mathrm{tr}^{\mathrm{t}}_{\partial \mathrm{V}} \, \mathbf{u}]\!] \bigg|_{\Xi_{ij}} = 0 \quad \forall \, \Xi_{ij} = V_i \cap V_j \, , \tag{4.16c}$$

$$\mathbf{u} \in H(\mathrm{div}, V) \qquad \iff \qquad [\![\mathrm{tr}^{\mathrm{n}}_{\partial \mathrm{V}} \, \mathbf{u}]\!] \bigg|_{\Xi_{ij}} = 0 \quad \forall \, \Xi_{ij} = V_i \cap V_j \, . \tag{4.16d}$$

4.3 Existence and uniqueness

The relaxed micromorphic model defines a symmetric positive definite bilinear form. As such, its existence and uniqueness can be shown using the Lax-Milgram theorem [18, 19].

Theorem 4.4 (Lax-Milgram)
Let X be a Hilbert space equipped with the norm $\| \cdot \|_X$,

1. *if a bilinear form $a : X \times X \to \mathbb{R}$ is bounded (and therefore continuous)*

$$\exists \, \alpha > 0 : \quad a(u, q) \leq \alpha \|u\|_X \|q\|_X \quad \forall \, u \in X, \forall q \in X \, , \tag{4.17}$$

2. *and is strongly coercive*

$$\exists \, \beta > 0 : \quad a(u, u) \geq \beta \|u\|_X^2 \quad \forall \, u \in X \, , \tag{4.18}$$

3. *then by the Lax-Milgram theorem there exists a unique solution for every right hand side $f \in X'$ with the stability estimate*

$$\|u\|_X \leq \frac{1}{\beta} \|f\|_{X'} \, , \tag{4.19}$$

where X' is the dual space of X and $\| \cdot \|_{X'}$ is the corresponding dual norm.

4.3.1 Inequalities

In the following we state several classical inequalities [18, 19] used in our proofs.

Lemma 4.1 (Cauchy-Schwarz inequality)
Let X be a vector space equipped with a scalar product, then there holds

$$\langle x, \, y \rangle_X \leq \|x\|_X \|y\|_X \quad \forall \, x, y \in X \, . \tag{4.20}$$

Lemma 4.2 (Triangle inequality)
Let X be a normed vector space, then there holds

$$\|x + y\|_X \leq \|x\|_X + \|y\|_X \quad \forall \, x, y \in X \, . \tag{4.21}$$

Lemma 4.3 (Young's inequality)
Let X be a vector space endowed with a scalar product, then there holds

$$\langle x, \, y \rangle_X \leq \frac{\|x\|_X^2}{2 \, \varepsilon} + \frac{\varepsilon \, \|y\|_X^2}{2} \quad \forall \begin{cases} x, y \in X \\ \varepsilon > 0 \end{cases} . \tag{4.22}$$

Lemma 4.4 (Poincaré-Friedrich's inequality)
Let V be a connected and bounded Lipschitz domain with non-vanishing Dirichlet boundary $A_D \subset \partial V$ with $|A_D| > 0$, then there holds

$$\exists\, c_F > 0 : \quad \|u\|_{L^2} \leq c_F \|\nabla u\|_{L^2} \quad \forall\, u \in H^1_{A_D}(V)\,, \tag{4.23}$$

such that c_F depends only on V and A_D.

Lemma 4.5 (Korn's inequality)
Let V be a connected and bounded Lipschitz domain with $A_D \subset \partial V$ and $|A_D| > 0$, then there holds

$$\exists\, c_K > 0 : \quad \|\mathrm{D}\mathbf{u}\|_{L^2} \leq c_K \|\operatorname{sym} \mathrm{D}\mathbf{u}\|_{L^2} \quad \forall\, \mathbf{u} \in [H^1_{A_D}(V)]^3\,, \tag{4.24}$$

such that c_K depends only on V and A_D.

We note that specifically for the relaxed micromorphic model, the generalized Korn's inequality [60–62, 79] is crucial for existence and uniqueness in the case of a semi-positive-definite rotational coupling tensor $\mathbb{C}_{\mathrm{c}}$.

Lemma 4.6 (Generalized Korn's inequality)
Let V be a connected and bounded Lipschitz domain with $A_D \subset \partial V$ and $|A_D| > 0$, then there holds

$$\exists\, c_G > 0 : \quad \|\boldsymbol{P}\|^2_{L^2} + \|\operatorname{Curl} \boldsymbol{P}\|^2_{L^2} \leq c_G(\|\operatorname{sym} \boldsymbol{P}\|^2_{L^2} + \|\operatorname{Curl} \boldsymbol{P}\|^2_{L^2}) \quad \forall\, \boldsymbol{P} \in H_{A_D}(\operatorname{Curl}, V)\,, \tag{4.25}$$

such that c_G depends only on V and A_D.

4.3.2 Antiplane shear

We start proofs of existence and uniqueness of the relaxed micromorphic model for antiplane shear [101] and postpone the treatment of more complex models to the subsequent subsections.

Theorem 4.5 (Well-posedness for antiplane shear)
Let the material constants $\mu_{\mathrm{e}}, \mu_{\mathrm{micro}}, \mu_{\mathrm{macro}}, L_{\mathrm{c}} > 0$, then the problem

$$a(\{\delta u, \delta \mathbf{p}\}, \{u, \mathbf{p}\}) = l(\{\delta u, \delta \mathbf{p}\}) \quad \forall \{\delta u, \delta \mathbf{p}\} \in X(A)\,, \tag{4.26}$$

where the bilinear and linear forms are according to Eq. (3.43)*, has a unique solution*

$$\{u, \mathbf{p}\} \in X(A) = H^1_0(A) \times H(\operatorname{div}\boldsymbol{R}, A)\,, \qquad \|\{u, \mathbf{p}\}\|_X = \|u\|_{H^1} + \|\mathbf{p}\|_{H(\operatorname{div}\boldsymbol{R})}\,, \tag{4.27}$$

and there holds the stability estimate

$$\|\{u, \mathbf{p}\}\|_X \leq \frac{1}{\beta}(\|f\|_{L^2} + \|\mathbf{m}\|_{L^2})\,, \qquad f \in L^2(A),\, \mathbf{m} \in [L^2(A)]^2\,, \tag{4.28}$$

with $\beta = \beta(\mu_{\mathrm{e}}, \mu_{\mathrm{micro}}, \mu_{\mathrm{macro}}, L_{\mathrm{c}}) > 0$.

Proof. The continuity of the bilinear form can be shown by employing the Cauchy-Schwarz and triangle inequalities

$$\begin{aligned}
a(\{\delta u, \delta\mathbf{p}\}, \{u, \mathbf{p}\}) &= \mu_{\mathrm{e}}\langle \nabla\delta u - \delta\mathbf{p},\, \nabla u - \mathbf{p}\rangle_{L^2} + \mu_{\mathrm{micro}}\langle \delta\mathbf{p},\, \mathbf{p}\rangle_{L^2} + \mu_{\mathrm{macro}} L_{\mathrm{c}}^2 \langle \operatorname{div}(\boldsymbol{R}\delta\mathbf{p}),\, \operatorname{div}(\boldsymbol{R}\mathbf{p})\rangle_{L^2} \\
&\overset{\text{CS}}{\leq} \mu_{\mathrm{e}} \|\nabla\delta u - \delta\mathbf{p}\|_{L^2} \|\nabla u - \mathbf{p}\|_{L^2} + \mu_{\mathrm{micro}} \|\delta\mathbf{p}\|_{L^2} \|\mathbf{p}\|_{L^2} \\
&\quad + \mu_{\mathrm{macro}} L_{\mathrm{c}}^2 \|\operatorname{div}(\boldsymbol{R}\delta\mathbf{p})\|_{L^2} \|\operatorname{div}(\boldsymbol{R}\mathbf{p})\|_{L^2} \\
&\leq c_1 [\|\nabla\delta u - \delta\mathbf{p}\|_{L^2} \|\nabla u - \mathbf{p}\|_{L^2} + \|\delta\mathbf{p}\|_{L^2} \|\mathbf{p}\|_{L^2} + \|\operatorname{div}(\boldsymbol{R}\delta\mathbf{p})\|_{L^2} \|\operatorname{div}(\boldsymbol{R}\mathbf{p})\|_{L^2}] \\
&\overset{\text{T}}{\leq} c_1 [(\|\nabla\delta u\|_{L^2} + \|\delta\mathbf{p}\|_{L^2})(\|\nabla u\|_{L^2} + \|\mathbf{p}\|_{L^2}) + \|\delta\mathbf{p}\|_{L^2} \|\mathbf{p}\|_{L^2} \\
&\quad + \|\operatorname{div}(\boldsymbol{R}\delta\mathbf{p})\|_{L^2} \|\operatorname{div}(\boldsymbol{R}\mathbf{p})\|_{L^2}] \\
&\leq 3\, c_1 \|\{\delta u, \delta\mathbf{p}\}\|_X \|\{u, \mathbf{p}\}\|_X \quad \forall \{\delta u, \delta\mathbf{p}\}, \{u, \mathbf{p}\} \in X(A)\,,
\end{aligned} \tag{4.29}$$

where $c_1 = \max\{\mu_{\mathrm{e}},\, \mu_{\mathrm{micro}},\, \mu_{\mathrm{macro}} L_{\mathrm{c}}^2\}$ such that the continuity constant reads $\alpha = 3\, c_1$.

In order to prove coercivity we use Young's, and Poincaré-Friedrich's inequalities

$$\begin{aligned}
a(\{u, \mathbf{p}\}, \{u, \mathbf{p}\}) &= \mu_{\mathrm{e}} \|\nabla u - \mathbf{p}\|_{L^2}^2 + \mu_{\mathrm{micro}} \|\mathbf{p}\|_{L^2}^2 + \mu_{\mathrm{macro}} L_{\mathrm{c}}^2 \|\operatorname{div}(\boldsymbol{R}\mathbf{p})\|_{L^2}^2 \\
&= \mu_{\mathrm{e}} (\|\nabla u\|_{L^2}^2 - 2\langle \nabla u,\, \mathbf{p}\rangle_{L^2}^2 + \|\mathbf{p}\|_{L^2}^2) + \mu_{\mathrm{micro}} \|\mathbf{p}\|_{L^2}^2 + \mu_{\mathrm{macro}} L_{\mathrm{c}}^2 \|\operatorname{div}(\boldsymbol{R}\mathbf{p})\|_{L^2}^2 \\
&\overset{\text{Y}}{\geq} \mu_{\mathrm{e}} (\|\nabla u\|_{L^2}^2 - \varepsilon \|\nabla u\|_{L^2}^2 - \frac{1}{\varepsilon} \|\mathbf{p}\|_{L^2} + \|\mathbf{p}\|_{L^2}^2) + \mu_{\mathrm{micro}} \|\mathbf{p}\|_{L^2}^2 + \mu_{\mathrm{macro}} L_{\mathrm{c}}^2 \|\operatorname{div}(\boldsymbol{R}\mathbf{p})\|_{L^2}^2 \\
&\geq c_2 (\|\nabla u\|_{L^2}^2 + \|\mathbf{p}\|_{L^2}^2 + \|\operatorname{div}(\boldsymbol{R}\mathbf{p})\|_{L^2}^2) \\
&\overset{\text{PF}}{\geq} c_2 (\frac{1}{2\, c_F^2} \|u\|_{L^2}^2 + \frac{1}{2} \|\nabla u\|_{L^2}^2 + \|\mathbf{p}\|_{L^2}^2 + \|\operatorname{div}(\boldsymbol{R}\mathbf{p})\|_{L^2}^2) \\
&\geq \frac{c_2}{2} (\frac{1}{c_F^2} \|u\|_{L^2}^2 + \|\nabla u\|_{L^2}^2 + \|\mathbf{p}\|_{L^2}^2 + \|\operatorname{div}(\boldsymbol{R}\mathbf{p})\|_{L^2}^2) \\
&\geq c_2\, c_3 (\|u\|_{L^2}^2 + \|\nabla u\|_{L^2}^2 + \|\mathbf{p}\|_{L^2}^2 + \|\operatorname{div}(\boldsymbol{R}\mathbf{p})\|_{L^2}^2) \\
&\overset{\text{Y}}{\geq} \frac{c_2\, c_3}{c_X} \|\{u, \mathbf{p}\}\|_X^2 \quad \forall\, \{u, \mathbf{p}\} \in X(A)\,,
\end{aligned} \tag{4.30}$$

with the constants

$$c_2 = \min\{\mu_{\mathrm{e}}(1 - \varepsilon),\, \mu_{\mathrm{e}}(1 - \frac{1}{\varepsilon}) + \mu_{\mathrm{micro}},\, \mu_{\mathrm{macro}} L_{\mathrm{c}}^2\}\,, \quad c_3 = \frac{1}{2} \min\{1,\, \frac{1}{c_F^2}\}\,, \quad c_X = 2 \max\{1,\, \frac{1}{2e},\, \frac{e}{2}\}\,. \tag{4.31}$$

Note that due to c_2 the constant ε must satisfy

$$\frac{\mu_{\mathrm{e}}}{\mu_{\mathrm{e}} + \mu_{\mathrm{micro}}} < \varepsilon < 1\,, \tag{4.32}$$

which is always possible for $\mu_{\mathrm{e}}, \mu_{\mathrm{micro}} > 0$. Therefore, the coercivity constant is given by $\beta = \dfrac{c_2\, c_3}{c_X}$. The continuity of the linear form $l(\{\delta u, \delta\mathbf{p}\})$ is obvious and thereby omitted. $\square$

In the case of antiplane shear we can show, that the microdistortion $\mathbf{p}$ reduces to a gradient field whenever the right hand side is given by a scalar potential.

Theorem 4.6 (Gradient condition)
Let the micro-moment take the form $\mathbf{m} = \nabla m$ *for some scalar field* $m \in H^1(A)$*, then the microdistortion field is compatible*

$$\exists\, p \in H^1(A) : \quad \mathbf{p} = \nabla p \,, \tag{4.33}$$

and independent of the characteristic length scale parameter L_c*.*

Proof. We make the ansatz $\mathbf{p} = \nabla p$ with $p \in H^1(A)$ and insert it into Problem. 4.26 while choosing $\delta u = 0$ to find

$$\int_A \mu_\mathrm{e} \langle \delta\mathbf{p},\, \nabla p - \nabla u \rangle + \mu_\mathrm{micro} \langle \delta\mathbf{p},\, \nabla p \rangle \,\mathrm{d}A = \int_A \langle \delta\mathbf{p},\, \nabla m \rangle \,\mathrm{d}A \quad \forall\, \delta\mathbf{p} \in H(\mathrm{curl}, A)\,. \tag{4.34}$$

As such, we can express ∇p in the form

$$\nabla p = \frac{1}{\mu_\mathrm{e} + \mu_\mathrm{micro}} \nabla(m + \mu_\mathrm{e} u)\,. \tag{4.35}$$

Inserting the latter result into Problem. 4.26 while setting $\delta\mathbf{p} = 0$ yields the Poisson problem

$$\int_A \frac{\mu_\mathrm{micro}}{\mu_\mathrm{e} + \mu_\mathrm{micro}} \langle \nabla \delta u,\, \nabla u \rangle \,\mathrm{d}A = \int_A \delta u\, f + \frac{\mu_\mathrm{e}}{\mu_\mathrm{e} + \mu_\mathrm{micro}} \langle \nabla \delta u,\, \nabla m \rangle \,\mathrm{d}A \quad \forall\, \delta u \in H^1(A)\,, \tag{4.36}$$

which is uniquely solvable. Since by the Lax-Milgram theorem the solution is unique, it follows that $\mathbf{p} = \nabla p$ and the resulting displacement field u are the only possible solutions. ☐

The case $L_\mathrm{c} = 0$ is also of interest, since it represents the scenario of a completely homogeneous domain.

Theorem 4.7 (Homogeneous antiplane continuum)
Let $\mu_\mathrm{e}, \mu_\mathrm{c} > 0$ *and* $L_\mathrm{c} = 0$*, then Problem. 4.26 has a unique solution in* $X(A) = H^1(A) \times [L^2(A)]^2$*.*

Proof. The proof of continuity follows the same lines as Eq. (4.29). The curl term is dropped such that the continuity constant is given by

$$\alpha = 2\, c_1 \,, \qquad\qquad c_1 = \min\{\mu_\mathrm{e},\, \mu_\mathrm{micro}\}\,. \tag{4.37}$$

The proof of coercivity is analogous to Eq. (4.30) where the dependence on $\mu_\mathrm{macro} L_\mathrm{c}^2$ is dropped in c_2. ☐

Remark 4.1
Note that if $L_\mathrm{c} = 0$ *and* $\mathbf{m} = \nabla m$ *it follows by Theorem 4.6 that*

$$\mathbf{p} = \nabla p \subset \ker(\mathrm{div}\boldsymbol{R}) \cap H(\mathrm{div}\boldsymbol{R}, A) \subset H(\mathrm{div}\boldsymbol{R}, A) \subset [L^2(A)]^2 \,, \tag{4.38}$$

such that the problem remains well-posed in $X(A) = H_0^1(A) \times H(\mathrm{div}\boldsymbol{R}, A)$*.*

4.3.3 Three-dimensional model

For the proof of the three-dimensional model [100] we first define the bounds of the material tensors on their respective spaces

$$\exists\, k_{\mathrm{e}}, c_{\mathrm{e}} > 0 : \qquad k_{\mathrm{e}}\|\boldsymbol{T}\|^2 \leq \langle \boldsymbol{T},\, \mathbb{C}_{\mathrm{e}}\, \boldsymbol{T}\rangle \leq c_{\mathrm{e}}\|\boldsymbol{T}\|^2 \qquad \forall\, \boldsymbol{T} \in \mathbb{R}^{3\times 3}\,, \tag{4.39a}$$

$$\exists\, k_{\mathrm{micro}}, c_{\mathrm{micro}} > 0 : \qquad k_{\mathrm{micro}}\|\boldsymbol{T}\|^2 \leq \langle \boldsymbol{T},\, \mathbb{C}_{\mathrm{micro}}\, \boldsymbol{T}\rangle \leq c_{\mathrm{micro}}\|\boldsymbol{T}\|^2 \qquad \forall\, \boldsymbol{T} \in \mathbb{R}^{3\times 3}\,, \tag{4.39b}$$

$$\exists\, k_{\mathrm{c}}, c_{\mathrm{c}} > 0 : \qquad k_{\mathrm{c}}\|\boldsymbol{T}\|^2 \leq \langle \boldsymbol{A},\, \mathbb{C}_{\mathrm{c}}\, \boldsymbol{A}\rangle \leq c_{\mathrm{c}}\|\boldsymbol{A}\|^2 \qquad \forall\, \boldsymbol{A} \in \mathfrak{so}(3)\,, \tag{4.39c}$$

where the positive definiteness of $\mathbb{C}_{\mathrm{c}}$ on $\mathfrak{so}(3)$ is assumed for the first part of the proof. This restriction is later relaxed to semi-positive-definiteness on $\mathfrak{so}(3)$ using the generalized Korn's inequality.

Theorem 4.8 (Well-posedness three-dimensional model I)
Let $\mu_{\mathrm{macro}}, L_{\mathrm{c}} > 0$ and $\mathbb{C}_{\mathrm{e}}, \mathbb{C}_{\mathrm{micro}}$ be positive definite on $\mathbb{R}^{3\times 3}$. Further let $\mathbb{C}_{\mathrm{c}}$ be positive definite on $\mathfrak{so}(3)$, then the problem

$$a(\{\delta\mathbf{u}, \delta\boldsymbol{P}\}, \{\mathbf{u}, \boldsymbol{P}\}) = l(\{\delta\mathbf{u}, \delta\boldsymbol{P}\}) \quad \forall\{\delta\mathbf{u}, \delta\boldsymbol{P}\} \in X(V)\,, \tag{4.40}$$

where the bilinear and linear forms are according to Eq. (3.8) *and Eq.* (3.9)*, has a unique solution*

$$\{\mathbf{u}, \boldsymbol{P}\} \in X(V) = [H_0^1(V)]^3 \times H(\mathrm{Curl}, V)\,, \qquad \|\{\mathbf{u}, \boldsymbol{P}\}\|_X = \|\mathbf{u}\|_{H^1} + \|\boldsymbol{P}\|_{H(\mathrm{Curl})}\,, \tag{4.41}$$

and there holds the stability estimate

$$\|\{\mathbf{u}, \boldsymbol{P}\}\|_X \leq \frac{1}{\beta}(\|\mathbf{f}\|_{L^2} + \|\boldsymbol{M}\|_{L^2})\,, \qquad \mathbf{f} \in [L^2(V)]^3,\ \boldsymbol{M} \in [L^2(V)]^{3\times 3}\,, \tag{4.42}$$

with $\beta = \beta(\mathbb{C}_{\mathrm{e}}, \mathbb{C}_{\mathrm{micro}}, \mathbb{C}_{\mathrm{c}}, \mu_{\mathrm{macro}}, L_{\mathrm{c}}) > 0$.

Proof. Continuity of the bilinear form follows from the Cauchy-Schwarz and triangle inequalities

$$\begin{aligned}
a(\{\delta\mathbf{u}, \delta\boldsymbol{P}\}, \{\mathbf{u}, \boldsymbol{P}\}) &\overset{\mathrm{CS}}{\leq} c_{\mathrm{e}}\|\operatorname{sym}(\mathrm{D}\delta\mathbf{u} - \delta\boldsymbol{P})\|_{L^2}\|\operatorname{sym}(\mathrm{D}\mathbf{u} - \boldsymbol{P})\|_{L^2} + c_{\mathrm{micro}}\|\operatorname{sym}\delta\boldsymbol{P}\|_{L^2}\|\operatorname{sym}\boldsymbol{P}\|_{L^2} \\
&\qquad + c_{\mathrm{c}}\|\operatorname{skew}(\mathrm{D}\delta\mathbf{u} - \delta\boldsymbol{P})\|_{L^2}\|\operatorname{skew}(\mathrm{D}\mathbf{u} - \boldsymbol{P})\|_{L^2} + \mu_{\mathrm{macro}}L_{\mathrm{c}}^2\|\operatorname{Curl}\delta\boldsymbol{P}\|_{L^2}\|\operatorname{Curl}\boldsymbol{P}\|_{L^2} \\
&\leq c_1\,[\|\operatorname{sym}(\mathrm{D}\delta\mathbf{u} - \delta\boldsymbol{P})\|_{L^2}\|\operatorname{sym}(\mathrm{D}\mathbf{u} - \boldsymbol{P})\|_{L^2} + \|\operatorname{sym}\delta\boldsymbol{P}\|_{L^2}\|\operatorname{sym}\boldsymbol{P}\|_{L^2} \\
&\qquad + \|\operatorname{skew}(\mathrm{D}\delta\mathbf{u} - \delta\boldsymbol{P})\|_{L^2}\|\operatorname{skew}(\mathrm{D}\mathbf{u} - \boldsymbol{P})\|_{L^2} + \|\operatorname{Curl}\delta\boldsymbol{P}\|_{L^2}\|\operatorname{Curl}\boldsymbol{P}\|_{L^2}] \\
&\overset{\mathrm{T}}{\leq} c_1\,[(\|\operatorname{sym}\mathrm{D}\delta\mathbf{u}\|_{L^2} + \|\operatorname{sym}\delta\boldsymbol{P}\|_{L^2})(\|\operatorname{sym}\mathrm{D}\mathbf{u}\|_{L^2} + \|\operatorname{sym}\boldsymbol{P}\|_{L^2}) + \|\operatorname{sym}\delta\boldsymbol{P}\|_{L^2}\|\operatorname{sym}\boldsymbol{P}\|_{L^2} \\
&\qquad + (\|\operatorname{skew}\mathrm{D}\delta\mathbf{u}\|_{L^2} + \|\operatorname{skew}\delta\boldsymbol{P}\|_{L^2})(\|\operatorname{skew}\mathrm{D}\mathbf{u}\|_{L^2} + \|\operatorname{skew}\boldsymbol{P}\|_{L^2}) \\
&\qquad + \|\operatorname{Curl}\delta\boldsymbol{P}\|_{L^2}\|\operatorname{Curl}\boldsymbol{P}\|_{L^2}] \\
&\leq c_1\,[2\,(\|\mathrm{D}\delta\mathbf{u}\|_{L^2} + \|\delta\boldsymbol{P}\|_{L^2})(\|\mathrm{D}\mathbf{u}\|_{L^2} + \|\boldsymbol{P}\|_{L^2}) + \|\delta\boldsymbol{P}\|_{L^2}\|\boldsymbol{P}\|_{L^2} \\
&\qquad + \|\operatorname{Curl}\delta\boldsymbol{P}\|_{L^2}\|\operatorname{Curl}\boldsymbol{P}\|_{L^2}] \\
&\leq 2\,c_1\,[(\|\mathrm{D}\delta\mathbf{u}\|_{L^2} + \|\delta\boldsymbol{P}\|_{L^2})(\|\mathrm{D}\mathbf{u}\|_{L^2} + \|\boldsymbol{P}\|_{L^2}) + \|\delta\boldsymbol{P}\|_{L^2}\|\boldsymbol{P}\|_{L^2} \\
&\qquad + \|\operatorname{Curl}\delta\boldsymbol{P}\|_{L^2}\|\operatorname{Curl}\boldsymbol{P}\|_{L^2}] \\
&\leq 6\,c_1\,\|\{\delta\mathbf{u}, \delta\boldsymbol{P}\}\|_X\|\{\mathbf{u}, \boldsymbol{P}\}\|_X \quad \forall\,\{\delta\mathbf{u}, \delta\boldsymbol{P}\}, \{\mathbf{u}, \boldsymbol{P}\} \in X(V)\,,
\end{aligned} \tag{4.43}$$

with the constant $c_1 = \max\{c_\mathrm{e},\, c_\mathrm{micro},\, c_\mathrm{c},\, \mu_\mathrm{macro} L_\mathrm{c}^2\}$. The continuity constant reads $\alpha = 6\, c_1$.

Coercivity is shown using Young's, Korn's, and Poincaré-Freidrich's inequalities

$$
\begin{aligned}
a(\{\mathbf{u}, \boldsymbol{P}\}, \{\mathbf{u}, \boldsymbol{P}\}) &\geq k_\mathrm{e}(\|\operatorname{sym}\mathrm{D}\mathbf{u}\|_{L^2}^2 - 2\langle \operatorname{sym}\mathrm{D}\mathbf{u},\, \operatorname{sym}\boldsymbol{P}\rangle_{L^2} + \|\operatorname{sym}\boldsymbol{P}\|_{L^2}^2) + k_\mathrm{micro}\|\operatorname{sym}\boldsymbol{P}\|_{L^2}^2 \\
&\quad + k_\mathrm{c}(\|\operatorname{skew}\mathrm{D}\mathbf{u}\|_{L^2}^2 - 2\langle \operatorname{skew}\mathrm{D}\mathbf{u},\, \operatorname{skew}\boldsymbol{P}\rangle_{L^2} + \|\operatorname{skew}\boldsymbol{P}\|_{L^2}^2) + \mu_\mathrm{macro} L_\mathrm{c}\|\operatorname{Curl}\boldsymbol{P}\|_{L^2}^2 \\
&\overset{\mathrm{Y}}{\geq} k_\mathrm{e}(\|\operatorname{sym}\mathrm{D}\mathbf{u}\|_{L^2}^2 - \varepsilon\|\operatorname{sym}\mathrm{D}\mathbf{u}\|_{L^2} - \frac{1}{\varepsilon}\|\operatorname{sym}\boldsymbol{P}\|_{L^2}^2 + \|\operatorname{sym}\boldsymbol{P}\|_{L^2}^2) + k_\mathrm{micro}\|\operatorname{sym}\boldsymbol{P}\|_{L^2}^2 \\
&\quad + k_\mathrm{c}(\|\operatorname{skew}\mathrm{D}\mathbf{u}\|_{L^2}^2 - \epsilon\|\operatorname{skew}\mathrm{D}\mathbf{u}\|_{L^2}^2 - \frac{1}{\epsilon}\|\operatorname{skew}\boldsymbol{P}\|_{L^2}^2 + \|\operatorname{skew}\boldsymbol{P}\|_{L^2}^2) \\
&\quad + \mu_\mathrm{macro} L_\mathrm{c}\|\operatorname{Curl}\boldsymbol{P}\|_{L^2}^2 \\
&\overset{*}{\geq} k_\mathrm{e}(\|\operatorname{sym}\mathrm{D}\mathbf{u}\|_{L^2}^2 - \varepsilon\|\operatorname{sym}\mathrm{D}\mathbf{u}\|_{L^2}^2 - \frac{1}{\varepsilon}\|\operatorname{sym}\boldsymbol{P}\|_{L^2}^2 + \|\operatorname{sym}\boldsymbol{P}\|_{L^2}^2) + k_\mathrm{micro}\|\operatorname{sym}\boldsymbol{P}\|_{L^2}^2 \\
&\quad + k_\mathrm{c}(\|\mathrm{D}\mathbf{u}\|_{L^2}^2 - \epsilon\|\mathrm{D}\mathbf{u}\|_{L^2}^2 - \frac{1}{\epsilon}\|\operatorname{skew}\boldsymbol{P}\|_{L^2}^2 + \|\operatorname{skew}\boldsymbol{P}\|_{L^2}^2) \\
&\quad + \mu_\mathrm{macro} L_\mathrm{c}\|\operatorname{Curl}\boldsymbol{P}\|_{L^2}^2 \\
&\overset{\mathrm{K}}{\geq} k_\mathrm{e}(\frac{1}{c_K^2}[\|\mathrm{D}\mathbf{u}\|_{L^2}^2 - \varepsilon\|\mathrm{D}\mathbf{u}\|_{L^2}^2] - \frac{1}{\varepsilon}\|\operatorname{sym}\boldsymbol{P}\|_{L^2}^2 + \|\operatorname{sym}\boldsymbol{P}\|_{L^2}^2) + k_\mathrm{micro}\|\operatorname{sym}\boldsymbol{P}\|_{L^2}^2 \\
&\quad + k_\mathrm{c}(\|\mathrm{D}\mathbf{u}\|_{L^2}^2 - \epsilon\|\mathrm{D}\mathbf{u}\|_{L^2}^2 - \frac{1}{\epsilon}\|\operatorname{skew}\boldsymbol{P}\|_{L^2}^2 + \|\operatorname{skew}\boldsymbol{P}\|_{L^2}^2) + \mu_\mathrm{macro} L_\mathrm{c}\|\operatorname{Curl}\boldsymbol{P}\|_{L^2}^2 \\
&\geq c_2\,(\|\mathrm{D}\mathbf{u}\|_{L^2}^2 + \|\boldsymbol{P}\|_{L^2}^2 + \|\operatorname{Curl}\boldsymbol{P}\|_{L^2}^2) \\
&\overset{\mathrm{PF}}{\geq} c_2\,(\frac{1}{2\,c_F^2}\|\mathbf{u}\|_{L^2}^2 + \frac{1}{2}\|\mathrm{D}\mathbf{u}\|_{L^2}^2 + \|\boldsymbol{P}\|_{L^2}^2 + \|\operatorname{Curl}\boldsymbol{P}\|_{L^2}^2) \\
&\geq c_2\, c_3\,(\|\mathbf{u}\|_{L^2}^2 + \|\mathrm{D}\mathbf{u}\|_{L^2}^2 + \|\boldsymbol{P}\|_{L^2}^2 + \|\operatorname{Curl}\boldsymbol{P}\|_{L^2}^2) \\
&\overset{\mathrm{Y}}{\geq} \frac{c_2\, c_3}{c_X}\|\{\mathbf{u}, \boldsymbol{P}\}\|_X^2 \quad \forall\, \{\mathbf{u}, \boldsymbol{P}\} \in X(V)\,,
\end{aligned}
\tag{4.44}
$$

where we used the orthogonality of sym-skew scalar products. The star * indicates the definition $1 - \epsilon < 0$. Consequently, the constants read

$$
\begin{aligned}
&c_2 = \min\{(1-\varepsilon)\frac{k_\mathrm{e}}{c_K^2} + (1-\epsilon)k_\mathrm{c},\, (1 - \frac{1}{\varepsilon})k_\mathrm{e} + k_\mathrm{micro},\, (1 - \frac{1}{\epsilon})k_\mathrm{c},\, \mu_\mathrm{macro} L_\mathrm{c}^2\,\}\,, \quad c_3 = \frac{1}{2}\min\{1,\, \frac{1}{c_F^2}\}\,, \\
&c_X = 2\max\{1,\, \frac{1}{2e},\, \frac{e}{2}\}\,.
\end{aligned}
\tag{4.45}
$$

Further, one finds

$$
\frac{k_\mathrm{e}}{k_\mathrm{e} + k_\mathrm{micro}} < \varepsilon < 1 + \frac{(1-\epsilon)k_\mathrm{c}\, c_K^2}{k_\mathrm{e}}\,, \qquad 1 < \epsilon < 1 + \left(1 - \frac{k_\mathrm{e}}{k_\mathrm{e} + k_\mathrm{micro}}\right)\frac{k_\mathrm{e}}{k_\mathrm{c}\, c_K^2}\,,
\tag{4.46}
$$

which is always satisfied for $k_\mathrm{micro}, k_\mathrm{c} > 0$. The coercivity constant reads $\beta = \dfrac{c_2\, c_3}{c_X}$. $\square$

For the second part of the proof we assume positive semi-definiteness such that $\mathbb{C}_\mathrm{c} = 0$ is allowed as long as the Dirichlet boundary of the microdistortion does not vanish $A_D^P \neq \emptyset$. Note that due to the definition of the consistent coupling condition this is always the case, since a Dirichlet boundary for the displacement field $\mathbf{u}$ is always required.

Theorem 4.9 (Well-posedness three-dimensional model II)
Let $\mu_{\mathrm{macro}}, L_{\mathrm{c}} > 0$ and $\mathbb{C}_{\mathrm{e}}, \mathbb{C}_{\mathrm{micro}}$ be positive definite on $\mathbb{R}^{3\times3}$. Further let $\mathbb{C}_{\mathrm{c}} = 0$ and $A_D^P \neq \emptyset$, then the problem

$$a(\{\delta\mathbf{u}, \delta\boldsymbol{P}\}, \{\mathbf{u}, \boldsymbol{P}\}) = l(\{\delta\mathbf{u}, \delta\boldsymbol{P}\}) \quad \forall\{\delta\mathbf{u}, \delta\boldsymbol{P}\} \in X(V)\,, \tag{4.47}$$

where the bilinear and linear forms are according to Eq. (3.8) *and Eq.* (3.9)*, has a unique solution*

$$\{\mathbf{u}, \boldsymbol{P}\} \in X(V) = [H_0^1(V)]^3 \times H_0(\mathrm{Curl}, V)\,, \qquad \|\{\mathbf{u}, \boldsymbol{P}\}\|_X = \|\mathbf{u}\|_{H^1} + \|\boldsymbol{P}\|_{H(\mathrm{Curl})}\,, \tag{4.48}$$

and there holds the stability estimate

$$\|\{\mathbf{u}, \boldsymbol{P}\}\|_X \leq \frac{1}{\beta}(\|\mathbf{f}\|_{L^2} + \|\boldsymbol{M}\|_{L^2})\,, \qquad \mathbf{f} \in [L^2(V)]^3,\ \boldsymbol{M} \in [L^2(V)]^{3\times3}\,, \tag{4.49}$$

with $\beta = \beta(\mathbb{C}_{\mathrm{e}}, \mathbb{C}_{\mathrm{micro}}, \mu_{\mathrm{macro}}, L_{\mathrm{c}}) > 0$.

Proof. The continuity of the bilinear form follows the same lines as in Eq. (4.43). The skew-symmetric part is dropped and the continuity constant results in $\alpha = 3\,c_1$.

In order to prove coercivity we make use of Young's, Korn's, Generalized Korn's, and Poincaré-Friedrich's inequalities

$$\begin{aligned}
a(\{\mathbf{u}, \boldsymbol{P}\}, \{\mathbf{u}, \boldsymbol{P}\}) &\geq k_{\mathrm{e}}(\|\operatorname{sym}\mathrm{D}\mathbf{u}\|_{L^2}^2 - 2\langle\operatorname{sym}\mathrm{D}\mathbf{u}, \operatorname{sym}\boldsymbol{P}\rangle_{L^2} + \|\operatorname{sym}\boldsymbol{P}\|_{L^2}^2) \\
&\qquad + k_{\mathrm{micro}}\|\operatorname{sym}\boldsymbol{P}\|_{L^2}^2 + \mu_{\mathrm{macro}}L_{\mathrm{c}}\|\operatorname{Curl}\boldsymbol{P}\|_{L^2}^2 \\
&\overset{\mathrm{Y}}{\geq} k_{\mathrm{e}}(\|\operatorname{sym}\mathrm{D}\mathbf{u}\|_{L^2}^2 - \varepsilon\|\operatorname{sym}\mathrm{D}\mathbf{u}\|_{L^2}^2 - \frac{1}{\varepsilon}\|\operatorname{sym}\boldsymbol{P}\|_{L^2}^2 + \|\operatorname{sym}\boldsymbol{P}\|_{L^2}^2) \\
&\qquad + k_{\mathrm{micro}}\|\operatorname{sym}\boldsymbol{P}\|_{L^2}^2 + \mu_{\mathrm{macro}}L_{\mathrm{c}}\|\operatorname{Curl}\boldsymbol{P}\|_{L^2}^2 \\
&\geq c_2\,(\|\operatorname{sym}\mathrm{D}\mathbf{u}\|_{L^2}^2 + \|\operatorname{sym}\boldsymbol{P}\|_{L^2}^2 + \|\operatorname{Curl}\boldsymbol{P}\|_{L^2}^2) \\
&\overset{\mathrm{K}}{\geq} c_2\,(\frac{1}{c_K^2}\|\mathrm{D}\mathbf{u}\|_{L^2}^2 + \|\operatorname{sym}\boldsymbol{P}\|_{L^2}^2 + \|\operatorname{Curl}\boldsymbol{P}\|_{L^2}^2) \\
&\overset{\mathrm{GK}}{\geq} c_2\,(\frac{1}{c_K^2}\|\mathrm{D}\mathbf{u}\|_{L^2}^2 + \frac{1}{c_G}[\|\boldsymbol{P}\|_{L^2}^2 + \|\operatorname{Curl}\boldsymbol{P}\|_{L^2}^2]) \\
&\overset{\mathrm{PF}}{\geq} c_2\,(\frac{1}{c_K^2}[\frac{1}{2\,c_F^2}\|\mathbf{u}\|_{L^2}^2 + \frac{1}{2}\|\mathrm{D}\mathbf{u}\|_{L^2}^2] + \frac{1}{c_G}[\|\boldsymbol{P}\|_{L^2}^2 + \|\operatorname{Curl}\boldsymbol{P}\|_{L^2}^2]) \\
&\geq c_2\,c_3\,(\|\mathbf{u}\|_{L^2}^2 + \|\mathrm{D}\mathbf{u}\|_{L^2}^2 + \|\boldsymbol{P}\|_{L^2}^2 + \|\operatorname{Curl}\boldsymbol{P}\|_{L^2}^2) \\
&\overset{\mathrm{Y}}{\geq} \frac{c_2\,c_3}{c_X}\|\{\mathbf{u}, \boldsymbol{P}\}\|_X^2 \quad \forall\,\{\mathbf{u}, \boldsymbol{P}\} \in X(V)\,.
\end{aligned} \tag{4.50}$$

The corresponding constants read

$$\begin{aligned}
&c_2 = \min\{(1-\varepsilon)k_{\mathrm{e}},\ (1-\frac{1}{\varepsilon})k_{\mathrm{e}} + k_{\mathrm{micro}},\ \mu_{\mathrm{macro}}L_{\mathrm{c}}^2\}\,, \qquad c_3 = \frac{1}{2}\min\{1,\ \frac{1}{c_K^2\,c_F^2},\ \frac{1}{c_G}\}\,, \\
&c_X = 2\max\{1, \frac{1}{2e}, \frac{e}{2}\}\,,
\end{aligned} \tag{4.51}$$

with

$$\frac{k_{\mathrm{e}}}{k_{\mathrm{e}} + k_{\mathrm{micro}}} < \varepsilon < 1 \,. \tag{4.52}$$

The coercivity constant is given by $\beta = \dfrac{c_2 \, c_3}{c_X}$. ☐

The case of $L_{\mathrm{c}} = 0$ yields a loss in regularity for the microdistortion $\boldsymbol{P} \in [L^2(V)]^{3\times3}$. Unlike in the reduced model of antiplane shear, this does not imply $\boldsymbol{P} = \mathrm{D}\mathbf{v}$ for some vector field $\mathbf{v} \in [H^1(V)]^3$, such that the $H(\mathrm{Curl})$-space does not guarantee well-posedness.

Theorem 4.10 (Homogeneous relaxed micromorphic continuum)
Let $\mathbb{C}_{\mathrm{e}}, \mathbb{C}_{\mathrm{micro}}, \mathbb{C}_{\mathrm{c}}$ be positive definite, $L_{\mathrm{c}} = 0$ and $X = [H^1(V)]^3 \times [L^2(V)]^{3\times3}$ then Problem. 4.40 is uniquely solvable.

Proof. The proof of continuity and coercivity is analogous to Theorem 4.8 with the modification of the constants to

$$\alpha = 3\, c_1 \quad c_1 = \max\{c_{\mathrm{e}},\, c_{\mathrm{micro}},\, c_{\mathrm{c}}\} \,, \quad c_2 = \min\{(1-\varepsilon)\frac{k_{\mathrm{e}}}{c_K^2} + (1-\epsilon)k_{\mathrm{c}},\, (1-\frac{1}{\varepsilon})k_{\mathrm{e}} + k_{\mathrm{micro}},\, (1-\frac{1}{\epsilon})k_{\mathrm{c}}\} \,, \tag{4.53}$$

where the coercivity constant follows accordingly. ☐

Remark 4.2
Note that the semi positive-definite case $\mathbb{C}_{\mathrm{c}} = 0$ is no longer well-posed since the space $L^2(V)$ does not allow for boundary conditions, such that the lower limit cannot be bound using the generalized Korn inequality. Setting $L_{\mathrm{c}} = 0$ and $\mathbb{C}_{\mathrm{c}} = 0$ results in a loss of control over the skew-symmetric part of the microdistortion $\operatorname{skew} \boldsymbol{P}$ leading to unstable results. Consequently, only the gradient of the displacement field $\mathrm{D}\mathbf{u}$ remains controllable.

Remark 4.3
In [58, 83] it is shown that for certain sufficiently smooth data, the regularity of the microdistortion can yet be improved to $\boldsymbol{P} \in [H^1(V)]^{3\times3}$.

4.3.4 Plane strain

The proof of well-posedness of the plane strain model is analogous to the proof of the full three-dimensional model.

Theorem 4.11 (Well-posedness plane strain I)
Let $\mu_{\mathrm{macro}}, L_{\mathrm{c}} > 0$ and $\mathbb{C}_{\mathrm{e}}, \mathbb{C}_{\mathrm{micro}}$ be positive definite on $\mathbb{R}^{2\times2}$. Further let $\mathbb{C}_{\mathrm{c}}$ be positive definite on $\mathfrak{so}(2)$, then the problem

$$a(\{\delta\mathbf{u}, \delta\boldsymbol{P}\}, \{\mathbf{u}, \boldsymbol{P}\}) = l(\{\delta\mathbf{u}, \delta\boldsymbol{P}\}) \quad \forall \{\delta\mathbf{u}, \delta\boldsymbol{P}\} \in X(A) \,, \tag{4.54}$$

where the bilinear and linear forms are according to Eq. (3.27), has a unique solution

$$\{\mathbf{u}, \boldsymbol{P}\} \in X(A) = [H_0^1(A)]^2 \times H(\mathrm{Curl}, A) \,, \qquad \|\{\mathbf{u}, \boldsymbol{P}\}\|_X = \|\mathbf{u}\|_{H^1} + \|\boldsymbol{P}\|_{H(\mathrm{Curl})} \,, \tag{4.55}$$

and there holds the stability estimate

$$\|\{\mathbf{u}, \boldsymbol{P}\}\|_X \leq \frac{1}{\beta}(\|\mathbf{f}\|_{L^2} + \|\boldsymbol{M}\|_{L^2}) \,, \qquad \mathbf{f} \in [L^2(V)]^2,\, \boldsymbol{M} \in [L^2(V)]^{2\times2} \,, \tag{4.56}$$

with $\beta = \beta(\mathbb{C}_{\mathrm{e}}, \mathbb{C}_{\mathrm{micro}}, \mathbb{C}_{\mathrm{c}}, \mu_{\mathrm{macro}}, L_{\mathrm{c}}) > 0$.

Proof. The proof follows the same lines as Theorem 4.8 with an adaption of the space and boundary conditions for two-dimensional domains. $\square$

Theorem 4.12 (Well-posedness plane strain II)
Let $\mu_{\mathrm{macro}}, L_{\mathrm{c}} > 0$ *and* $\mathbb{C}_{\mathrm{e}}, \mathbb{C}_{\mathrm{micro}}$ *be positive definite on* $\mathbb{R}^{2\times 2}$*. Further let* $\mathbb{C}_{\mathrm{c}} = 0$ *and* $s_D^P \neq \emptyset$*, then the problem*

$$a(\{\delta\mathbf{u}, \delta\boldsymbol{P}\}, \{\mathbf{u}, \boldsymbol{P}\}) = l(\{\delta\mathbf{u}, \delta\boldsymbol{P}\}) \quad \forall \{\delta\mathbf{u}, \delta\boldsymbol{P}\} \in X(A)\,, \tag{4.57}$$

where the bilinear and linear forms are according to Eq. (3.27)*, has a unique solution*

$$\{\mathbf{u}, \boldsymbol{P}\} \in X(A) = [H_0^1(A)]^2 \times H_0(\mathrm{Curl}, A)\,, \qquad \|\{\mathbf{u}, \boldsymbol{P}\}\|_X = \|\mathbf{u}\|_{H^1} + \|\boldsymbol{P}\|_{H(\mathrm{Curl})}\,, \tag{4.58}$$

and there holds the stability estimate

$$\|\{\mathbf{u}, \boldsymbol{P}\}\|_X \leq \frac{1}{\beta}(\|\mathbf{f}\|_{L^2} + \|\boldsymbol{M}\|_{L^2})\,, \qquad \mathbf{f} \in [L^2(A)]^2,\ \boldsymbol{M} \in [L^2(A)]^{2\times 2}\,, \tag{4.59}$$

with $\beta = \beta(\mathbb{C}_{\mathrm{e}}, \mathbb{C}_{\mathrm{micro}}, \mu_{\mathrm{macro}}, L_{\mathrm{c}}) > 0$*.*

Proof. The proof follows the same lines as Theorem 4.9 with an adaption of the space and boundary conditions. Specifically, the tangential projection is computed using the scalar product instead of the cross product. $\square$

The case of $L_{\mathrm{c}} = 0$ follows analogously to the three-dimensional case.

Theorem 4.13 (Homogeneous plane strain model)
Let $\mathbb{C}_{\mathrm{e}}, \mathbb{C}_{\mathrm{micro}}, \mathbb{C}_{\mathrm{c}}$ *be positive definite,* $L_{\mathrm{c}} = 0$ *and* $X = [H^1(A)]^2 \times [L^2(A)]^{2\times 2}$ *then Problem. 4.54 is uniquely solvable.*

Proof. The proof is the same as in Theorem 4.10 and only holds for a positive definite $\mathbb{C}_{\mathrm{c}}$ on $\mathfrak{so}(2)$. $\square$

5 The Finite Element Method

The finite element method [18, 19, 23, 111] is a specific approach for computing discrete solutions for partial differential equations using Galerkin projections

$$\text{Find } u \in X : \quad a(u,v) = f(v) \quad \forall\, v \in X \,, \tag{5.1}$$

such that the discrete problem reads

$$\text{Find } u^h \in X^h : \quad a(u^h,v^h) = f(v^h) \quad \forall\, v^h \in X^h \,, \tag{5.2}$$

and the discrete space X^h is spanned by so called finite elements, leading to a system of algebraic equations. This work deals with conforming finite elements such that $X^h \subset X$. Under certain assumptions, one can show that the discrete solution u^h converges towards the analytical solution u for an element size tending to zero $h \to 0$.

This chapter is devoted to the introduction of the theory of finite element approximations. Further, this chapter demonstrates a priori convergence estimates for relaxed micromorphic continua.

5.1 Triangulations

A preparatory step in the finite element method with triangular elements is the so called triangulation also known as meshing [44, 66, 95]. The domain is decomposed into a finite number of triangles in two dimensions or tetrahedra in three dimensions (other geometric forms such as quads, hexahedra, prisms, or pyramids are also used but can be represented by triangles or tetrahedra).

Definition 5.1 (Regular triangulation)
A triangulation A^h of A is called regular if

1. *The elements are non-overlapping and their intersection is either an edge s_{ij} or a vertex v_{ij}*

$$A_i \cap A_j = \begin{cases} v_{ij} \\ s_{ij} \end{cases} , \qquad A_i, A_j \in A^h \,, \qquad i \neq j \,. \tag{5.3}$$

2. *The domain is given by the finite union of the elements*

$$A = \bigcup_{e=1}^{n} A_e \,, \qquad A_e \in A^h \,. \tag{5.4}$$

For affine maps each triangle is mapped from the reference domain Γ into the physical domain A_e by the barycentric mapping

$$\mathbf{x}(\xi,\eta) = (1-\xi-\eta)\mathbf{x}_1 + \eta\,\mathbf{x}_2 + \xi\,\mathbf{x}_3 \,, \qquad \mathbf{x} : \Gamma \to A_e \,, \qquad \Gamma = \{(\xi,\eta) \in [0,1]^2 \mid \xi + \eta \leq 1\} \,, \tag{5.5}$$

where $\mathbf{x}_i$ represent the coordinates of the vertices of one triangle in the physical domain, see Fig. 5.1. The corresponding Jacobi matrix reads

$$\boldsymbol{J} = \mathrm{D}\mathbf{x} = \begin{bmatrix} \mathbf{x}_3 - \mathbf{x}_1 & \mathbf{x}_2 - \mathbf{x}_1 \end{bmatrix} \in \mathbb{R}^{2\times 2} \,. \tag{5.6}$$

Analogously, one defines a regular tetrahedralization.

Definition 5.2 (Regular tetrahedralization)
A tetrahedralization V^h of V is called regular if

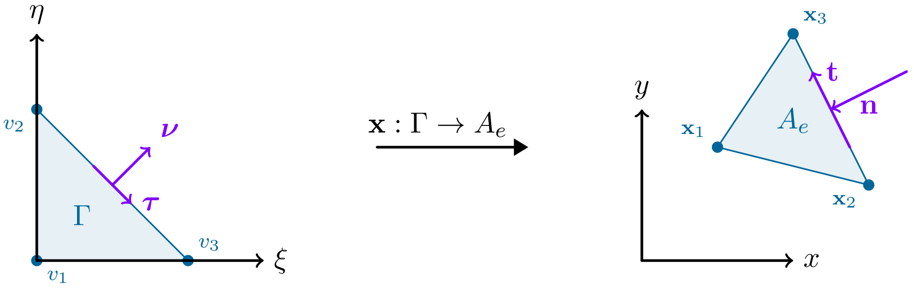

Figure 5.1: Barycentric mapping of the reference triangle to an element in the physical domain.

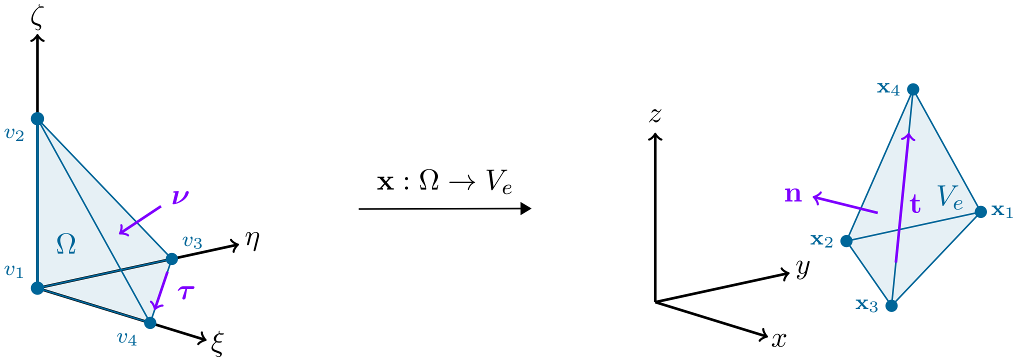

Figure 5.2: Barycentric mapping of the reference tetrahedron to an element in the physical domain.

1. *The elements are non-overlapping and their intersection is either a surface* A_{ij}*, an edge* s_{ij} *or a vertex* v_{ij}

$$V_i \cap V_j = \begin{cases} v_{ij} \\ s_{ij} \\ A_{ij} \end{cases}, \qquad V_i, V_j \in V^h , \qquad i \neq j . \tag{5.7}$$

2. *The domain is given by the finite union of the elements*

$$V = \bigcup_{e=1}^{n} V_e , \qquad V_e \subset V^h . \tag{5.8}$$

The tetrahedra are mapped from the reference tetrahedron by the three-dimensional barycentric coordinates (see Fig. 5.2)

$$\begin{aligned} &\mathbf{x}(\xi,\eta,\zeta) = (1-\xi-\eta-\zeta)\mathbf{x}_1 + \zeta\,\mathbf{x}_2 + \eta\,\mathbf{x}_3 + \xi\,\mathbf{x}_4 , && \mathbf{x} : \Omega \to V_e , \\ &\Omega = \{(\xi,\eta,\zeta) \in [0,1]^3 \mid \xi+\eta+\zeta \leq 1\} . \end{aligned} \tag{5.9}$$

and the corresponding Jacobi matrix reads

$$\boldsymbol{J} = \mathrm{D}\mathbf{x} = \begin{bmatrix} \mathbf{x}_4 - \mathbf{x}_1 & \mathbf{x}_3 - \mathbf{x}_1 & \mathbf{x}_2 - \mathbf{x}_1 \end{bmatrix} \in \mathbb{R}^{3\times 3} . \tag{5.10}$$

Remark 5.1
An important consequence of affine maps is that the polynomial space is preserved on the physical domain, thus allowing for error estimates based on polynomials [110].

Remark 5.2
The introduced orientation of the element is clockwise. This is a deviation from the classical counter-clockwise approach but is intrinsic to the subsequent construction of higher order elements based on Bernstein polynomials.

The Frobenius norm of the Jacobi matrix is an indicator of the change in size from the triangle on the reference domain to the triangle on the physical domain such that

$$h = \|\boldsymbol{J}\|_F \, , \qquad\qquad h_V = \max_{h \in A^h} h(A) \, , \tag{5.11}$$

where h_V represents the maximum size of an element of the discretization. The following definitions of shape regularity and uniformity arise accordingly [19]

Definition 5.3 (Shape regularity and uniformity)

1. *A triangulation is called shape-regular if the condition number of the mapping is bounded for all elements*
$$\exists \, c_1, c_2 > 0 : \quad c_1 \leq \|\boldsymbol{J}\|_F \|\boldsymbol{J}^{-1}\|_F \leq c_2 \quad \forall \, A_e \in A^h \, . \tag{5.12}$$
2. *The triangulation is quasi-uniform if*
$$\exists \, c_1, c_2 > 0 : \quad c_1 \, h \leq h_V \leq c_2 \, h \quad \forall \, h \in \operatorname{span}\{h(\mathbf{x} \in A)\} \, . \tag{5.13}$$
3. *The triangulation is uniform if*
$$\exists \, h > 0 : \quad h = h_e \quad \forall \, h_e \in \operatorname{span}\{h(\mathbf{x} \in A)\} \, . \tag{5.14}$$

The definition can be applied analogously to tetrahedra.

In shape regular triangulations the elements do not degenerate for $h \to 0$, meaning the angles of the triangles are bound away from 0 and 180 degrees. A quasi-uniform triangulation implies the elements have a nearly uniform size throughout the domain. In a uniform triangulation, every element has the same size.

Next, we introduce the definition of a finite element according to Ciarlet [23].

Definition 5.4 (Finite Element)
The triplet $\{\Omega, S, \mathcal{D}\}$ is called a finite element if

1. *the element's domain $\Omega \subset \mathbb{R}^3$ is a bounded and closed set with a non-empty interior and a piece-wise smooth boundary,*
2. *the space of shape functions S is finite dimensional,*
3. *the set of degrees of freedom spans the dual space of S*
$$\operatorname{span}\{d_1, d_2, \dots, d_n\} = S' \, , \qquad\qquad d_1, d_2, \dots, d_n \in \mathcal{D} \, . \tag{5.15}$$

With the definition of the triangulation and the finite element we can define the finite element space.

Definition 5.5 (Finite element space)
Let A^h be a regular triangulation on $A \subset \mathbb{R}^2$ where each triangle is equipped with a finite element $\{A_e, S(A_e), \mathcal{D}(A_e)\}$, the finite element space is given by

$$X^h = \{u \in \bigcup_{A_e \in A^h} S(A_e) \mid \mathcal{D}(u)\Big|_{A_i} = \mathcal{D}(u)\Big|_{A_j} \quad \forall \, \mathcal{D} \in \mathcal{D}(A_i) \cap \mathcal{D}(A_j)\} \, , \tag{5.16}$$

where the degrees of freedom shared between elements coincide.

5.2 A priori convergence estimates

In this section we give a priori convergence estimates for relaxed micromorphic continua models. Although the relaxed micromorphic model is proved to be well-posed using the Lax-Milgram theorem, such that the employment of the de Rham complex is not strictly necessary (the relaxed micromorphic model is not a mixed formulation and does rely on kernel coercivity), we note that both the consistent coupling condition and convergence estimates can be treated with its apparatus. In fact, the consistent coupling condition can only be exactly satisfied in the general sense by using polynomial sequences. Further, the error estimates are bound by the convergence of the displacement field, such that using a higher order polynomial for the microdistortion in comparison to the displacement does not improve the convergence rate. Further, re-stabilization of the formulation with respect to the characteristic length parameter L_c can be done with mixed formulations relying on the de Rham complex [100,101].

The basis for the following estimates is Cea's lemma [19], which can be applied due to the proofs of existence and uniqueness using the Lax-Milgram theorem.

Lemma 5.1 (Cea's quasi-best approximation)
Let X be a Hilbert space, $u \in X$ be the analytical solution and $u^h \in X^h$ the finite subspace approximation. Further, let the corresponding bilinear form satisfy the Lax-Milgram theorem, then there holds

$$\|u - u^h\|_X \leq \frac{\alpha}{\beta} \inf_{q \in X^h} \|u - q\|_X \, , \tag{5.17}$$

where α and β are the continuity and coercivity constants, respectively.

Further, a few results of interpolation theory are required in order to frame the convergence rate with respect to the element's size and polynomial power.

Lemma 5.2 (H^1-interpolation estimates)
Let Π_g^p be an element-wise projection-based interpolant from $H^1(V)$ to a subspace of piece-wise polynomials with global C^0-continuity, then there holds [110]

$$\exists\, c > 0 : \quad \|u - \Pi_g^p u\|_{H^r} \leq c\, h^{p+1-r} |u|_{H^{p+1}} \, , \qquad r \in \{0,1\} \, , \quad p \in \mathbb{N} \, , \tag{5.18}$$

for a uniform and regular triangulation where the constant is not a function of element size or the analytical solution $c \neq c(h,u)$. The latter is a consequence of the Bramble-Hilbert lemma.

Lemma 5.3 ($H(\mathrm{curl})$-interpolation estimates)
Let Π_c^p be an element-wise projection-based interpolant from $H(\mathrm{curl}, V)$ to $\mathcal{N}_I^p$, then there holds (see [70, 71])

$$\exists\, c > 0 : \quad \|\mathbf{p} - \Pi_c^p \mathbf{p}\|_{L^2} \leq c\, h^{p+1} |\mathbf{p}|_{H^{p+1}} \, , \qquad p \in \mathbb{N}_0 \, , \tag{5.19}$$

for a uniform and regular triangulation such that the constant does not depend on the element size or the analytical solution $c \neq c(h, \mathbf{p})$.

Lemma 5.4 ($H(\mathrm{div})$-interpolation estimates)
Let Π_d^p be an element-wise projection-based interpolant from $H(\mathrm{div}, V)$ to $\mathcal{RT}^p$ (see [87]), then there holds

$$\exists\, c > 0 : \quad \|\mathbf{p} - \Pi_d^p \mathbf{p}\|_{L^2} \leq c\, h^{p+1} |\mathbf{p}|_{H^{p+1}} \, , \qquad p \in \mathbb{N}_0 \, , \tag{5.20}$$

for a uniform and regular triangulation with $c \neq c(h, \mathbf{p})$.

Lemma 5.5 (L^2-interpolation estimates)
Let Π_o^p be an element-wise projection-based interpolant from $L^2(V)$ to $P^p(V)$, then there holds [110]

$$\exists\, c > 0 : \quad \|u - \Pi_o^p u\|_{L^2} \leq c\, h^{p+1} |u|_{H^{p+1}} \,, \qquad\qquad p \in \mathbb{N}_0 \,, \tag{5.21}$$

for a uniform and regular triangulation such that $c \neq c(h, u)$.

We employ the projection-based interpolants based on the works of [20, 30, 70, 71, 87] for the application of Dirichlet boundary conditions. The corresponding degrees of freedom are specified in the following sections. The interpolants commute on the de Rham complex for contractible domains and sufficiently smooth functions. The first complex is based on the Nédélec elements of the first type and Raviart-Thomas elements, see Fig. 5.3. An alternative construction of the complex can be achieved with Nédélec elements of the second type and Brezzi-Douglas-Marini elements, see Fig. 5.4. One can also introduce complexes where the element types are mixed.

Remark 5.3
The canonical interpolation operators assume additional smoothness on the function spaces, as for example point evaluation is not well-defined for $u \in H^1(V)$. As such, for our theoretical convergence proofs we make use of the L^2-bounded commuting projections recently introduced in [10] whereas the usual projection operators are employed in the finite element implementation.

The degree reduction of the polynomial spaces is given by the exact polynomial sequences (see Fig. 5.5), where $P(V)$ and $\widetilde{P}(V)$ are the respective spaces of polynomials and homogeneous polynomials on the domain

$$\begin{aligned} P^p(V) &= \operatorname{span}\{x^i y^j z^k \mid i,j,k \in \mathbb{N}_0 \,,\; i+j+k \leq p\} \,, \\ \widetilde{P}^p(V) &= \operatorname{span}\{x^i y^j z^k \mid i,j,k \in \mathbb{N}_0 \,,\; i+j+k = p\} \,. \end{aligned} \tag{5.22}$$

The diagrams commute if for sufficiently smooth functions there hold the relations

$$\begin{aligned} \nabla \Pi_g u &= \Pi_c \nabla u && \forall\, u \in H^1(V) \,, \\ \operatorname{curl} \Pi_c \mathbf{p} &= \Pi_d \operatorname{curl} \mathbf{p} && \forall\, \mathbf{p} \in H(\operatorname{curl}, V) \,, \\ \operatorname{div} \Pi_d \mathbf{d} &= \Pi_o \operatorname{div} \mathbf{d} && \forall\, \mathbf{d} \in H(\operatorname{div}, V) \,, \end{aligned} \tag{5.23}$$

in three-dimensions. In two dimensions the curl operator maps directly to the Lebesgue space

$$\operatorname{div}(\boldsymbol{R}\Pi_c \mathbf{p}) = \Pi_o \operatorname{div}(\boldsymbol{R}\mathbf{p}) \qquad\qquad \forall\, \mathbf{p} \in H(\operatorname{div}\boldsymbol{R}, A) \,. \tag{5.24}$$

5.2.1 Antiplane shear

We state the convergence estimate for the reduced relaxed micromorphic model of antiplane shear [101].

Lemma 5.6 (Antiplane shear convergence)
Let $\{u, \mathbf{p}\} \in H^{p+1}(A) \times H^p(\operatorname{div}\boldsymbol{R}, A)$ be a smooth exact solution with $H^p(\operatorname{div}\boldsymbol{R}, A) = \{\mathbf{p} \in [H^p(A)]^2 \mid \operatorname{div}(\boldsymbol{R}\mathbf{p}) \in H^p(A)\}$. Further, let $X^h(A) = U^p(A) \times \mathcal{N}_I^{p-1}(A) \subset X(A)$, then the approximate solution converges at an optimal rate

$$\|\{u, \mathbf{p}\} - \{u^h, \mathbf{p}^h\}\|_X \leq c\, h^p \left(|u|_{H^{p+1}} + |\mathbf{p}|_{H^p} + |\operatorname{div}(\boldsymbol{R}\mathbf{p})|_{H^p}\right) , \quad c = c(\mu_{\mathrm{e}}, \mu_{\mathrm{micro}}, \mu_{\mathrm{macro}}, L_{\mathrm{c}}^2) \,, \tag{5.25}$$

$$\begin{tikzcd}
\mathbb{R} \arrow[r, "\mathrm{id}"] & H^1(V) \arrow[r, "\nabla"] \arrow[d, swap, "\Pi_g^p"] & H(\mathrm{curl}, V) \arrow[r, "\mathrm{curl}"] \arrow[d, swap, "\Pi_c^{p-1}"] & H(\mathrm{div}, V) \arrow[r, "\mathrm{div}"] \arrow[d, swap, "\Pi_d^{p-1}"] & L^2(V) \arrow[d, swap, "\Pi_o^{p-1}"] \\
\mathbb{R} \arrow[r] & U^p(V) \arrow[r, "\nabla"] & \mathcal{N}_I^{p-1}(V) \arrow[r, "\mathrm{curl}"] & \mathcal{RT}^{p-1}(V) \arrow[r, "\mathrm{div}"] & P^{p-1}(V)
\end{tikzcd}$$

(a)

$$\begin{tikzcd}
\mathbb{R} \arrow[r, "\mathrm{id}"] & H^1(A) \arrow[r, "\nabla"] \arrow[d, swap, "\Pi_g^p"] & H(\mathrm{div}\boldsymbol{R}, A) \arrow[r, "\mathrm{div}\boldsymbol{R}"] \arrow[d, swap, "\Pi_c^{p-1}"] & L^2(A) \arrow[d, swap, "\Pi_o^{p-1}"] \\
\mathbb{R} \arrow[r] & U^p(A) \arrow[r, "\nabla"] & \mathcal{N}_I^{p-1}(A) \arrow[r, "\mathrm{div}\boldsymbol{R}"] & P^{p-1}(A)
\end{tikzcd}$$

(b)

Figure 5.3: De Rham complexes for (a) three- and (b) two-dimensional domains using Nédélec elements of the first type and Raviart-Thomas elements. The differential and interpolation operators commute between the continuous and discrete spaces.

$$\begin{tikzcd}
\mathbb{R} \arrow[r, "\mathrm{id}"] & H^1(V) \arrow[r, "\nabla"] \arrow[d, swap, "\Pi_g^p"] & H(\mathrm{curl}, V) \arrow[r, "\mathrm{curl}"] \arrow[d, swap, "\Pi_c^{p-1}"] & H(\mathrm{div}, V) \arrow[r, "\mathrm{div}"] \arrow[d, swap, "\Pi_d^{p-2}"] & L^2(V) \arrow[d, swap, "\Pi_o^{p-3}"] \\
\mathbb{R} \arrow[r] & U^p(V) \arrow[r, "\nabla"] & \mathcal{N}_{II}^{p-1}(V) \arrow[r, "\mathrm{curl}"] & \mathcal{BDM}^{p-2}(V) \arrow[r, "\mathrm{div}"] & P^{p-3}(V)
\end{tikzcd}$$

(a)

$$\begin{tikzcd}
\mathbb{R} \arrow[r, "\mathrm{id}"] & H^1(A) \arrow[r, "\nabla"] \arrow[d, swap, "\Pi_g^p"] & H(\mathrm{div}\boldsymbol{R}, A) \arrow[r, "\mathrm{div}\boldsymbol{R}"] \arrow[d, swap, "\Pi_c^{p-1}"] & L^2(A) \arrow[d, swap, "\Pi_o^{p-2}"] \\
\mathbb{R} \arrow[r] & U^p(A) \arrow[r, "\nabla"] & \mathcal{N}_{II}^{p-1}(A) \arrow[r, "\mathrm{div}\boldsymbol{R}"] & P^{p-2}(A)
\end{tikzcd}$$

(b)

Figure 5.4: De Rham complexes for (a) three- and (b) two-dimensional domains using Nédélec elements of the second type and Brezzi-Douglas-Marini elements. The differential and interpolation operators commute between the continuous and discrete spaces.

$$\begin{tikzcd} P^p(V) \arrow[r, "\nabla"] & {[P^{p-1}(V)]^3 \oplus \mathbf{x} \times [\widetilde{P}^{p-1}(V)]^3} \arrow[r, "\mathrm{curl}"] & {[P^{p-1}(V)]^3 \oplus \widetilde{P}^{p-1}(V)\,\mathbf{x}} \arrow[r, "\mathrm{div}"] & P^{p-1}(V) \end{tikzcd}$$

(a)

$$\begin{tikzcd} P^p(V) \arrow[r, "\nabla"] & {[P^{p-1}(V)]^3} \arrow[r, "\mathrm{curl}"] & {[P^{p-2}(V)]^3} \arrow[r, "\mathrm{div}"] & P^{p-3}(V) \end{tikzcd}$$

(b)

$$\begin{tikzcd} P^p(A) \arrow[r, "\nabla"] & {[P^{p-1}(A)]^2 \oplus \boldsymbol{R}\,\widetilde{P}^{p-1}(A)\,\mathbf{x}} \arrow[r, "\mathrm{div}\boldsymbol{R}"] & P^{p-1}(A) \end{tikzcd}$$

(c)

$$\begin{tikzcd} P^p(A) \arrow[r, "\nabla"] & {[P^{p-1}(A)]^2} \arrow[r, "\mathrm{div}\boldsymbol{R}"] & P^{p-2}(A) \end{tikzcd}$$

(d)

Figure 5.5: Polynomial sequence of first type Nédélec and Raviart Thomas spaces (a) followed by the polynomial sequence of second type Nédélec and Brezzi-Douglas-Marini spaces (b) on three-dimensional domains. (c) and (d) depict the polynomial sequences of the first and second type Nédélec spaces on two-dimensional domains, respectively.

Proof. By using Cea's lemma, Young's inequality and inserting the interpolation operators of the commuting diagram one finds

$$\begin{aligned}
\|\{u,\mathbf{p}\} - \{u^h,\mathbf{p}^h\}\|_X^2 &\leq c \inf_{\{\delta u^h, \delta \mathbf{p}^h\} \in X^h} \|\{u,\mathbf{p}\} - \{\delta u^h, \delta \mathbf{p}^h\}\|_X^2 \\
&\leq c\,(\|u - \Pi_g^p u\|_{H^1} + \|\mathbf{p} - \Pi_c^{p-1}\mathbf{p}\|_{H(\mathrm{div}\boldsymbol{R})})^2 \\
&\overset{\mathrm{Y}}{\leq} c\,(\|u - \Pi_g^p u\|_{H^1}^2 + \|\mathbf{p} - \Pi_c^{p-1}\mathbf{p}\|_{H(\mathrm{div}\boldsymbol{R})}^2) \\
&= c\,(\|u - \Pi_g^p u\|_{H^1}^2 + \|\mathbf{p} - \Pi_c^{p-1}\mathbf{p}\|_{L^2}^2 + \|\mathrm{div}(\boldsymbol{R}\mathbf{p}) - \mathrm{div}(\boldsymbol{R}\Pi_c^{p-1}\mathbf{p})\|_{L^2}^2) \\
&= c\,(\|u - \Pi_g^p u\|_{H^1}^2 + \|\mathbf{p} - \Pi_c^{p-1}\mathbf{p}\|_{L^2}^2 + \|(\mathrm{id} - \Pi_o^{p-1})\mathrm{div}(\boldsymbol{R}\mathbf{p})\|_{L^2}^2) \\
&\leq c\,(h^{2(p+1)}|u|_{H^{p+1}}^2 + h^{2p}|\mathbf{p}|_{H^p}^2 + h^{2p}|\mathrm{div}(\boldsymbol{R}\mathbf{p})|_{H^p}^2) \\
&\leq c h^{2p}\,(|u|_{H^{p+1}}^2 + |\mathbf{p}|_{H^p}^2 + |\mathrm{div}(\boldsymbol{R}\mathbf{p})|_{H^p}^2)\,,
\end{aligned} \tag{5.26}$$

where $|\cdot|_{H^p}$ denotes a Sobolev semi-norm. □

If the Nédélec space of the second type $\mathcal{N}_{II}$ is employed instead of the Nédélec space of the first type $\mathcal{N}_I$, then the next interpolant in the sequence becomes Π_o^{p-2} and one order of convergence is lost in the curl term. However, as shown in Section 3.2.3, several cases reduce the microdistortion to a gradient field $\mathbf{p} = \nabla p$ such that optimal convergence is maintained.

5.2.2 Three-dimensional model

Next we consider the convergence of the full three-dimensional relaxed micromorphic model [100].

Lemma 5.7 (Relaxed micromorphic model convergence)
Let $\{\mathbf{u}, \boldsymbol{P}\} \in [H^{p+1}(V)]^3 \times H^p(\mathrm{Curl}, V)$ be an exact and smooth solution. Further, let $\{\mathbf{u}^h, \boldsymbol{P}^h\} \in$

$[U^p(V)]^3 \times [\mathcal{N}_I^{p-1}(V)]^3 \subset [H^{p+1}(V)]^3 \times H^p(\mathrm{Curl}, V)$, *then the discrete solution* $\{\mathbf{u}^h, \boldsymbol{P}^h\} \in X^h$ *converges at the optimal rate*

$$\|\{\mathbf{u}, \boldsymbol{P}\} - \{\mathbf{u}^h, \boldsymbol{P}^h\}\|_X \leq c\, h^p(|\mathbf{u}|_{H^{p+1}} + |\boldsymbol{P}|_{H^p} + |\operatorname{Curl} \boldsymbol{P}|_{H^p}) \,, \quad c = c(\mathbb{C}_{\mathrm{e}}, \mathbb{C}_{\mathrm{micro}}, \mathbb{C}_{\mathrm{c}}, \mu_{\mathrm{macro}}, L_{\mathrm{c}}) \,. \tag{5.27}$$

Proof. We apply Cea's lemma, Young's inequality and the commuting interpolants to find

$$\begin{aligned}
\|\{\mathbf{u}, \boldsymbol{P}\} - \{\mathbf{u}^h, \boldsymbol{P}^h\}\|_X^2 &\leq c \inf_{\{\delta\mathbf{u}^h, \delta\boldsymbol{P}^h\} \in X^h} \|\{\mathbf{u}, \boldsymbol{P}\} - \{\delta\mathbf{u}^h, \delta\boldsymbol{P}^h\}\|_X^2 \\
&\leq c\,(\|\mathbf{u} - \Pi_g^p \mathbf{u}\|_{H^1} + \|\boldsymbol{P} - \Pi_c^{p-1}\boldsymbol{P}\|_{H(\mathrm{Curl})})^2 \\
&\overset{\mathrm{Y}}{\leq} c\,(\|\mathbf{u} - \Pi_g^p \mathbf{u}\|_{H^1}^2 + \|\boldsymbol{P} - \Pi_c^{p-1}\boldsymbol{P}\|_{H(\mathrm{Curl})}^2) \\
&= c\,(\|\mathbf{u} - \Pi_g^p \mathbf{u}\|_{H^1}^2 + \|\boldsymbol{P} - \Pi_c^{p-1}\boldsymbol{P}\|_{L^2}^2 + \|\operatorname{Curl} \boldsymbol{P} - \operatorname{Curl} \Pi_c^{p-1}\boldsymbol{P}\|_{L^2}^2) \\
&= c\,(\|\mathbf{u} - \Pi_g^p \mathbf{u}\|_{H^1}^2 + \|\boldsymbol{P} - \Pi_c^{p-1}\boldsymbol{P}\|_{L^2}^2 + \|(\mathrm{id} - \Pi_d^{p-1}) \operatorname{Curl} \boldsymbol{P}\|_{L^2}^2) \\
&\leq c\,(h^{2(p+1)}|\mathbf{u}|_{H^{p+1}}^2 + h^{2p}|\boldsymbol{P}|_{H^p}^2 + h^{2p}|\operatorname{Curl} \boldsymbol{P}|_{H^p}^2) \\
&\leq c h^{2p}\,(|\mathbf{u}|_{H^{p+1}}^2 + |\boldsymbol{P}|_{H^p}^2 + |\operatorname{Curl} \boldsymbol{P}|_{H^p}^2) \,,
\end{aligned} \tag{5.28}$$

relating to the Sobolev semi-norms. □

The application of the Nédélec element of the second type instead of the first type leads to a lower order of convergence in the Curl terms ($\Pi_d^{p-2} \operatorname{Curl} \boldsymbol{P}$) when the microdistortion $\boldsymbol{P}$ is not a gradient field. Unlike in antiplane shear, there are fewer scenarios for which the microdistortion field is reduced to a gradient field. As such, we take a closer look at the convergence behaviour. We start by considering an s-regular problem.

Definition 5.6 (s-regularity)
We call Problem. 3.14 s-regular if there holds for the solution $\{\mathbf{u}, \boldsymbol{P}\} \in X$

$$|\mathbf{u}|_{H^{s+1}} + \|\boldsymbol{P}\|_{H^s(\mathrm{Curl})} \leq \|\mathbf{f}\|_{L^2} + \|\boldsymbol{M}\|_{L^2} \,, \tag{5.29}$$

with $s \in (0, 1]$ *and*

$$\|\boldsymbol{P}\|_{H^s(\mathrm{Curl})}^2 = \|\boldsymbol{P}\|_{H^s}^2 + \|\operatorname{Curl} \boldsymbol{P}\|_{H^s}^2 \,, \tag{5.30}$$

such that an improved stability estimate is found.

We can now introduce an improved convergence estimate for the s-regular problem with an Aubin-Nitsche technique using the Nédélec elements of the second type.

Lemma 5.8 (Improved convergence estimate I)
Let $\{\mathbf{u}, \boldsymbol{P}\} \in [H^{p+1}(V)]^3 \times H^p(\mathrm{Curl}, V)$ *be an exact smooth solution for the s-regular problem and* $X^h = [U^p(V)]^3 \times [\mathcal{N}_{II}^{p-1}(V)]^3 \subset [H^{p+1}(V)]^3 \times H^p(\mathrm{Curl}, V)$ *then the discrete solution* $\{\mathbf{u}^h, \boldsymbol{P}^h\}$ *converges with*

$$\|\mathbf{u} - \mathbf{u}^h\|_{H^1} + \|\boldsymbol{P} - \boldsymbol{P}^h\|_{L^2} \leq c\, h^{p-1+s}(|\mathbf{u}|_{H^{p+1}} + |\boldsymbol{P}|_{H^p} + |\operatorname{Curl} \boldsymbol{P}|_{H^{p-1}}) \,, \qquad s \in (0, 1] \,. \tag{5.31}$$

Proof. In order to prove the improved estimate we formulate a dual problem. We define the right hand side as

$$\mathbf{f} = \mathbf{u} - \mathbf{u}^h\,, \qquad\qquad \boldsymbol{M} = \boldsymbol{P} - \boldsymbol{P}^h\,. \tag{5.32}$$

As such, the dual problem reads: find $\{\mathbf{v}, \boldsymbol{Q}\} \in X$ such that

$$a(\{\delta\mathbf{v}, \delta\boldsymbol{Q}\}, \{\mathbf{v}, \boldsymbol{Q}\}) = \int_V \langle \delta\mathbf{v},\, \mathbf{u} - \mathbf{u}^h \rangle + \langle \delta\boldsymbol{Q},\, \boldsymbol{P} - \boldsymbol{P}^h \rangle \,\mathrm{d}V \qquad \forall\, \{\delta\mathbf{v}, \delta\boldsymbol{Q}\} \in X\,, \tag{5.33}$$

where the bilinear form of the three-dimensional relaxed micromorphic model Eq. (3.8) is employed. By using the Galerkin orthogonality with the test functions $\{\delta\mathbf{v}, \delta\boldsymbol{Q}\} = \{\mathbf{u} - \mathbf{u}^h, \boldsymbol{P} - \boldsymbol{P}^h\}$

$$\begin{aligned} &a(\{\mathbf{u} - \mathbf{u}^h, \boldsymbol{P} - \boldsymbol{P}^h\}, \{\mathbf{v} - \Pi_g^p\mathbf{v} + \Pi_g^p\mathbf{v},\, \boldsymbol{Q} - \Pi_c^{p-1}\boldsymbol{Q} + \Pi_c^{p-1}\boldsymbol{Q}\}) \\ &\qquad = a(\{\mathbf{u} - \mathbf{u}^h, \boldsymbol{P} - \boldsymbol{P}^h\}, \{\mathbf{v} - \Pi_g^p\mathbf{v},\, \boldsymbol{Q} - \Pi_c^{p-1}\boldsymbol{Q}\})\,, \end{aligned} \tag{5.34}$$

the continuity of the bilinear form and the improved stability estimate one finds

$$\begin{aligned} \|\mathbf{u} - \mathbf{u}^h\|_{L^2}^2 + \|\boldsymbol{P} - \boldsymbol{P}^h\|_{L^2}^2 &\overset{\text{GO}}{=} a(\{\mathbf{u} - \mathbf{u}^h, \boldsymbol{P} - \boldsymbol{P}^h\}, \{\mathbf{v} - \Pi_g^p\mathbf{v},\, \boldsymbol{Q} - \Pi_c^{p-1}\boldsymbol{Q}\}) \\ &\overset{\text{C}}{\leq} \alpha\|\{\mathbf{u} - \mathbf{u}^h, \boldsymbol{P} - \boldsymbol{P}^h\}\|_X(\|\mathbf{v} - \Pi_g^p\mathbf{v}\|_{H^1} + \|\boldsymbol{Q} - \Pi_c^{p-1}\boldsymbol{Q}\|_{H(\mathrm{curl})}) \\ &\leq \alpha h^s\|\{\mathbf{u} - \mathbf{u}^h, \boldsymbol{P} - \boldsymbol{P}^h\}\|_X(|\mathbf{v}|_{H^{s+1}} + \|\boldsymbol{Q}\|_{H^s(\mathrm{Curl})}) \\ &\overset{\text{S}}{\leq} \alpha h^s\|\{\mathbf{u} - \mathbf{u}^h, \boldsymbol{P} - \boldsymbol{P}^h\}\|_X(\|\mathbf{u} - \mathbf{u}^h\|_{L^2} + \|\boldsymbol{P} - \boldsymbol{P}^h\|_{L^2})\,, \end{aligned} \tag{5.35}$$

where the term on the left is the right hand side of the dual problem. The right hand side can be estimated using Young's inequality

$$\begin{aligned} \|\mathbf{u} - \mathbf{u}^h\|_{L^2}^2 + \|\boldsymbol{P} - \boldsymbol{P}^h\|_{L^2}^2 &= (\|\mathbf{u} - \mathbf{u}^h\|_{L^2} + \|\boldsymbol{P} - \boldsymbol{P}^h\|_{L^2})^2 - 2\|\mathbf{u} - \mathbf{u}^h\|_{L^2}\|\boldsymbol{P} - \boldsymbol{P}^h\|_{L^2} \\ &\overset{\text{Y}}{\geq} (\|\mathbf{u} - \mathbf{u}^h\|_{L^2} + \|\boldsymbol{P} - \boldsymbol{P}^h\|_{L^2})^2 - \|\mathbf{u} - \mathbf{u}^h\|_{L^2}^2 - \|\boldsymbol{P} - \boldsymbol{P}^h\|_{L^2}^2 \\ &= 2\|\mathbf{u} - \mathbf{u}^h\|_{L^2}\|\boldsymbol{P} - \boldsymbol{P}^h\|_{L^2} \\ &\overset{\text{Y}}{\geq} \frac{1}{2}(\|\mathbf{u} - \mathbf{u}^h\|_{L^2} + \|\boldsymbol{P} - \boldsymbol{P}^h\|_{L^2})^2\,. \end{aligned} \tag{5.36}$$

Thus, we can reformulate to find

$$(\|\mathbf{u} - \mathbf{u}^h\|_{L^2} + \|\boldsymbol{P} - \boldsymbol{P}^h\|_{L^2})^2 \leq 2\alpha h^s\|\{\mathbf{u} - \mathbf{u}^h, \boldsymbol{P} - \boldsymbol{P}^h\}\|_X(\|\mathbf{u} - \mathbf{u}^h\|_{L^2} + \|\boldsymbol{P} - \boldsymbol{P}^h\|_{L^2})\,. \tag{5.37}$$

Dividing by the error estimate and applying the convergence estimate for $\|\{\mathbf{u} - \mathbf{u}^h, \boldsymbol{P} - \boldsymbol{P}^h\}\|_X$ yields

$$\begin{aligned} \|\mathbf{u} - \mathbf{u}^h\|_{L^2} + \|\boldsymbol{P} - \boldsymbol{P}^h\|_{L^2} &\leq 2\alpha h^s\|\{\mathbf{u} - \mathbf{u}^h, \boldsymbol{P} - \boldsymbol{P}^h\}\|_X \\ &\leq 2\alpha h^{p-1+s}(|\mathbf{u}|_{H^{p+1}}^2 + |\boldsymbol{P}|_{H^p}^2 + |\operatorname{Curl}\boldsymbol{P}|_{H^{p-1}}^2)\,, \end{aligned} \tag{5.38}$$

completing the claim for the L^2-norm of $\mathbf{u}$ and $\boldsymbol{P}$. The improvement to the H^1-norm of the displacement $\mathbf{u}$ follows by first considering the Galerkin orthogonality over a vanishing $\delta\boldsymbol{P}$-test field

$$\begin{aligned} a(\{\delta\mathbf{u}^h, 0\}, \{\mathbf{u} - \mathbf{u}^h, \boldsymbol{P} - \boldsymbol{P}^h\}) = \int_V &\langle \operatorname{sym}\mathrm{D}\delta\mathbf{u}^h,\, \mathbb{C}_{\mathrm{e}}\operatorname{sym}[\mathrm{D}(\mathbf{u} - \mathbf{u}^h) - (\boldsymbol{P} - \boldsymbol{P}^h)]\rangle \\ &+ \langle \operatorname{skew}\mathrm{D}\delta\mathbf{u}^h,\, \mathbb{C}_{\mathrm{c}}\operatorname{skew}[\mathrm{D}(\mathbf{u} - \mathbf{u}^h) - (\boldsymbol{P} - \boldsymbol{P}^h)]\rangle \,\mathrm{d}V = 0\,. \end{aligned} \tag{5.39}$$

We shorten the form by defining $\widetilde{\mathbb{C}}_e = \mathbb{C}_\mathrm{e}\mathbb{S}$ with $\mathbb{S} : \mathbb{R}^{3\times 3} \to \mathit{Sym}(3)$ and using $\mathbb{C}_\mathrm{c} = \mu_\mathrm{c}\mathbb{A}$ with $\mathbb{A} : \mathbb{R}^{3\times 3} \to \mathfrak{so}(3)$. Further, we add and subtract $\Pi_g^p\mathbf{u}$ to find

$$\begin{aligned} a(\{\delta\mathbf{u}^h, 0\}, \{\mathbf{u} - \Pi_g^p\mathbf{u} + \Pi_g^p\mathbf{u} - \mathbf{u}^h, \boldsymbol{P} - \boldsymbol{P}^h\}) &= \int_V \langle \mathrm{D}\delta\mathbf{u}^h,\, (\widetilde{\mathbb{C}}_e + \mathbb{C}_\mathrm{c})[\mathrm{D}(\mathbf{u} - \Pi_g^d\mathbf{u} + \Pi_g^p\mathbf{u} - \mathbf{u}^h) - (\boldsymbol{P} - \boldsymbol{P}^h)]\rangle \,\mathrm{d}V \\ &= a(\{\delta\mathbf{u}^h, 0\}, \{\mathbf{u} - \Pi_g^p\mathbf{u}, \boldsymbol{P} - \boldsymbol{P}^h\}) \\ &\quad + \int_V \langle \mathrm{D}\delta\mathbf{u}^h,\, (\widetilde{\mathbb{C}}_e + \mathbb{C}_\mathrm{c})\mathrm{D}(\Pi_g^p\mathbf{u} - \mathbf{u}^h)\rangle \,\mathrm{d}V = 0\,. \end{aligned} \tag{5.40}$$

Consequently, we can formulate

$$\begin{aligned} \sqrt{\int_V \langle \mathrm{D}(\Pi_g\mathbf{u} - \mathbf{u}^h),\, (\widetilde{\mathbb{C}}_e + \mathbb{C}_\mathrm{c})\mathrm{D}(\Pi_g\mathbf{u} - \mathbf{u}^h)\rangle \,\mathrm{d}V} &= \sup_{\delta\mathbf{u}^h \in U^p} \frac{\int_V \langle \mathrm{D}\delta\mathbf{u}^h,\, (\widetilde{\mathbb{C}}_e + \mathbb{C}_\mathrm{c})\mathrm{D}(\Pi_g^p\mathbf{u} - \mathbf{u}^h)\rangle \,\mathrm{d}V}{\sqrt{\int_V \langle \mathrm{D}\delta\mathbf{u}^h,\, (\widetilde{\mathbb{C}}_e + \mathbb{C}_\mathrm{c})\mathrm{D}\delta\mathbf{u}^h\rangle \,\mathrm{d}V}} \\ &= \sup_{\delta\mathbf{u}^h \in U^p} \frac{-a(\{\delta\mathbf{u}^h, 0\}, \{\mathbf{u} - \Pi_g^p\mathbf{u}, \boldsymbol{P} - \boldsymbol{P}^h\})}{\sqrt{\int_V \langle \mathrm{D}\delta\mathbf{u}^h,\, (\widetilde{\mathbb{C}}_e + \mathbb{C}_\mathrm{c})\mathrm{D}\delta\mathbf{u}^h\rangle \,\mathrm{d}V}}\,. \end{aligned} \tag{5.41}$$

We estimate the numerator with the Cauchy-Schwarz and triangle inequalities

$$\begin{aligned} -a(\{\delta\mathbf{u}^h, 0\}, \{\mathbf{u} - \Pi_g^p\mathbf{u}, \boldsymbol{P} - \boldsymbol{P}^h\}) &= -\int_V \langle \mathrm{D}\delta\mathbf{u}^h,\, (\widetilde{\mathbb{C}}_e + \mathbb{C}_\mathrm{c})[\mathrm{D}(\mathbf{u} - \Pi_g^p\mathbf{u}) - (\boldsymbol{P} - \boldsymbol{P}^h)]\rangle \,\mathrm{d}V \\ &= \int_V \langle \mathrm{D}\delta\mathbf{u}^h,\, (\widetilde{\mathbb{C}}_e + \mathbb{C}_\mathrm{c})[\mathrm{D}(\Pi_g^p\mathbf{u} - \mathbf{u}) + (\boldsymbol{P} - \boldsymbol{P}^h)]\rangle \,\mathrm{d}V \\ &\overset{\mathrm{CS}}{\leq} \|\mathrm{D}\delta\mathbf{u}^h\|_{L^2} \|(\widetilde{\mathbb{C}}_e + \mathbb{C}_\mathrm{c})[\mathrm{D}(\Pi_g^p\mathbf{u} - \mathbf{u}) + (\boldsymbol{P} - \boldsymbol{P}^h)]\|_{L^2} \\ &\leq c_1 \,\|\mathrm{D}\delta\mathbf{u}^h\|_{L^2} \|\mathrm{D}(\Pi_g^p\mathbf{u} - \mathbf{u}) + (\boldsymbol{P} - \boldsymbol{P}^h)\|_{L^2} \\ &\overset{\mathrm{T}}{\leq} c_1 \,\|\mathrm{D}\delta\mathbf{u}^h\|_{L^2} (\|\mathrm{D}(\Pi_g^p\mathbf{u} - \mathbf{u})\|_{L^2} + \|\boldsymbol{P} - \boldsymbol{P}^h\|_{L^2}) \\ &\leq c_1 \,\|\mathrm{D}\delta\mathbf{u}^h\|_{L^2} (\|\Pi_g^p\mathbf{u} - \mathbf{u}\|_{H^1} + \|\boldsymbol{P} - \boldsymbol{P}^h\|_{L^2})\,. \end{aligned} \tag{5.42}$$

The denominator is estimated using the infimum of the material tensors

$$\sqrt{\int_V \langle \mathrm{D}\delta\mathbf{u}^h,\, (\widetilde{\mathbb{C}}_e + \mathbb{C}_\mathrm{c})\mathrm{D}\delta\mathbf{u}^h\rangle \,\mathrm{d}V} \geq \sqrt{\int_V c_2 \,\langle \mathrm{D}\delta\mathbf{u}^h,\, \mathrm{D}\delta\mathbf{u}^h\rangle \,\mathrm{d}V} = c_2 \,\|\mathrm{D}\delta\mathbf{u}^h\|_{L^2}\,. \tag{5.43}$$

Thus, we can reduce Eq. (5.41) to

$$\|\Pi_g^p\mathbf{u} - \mathbf{u}\|_{H^1} + \|\boldsymbol{P} - \boldsymbol{P}^h\|_{L^2} \leq \frac{c_2}{c_1} \|\{\mathbf{u}, \boldsymbol{P}\} - \{\mathbf{u}^h, \boldsymbol{P}^h\}\|_X \leq c\, h^{p-1+s} |\{\mathbf{u}, \boldsymbol{P}\}|_{H^{p+1}}\,, \tag{5.44}$$

completing the proof for the case of a positive definite material tensor $\mathbb{C}_\mathrm{c}$. In case of a semi positive definite $\mathbb{C}_\mathrm{c}$ the proof follows by using the generalized Korn's inequality for incompatible tensor fields.

□

Remark 5.4

From the proof it is clear that the convergence rate of the displacement field $\mathbf{u}^h$ *is not better for the* L^2*-norm in comparison with* H^1*-norm.*

Remark 5.5
The s-regularity of Eq. (3.8) *is not discussed in this work. However, we mention that for both the Laplace as well as Maxwell's equations there holds* $s = 1$ *for convex domains* V*.*

The s-regularity of the problem also allows us to improve the error estimates for the formulation using the Nédélec element of the first type.

Corollary 1 (Improved convergence estimate II)
Let $\{\mathbf{u}, \boldsymbol{P}\} \in [H^{p+1}(V)]^3 \times H^p(\mathrm{Curl}, V)$ *be an exact smooth solution for the s-regular problem and* $X^h = [U^p(V)]^3 \times [\mathcal{N}_I^{p-1}(V)]^3 \subset [H^{p+1}(V)]^3 \times H^p(\mathrm{Curl}, V)$ *then the discrete solution* $\{\mathbf{u}^h, \boldsymbol{P}^h\}$ *converges with*

$$\|\mathbf{u} - \mathbf{u}^h\|_{H^1} + \|\boldsymbol{P} - \boldsymbol{P}^h\|_{L^2} \leq c\, h^{p+s}(|\mathbf{u}|_{H^{p+1}} + |\boldsymbol{P}|_{H^p} + |\,\mathrm{Curl}\,\boldsymbol{P}|_{H^p})\,, \qquad s \in (0,1]\,. \tag{5.45}$$

Proof. The proof follows the same lines of the proof for Lemma 5.8, where the interpolation error in Curl of the microdistortion $\mathrm{Curl}\,\boldsymbol{P}$ is now estimated with the Nédélec element of the first type, thus retrieving Lemma 5.7. ☐

5.3 Low order triangular elements

5.3.1 Linear and quadratic Lagrange elements

For the lowest order H^1-conforming subspace we consider Lagrangian elements [16, 111]. Lagrangian elements are defined using the point-evaluation degrees of freedom

$$l_{ij}(u) = \delta_{ij} u \bigg|_{\boldsymbol{\xi}_j}\,, \tag{5.46}$$

and the polynomial space P^p over some triangular domain. Consequently, the Lagrangian finite element in the reference domain is defined by the triplet $\mathcal{L}^p = \{\Gamma, P^p, \mathrm{span}\{l_{ij}\}\}$ with $\Gamma = \{(\xi, \eta) \in [0,1]^2 \mid \xi + \eta \leq 1\}$. The evaluation points $\boldsymbol{\xi}_j$ on the boundary of the element are shared with neighbouring elements to enforce C^0-conformity. In the lowest order $p = 1$, the resulting base functions are simply the barycentric functions

$$n_1(\xi, \eta) = 1 - \xi - \eta\,, \qquad n_2(\xi, \eta) = \eta\,, \qquad n_3(\xi, \eta) = \xi\,. \tag{5.47}$$

Taking the polynomial degree $p = 2$ and choosing the edge middle points as additional evaluation points yields the base functions of the quadratic Lagrangian triangle element

$$\begin{aligned} &n_1(\xi, \eta) = (\eta + \xi - 1)(2\eta + 2\xi - 1)\,, && n_2(\xi, \eta) = 2\eta(\eta - 1)\,, && n_3(\xi, \eta) = 2\xi(\xi - 1)\,, \\ &n_4(\xi, \eta) = 4\eta(1 - \eta - \xi)\,, && n_5(\xi, \eta) = 4\xi(1 - \eta - \xi)\,, && n_6(\xi, \eta) = 4\eta\xi\,. \end{aligned} \tag{5.48}$$

Due to the simple nature of the degrees of freedom, the projection of a continuous function reduces to an evaluation of the function at the element's nodes. A sample of the barycentric and Lagrangian base functions is depicted in Fig. 5.6.

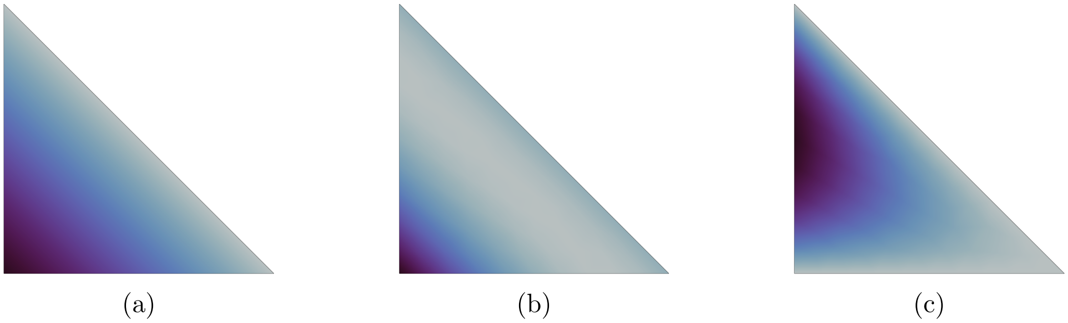
(a) (b) (c)

Figure 5.6: The first barycentric base function (a), the first quadratic Lagrangian vertex base function (b) and the quadratic Lagrangian edge base function (c).

5.3.2 Linear Nédélec elements of the second type

The lowest order Nédélec elements of the second type [71] are characterized by degrees of freedom of tangential projections on edges of the triangle element

$$l_{ij}(\mathbf{p}) = \int_{\mu_i} q_j \langle \boldsymbol{\tau}, \, \mathbf{p} \rangle \, \mathrm{d}\mu \,, \qquad q_j \in P^1(\mu_i) \,. \tag{5.49}$$

Here, the degrees of freedom are formulated on the reference domain, see Fig. 5.1. Consequently, the finite element triplet reads $\mathcal{N}_{II}^1 = \{\Gamma, P^1, \mathrm{span}\{l_{ij}\}\}$. We note that the resulting base functions are directly dependent on the choice of test functions q_j. Choosing the test functions

$$q_1(\mu) = 4 - 6\mu \,, \qquad q_2(\mu) = 6\mu - 2 \,, \tag{5.50}$$

on the left and bottom unit edges with $\mu \in [0, 1]$, and

$$q_1(\mu) = 2\sqrt{2} - 3\mu \,, \qquad q_2(\mu) = 3\mu - \sqrt{2} \,, \tag{5.51}$$

on the right slanted edge with $\mu \in [0, \sqrt{2}]$, results in the Lagrange-Nédélec basis

$$\begin{aligned} \boldsymbol{\vartheta}_1(\xi, \eta) &= \begin{bmatrix} 0 \\ 1 - \xi - \eta \end{bmatrix} , & \boldsymbol{\vartheta}_2(\xi, \eta) &= \begin{bmatrix} \eta \\ \eta \end{bmatrix} , & \boldsymbol{\vartheta}_3(\xi, \eta) &= \begin{bmatrix} 1 - \xi - \eta \\ 0 \end{bmatrix} , \\ \boldsymbol{\vartheta}_4(\xi, \eta) &= \begin{bmatrix} \xi \\ \xi \end{bmatrix} , & \boldsymbol{\vartheta}_5(\xi, \eta) &= \begin{bmatrix} \eta \\ 0 \end{bmatrix} , & \boldsymbol{\vartheta}_6(\xi, \eta) &= \begin{bmatrix} 0 \\ -\xi \end{bmatrix} . \end{aligned} \tag{5.52}$$

The base functions for the first edge $\boldsymbol{\vartheta}_1$ and $\boldsymbol{\vartheta}_2$ are depicted in Fig. 5.7.

5.3.3 The lowest order Nédélec elements of the first type

The lowest order Nédélec elements of the first type [70] contain the space $\mathcal{N}_{II}$ with a minimal enrichment of solenoidal polynomials, such that the discrete kernel of the next polynomial space in the sequence is complete. The corresponding degrees of freedom are given by

$$l_i(\mathbf{p}) = \int_{\mu_i} \langle \boldsymbol{\tau}, \, \mathbf{p} \rangle \, \mathrm{d}\mu \,, \tag{5.53}$$

with the polynomial space on the reference element

$$[P^0(\Gamma)]^2 \oplus \boldsymbol{R} \widetilde{P}^0(\Gamma) \boldsymbol{\xi} = [P^0(\Gamma)]^2 \oplus \boldsymbol{R} \, \boldsymbol{\xi} = \mathrm{span}\{ \begin{bmatrix} 1 \\ 0 \end{bmatrix} , \begin{bmatrix} 0 \\ 1 \end{bmatrix} , \begin{bmatrix} \eta \\ -\xi \end{bmatrix} \} \,. \tag{5.54}$$

(a) (b)

Figure 5.7: The first (a) and second (b) base functions for the Lagrange-Nédélec element of the second type, belonging to the first edge.

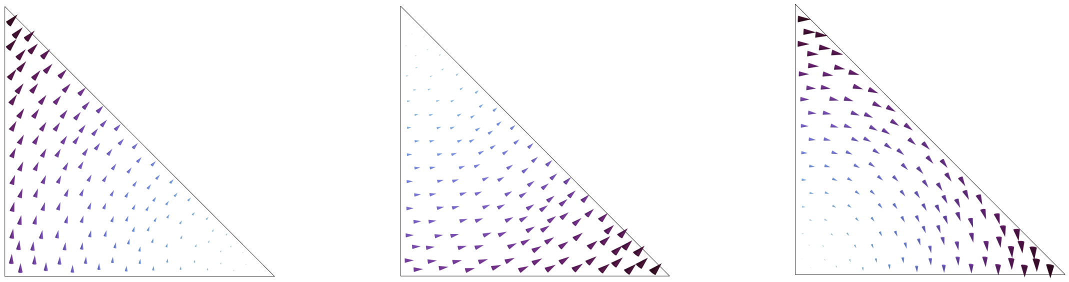

(a) (b) (c)

Figure 5.8: The base functions of the lowest order Nédélec element of the first type on the reference triangle belonging to the left (a), bottom (b) and slanted (c) edges.

Consequently, the lowest order Nédélec element reads $\mathcal{N}_I^0 = \{\Gamma, [P^0]^2 \oplus \boldsymbol{R}\boldsymbol{\xi}, \text{span}\{l_i\}\}$. Applying the degrees of freedom to the reference triangle results in the base functions

$$\boldsymbol{\vartheta}_1(\xi,\eta) = \begin{bmatrix} \eta \\ 1-\xi \end{bmatrix} , \qquad \boldsymbol{\vartheta}_2(\xi,\eta) = \begin{bmatrix} 1-\eta \\ \xi \end{bmatrix} , \qquad \boldsymbol{\vartheta}_3(\xi,\eta) = \begin{bmatrix} \eta \\ -\xi \end{bmatrix} , \tag{5.55}$$

depicted in Fig. 5.8.

Remark 5.6
Note that the base functions are in fact linear combinations of the base functions of $\mathcal{N}_{II}^1$*, such that* $\vartheta_1^I = \boldsymbol{\vartheta}_1^{II} + \boldsymbol{\vartheta}_2^{II}$, $\boldsymbol{\vartheta}_2^I = \boldsymbol{\vartheta}_3^{II} + \boldsymbol{\vartheta}_4^{II}$ *and* $\boldsymbol{\vartheta}_3^I = \boldsymbol{\vartheta}_5^{II} + \boldsymbol{\vartheta}_6^{II}$.

5.4 Low order tetrahedral elements

5.4.1 Linear and quadratic Lagrange elements

In three-dimensions one can construct a low-order H^1-conforming subspace using the same Lagrangian degrees of freedom as for triangles

$$l_{ij}(u) = \delta_{ij} u \Big|_{\boldsymbol{\xi}_j} . \tag{5.56}$$

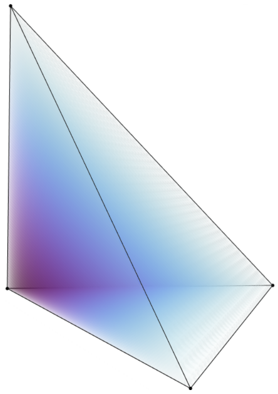

Figure 5.9: The barycentric function of the first vertex on the reference tetrahedron.

In three-dimensions the result of the linear polynomial space are the barycentric coordinates (see Fig. 5.9)

$$n_1(\xi,\eta,\zeta) = 1-\xi-\eta-\zeta\,, \qquad n_2(\xi,\eta,\zeta) = \zeta\,, \qquad n_3(\xi,\eta,\zeta) = \eta\,, \qquad n_4(\xi,\eta,\zeta) = \xi\,. \tag{5.57}$$

Taking the quadratic polynomial degree $p = 2$ and choosing the midpoints of the edges as additional evaluation points yields the quadratic Lagrangian base functions

$$\begin{aligned} n_1(\xi,\eta,\zeta) &= (1-\eta-\xi-\zeta)\,(1-2\eta-2\xi-2\zeta)\ , & n_2(\xi,\eta,\zeta) &= \zeta\,(2\zeta-1)\ , \\ n_3(\xi,\eta,\zeta) &= \eta\,(2\eta-1)\ , & n_4(\xi,\eta,\zeta) &= \xi\,(2\xi-1)\ , \\ \\ n_5(\xi,\eta,\zeta) &= 4\zeta\,(1-\xi-\eta-\zeta)\ , & n_6(\xi,\eta,\zeta) &= 4\eta\,(1-\xi-\eta-\zeta)\ , \\ n_7(\xi,\eta,\zeta) &= 4\xi\,(1-\xi-\eta-\zeta)\ , & n_8(\xi,\eta,\zeta) &= 4\eta\zeta\,, \\ n_9(\xi,\eta,\zeta) &= 4\xi\zeta\,, & n_{10}(\xi,\eta,\zeta) &= 4\eta\xi\,. \end{aligned} \tag{5.58}$$

Evaluation of boundary conditions is done by computing the value of the function at each node.

5.4.2 Linear Nédélec elements of the second type

The degrees of freedom of the lowest order Nédélec element of the second type are same as for triangles, see Eq. (5.49). However, the reference domain changes to the unit tetrahedron such that the finite element is given by the triplet $\mathcal{N}_{II}^1 = \{\Omega, P^1, \mathrm{span}\{l_{ij}\}\}$ with $\Omega = \{(\xi,\eta,\zeta) \in [0,1]^3 \mid \xi+\eta+\zeta \leq 1\}$. Using the test functions from Eq. (5.50) and Eq. (5.51) for the straight and slanted edges, respectively, yields the base functions

$$\boldsymbol{\vartheta}_1(\xi,\eta,\zeta) = \begin{bmatrix} 0 \\ 0 \\ 1-\xi-\eta-\zeta \end{bmatrix}, \quad \boldsymbol{\vartheta}_2(\xi,\eta,\zeta) = \begin{bmatrix} \zeta \\ \zeta \\ \zeta \end{bmatrix}, \quad \boldsymbol{\vartheta}_3(\xi,\eta,\zeta) = \begin{bmatrix} 0 \\ 1-\xi-\eta-\zeta \\ 0 \end{bmatrix},$$

$$\boldsymbol{\vartheta}_4(\xi,\eta,\zeta) = \begin{bmatrix} \eta \\ \eta \\ \eta \end{bmatrix}, \quad \boldsymbol{\vartheta}_5(\xi,\eta,\zeta) = \begin{bmatrix} 1-\xi-\eta-\zeta \\ 0 \\ 0 \end{bmatrix}, \quad \boldsymbol{\vartheta}_6(\xi,\eta,\zeta) = \begin{bmatrix} \xi \\ \xi \\ \xi \end{bmatrix},$$

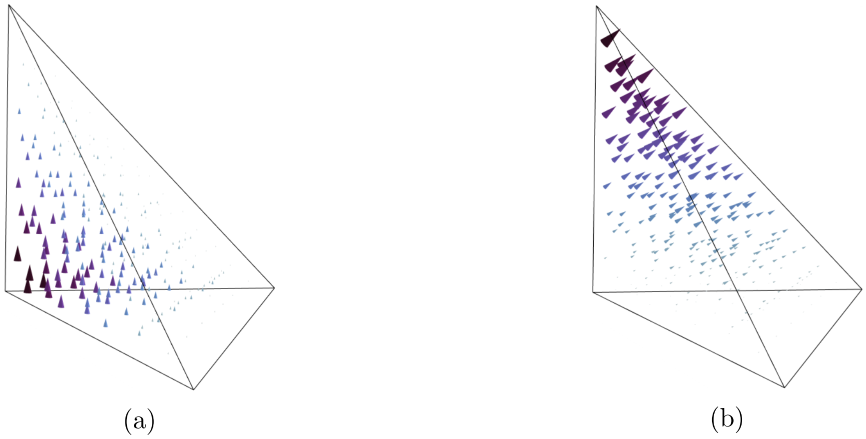
(a) (b)

Figure 5.10: The first (a) and second (b) base function for the Lagrange-Nédélec element of the second type on the reference tetrahedron. The base functions belong to the first edge.

$$\boldsymbol{\vartheta}_7(\xi,\eta,\zeta) = \begin{bmatrix}0\\ \zeta\\ 0\end{bmatrix}, \qquad \boldsymbol{\vartheta}_8(\xi,\eta,\zeta) = \begin{bmatrix}0\\ 0\\ -\eta\end{bmatrix}, \qquad \boldsymbol{\vartheta}_9(\xi,\eta,\zeta) = \begin{bmatrix}\zeta\\ 0\\ 0\end{bmatrix},$$

$$\boldsymbol{\vartheta}_{10}(\xi,\eta,\zeta) = \begin{bmatrix}0\\ 0\\ -\xi\end{bmatrix}, \qquad \boldsymbol{\vartheta}_{11}(\xi,\eta,\zeta) = \begin{bmatrix}\eta\\ 0\\ 0\end{bmatrix}, \qquad \boldsymbol{\vartheta}_{12}(\xi,\eta,\zeta) = \begin{bmatrix}0\\ -\xi\\ 0\end{bmatrix}. \tag{5.59}$$

The base functions of the first edge are depicted in Fig. 5.10.

5.4.3 The lowest order Nédélec elements of the first type

The degrees of freedom of the lowest order Nédélec element of the first type for tetrahedra are analogous to Eq. (5.53) with the adjustment of the polynomial space to

$$[P^0(\Omega)]^3 \oplus \boldsymbol{\xi} \times [\widetilde{P}^0(\Omega)]^3 = \operatorname{span}\{ \begin{bmatrix}1\\0\\0\end{bmatrix}, \begin{bmatrix}0\\1\\0\end{bmatrix}, \begin{bmatrix}0\\0\\1\end{bmatrix}, \begin{bmatrix}0\\ \zeta\\ -\eta\end{bmatrix}, \begin{bmatrix}-\zeta\\ 0\\ \xi\end{bmatrix}, \begin{bmatrix}\eta\\ -\xi\\ 0\end{bmatrix} \}. \tag{5.60}$$

Applying the degrees of freedom to the unit tetrahedron $\Omega = \{(\xi,\eta,\zeta) \in [0,1]^3 \mid \xi+\eta+\zeta \leq 1\}$ yields the lowest order base functions (see Fig. 5.11)

$$\boldsymbol{\vartheta}_1(\xi,\eta,\zeta) = \begin{bmatrix}\zeta\\ \zeta\\ 1-\xi-\eta\end{bmatrix}, \qquad \boldsymbol{\vartheta}_2(\xi,\eta,\zeta) = \begin{bmatrix}\eta\\ 1-\xi-\zeta\\ \eta\end{bmatrix}, \qquad \boldsymbol{\vartheta}_3(\xi,\eta,\zeta) = \begin{bmatrix}1-\eta-\zeta\\ \xi\\ \xi\end{bmatrix},$$

$$\boldsymbol{\vartheta}_4(\xi,\eta,\zeta) = \begin{bmatrix}0\\ \zeta\\ -\eta\end{bmatrix}, \qquad \boldsymbol{\vartheta}_5(\xi,\eta,\zeta) = \begin{bmatrix}\zeta\\ 0\\ -\xi\end{bmatrix}, \qquad \boldsymbol{\vartheta}_6(\xi,\eta,\zeta) = \begin{bmatrix}\eta\\ -\xi\\ 0\end{bmatrix}. \tag{5.61}$$

Remark 5.7

Here too, the base functions are in fact linear combinations of the base functions of the $\mathcal{N}^1_{II}$-space, such that

$$\vartheta^I_1 = \boldsymbol{\vartheta}^{II}_1 + \boldsymbol{\vartheta}^{II}_2, \qquad \vartheta^I_2 = \boldsymbol{\vartheta}^{II}_3 + \boldsymbol{\vartheta}^{II}_4, \qquad \vartheta^I_3 = \boldsymbol{\vartheta}^{II}_5 + \boldsymbol{\vartheta}^{II}_6,$$

$$\vartheta^I_4 = \boldsymbol{\vartheta}^{II}_7 + \boldsymbol{\vartheta}^{II}_8, \qquad \vartheta^I_5 = \boldsymbol{\vartheta}^{II}_9 + \boldsymbol{\vartheta}^{II}_{10}, \qquad \vartheta^I_6 = \boldsymbol{\vartheta}^{II}_{11} + \boldsymbol{\vartheta}^{II}_{12}.$$

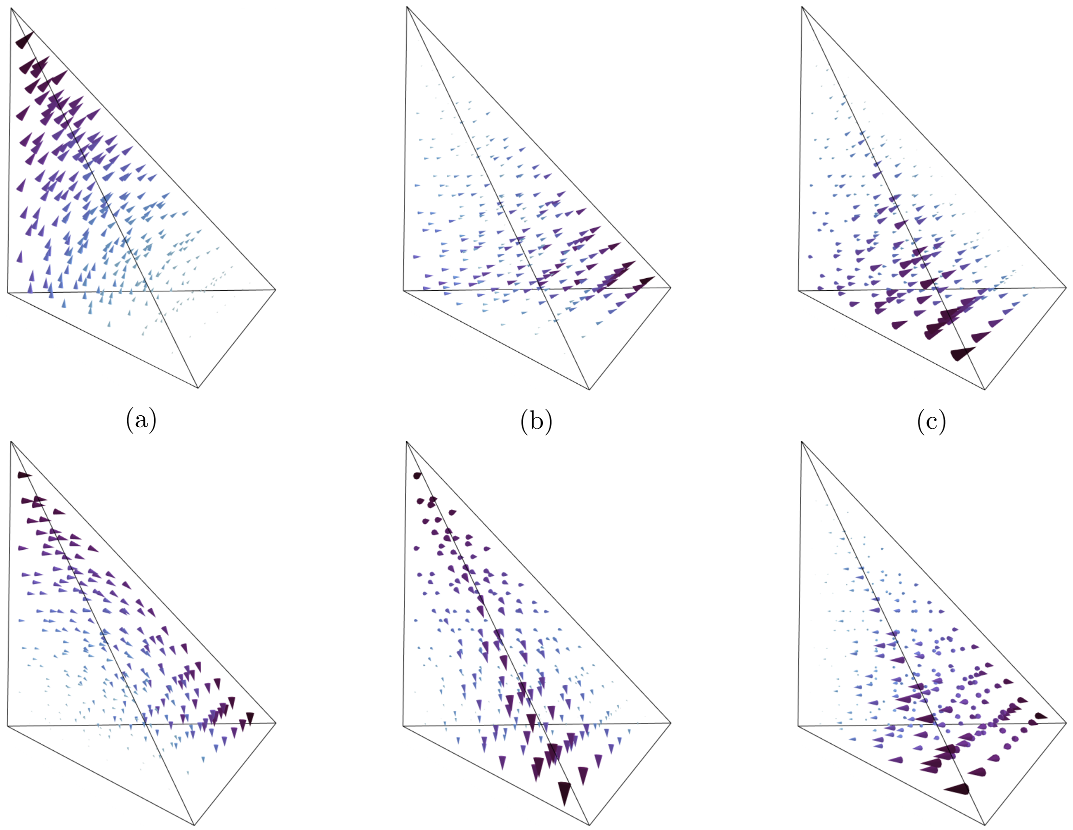

(a) (b) (c)

(d) (e) (f)

Figure 5.11: The base functions of the lowest order Nédélec element of the first type on the reference tetrahedron, belonging to their corresponding edges: (1-6):(a-f).

5.5 Consistent transformations

5.5.1 Piola transformations

In this work, base functions are defined on the reference elements. Consistent transformations are employed to map the base functions from the reference element to the physical element [69], and every element in the physical domain is mapped from the same reference domain. Since the mapping of the physical space is achieved via barycentric functions, the polynomial degree is maintained across transformations.

The scalar base functions transform via

$$n(\mathbf{x}) = n \circ [\mathbf{x}^{-1}(\boldsymbol{\xi})]\,, \qquad \nabla_x n = \boldsymbol{J}^{-T}\nabla_\xi n\,, \tag{5.62}$$

where the result concerning the Jacobi matrix is a direct consequence of the chain rule.

Nédélec elements are defined via their action on the tangent vectors of the element. Consequently, a consistent transformation is given by the equality

$$\langle \boldsymbol{\theta},\, \mathbf{t}\rangle \mathrm{d}s = \langle \boldsymbol{\theta},\, \mathrm{d}\mathbf{s}\rangle = \langle \boldsymbol{\theta},\, \boldsymbol{J}\mathrm{d}\boldsymbol{\mu}\rangle = \langle \boldsymbol{\vartheta},\, \mathrm{d}\boldsymbol{\mu}\rangle = \langle \boldsymbol{\vartheta},\, \boldsymbol{\tau}\rangle \mathrm{d}\mu \quad \iff \quad \boldsymbol{\theta} = \boldsymbol{J}^{-T}\boldsymbol{\vartheta}\,, \tag{5.63}$$

known as the covariant Piola transformation. This is the same transformation as for gradients, thus respecting the commuting property Eq. (5.23). Further, due to

$$\nabla_x \times \boldsymbol{J}^{-T} = \nabla_x \times \nabla_x \boldsymbol{\xi} = 0\,, \tag{5.64}$$

vectors mapped by the covariant Piola transformation exhibit the following transformation of the curl operator

$$\operatorname{curl}_x \boldsymbol{\theta} = \nabla_x \times \boldsymbol{\theta} = (\boldsymbol{J}^{-T}\nabla_\xi) \times (\boldsymbol{J}^{-T}\boldsymbol{\vartheta}) = \operatorname{cof}(\boldsymbol{J}^{-T})(\nabla_\xi \times \boldsymbol{\vartheta}) = \frac{1}{\det \boldsymbol{J}} \boldsymbol{J} \operatorname{curl}_\xi \boldsymbol{\vartheta} \,, \tag{5.65}$$

being the so called contravariant Piola transformation. For two-dimensional domains the formula reduces to

$$\operatorname{div}_x(\boldsymbol{R}\boldsymbol{\theta}) = \frac{1}{\det \boldsymbol{J}} \operatorname{div}_\xi(\boldsymbol{R}\boldsymbol{\vartheta}) \,, \qquad \boldsymbol{R} = \begin{bmatrix} 0 & 1 \\ -1 & 0 \end{bmatrix} , \tag{5.66}$$

since the two-dimensional curl operator transforms via

$$\begin{aligned}
\int_A q \operatorname{div}_x(\boldsymbol{R}\boldsymbol{\theta}) \,\mathrm{d}A &= \oint_{\partial A} q \, \langle \boldsymbol{\theta}, \, \mathbf{t} \rangle \,\mathrm{d}s + \int_A \langle \boldsymbol{R} \nabla_x q, \, \boldsymbol{\theta} \rangle \,\mathrm{d}A \\
&= \oint_{\partial\Gamma} \hat{q} \, \langle \boldsymbol{J}^{-T}\boldsymbol{\vartheta}, \, \boldsymbol{J}\boldsymbol{\tau} \rangle \,\mathrm{d}\mu + \int_\Gamma \langle \boldsymbol{R}\boldsymbol{J}^{-T} \nabla_\xi \hat{q}, \, \boldsymbol{J}^{-T}\boldsymbol{\vartheta} \rangle \det \boldsymbol{J} \,\mathrm{d}\Gamma \\
&= \oint_{\partial\Gamma} \hat{q} \, \langle \boldsymbol{J}^{-T}\boldsymbol{\vartheta}, \, \boldsymbol{J}\boldsymbol{\tau} \rangle \,\mathrm{d}\mu + \int_\Gamma \langle \frac{1}{\det \boldsymbol{J}} \boldsymbol{J}\boldsymbol{R} \nabla_\xi \hat{q}, \, \boldsymbol{J}^{-T}\boldsymbol{\vartheta} \rangle \det \boldsymbol{J} \,\mathrm{d}\Gamma \\
&= \oint_{\partial\Gamma} \hat{q} \, \langle \boldsymbol{\vartheta}, \, \boldsymbol{\tau} \rangle \,\mathrm{d}\mu + \int_\Gamma \langle \boldsymbol{R} \nabla_\xi \hat{q}, \, \boldsymbol{\vartheta} \rangle \,\mathrm{d}\Gamma \\
&= \int_\Gamma \hat{q} \operatorname{div}_\xi(\boldsymbol{R}\boldsymbol{\vartheta}) \,\mathrm{d}\Gamma = \int_A q \operatorname{div}_\xi(\boldsymbol{R}\boldsymbol{\vartheta}) \, \frac{1}{\det \boldsymbol{J}} \mathrm{d}A \qquad \forall q \in C^\infty(\overline{A}) \,,
\end{aligned} \tag{5.67}$$

with the special identity in two dimensions

$$\operatorname{cof} \boldsymbol{J} = (\det \boldsymbol{J}) \boldsymbol{J}^{-T} = \boldsymbol{R}^T \boldsymbol{J} \boldsymbol{R} \,, \qquad \boldsymbol{J} \in \mathbb{R}^{2\times 2} \,. \tag{5.68}$$

The contravariant Piola transformation is compatible with the commuting diagram and preserves normal projections on the element's boundary. To see this characteristic define the base function $\boldsymbol{\phi}$ in the reference domain and $\boldsymbol{\varphi}$ in the physical domain and equate their normal projections on the outer surface of both domains

$$\langle \boldsymbol{\varphi}, \, \mathbf{n} \rangle \mathrm{d}A = \langle \boldsymbol{\varphi}, \, \mathrm{d}\mathbf{A} \rangle = \langle \boldsymbol{\varphi}, \, \operatorname{cof}(\boldsymbol{J}) \mathrm{d}\boldsymbol{\Gamma} \rangle = \langle \boldsymbol{\phi}, \, \mathrm{d}\boldsymbol{\Gamma} \rangle = \langle \boldsymbol{\phi}, \, \boldsymbol{\nu} \rangle \mathrm{d}\Gamma \quad \iff \quad \boldsymbol{\varphi} = \frac{1}{\det \boldsymbol{J}} \boldsymbol{J} \boldsymbol{\phi} \,. \tag{5.69}$$

5.5.2 The orientation problem

Due to differing edge and face mappings between neighbouring elements the co- and contravariant Piola transformations do not suffice to assert the consistent orientation of the tangential or normal projections of the base functions. The transformations control the size of the projections, but not whether these are parallel or anti-parallel with respect to neighbouring elements. Consistent projections are a key requirement in ensuring no jumps occur in the trace of the respective space and as such, there exist various methods for dealing with this so called orientation problem such as correction functions, reparametrization, and multiple reference elements [4, 9, 42, 101, 110]. In this work we present a solution based on the sequencing of vertices and the separation of orientational data. We define the following rule for the orientation of edges

$$e = \{v_i, \, v_j\} \qquad \text{s.t.} \quad i < j \,. \tag{5.70}$$

This means each edge starts at the lower vertex index and ends at the higher vertex index. This definition determines the orientation of the edge tangent vector, compare Fig. 5.12, and consequently, the tangential projection of the Nédélec base functions. Analogously, for surfaces we define

$$f = \{v_i,\, v_j,\, v_k\} \qquad \text{s.t.} \quad i < j < k\,, \tag{5.71}$$

such that each surface is given by a sequence of increasing vertex indices. The orientation of the surface normal is given according to the left-hand rule. In other words, the direction of the normal is determined by the cross product of the vectors arising from the edges $\{v_i,\, v_j\}$ and $\{v_i,\, v_k\}$

$$\mathbf{n}_{ijk} = \mathbf{t}_{ij} \times \mathbf{t}_{ik}\,. \tag{5.72}$$

The orientation of the Nédélec base functions is according to these rules. Consequently, in order to map each tetrahedron in the mesh to this orientation, we define each element as an increasing vertex-index sequence

$$T = \{v_i,\, v_j,\, v_k,\, v_l\} \qquad \text{s.t.} \quad i < j < k < l\,, \tag{5.73}$$

as depicted in Fig. 5.12. The latter ensures the consistent orientation of the base functions, since they are all mapped from the same reference domain. However, integration in the reference element is achieved using the determinant of the Jacobi matrix

$$\int_{V_e} \mathrm{d}V = \int_{\Omega} \det \boldsymbol{J}\, \mathrm{d}\Omega\,, \tag{5.74}$$

which may become negative if the mapping from the reference to the physical domain contains a reflection. This can be circumvented by taking only the absolute value of the determinant

$$\int_{V_e} \mathrm{d}V = \int_{\Omega} |\det \boldsymbol{J}|\, \mathrm{d}\Omega\,. \tag{5.75}$$

Consequently, consistency is guaranteed by mapping from a single reference element such that, correction functions or considerations of neighbouring elements are not required.

Remark 5.8
The absolute value $|\det \boldsymbol{J}|$ *is only used for the integration over the element. In all other use-cases, the information of the sign is necessary and* $\det \boldsymbol{J}$ *is employed.*

5.6 Embedding of boundary conditions

The Dirichlet boundary conditions of the displacement are applied using the point-wise evaluation of the Lagrangian functionals Eqs. (5.46) and (5.56). As such, on each edge of the Dirichlet boundary there exists the following parametrization for $\alpha \in [0, 1]$

$$\begin{aligned}(\Pi_g^1 u) \circ \alpha \Big|_s &= \widetilde{u}\Big|_{v_1} n_1(\alpha) + \widetilde{u}\Big|_{v_2} n_2(\alpha) \\ &= \widetilde{u}\Big|_{v_1} (1-\alpha) + \widetilde{u}\Big|_{v_2} \alpha\,,\end{aligned} \tag{5.76a}$$

$$\begin{aligned}(\Pi_g^2 u) \circ \alpha \Big|_s &= \widetilde{u}\Big|_{v_1} n_1(\alpha) + \widetilde{u}\Big|_{v_m} n_m(\alpha) + \widetilde{u}\Big|_{v_2} n_2(\alpha) \\ &= \widetilde{u}\Big|_{v_1} (2\alpha-1)(\alpha-1) + \widetilde{u}\Big|_{v_m} 4\alpha(1-\alpha) + \widetilde{u}\Big|_{v_2} \alpha(2\alpha-1)\,,\end{aligned} \tag{5.76b}$$

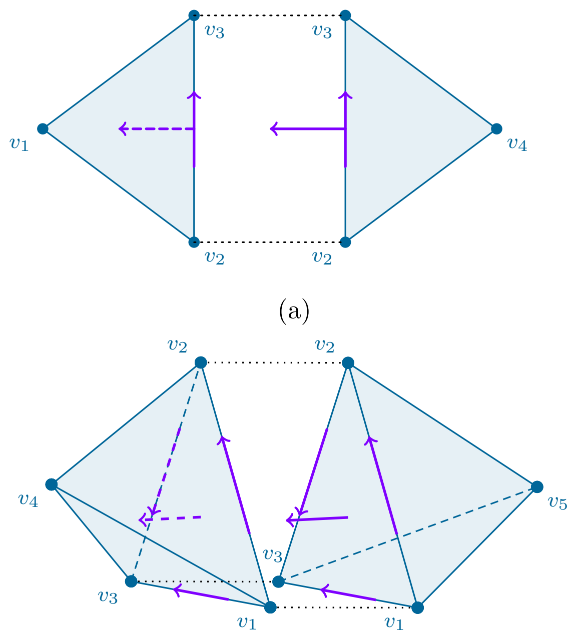

$$f_1 = \{v_1,\, v_2,\, v_3\}$$

$$f_2 = \{v_2,\, v_3,\, v_4\}$$

(a)

$$T_1 = \{v_1,\, v_2,\, v_3,\, v_4\}$$

$$T_2 = \{v_1,\, v_2,\, v_3,\, v_5\}$$

(b)

Figure 5.12: Consistent orientations on two-dimensional (a) and three-dimensional domains (b) using vertex sequences. Edges are oriented from the lower to the higher vertex and faces according to the left-hand rule starting from the lowest vertex across the middle to the highest. On two-dimensional domains the orientation of the surface normal is determined by a rotation of the edge tangent. On three-dimensional domains the cross product of the surface tangents belonging to the lowest sequences determines the orientation of the surface normal.

where the first equation is the linear case and the second equation is the quadratic case. The vertices v_1 and v_2 represent the start and the end of the edge, respectively. The midpoint of the edge is given by v_m.

In order to exactly satisfy the consistent coupling condition in the discrete setting, we first build the Lagrangian interpolation of the displacement field on the Dirichlet boundary. The gradient of the discrete displacement field is then used to construct the boundary condition of the microdistortion

$$\langle \mathbf{t},\, \widetilde{\mathbf{p}}^h \rangle \bigg|_{A_D} = \langle \mathbf{t},\, \Pi_c(\nabla \Pi_g \widetilde{u}) \rangle \bigg|_{A_D} , \tag{5.77}$$

where we consider one row of the displacement and the microdistortion fields at a time. Each edge of the finite element mesh is mapped from the unit domain by the barycentric coordinates (see Fig. 5.13,- the same is valid in three dimensions)

$$\mathbf{x}(\alpha) = \lambda_1 \mathbf{x}_1 + \lambda_2 \mathbf{x}_2 = (1-\alpha)\mathbf{x}_1 + \alpha \mathbf{x}_2 \, . \tag{5.78}$$

For the purpose of consistency, we apply this also for the reference element such that

$$\boldsymbol{\xi}(\alpha) = \lambda_1 \boldsymbol{\xi}_1 + \lambda_2 \boldsymbol{\xi}_2 = (1-\alpha)\boldsymbol{\xi}_1 + \alpha \boldsymbol{\xi}_2 \, . \tag{5.79}$$

Consequently, the chain rule yields

$$\frac{\mathrm{d}}{\mathrm{d}\alpha}(u \circ \mathbf{x} \circ \boldsymbol{\xi})(\alpha) = \langle \nabla_\xi u,\, \boldsymbol{\tau} \rangle = \langle \nabla_x u,\, \mathbf{t} \rangle \, , \tag{5.80}$$

such that the consistent coupling condition reduces to

$$\langle \widetilde{\mathbf{p}}^h,\, \mathbf{t} \rangle \bigg|_{A_D} = \frac{\mathrm{d}}{\mathrm{d}\alpha} \Pi_g \widetilde{u} \bigg|_{A_D} \, . \tag{5.81}$$

In case of the lowest order sequence $\mathcal{L}^1 \overset{\nabla}{\to} \mathcal{N}_I^0$ the Nédélec base functions yield a constant tangential projection of unity on the edges and the evaluation simplifies to

$$c_1 : \quad \langle \mathbf{p}^h,\, \mathbf{t} \rangle \bigg|_{s_i} = \langle c_1 \, \boldsymbol{\theta}_1,\, \mathbf{t} \rangle \bigg|_{s_i} = c_1 = \frac{\mathrm{d}}{\mathrm{d}\alpha} \Pi_g \widetilde{u} \bigg|_{s_i} = \frac{\mathrm{d}}{\mathrm{d}\alpha} \left(\widetilde{u} \bigg|_{v_1} (1-\alpha) + \widetilde{u} \bigg|_{v_2} \alpha \right) = \widetilde{u} \bigg|_{v_2} - \widetilde{u} \bigg|_{v_1} , \tag{5.82}$$

for each edge s_i in A_D. Thus, on each edge of the Dirichlet boundary we find

$$\langle \mathbf{t},\, \Pi_c \mathbf{p} \rangle \bigg|_{s_i} = \langle \mathbf{t},\, c_1 \, \boldsymbol{\theta}_1 \rangle \bigg|_{s_i} \, . \tag{5.83}$$

In the quadratic sequence $\mathcal{L}^2 \overset{\nabla}{\to} \mathcal{N}_{II}^1$ on each vertex of an edge, the Nédélec base functions produce a tangential projection of unity. As such, the evaluation can be carried out via

$$\begin{aligned} c_1 : \quad \langle \mathbf{p}^h,\, \mathbf{t} \rangle \bigg|_{v_1} &= \langle c_1 \, \boldsymbol{\theta}_1,\, \mathbf{t} \rangle \bigg|_{v_1} = c_1 = \frac{\mathrm{d}}{\mathrm{d}\alpha} \left(\widetilde{u} \bigg|_{v_1} (2\alpha-1)(\alpha-1) + \widetilde{u} \bigg|_{v_m} 4\alpha(1-\alpha) + \widetilde{u} \bigg|_{v_2} \alpha(2\alpha-1) \right) \bigg|_{v_1} \\ &= -3\widetilde{u} \bigg|_{v_1} + 4\widetilde{u} \bigg|_{v_m} - \widetilde{u} \bigg|_{v_2} , \end{aligned} \tag{5.84}$$

$$\begin{aligned} c_2 : \quad \langle \mathbf{p}^h,\, \mathbf{t} \rangle \bigg|_{v_2} &= \langle c_2 \, \boldsymbol{\theta}_2,\, \mathbf{t} \rangle \bigg|_{v_2} = c_2 = \frac{\mathrm{d}}{\mathrm{d}\alpha} \left(\widetilde{u} \bigg|_{v_2} (2\alpha-1)(\alpha-1) + \widetilde{u} \bigg|_{v_m} 4\alpha(1-\alpha) + \widetilde{u} \bigg|_{v_2} \alpha(2\alpha-1) \right) \bigg|_{v_2} \\ &= \widetilde{u} \bigg|_{v_1} - 4\widetilde{u} \bigg|_{v_m} + 3\widetilde{u} \bigg|_{v_2} , \end{aligned} \tag{5.85}$$

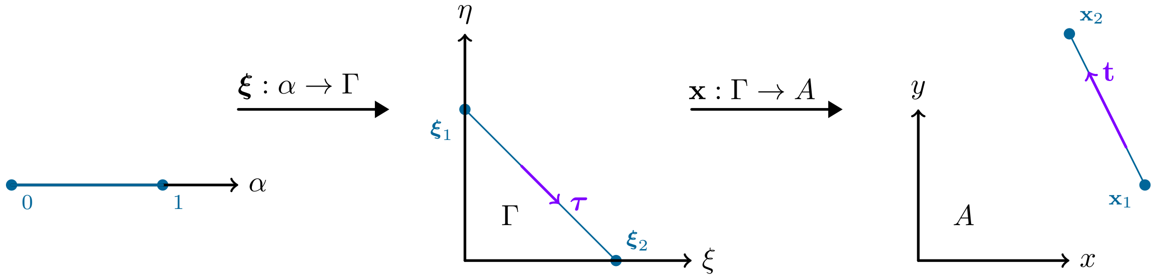

Figure 5.13: Barycentric mapping of edges from the unit domain to the reference triangle and onto the physical domain.

for each edge s_i in A_D. The microdistortion on each edge of the Dirichlet boundary is therefore given by

$$\langle \mathbf{t},\, \Pi_c \mathbf{p} \rangle \Big|_{s_i} = \langle \mathbf{t},\, c_1\, \boldsymbol{\theta}_1 + c_2\, \boldsymbol{\theta}_2 \rangle \Big|_{s_i} . \tag{5.86}$$

5.7 Assembly of element matrices

The base functions on the physical element allow for the element-wise computation of stiffness matrices [16]. These matrices are then assembled into a global (sparse) matrix, representing the total stiffness of the system. The assembly process is derived from the definition of the trial and test functions as

$$u^h(x,y,z) = \bigcup_{e=1}^{n} u_e^h \,, \qquad \delta u^h(x,y,z) = \bigcup_{e=1}^{n} \delta u_e^h \,, \tag{5.87}$$

such that the global stiffness matrix and load vector read

$$\boldsymbol{K} = \bigcup_{e=1}^{n} \boldsymbol{K}_e \,, \qquad \mathbf{f}^d = \bigcup_{e=1}^{n} \mathbf{f}_e \,, \tag{5.88}$$

where $(\cdot)^d$ represents discrete values. The correspondence between the local and global stiffness terms is derived from node sequencing. Following the assembly, the solution of the discrete system

$$\mathbf{u}^d = \boldsymbol{K}^{-1} \mathbf{f}^d \,, \tag{5.89}$$

can then be computed.

Remark 5.9
In the hp-FEA software Rayse the conjugate gradient method is employed to compute the solution, since both linear elasticity and the relaxed micromorphic model induce symmetric positive definite bilinear forms.

5.7.1 Element matrix

We define the element-wise interpolation operators as matrices of the base functions. For antiplane shear this results in

$$u_e(\xi,\eta) = \boldsymbol{N}(\xi,\eta)\mathbf{u}_e^d \,, \qquad \mathbf{p}_e(\xi,\eta) = \boldsymbol{\Theta}(\xi,\eta)\mathbf{p}_e^d \,, \tag{5.90}$$

where the matrices are given by

$$\begin{aligned}
\boldsymbol{N} &= \begin{bmatrix} n_1 & n_2 & \dots & n_m \end{bmatrix} , & \nabla \boldsymbol{N} &= \begin{bmatrix} \nabla n_1 & \nabla n_2 & \dots & \nabla n_m \end{bmatrix} , \\
\boldsymbol{\Theta} &= \begin{bmatrix} \boldsymbol{\theta}_1 & \boldsymbol{\theta}_2 & \dots & \boldsymbol{\theta}_m \end{bmatrix} , & \operatorname{curl} \boldsymbol{\Theta} &= \begin{bmatrix} \operatorname{curl} \boldsymbol{\theta}_1 & \operatorname{curl} \boldsymbol{\theta}_2 & \dots & \operatorname{curl} \boldsymbol{\theta}_m \end{bmatrix} ,
\end{aligned} \tag{5.91}$$

such that the element stiffness matrix and load vector read

$$\begin{aligned}
\boldsymbol{K}_e &= \int_{A_e} \mu_{\mathrm{e}} (\nabla \boldsymbol{N} - \boldsymbol{\Theta})^T (\nabla \boldsymbol{N} - \boldsymbol{\Theta}) + \mu_{\mathrm{micro}} \boldsymbol{\Theta}^T \boldsymbol{\Theta} + \mu_{\mathrm{macro}} L_{\mathrm{c}}^2 (\operatorname{curl} \boldsymbol{\Theta})^T (\operatorname{curl} \boldsymbol{\Theta}) \, \mathrm{d}A , \\
\mathbf{f}_e &= \int_{A_e} f \boldsymbol{N}^T + \boldsymbol{\Theta}^T \mathbf{m} \, \mathrm{d}A .
\end{aligned} \tag{5.92}$$

In case of the full three-dimensional model one finds

$$\mathbf{u}_e(\xi, \eta, \zeta) = \boldsymbol{N}(\xi, \eta, \zeta) \mathbf{u}_e^d , \qquad \boldsymbol{P}_e(\xi, \eta, \zeta) = \boldsymbol{\Theta}(\xi, \eta, \zeta) \boldsymbol{P}_e^d , \tag{5.93}$$

with

$$\begin{aligned}
\boldsymbol{N} &= \begin{bmatrix} n_1 \boldsymbol{I} & n_2 \boldsymbol{I} & \dots & n_m \boldsymbol{I} \end{bmatrix} , \\
\mathrm{D} \boldsymbol{N} &= \begin{bmatrix} \nabla n_1 & \mathbf{o} & \mathbf{o} & & \nabla n_n & \mathbf{o} & \mathbf{o} \\ \mathbf{o} & \nabla n_1 & \mathbf{o} & \cdots & \mathbf{o} & \nabla n_m & \mathbf{o} \\ \mathbf{o} & \mathbf{o} & \nabla n_1 & & \mathbf{o} & \mathbf{o} & \nabla n_m \end{bmatrix} , \\
\boldsymbol{\Theta} &= \begin{bmatrix} \boldsymbol{\theta}_1 & \mathbf{o} & \mathbf{o} & & \boldsymbol{\theta}_m & \mathbf{o} & \mathbf{o} \\ \mathbf{o} & \boldsymbol{\theta}_1 & \mathbf{o} & \cdots & \mathbf{o} & \boldsymbol{\theta}_m & \mathbf{o} \\ \mathbf{o} & \mathbf{o} & \boldsymbol{\theta}_1 & & \mathbf{o} & \mathbf{o} & \boldsymbol{\theta}_m \end{bmatrix} , \\
\operatorname{Curl} \boldsymbol{\Theta} &= \begin{bmatrix} \operatorname{curl} \boldsymbol{\theta}_1 & \mathbf{o} & \mathbf{o} & & \operatorname{curl} \boldsymbol{\theta}_m & \mathbf{o} & \mathbf{o} \\ \mathbf{o} & \operatorname{curl} \boldsymbol{\theta}_1 & \mathbf{o} & \cdots & \mathbf{o} & \operatorname{curl} \boldsymbol{\theta}_m & \mathbf{o} \\ \mathbf{o} & \mathbf{o} & \operatorname{curl} \boldsymbol{\theta}_1 & & \mathbf{o} & \mathbf{o} & \operatorname{curl} \boldsymbol{\theta}_m \end{bmatrix} ,
\end{aligned} \tag{5.94}$$

where $\mathbf{o} \in \mathbb{R}^3$ is a vector of zeros and $\boldsymbol{I} \in \mathbb{R}^{3 \times 3}$ is the identity matrix.

The material tensors are reinterpreted as nine dimensional matrices and the symmetry and matrix-trace operators are directly embedded in their definition (see Appendix A)

$$(\lambda \mathbb{1} \otimes \mathbb{1} + 2\mu \, \mathbb{J}) \operatorname{sym} \boldsymbol{P} = (\lambda \mathbb{1} \otimes \mathbb{1} + 2\mu \, \mathbb{J}) \mathbb{S} \, \boldsymbol{P} = (\lambda \mathbb{1} \otimes \mathbb{1} + 2\mu \, \mathbb{S}) \boldsymbol{P} = \mathbb{C} \boldsymbol{P} . \tag{5.95}$$

Consequently, the element stiffness matrix and load vector are given by

$$\begin{aligned}
\boldsymbol{K}_e &= \int_{V_e} (\mathrm{D} \boldsymbol{N} - \boldsymbol{\Theta})^T (\mathbb{C}_{\mathrm{e}} + \mathbb{C}_{\mathrm{c}}) (\mathrm{D} \boldsymbol{N} - \boldsymbol{\Theta}) + \boldsymbol{\Theta}^T \mathbb{C}_{\mathrm{micro}} \boldsymbol{\Theta} + \mu_{\mathrm{macro}} L_{\mathrm{c}}^2 (\operatorname{Curl} \boldsymbol{\Theta})^T (\operatorname{Curl} \boldsymbol{\Theta}) \, \mathrm{d}V , \\
\mathbf{f}_e &= \int_{V_e} \boldsymbol{N}^T \mathbf{f} + \boldsymbol{\Theta}^T \boldsymbol{M} \, \mathrm{d}V .
\end{aligned} \tag{5.96}$$

The stiffness matrix and load vector for the case of plane strain is analogous to the three-dimensional case but reduces of the dimensions of the matrices.

5.7.2 Partitioning

In general, the global stiffness matrix contains terms related to the boundary conditions. This a result of the embedding

$$\mathbf{u} = \widehat{\mathbf{u}} + \widetilde{\mathbf{u}}\,, \tag{5.97}$$

where $\mathbf{u}$ is the total displacement field, $\widehat{\mathbf{u}}$ is the unknown displacement field and $\widetilde{\mathbf{u}}$ is the prescribed displacement field on the Dirichlet boundary. This leads to a natural partition of an element's discrete displacement vector and stiffness matrix

$$\mathbf{u}_e = \begin{bmatrix} \mathbf{u}_f \\ \mathbf{u}_p \end{bmatrix}, \qquad \boldsymbol{K}_e = \begin{bmatrix} \boldsymbol{K}_{ff} & \boldsymbol{K}_{fp} \\ \boldsymbol{K}_{pf} & \boldsymbol{K}_{pp} \end{bmatrix}. \tag{5.98}$$

There are various approaches to deal with the partition such as assembling multiple global matrices or using only parts of the total global matrix. In this work we apply the partition directly at the element level such that

$$\boldsymbol{K}_{ff}\mathbf{u}_f = \mathbf{f}_f^*\,, \qquad \mathbf{f}_f^* = \mathbf{f}_f - \boldsymbol{K}_{fp}\mathbf{u}_p\,. \tag{5.99}$$

Thus, the procedure follows by assembling a single global stiffness matrix for $\boldsymbol{K}_{ff}$ and a single global load vector for $\mathbf{f}_f$.

6 Higher Order Finite Elements

The previous chapter introduced the classical finite element method, where convergence is achieved by mesh-refinement, i.e., h-refinement. As per the error estimates, h-refinement yields algebraic convergence. An alternative methodology suggests increasing the polynomial degree instead, being the so called p-refinement [12, 13]. Reconsidering the error estimates, it becomes clear the latter implies exponential convergence for highly smooth fields [110]. If the solution is piece-wise smooth and contains singularities, p-refinement yields algebraic convergence [110]. The idea of hp-FEM [29, 31, 103, 105] is essentially the combination of both refinement methods, thus allowing to recover exponential convergence.

In this section we introduce methods for the construction of efficient higher order finite elements for classical Hilbert spaces. The methods represent a general approach, independent of the polynomial basis and a specification of degrees of freedom. Further, a clear split of the base functions between the kernel and range of the corresponding space with the exception of the lowest-order base functions is possible with the method and derived intuitively.

Since the construction is introduced independently of degrees of freedom, the degrees of freedom from [30] are used to embed boundary conditions and uphold exact sequence properties.

This work relies on Bernstein polynomials and Bézier triangles and tetrahedra for the definition of higher order finite elements. In [2] it is shown that Bernstein polynomials allow for optimal complexity in the assembly procedure of finite element programs. This feature is a result of their natural factorization by the Duffy transformation. For a thorough treatment of Bernstein polynomials we recommend [59].

6.1 Preliminaries

Traditionally, higher order finite elements are constructed using hierarchical polynomials [103, 110]. The latter has the advantage that the basis does not change between p-refinements, but rather a new base function is added to the previously employed basis. Further, the Legendre polynomial basis for example, is orthogonal in the L^2-scalar product over the domain $[-1, 1]$ and as such, yields better matrix condition numbers. However, this characteristic is restricted to problems with constant coefficients. In addition, the hierarchical basis is not intrinsically nodal (in the sense of symmetry) in contrast to the Lagrangian and the Bernstein polynomials used in this work.

6.1.1 Bernstein polynomials

Bernstein polynomials of order p are given by the binomial expansion of the barycentric representation of the unit line

$$1 = (\lambda_1 + \lambda_2)^p = ((1-\xi) + \xi)^p = \sum_{i=0}^{p} \binom{p}{i} \xi^i (1-\xi)^{p-i} = \sum_{i=0}^{p} \frac{p!}{i!(p-i)!} \xi^i (1-\xi)^{p-i} \, , \tag{6.1}$$

where $\xi \in [0, 1]$. The Bernstein polynomial reads

$$b_i^p(\xi) = \binom{p}{i} \xi^i (1-\xi)^{p-i} \, . \tag{6.2}$$

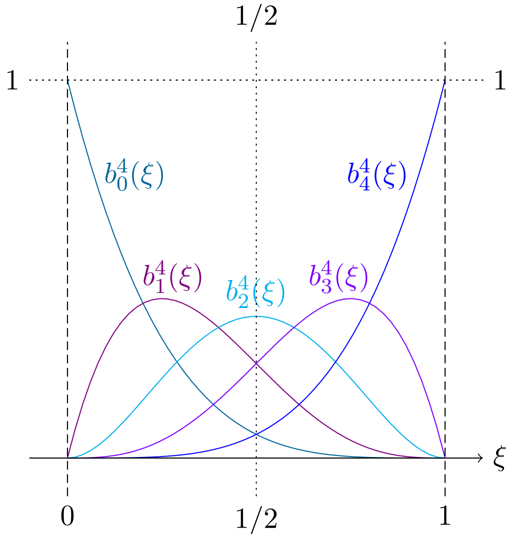

Figure 6.1: Bernstein base functions of degree $p = 4$ on the unit domain. Their sum forms a partition of unity. The base functions are symmetric for $\xi = 0.5$ with respect to their indices and always positive.

A direct result of the binomial expansion is that Bernstein polynomials form a partition of unity (see Fig. 6.1)

$$\sum_{i=0}^{p} b_i^p(\xi) = 1\,. \tag{6.3}$$

Another consequence is that Bernstein polynomials are non-negative and smaller equal one

$$0 \leq b_i^p(\xi) \leq 1\,, \qquad\qquad \xi \in [0,1]\,. \tag{6.4}$$

A necessary condition for the use of Bernstein polynomials in finite element approximations is for them to span the entire polynomial space.

Theorem 6.1 (Span of Bernstein polynomials)
The span of Bernstein polynomials forms a basis of the one-dimensional polynomial space

$$P^p(s) = \mathrm{span}\{b_i^p\}\,, \qquad\qquad s \subseteq \mathbb{R}\,. \tag{6.5}$$

Proof. First we observe

$$\dim(\mathrm{span}\{b_i^p\}) = \dim P^p(s) = p+1\,. \tag{6.6}$$

The proof of linear Independence is achieved by contradiction. Let the set $\mathrm{span}\{b_i^p\}$ with $0 < i \leq p$ be linearly dependent, then there exists some combination with at least one non-zero constant $c_i \neq 0$ such that

$$\sum_{i=1}^{p} c_i b_i^p(\xi) = 0\,, \qquad\qquad \frac{\mathrm{d}}{\mathrm{d}\xi}\sum_{i=1}^{p} c_i b_i^p(\xi) = 0\,. \tag{6.7}$$

However, by the partition of unity property Eq. (6.3), only the full combination $(0 \leq i \leq p)$ generates a constant and by the exact sequence property the kernel of the differentiation operator is exactly the space of constants $\ker(\partial) = \mathbb{R}$. The linear independence of the full span also follows from the partition of unity property, since constants cannot be constructed otherwise. □

On the unit domain, the integral of Bernstein polynomials reads

$$\int_0^1 b_i^p(\xi)\mathrm{d}\xi = \frac{1}{p+1} \quad \forall\, b_i^p \in \operatorname{span}\{b_i^p\}\,, \tag{6.8}$$

thus allowing for fast evaluation of integrals with constants. Further, the multiplication of two Bernstein polynomials

$$b_i^p(\xi) b_j^q(\xi) = \frac{\begin{pmatrix} i+j \\ i \end{pmatrix}}{\begin{pmatrix} p+q \\ p \end{pmatrix}} b_{i+j}^{p+q}(\xi)\,, \tag{6.9}$$

yields a scaled Bernstein polynomial. The derivative of a Bernstein polynomial is given by the linear combination of two Bernstein polynomials of a lower degree

$$\frac{\mathrm{d}}{\mathrm{d}\xi} b_i^p(\xi) = p\,(b_{i-1}^{p-1}(\xi) - b_i^{p-1}(\xi))\,. \tag{6.10}$$

Lastly, Bernstein polynomials can be evaluated using the recursive formula

$$b_0^p(\xi) = (1-\xi)^p\,, \qquad b_{i+1}^p(\xi) = \frac{(p-i)\xi}{(p+1)(1-\xi)} b_i^p(\xi)\,, \qquad i \in \{0, 1, ..., p-1\}\,, \tag{6.11}$$

which allows for fast evaluation of the base functions.

Remark 6.1
Note that the formula implies $\lim_{\xi\to 1} b_{i+1}^p(\xi) = \infty$. *As such, evaluations using the formula are required to use* $\xi < 1$ *preferably with an additional tolerance. The limit case* $\xi = 1$ *is zero for all Bernstein function aside from the last function belonging to the vertex, which simply returns one.*

6.1.2 Dual numbers

Dual numbers [40] define an augmented algebra, where the derivative of a function can be computed simultaneously with the result of the function. This enhancement is also commonly used in forward automatic differentiation [17, 80], not to be confused with numerical differentiation, since unlike in numerical differentiation, automatic differentiation is no approximation and yields the exact derivative. The latter represents an alternative method to finding the derivatives of base functions, as opposed to explicit formulas or approximations. Dual numbers augment the classical numbers by adding a non-zero number ε with a zero square $\varepsilon^2 = 0$ (this is analogous to how complex numbers add i in order to allow for $i^2 = -1$).

Definition 6.1 (Dual number)
The dual number is defined by

$$x + x'\varepsilon\,, \qquad\qquad \varepsilon \ll 1\,, \tag{6.12}$$

where x' *is the derivative (only in automatic differentiation),* ε *is an abstract number (infinitesimal) and* $\varepsilon^2 = 0$.

The augmented algebra results automatically from the definition of the dual number.

Definition 6.2 (Augmented dual algebra)
The standard algebraic operations take the following form for dual numbers

1. *Addition and subtraction*

$$(x + x'\varepsilon) \pm (y + y'\varepsilon) = x \pm y + (x' \pm y')\varepsilon \,. \tag{6.13}$$

2. *Multiplication*

$$(x + x'\varepsilon)(y + y'\varepsilon) = xy + (xy' + x'y)\varepsilon \,, \tag{6.14}$$

   since $\varepsilon^2 = 0$.

3. *Division is achieved by first defining the inverse element*

$$(x + x'\varepsilon)(y + y'\varepsilon) = 1 \qquad \Longleftrightarrow \qquad y = \frac{1}{x},\, y' = -\frac{x'}{x^2} \,, \tag{6.15}$$

   such that

$$(x + x'\varepsilon)/(y + y'\varepsilon) = x/y + (x'/y - xy'/y^2)\varepsilon \,. \tag{6.16}$$

Application of the above definitions to polynomials

$$p(x+\varepsilon) = \sum_{i=0}^{\infty} c_i (x+\varepsilon)^i = \sum_{i=0}^{\infty}\sum_{j=0}^{1} c_i \binom{i}{j} x^{i-j}\varepsilon^j = \sum_{i=0}^{\infty} c_i x^i + \varepsilon \sum_{i=1}^{\infty} i\, c_i x^{i-1} = p(x) + p'(x)\varepsilon \,, \tag{6.17}$$

allows the extension to various types of analytical functions with a power-series representation (such as trigonometric or hyperbolic).

Definition 6.3 (General dual numbers function)
A function of a dual number is defined generally by

$$f(x + \varepsilon) = f(x) + f'(x)\varepsilon \,, \tag{6.18}$$

being the fundamental formula for forward automatic differentiation.

The definition of dual numbers makes them directly applicable to the general rules of differentiation, such as the chain rule or product rule, in which case the derivative is simply the composition of previous computations with ε.

The logic of dual numbers can be understood intuitively by the directional derivative

$$\frac{\mathrm{d}}{\mathrm{d}x} f(x) = \partial_{x'} f(x) = \frac{\mathrm{d}}{\mathrm{d}\varepsilon} f(x + x'\varepsilon)\bigg|_{\varepsilon=0} = \lim_{\varepsilon\to 0} \frac{f(x + x'\varepsilon) - f(x)}{\varepsilon} \,, \tag{6.19}$$

where dividing by ε and setting $\varepsilon = 0$ are deferred to the last step of the computation, being the extraction of the derivative and equivalent to the operation $f(x + \varepsilon) - f(x)$ with the augmented algebra of dual numbers.

Remark 6.2
In the implementation of the finite element software Rayse the Bernstein polynomials and their derivatives are computed simultaneously using the recursive formula with dual numbers.

6.1.3 Polytopal functions

In the following section the construction of higher order H^1- and $H(\text{curl})$-conforming spaces is presented. The construction is based on a polytopal association of base functions. The following definitions are employed

Definition 6.4 (Polytopal base functions)
Each base function is associated with its respective polytope and the underlying Hilbert space as follows:

1. *A vertex base function has a vanishing trace on all other vertices and non-neighbouring edges and faces.*
2. *An edge base function has a vanishing trace on all other edges and non-neighbouring faces.*
3. *A face base function has a vanishing trace on all other faces.*
4. *A cell base function has a vanishing trace on the entire boundary of the element.*

The latter definition is general and the respective trace may change according to the corresponding Hilbert space.

6.1.4 Commuting interpolants

We state the degrees of freedom introduced in [30]. A slightly modified version of the degrees of freedom is used to embed Dirichlet boundary conditions into the respective spaces.

Definition 6.5 (The H^1-interpolant)
The H^1-conforming interpolant is defined using the following degrees of freedom.

1. *Vertex point evaluation functionals*

$$l_i(u) = u \bigg|_{v_i} \, . \tag{6.20}$$

2. *The edge functionals read*

$$l_{ij}(u) = \int_{s_i} \frac{\partial u}{\partial s} \frac{\partial q_j}{\partial s} \, \mathrm{d}s \qquad \forall \, q_j \in P_0^p(s) \, . \tag{6.21}$$

3. *On each face the degrees of freedom are given by*

$$l_{ij}(u) = \int_{A_i} \langle \nabla_f u , \, \nabla_f q_j \rangle \, \mathrm{d}A \qquad \forall \, q_j \in P_0^p(A) \, , \tag{6.22}$$

   where ∇_f represents the surface gradient.

4. *Lastly, the cell functionals are tests of gradients*

$$l_i(u) = \int_V \langle \nabla u , \, \nabla q_i \rangle \, \mathrm{d}V \qquad \forall \, q \in P_0^p(V) \, . \tag{6.23}$$

The degrees of freedom define an H^1-conforming finite element and can be used to construct the interpolant $\Pi_g : H^1 \to U^h$.

Definition 6.6 (The $H(\mathrm{curl})$-interpolant)
One defines the $H(\mathrm{curl})$-interpolant by employing the following functionals

1. *On each edge the degrees of freedom are given by*

$$l_{ij}(\mathbf{p}) = \int_{s_i} q_j \langle \mathbf{p},\, \mathbf{t} \rangle \,\mathrm{d}s \qquad \forall\, q_j \in P^p(s)\,. \tag{6.24}$$

2. *The face-type functionals read*

$$l_{ij}(\mathbf{p}) = \int_{A_i} \langle \mathrm{curl}_f\, \mathbf{p},\, \mathrm{curl}_f\, \mathbf{q}_j \rangle \,\mathrm{d}A \qquad \forall\, \mathbf{q}_j \in [P_0^p(A)]^2 \cap \ker^{\perp}(\mathrm{curl})\,, \tag{6.25a}$$

$$l_{ij}(\mathbf{p}) = \int_{A_i} \langle \mathbf{p},\, \nabla q_j \rangle \,\mathrm{d}A \qquad \forall\, q_j \in P_0^{p+1}(A)\,, \tag{6.25b}$$

where curl_f *is the surface curl.*

3. *Finally, the cell degrees of freedom are given by*

$$l_i(\mathbf{p}) = \int_V \langle \mathrm{curl}\, \mathbf{p},\, \mathrm{curl}\, \mathbf{q}_i \rangle \,\mathrm{d}A \qquad \forall\, \mathbf{q}_i \in [P_0^p(V)]^3 \cap \ker^{\perp}(\mathrm{curl})\,, \tag{6.26a}$$

$$l_i(\mathbf{p}) = \int_V \langle \mathbf{p},\, \nabla q_i \rangle \,\mathrm{d}A \qquad \forall\, q_i \in P_0^{p+1}(V)\,. \tag{6.26b}$$

The degrees of freedom define a unisolvent $H(\mathrm{curl})$-conforming finite element. Further, using the degrees of freedom one can construct the projection based interpolant $\Pi_c : H(\mathrm{curl}) \to \mathcal{N}_I$.

6.2 Higher order triangular elements

6.2.1 Bézier elements

The base functions on the triangle reference element are defined using the binomial expansion of the barycentric coordinates on the domain $\Gamma = \{(\xi, \eta) \in [0,1]^2 \mid \xi + \eta \leq 1\}$

$$1 = (\lambda_1 + \lambda_2 + \lambda_3)^p = ([1 - \xi - \eta] + \eta + \xi)^p\,, \tag{6.27}$$

where the barycentric functions Eq. (5.47) are employed to map the domain. As such, the Bézier base functions read

$$b_{ij}^p(\lambda_1, \lambda_2, \lambda_3) = \binom{p}{i}\binom{p-i}{j} \lambda_1^{p-i-j} \lambda_2^j \lambda_3^i\,, \tag{6.28}$$

with the equivalent form

$$b_{ij}^p(\xi, \eta) = \binom{p}{i}\binom{p-i}{j} (1 - \xi - \eta)^{p-i-j} \eta^j \xi^i\,, \tag{6.29}$$

of which some examples are depicted in Fig. 6.2. The Duffy transformation

$$\boldsymbol{\xi} : [0,1]^2 \to \Gamma\,, \qquad \{\alpha, \beta\} \mapsto \{\xi, \eta\}\,, \tag{6.30}$$

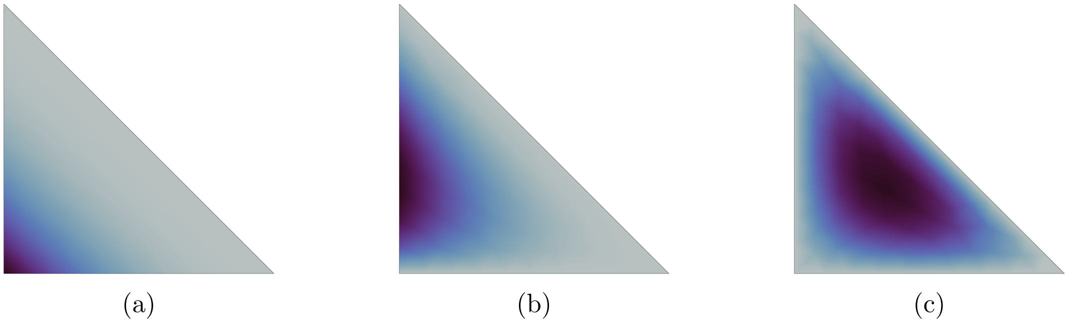

Figure 6.2: Cubic vertex (a), edge (b) and cell (c) Bézier base functions on the reference triangle.

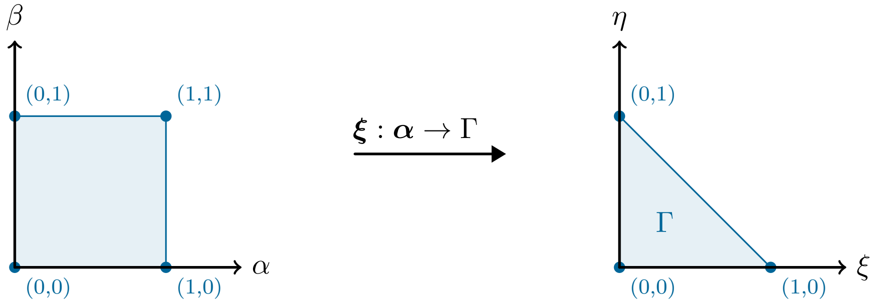

Figure 6.3: Duffy transformation from a quadrilateral to a triangle by collapse of the coordinate system.

given by the relations

$$\begin{aligned} \xi &= \alpha\,, & \eta &= (1-\alpha)\beta\,, \\ \alpha &= \xi\,, & \beta &= \frac{\eta}{1-\xi}\,, \end{aligned} \tag{6.31}$$

allows to view the triangle as a collapsed quadrilateral, see Fig. 6.3. Inserting the Duffy map into the definition of the Bézier base function yields the split

$$\begin{aligned} b^p_{ij}(\xi,\eta) &= \binom{p}{i}\binom{p-i}{j}(1-\xi-\eta)^{p-i-j}\eta^j\xi^i \\ &= \binom{p}{i}\binom{p-i}{j}(1-\alpha-[1-\alpha]\beta)^{p-i-j}(1-\alpha)^j\beta^j\alpha^i \\ &= \binom{p}{i}\binom{p-i}{j}(1-\alpha)^{p-i-j}(1-\beta)^{p-i-j}(1-\alpha)^j\beta^j\alpha^i \\ &= \binom{p}{i}(1-\alpha)^{p-i}\alpha^i\binom{p-i}{j}(1-\beta)^{p-i-j}\beta^j \\ &= b^p_i(\alpha)b^{p-i}_j(\beta)\,. \end{aligned} \tag{6.32}$$

In other words, the Duffy transformation results in a natural factorization of the Bézier triangle into Bernstein base functions [2]. The latter allows for fast evaluation using sum factorization. Further, it is now clear that Bézier triangles are given by the interpolation of Bézier curves, where the degree

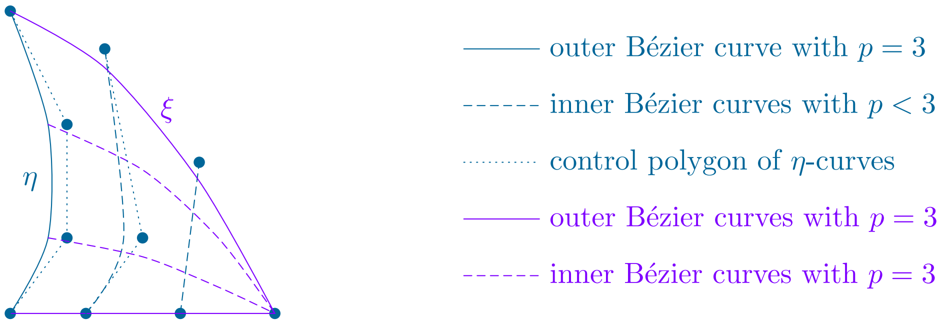

Figure 6.4: Bézier triangle built by interpolating Bézier curves with an ever decreasing polynomial degree.

of the polynomial decreases between each curve, see Fig. 6.4. In order to compute gradients on the reference domain one applies the chain rule

$$\nabla_\xi b_{ij}^p = (\mathrm{D}_\alpha \boldsymbol{\xi})^{-T} \nabla_\alpha b_{ij}^p\,, \qquad \mathrm{D}_\alpha \boldsymbol{\xi} = \begin{bmatrix} 1 & 0 \\ -\beta & 1-\alpha \end{bmatrix}, \qquad (\mathrm{D}_\alpha \boldsymbol{\xi})^{-T} = \frac{1}{1-\alpha} \begin{bmatrix} 1-\alpha & \beta \\ 0 & 1 \end{bmatrix}. \tag{6.33}$$

The factorization is naturally suited for the use of dual numbers since the $\boldsymbol{\alpha}$-gradient of a base function reads

$$\nabla_\alpha b_{ij}^p(\alpha, \beta) = \begin{bmatrix} b_j^{p-i} \dfrac{\mathrm{d}}{\mathrm{d}\alpha} b_i^p \\ b_i^p \dfrac{\mathrm{d}}{\mathrm{d}\beta} b_j^{p-i} \end{bmatrix}, \tag{6.34}$$

such that only the derivatives of the Bernstein base functions with respect to their parameter are required.

The Duffy transformation induces an intrinsic optimal order of traversal of the base functions, compare Fig. 6.5, namely

$$(i, j) = (0, 0) \to (0, 1) \to \ldots \to (2, 2) \to \ldots \to (i, p-i) \to \ldots \to (p, 0)\,, \tag{6.35}$$

which respects a clockwise orientation of the element and the global consistency definitions from Section 5.5.2. Thus the order of the sequence of discrete values on common edges is determined by the global orientation. In order to relate a base function to a polytopal piece of the element, one observes the following result.

Observation 6.1 (Triangle base functions)
The polytope of each base function $b_{ij}^p(\xi, \eta)$ can be determined as follows:

- *The indices $(0, 0)$, $(0, p)$ and $(p, 0)$ represent the first, second and last vertex base functions, respectively.*
- *The indices $(0, j)$ with $0 < j < p$ and $(i, 0)$ with $0 < i < p$ represent the first and second edge base functions, respectively. Base functions of the slanted edge are given by $(i, p-i)$ with $0 < i < p$.*
- *The remaining index combinations are cell base functions.*

With the latter observation, the construction of vertex-, edge- and cell base functions follows the intrinsic traversal order induced by the Duffy transformation and relates to a specific polytope via index-pairs.

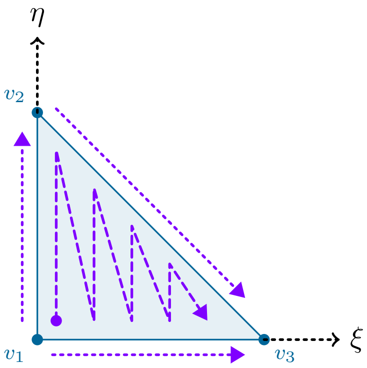

Figure 6.5: Traversal order of base functions. The purple lines represent the order in which the base functions are constructed by the factorized evaluation. Note that the traversal order on each edge is intrinsically from the lower to the higher vertex index.

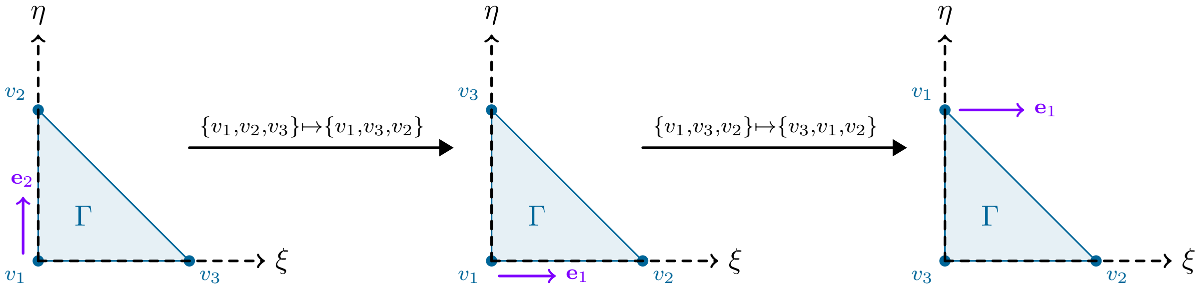

Figure 6.6: Derivation of a template vector on the remaining edges via permutations of the reference triangle using covariant Piola mappings.

6.2.2 Nédélec elements of the second type

Note that the continuity characteristic of tensor valued Hilbert spaces such as Nédélec and Raviart-Thomas is geometrical in nature. In fact, it is possible to define a template based on the polytopal building blocks of the reference element and assert the desired reduced continuity by the dyadic product with an H^1-conforming polynomial space U^p. The construction is independent of the degrees of freedom and allows for a simple definition of the base functions on the reference element using for example, the Lagrangian basis, or in this work the Bernstein basis.

We consider the decomposition of the reference triangle in Fig. 6.7. On the first vertex v_1 we define a vector with a projection of one on the tangent vector of the first edge e_{12} and a zero projection on the second edge e_{13}. Next we define a vector with a projection of one on the tangent vector of the first edge e_{12}. Further, we construct a normal vector on the first edge e_{12}. Lastly, we define two unit vectors in the cell. The remaining vectors for their respective polytopes can be computed by mapping the triangle c_{123} to various permutations of c_{ijk} on the unit domain and adjusting the sign to ensure a positive projection on the tangent vector, see Fig. 6.6.

Remark 6.3

The polytopal set is not unique and depends on the starting definition on the first polytopes and the resulting mapping. Further, one can change pure edge-type template vectors by adding or subtracting normal vectors without influencing the tangential projection.

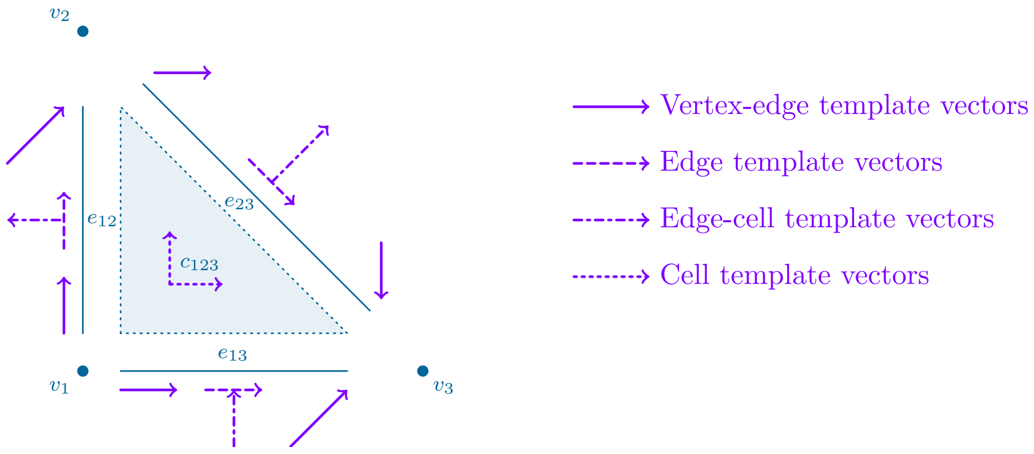

Figure 6.7: Template vectors for the reference triangle on their corresponding polytope.

The resulting template is given by the superset of the sets for the respective polytopes

$$\mathcal{T} = \{\mathcal{T}_1, \mathcal{T}_2, \mathcal{T}_3, \mathcal{T}_{12}, \mathcal{T}_{13}, \mathcal{T}_{23}, \mathcal{T}_{123}\}\,, \tag{6.36}$$

where the polytopal sets are defined via Cartesian base vectors, reading

$$\begin{aligned} &\mathcal{T}_1 = \{\mathbf{e}_2, \mathbf{e}_1\}\,, && \mathcal{T}_2 = \{\mathbf{e}_1 + \mathbf{e}_2, \mathbf{e}_1\}\,, && \mathcal{T}_3 = \{\mathbf{e}_1 + \mathbf{e}_2, -\mathbf{e}_2\}\,, \\ &\mathcal{T}_{12} = \{\mathbf{e}_2, -\mathbf{e}_1\}\,, && \mathcal{T}_{13} = \{\mathbf{e}_1, \mathbf{e}_2\}\,, && \mathcal{T}_{23} = \{(1/2)(\mathbf{e}_1 - \mathbf{e}_2), \mathbf{e}_1 + \mathbf{e}_2\}\,, \\ &\mathcal{T}_{123} = \{\mathbf{e}_1, \mathbf{e}_2\}\,. \end{aligned} \tag{6.37}$$

Theorem 6.2 (Linear independence)
The tensor product of the template with an H^1-conforming polynomial basis U^p yields a unisolvent Nédélec element of the second type

$$\mathcal{N}_{II}^p = \left\{ \bigoplus_{i=1}^{3} \mathcal{V}_i^p \otimes \mathcal{T}_i \right\} \oplus \left\{ \bigoplus_{j \in \mathcal{J}} \mathcal{E}_j^p \otimes \mathcal{T}_j \right\} \oplus \{\mathcal{C}_{123}^p \otimes \mathcal{T}_{123}\}\,, \qquad \mathcal{J} = \{(1,2), (1,3), (2,3)\}\,, \tag{6.38}$$

where $\mathcal{V}_i^p$ are the sets of the vertex base functions, $\mathcal{E}_j^p$ are the sets of edge base functions, $\mathcal{C}_{123}^p$ is the set of cell base functions, and the $\oplus$ indicates summation over non-overlapping spaces.

Proof. Under the assertion that the underlying H^1-conforming polynomial basis U^p is unisolvent, unisolvence of the $\mathcal{N}_{II}^p$ basis follows automatically, since each base function of U^p is multiplied with two linearly independent vectors, thus inheriting linear independence of the basis on the vectorial level. Further, the resulting basis has the required dimensionality

$$\dim[U^p(\Gamma)]^2 = \dim[P^p(\Gamma)]^2 = \dim \mathcal{N}_{II}^p(\Gamma)\,, \tag{6.39}$$

of the Nédélec finite element space. □

Theorem 6.3 ($H(\mathrm{div}\boldsymbol{R}, A)$-conformity)
The constructed element on the reference domain is conforming under covariant Piola transformations of the base functions and contravariant Piola transformations of their respective curls.

Proof. By construction, the tangential projection of each non-cell base function on the tangential vector of its respective polytope is the underlying H^1-conforming base function

$$\langle \boldsymbol{\tau}, \boldsymbol{\vartheta}_i \rangle = n_i \, . \tag{6.40}$$

Since the templates are constructed by permutations of the reference element, this characteristic is extended to every corresponding polytope. Lastly, the respective Piola transformations uphold the tangential and normal projections in the physical domain, such that conformity is guaranteed by the underlying U^p-space. □

Using the Bézier basis one finds the following base functions, which inherit the optimal complexity of the Bernstein basis.

Definition 6.7 (Bézier-Nédélec II triangle basis)
The following base functions are defined on the reference triangle.

- *On the edges the base function reads*

$$\begin{aligned}
e_{12}: \quad & \boldsymbol{\vartheta}(\xi,\eta) = b^p_{00}\mathbf{e}_2 \, , && \boldsymbol{\vartheta}(\xi,\eta) = b^p_{0p}(\mathbf{e}_1+\mathbf{e}_2) \, , \\
& \boldsymbol{\vartheta}(\xi,\eta) = b^p_{0j}\mathbf{e}_2 \, , \quad 0<j<p \, , \\
e_{13}: \quad & \boldsymbol{\vartheta}(\xi,\eta) = b^p_{00}\mathbf{e}_1 \, , && \boldsymbol{\vartheta}(\xi,\eta) = b^p_{p0}(\mathbf{e}_1+\mathbf{e}_2) \, , \\
& \boldsymbol{\vartheta}(\xi,\eta) = b^p_{i0}\mathbf{e}_1 \, , \quad 0<i<p \, , \\
e_{23}: \quad & \boldsymbol{\vartheta}(\xi,\eta) = b^p_{0p}\mathbf{e}_1 \, , && \boldsymbol{\vartheta}(\xi,\eta) = -b^p_{p0}\mathbf{e}_2 \, , \\
& \boldsymbol{\vartheta}(\xi,\eta) = (1/2)\, b^p_{i,p-i}(\mathbf{e}_1-\mathbf{e}_2) \, , \quad 0<i<p \, ,
\end{aligned} \tag{6.41}$$

  where the first two base functions for each edge are the vertex-edge base functions and the third equation generates pure edge base functions.

- *The cell base functions read*

$$\begin{aligned}
c_{123}: \quad & \boldsymbol{\vartheta}(\xi,\eta) = -b^p_{0j}\mathbf{e}_1 \, , && 0<j<p \, , \\
& \boldsymbol{\vartheta}(\xi,\eta) = b^p_{i0}\mathbf{e}_2 \, , && 0<i<p \, , \\
& \boldsymbol{\vartheta}(\xi,\eta) = b^p_{i,p-i}(\mathbf{e}_1+\mathbf{e}_2) \, , && 0<i<p \, , \\
& \boldsymbol{\vartheta}(\xi,\eta) = b^p_{ij}\mathbf{e}_2 \, , && 0<i<p \, , \quad 0<j<p-i \, , \\
& \boldsymbol{\vartheta}(\xi,\eta) = b^p_{ij}\mathbf{e}_1 \, , && 0<i<p \, , \quad 0<j<p-i \, ,
\end{aligned} \tag{6.42}$$

  where the first three are the respective edge-cell base functions. The remaining two are pure cell base functions.

A depiction of each of the polytopal base function for the cubic Bézier-Nédélec element is given in Fig. 6.8.

Remark 6.4
The Brezzi-Douglas-Marini element for $H(\mathrm{div}, A)$-conforming subspaces can be constructed in a similar manner or by rotating the current template by 90 degrees and adjusting the normal projections to one.

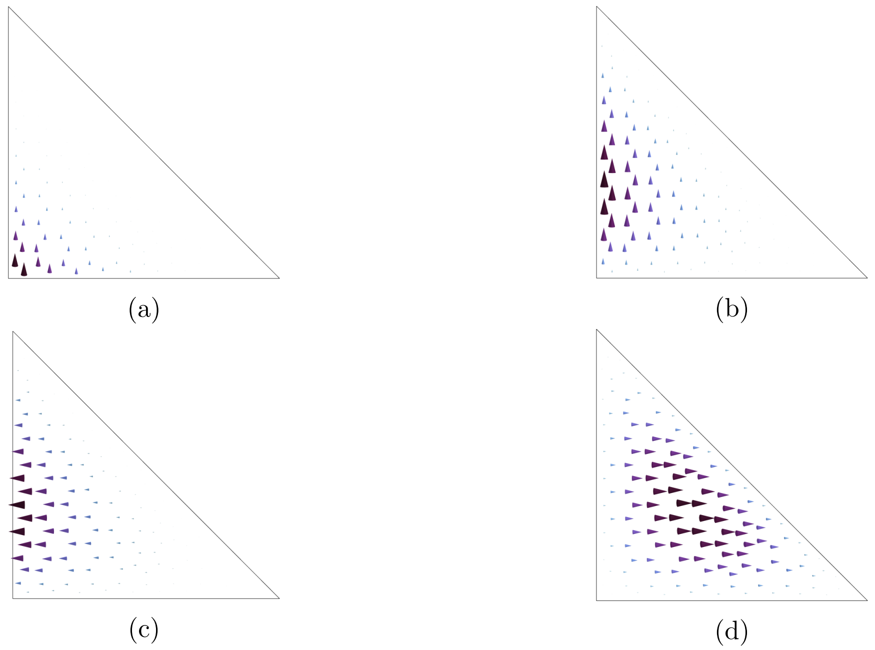

Figure 6.8: Cubic vertex-edge (a), edge (b), edge-cell (c) and pure cell (d) base functions of the Nédélec element of the second type on the reference triangle.

6.2.3 Nédélec elements of the first type

The Nédélec element of the second type has the disadvantage that its curl is a polynomial space of a lower degree $\operatorname{div}(\boldsymbol{R}\mathcal{N}_{II}^{p}) = P^{p-1}$. Consequently, one loses one order of convergence in the curl terms. In order to ameliorate the convergence rate one can employ the Nédélec elements of the first type, which enhance the polynomial space with base functions orthogonal to the kernel $\boldsymbol{\vartheta}_i \in \ker^{\perp}(\operatorname{div}\boldsymbol{R})$. This is not easy to do, as one must be able to split the space between kernel functions and non-kernel functions while maintaining conformity. Here we follow the ideas presented in [3,5,96,110], where one explicitly applies the operators in the exact polynomial sequences to construct the kernel of the next space. In this work, we complement the kernel space with our new approach and introduce a specific and intuitive polytopal template leading to non-kernel base functions.

We start with the kernel of $\mathcal{N}_I^p$ by taking gradients of the base functions of the U^{p+1} space while excluding the vertex base functions

$$\boldsymbol{\vartheta}_i(\xi,\eta) = \nabla_\xi n_i^{p+1} \, . \tag{6.43}$$

This yields $(p+2)(p+1)/2-3$ base functions. We augment the space by adding the lowest order Nédélec ($\mathcal{N}_I^0$) base functions of the first type from Eq. (5.55). Next we need to enhance the space with a minimal amount of base functions belonging to a higher degree polynomial space such that we find $\dim[\operatorname{div}(\boldsymbol{R}\mathcal{N}_I^p)] = \dim P^p = (p+2)(p+1)/2$ base functions and the curl spans the next polynomial space in the sequence. In order to do so we introduce the polytopal template

$$\mathcal{T} = \{\mathcal{T}_1, \mathcal{T}_2, \mathcal{T}_{12}, \mathcal{T}_{13}, \mathcal{T}_{23}, \mathcal{T}_{123}\} \, , \tag{6.44}$$

where the polytopal sets are derived from the lowest order Nédélec base functions of the first type in

Eq. (5.55)

$$\begin{aligned}
&\mathcal{T}_1 = \{\boldsymbol{\vartheta}_3^I\}\,, && \mathcal{T}_2 = \{\boldsymbol{\vartheta}_2^I\}\,, && \mathcal{T}_{12} = \{\boldsymbol{\vartheta}_3^I - \boldsymbol{\vartheta}_2^I\}\,, \\
&\mathcal{T}_{13} = \{\boldsymbol{\vartheta}_1^I + \boldsymbol{\vartheta}_3^I\}\,, && \mathcal{T}_{23} = \{\boldsymbol{\vartheta}_1^I - \boldsymbol{\vartheta}_2^I\}\,, && \mathcal{T}_{123} = \{\boldsymbol{\vartheta}_1^I - \boldsymbol{\vartheta}_2^I + \boldsymbol{\vartheta}_3^I\}\,. \qquad (6.45)
\end{aligned}$$

From the depiction in Fig. 6.9 it is intuitively apparent, that the template vectors represent the components needed to generate rotational flux. The remaining base functions are given by the tensor product

$$\left\{\bigoplus_{i=1}^{2} \mathcal{V}_i^p \otimes \mathcal{T}_i\right\} \oplus \left\{\bigoplus_{j\in\mathcal{J}} \mathcal{E}_j^p \otimes \mathcal{T}_j\right\} \oplus \{\mathcal{C}_{123}^p \otimes \mathcal{T}_{123}\}\,, \qquad \mathcal{J} = \{(1,2),(1,3),(2,3)\}\,. \qquad (6.46)$$

This generates exactly $2p + (p-1)p/2$ base functions. Adding the constants from $\dim[\operatorname{div}(\boldsymbol{R}\mathcal{N}_I^0)] = 1$ satisfies the dimensionality of the polynomial space $2p + (p-1)p/2 + 1 = (p+2)(p+1)/2 = \dim P^p$. Further, since $\boldsymbol{\vartheta}_i$ belongs to $[P^0]^2 \oplus \boldsymbol{R}\widetilde{P}^0\boldsymbol{\xi}$ the resulting base functions $n_i^p\boldsymbol{\vartheta}_i$ clearly belongs to $[P^p]^2 \oplus \boldsymbol{R}\widetilde{P}^p\boldsymbol{\xi}$. The complete Nédélec space reads

$$\begin{aligned}
\mathcal{N}_I^p = \mathcal{N}_I^0 &\oplus \left\{\bigoplus_{j\in\mathcal{J}} \nabla\mathcal{E}_j^{p+1}\right\} \oplus \nabla\mathcal{C}_{123}^{p+1} \oplus \left\{\bigoplus_{i=1}^{2} \mathcal{V}_i^p \otimes \mathcal{T}_i\right\} \oplus \left\{\bigoplus_{j\in\mathcal{J}} \mathcal{E}_j^p \otimes \mathcal{T}_j\right\} \oplus \{\mathcal{C}_{123}^p \otimes \mathcal{T}_{123}\}\,, \\
\mathcal{J} &= \{(1,2),(1,3),(2,3)\}\,. \qquad (6.47)
\end{aligned}$$

Theorem 6.4 (Linear independence)
The set of base functions given by the lowest order Nédélec elements, the gradients of an H^1-conforming polynomial subspace U^{p+1} excluding vertex base functions, and the tensor product of the U^p base functions with the polytopal template yield a linearly independent polynomial basis for $\mathcal{N}_I^p$.

Proof. We start by showing the gradients of the U^p base functions are linearly independent of each other by using contradiction. Assume the set of gradients is linearly dependent, then there holds

$$\sum_i c_i \nabla_\xi n_i = \nabla_\xi \sum_i c_i n_i = 0\,, \qquad (6.48)$$

for some combination of constants c_i where not all c_i values are zero. However, the vertex base functions are not employed. Thus, if the basis satisfies the partition of unity property, then the kernel of the gradient operator, namely constants $\mathbb{R}$, is missing and the exact sequence property yields a contradiction (see Fig. 4.2). The same holds true for a hierarchical polynomial basis, since the vertex base functions are used to capture constants.

The base functions of the lowest order Nédélec elements of the first type are linearly independent of the gradients since their tangential traces on the edges of the triangle are constant $\operatorname{tr}^{\mathrm{t}}_{\partial\mathrm{A}}\,\boldsymbol{\vartheta}_i|_{\mu_i} \in \mathbb{R}$, whereas the tangential traces of the edge gradients are at least linear and the tangential traces of the cell gradients vanish on the entire boundary. Together, the three lowest order base functions span the constant space $[P^0]^2 = \mathbb{R}^2$. Further, their curls span the constant space $\mathbb{R}$.

In order to complete the proof we must show that the remaining base functions are non-gradients and linearly independent of the lowest order base functions. Observe that the template vectors have the general form

$$\boldsymbol{\vartheta}^I = \begin{bmatrix} c_1\eta - c_2 \\ c_3 - c_1\xi \end{bmatrix}\,, \qquad c_1 \in \{1,2,3\}\,, \qquad c_2, c_3 \in \{0,1\}\,, \qquad (6.49)$$

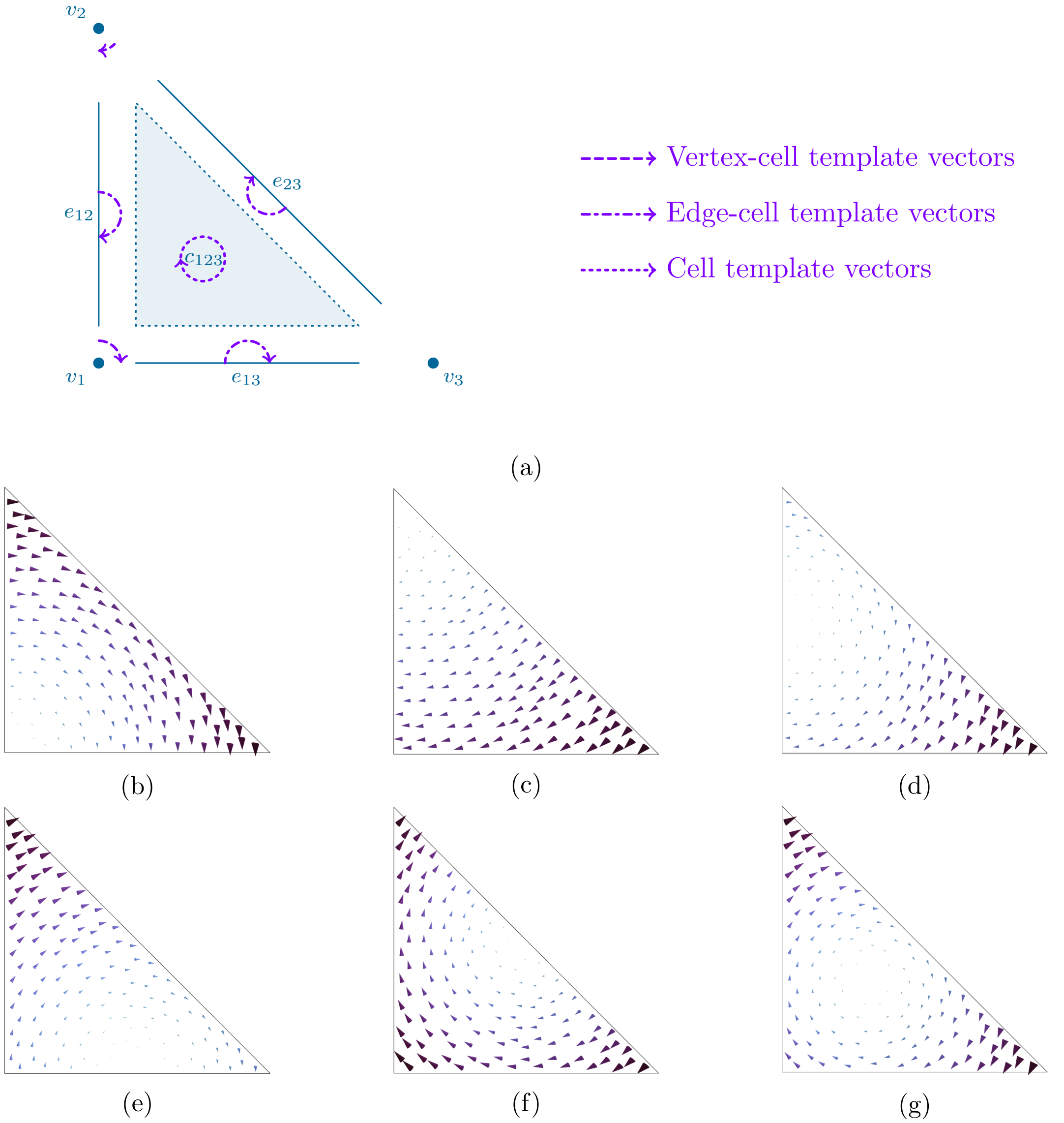

(a)

(b) (c) (d)

(e) (f) (g)

Figure 6.9: Template vectors on the reference triangle for base functions orthogonal to the kernel of the curl operator (a). Templates of the vertices (b)-(c), followed by the templates of the edges (d)-(f) and lastly, the cell template (g).

such that the curl of the base function reads

$$\operatorname{div}_\xi(\boldsymbol{R} n \boldsymbol{\vartheta}^I) = \langle \nabla_\xi n ,\, \boldsymbol{R}\boldsymbol{\vartheta}^I \rangle - 2c_1 n = (c_3 - c_1\xi) n_{,\xi} + (c_2 - c_1\eta) n_{,\eta} - 2c_1 n \, . \tag{6.50}$$

Clearly, the polynomial order of the underlying scalar base function n is maintained under the curl operator. Therefore, under the assumption of a hierarchical basis in the base functions n_i (for example Legendre) it is clear that the curl operator maps to linearly independent base functions, irrespective of the choice of c_1, c_2 and c_3. Consequently, the template yields non-gradient base functions due to the exact sequence in Fig. 4.1 and

$$\operatorname{div}_\xi(\boldsymbol{R}[c_1 \boldsymbol{R}\boldsymbol{\xi} + \mathbf{c}] P^p(\Gamma)) = P^p(\Gamma) \, , \qquad \mathbf{c} = \begin{bmatrix} -c_2 \\ c_3 \end{bmatrix} \, , \tag{6.51}$$

such that

$$\operatorname{div}_\xi(\boldsymbol{R} \sum_{i=0}^{p} c_i n_i \boldsymbol{\vartheta}^I) = 0 \quad \iff \quad c_i = 0 \quad \forall \, i \in \{0, 1, ..., p\} \, . \tag{6.52}$$

Further, we can switch the base functions with any other basis that spans the same polynomial space since it is in fact equivalent to an alternative expression of the hierarchical basis. Doing so clearly maintains the linear independence of the vectorial base functions due to the inherited linear independence from the underlying scalar basis. The latter can be easily observed when considering the normal-traces of the vectorial base functions on the edges. If the complete span of n_i is employed, then the constant element is present and the curl maps also to the space of constants $\mathbb{R}$. However, this space is already obtained by employing the $\mathcal{N}_I^0$-basis in the construction and as such, leads to linear dependence. By removing the last vertex base function the hierarchical basis no longer contains the space of constants, thus asserting linear independence of the total construction. The same holds true for any other basis that satisfies the partition of unity property since removing one base function cancels this characteristic and removes the constant element from the space. The latter in conjunction with the vanishing trace on the edges of the element asserts linear independence from the lowest order base functions. $\square$

Theorem 6.5 ($H(\operatorname{div}\boldsymbol{R}, A)$-conformity)
The resulting finite element is $H(\operatorname{div}\boldsymbol{R})$*-conforming under Piola mappings.*

Proof. The lowest order Nédélec base functions are $H(\operatorname{div}\boldsymbol{R})$-conforming by their degrees of freedom. The gradient base functions are conforming due to the exact sequence property $\nabla H^1 \subset H(\operatorname{div}\boldsymbol{R})$, see Fig. 4.1. Lastly, the remaining base functions are cell-type and do not affect the conformity of the finite element.

The Piola transformations maintain the conformity of the base functions across the mapping from the reference to the physical element. $\square$

Applying the construction to the Bézier basis yields the following base functions.

Definition 6.8 (Bézier-Nédélec I triangle basis)
We define the base functions on the reference triangle.

- *On the edges we employ the lowest order Nédélec base functions and the edge gradients*

$$\begin{aligned}
e_{12}: \quad & \boldsymbol{\vartheta}(\xi,\eta) = \boldsymbol{\vartheta}_1^I\,, && \\
& \boldsymbol{\vartheta}(\xi,\eta) = \nabla_\xi b_{0j}^{p+1}\,, && 0 < j < p+1\,, \\
e_{13}: \quad & \boldsymbol{\vartheta}(\xi,\eta) = \boldsymbol{\vartheta}_2^I\,, && \\
& \boldsymbol{\vartheta}(\xi,\eta) = \nabla_\xi b_{i0}^{p+1}\,, && 0 < i < p+1\,, \\
e_{23}: \quad & \boldsymbol{\vartheta}(\xi,\eta) = \boldsymbol{\vartheta}_3^I\,, && \\
& \boldsymbol{\vartheta}(\xi,\eta) = \nabla_\xi b_{i,p+1-i}^{p+1}\,, && 0 < i < p+1\,.
\end{aligned} \tag{6.53}$$

- *The cell functions read*

$$\begin{aligned}
c_{123}: \quad & \boldsymbol{\vartheta}(\xi,\eta) = b_{00}^{p}\boldsymbol{\vartheta}_3^I\,, && \\
& \boldsymbol{\vartheta}(\xi,\eta) = b_{0p}^{p}\boldsymbol{\vartheta}_2^I\,, && \\
& \boldsymbol{\vartheta}(\xi,\eta) = b_{0j}^{p}(\boldsymbol{\vartheta}_3^I - \boldsymbol{\vartheta}_2^I)\,, && 0 < j < p\,, \\
& \boldsymbol{\vartheta}(\xi,\eta) = b_{i0}^{p}(\boldsymbol{\vartheta}_1^I + \boldsymbol{\vartheta}_3^I)\,, && 0 < i < p\,, \\
& \boldsymbol{\vartheta}(\xi,\eta) = b_{i,p-i}^{p}(\boldsymbol{\vartheta}_1^I - \boldsymbol{\vartheta}_2^I)\,, && 0 < i < p\,, \\
& \boldsymbol{\vartheta}(\xi,\eta) = b_{ij}^{p}(\boldsymbol{\vartheta}_1^I - \boldsymbol{\vartheta}_2^I + \boldsymbol{\vartheta}_3^I)\,, && 0 < i < p\,, \quad 0 < j < p-i\,, \\
& \boldsymbol{\vartheta}(\xi,\eta) = \nabla_\xi b_{ij}^{p+1}\,, && 0 < i < p+1\,, \quad 0 < j < p+1-i\,,
\end{aligned} \tag{6.54}$$

where the last formula gives the cell gradients and the remaining base functions are non-gradients.

A depiction of the higher order base functions is given in Fig. 6.10. Visualizations of the lowest order base functions are available in Fig. 5.8.

6.3 Higher order tetrahedral elements

6.3.1 Bézier elements

Analogously to triangle elements, the Bézier tetrahedra on the unit tetrahedron $\Omega = \{\xi,\eta,\zeta \in [0,1] \mid \xi+\eta+\zeta \leq 1\}$ are defined using the barycentric coordinates by expanding the coefficients of

$$(\lambda_1+\lambda_2+\lambda_3+\lambda_4)^p = ([1-\xi-\eta-\zeta]+\zeta+\eta+\xi)^p = 1\,, \tag{6.55}$$

into

$$b_{ijk}^p(\lambda_1,\lambda_2,\lambda_3,\lambda_4) = \binom{p}{i}\binom{p-i}{j}\binom{p-i-j}{k}\lambda_1^{p-i-j-k}\lambda_2^k\lambda_3^j\lambda_4^k\,, \tag{6.56}$$

with the equivalent form

$$b_{ijk}^p(\xi,\eta,\zeta) = \binom{p}{i}\binom{p-i}{j}\binom{p-i-j}{k}(1-\xi-\eta-\zeta)^{p-i-j-k}\zeta^k\eta^j\xi^i\,. \tag{6.57}$$

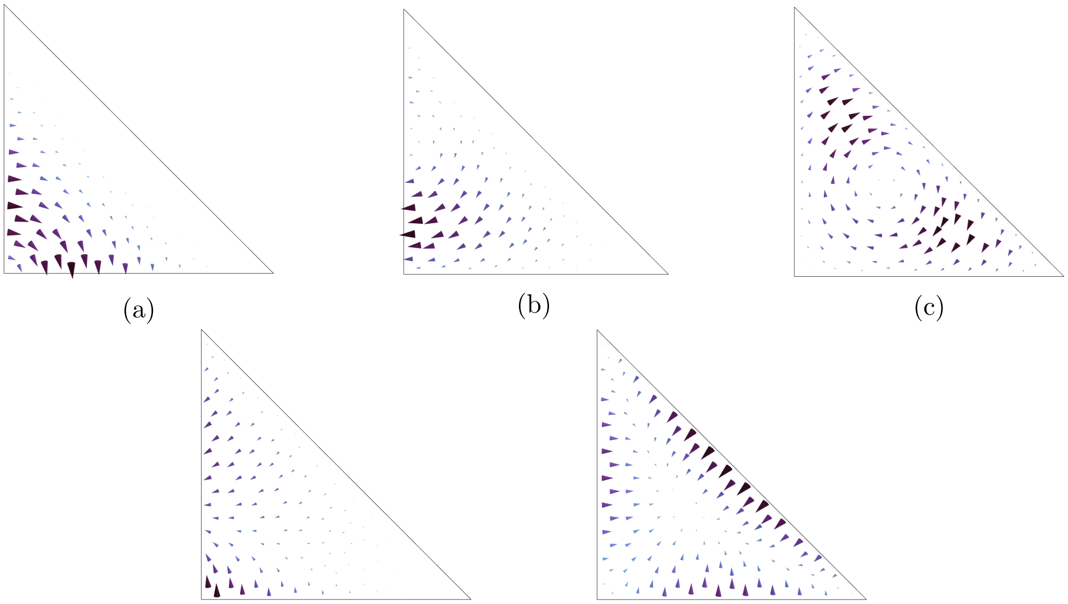
(a) (b) (c) (d) (e)

Figure 6.10: Non-gradient vertex-cell (a), edge-cell (b) and pure cell (c) base functions of the cubic Bézier basis. Gradient edge (d) and cell (e) base functions.

We construct the Duffy transformation by mapping of the unit tetrahedron as a collapsed hexahedron

$$\boldsymbol{\xi} : [0,1]^3 \to \Omega \,, \qquad \{\alpha, \beta, \gamma\} \mapsto \{\xi, \eta, \zeta\} \,, \tag{6.58}$$

using the relations

$$\begin{aligned} \xi &= \alpha \,, & \eta &= (1-\alpha)\beta \,, & \zeta &= (1-\alpha)(1-\beta)\gamma \,, \\ \alpha &= \xi \,, & \beta &= \frac{\eta}{1-\xi} \,, & \gamma &= \frac{\zeta}{1-\xi-\eta} \,, \end{aligned} \tag{6.59}$$

as depicted in Fig. 6.11. Applying the Duffy transformation to Bézier tetrahedra

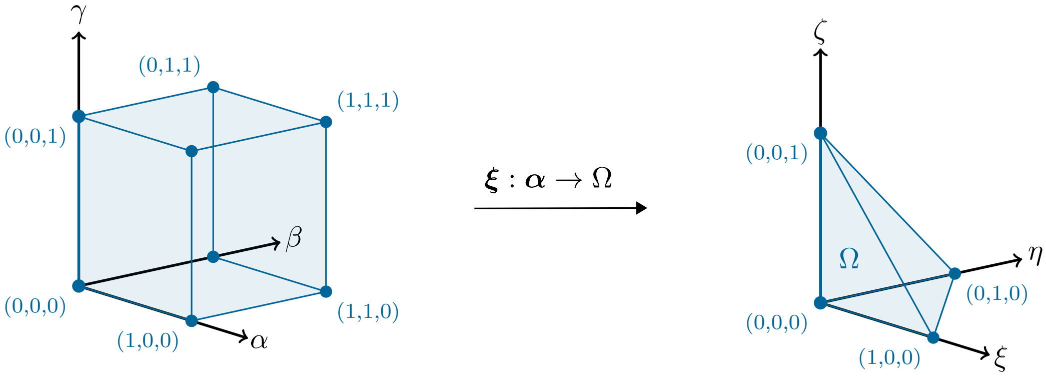

Figure 6.11: Duffy mapping of the unit hexahedron to the unit tetrahedron.

$$\begin{aligned}
b^p_{ijk}(\xi,\eta,\zeta) &= \binom{p}{i}\binom{p-i}{j}\binom{p-i-j}{k}(1-\xi-\eta-\zeta)^{p-i-j-k}\zeta^k\eta^j\xi^i \\
&= \binom{p}{i}\binom{p-i}{j}\binom{p-i-j}{k}(1-\alpha-(1-\alpha)\beta-(1-\alpha)(1-\beta)\gamma)^{p-i-j-k} \\
&\quad \cdot (1-\alpha)^k(1-\beta)^k\gamma^k(1-\alpha)^j\beta^j\alpha^i \\
&= \binom{p}{i}\binom{p-i}{j}\binom{p-i-j}{k}(1-\alpha)^{p-i-j-k}(1-\beta)^{p-i-j-k}(1-\gamma)^{p-i-j-k} \\
&\quad \cdot (1-\alpha)^k(1-\beta)^k\gamma^k(1-\alpha)^j\beta^j\alpha^i \\
&= \binom{p}{i}(1-\alpha)^{p-i}\alpha^i\binom{p-i}{j}(1-\beta)^{p-i-j}\beta^j\binom{p-i-j}{k}(1-\gamma)^{p-i-j-k}\gamma^k \\
&= b^p_i(\alpha)b^{p-i}_j(\beta)b^{p-i-j}_k(\gamma)\,, \qquad (6.60)
\end{aligned}$$

leads to an intrinsic factorization via Bernstein base functions, which allow for fast evaluations using sum factorization [2]. Further, since the pair $b^{p-i}_j(\beta)b^{p-i-j}_k(\gamma)$ spans a Bézier triangle, it is clear that the multiplication with $b^p_i(\alpha)$ interpolates between said triangle and a point in space, effectively spanning a tetrahedron. In order to compute gradients the chain rule is employed with respect to the Duffy transformation

$$\nabla_\xi b^p_{ijk} = (\mathrm{D}_\alpha\boldsymbol{\xi})^{-T}\nabla_\alpha b^p_{ijk}\,, \qquad \mathrm{D}_\alpha\boldsymbol{\xi} = \begin{bmatrix} 1 & 0 & 0 \\ -\beta & 1-\alpha & 0 \\ (\beta-1)\gamma & (\alpha-1)\gamma & (1-\alpha)(1-\beta)\end{bmatrix}\,,$$

$$(\mathrm{D}_\alpha\boldsymbol{\xi})^{-T} = \frac{1}{(1-\alpha)(1-\beta)}\begin{bmatrix}(1-\alpha)(1-\beta) & (1-\beta)\beta & \gamma \\ 0 & 1-\beta & \gamma \\ 0 & 0 & 1\end{bmatrix}\,. \qquad (6.61)$$

We use dual numbers to compute the derivative of each Bernstein base function and construct the $\boldsymbol{\alpha}$-gradient

$$\nabla_\alpha b^p_{ijk}(\alpha,\beta,\gamma) = \begin{bmatrix} b^{p-i}_j b^{p-i-j}_k \dfrac{\mathrm{d}}{\mathrm{d}\alpha} b^p_i \\ b^p_i b^{p-i-j}_k \dfrac{\mathrm{d}}{\mathrm{d}\beta} b^{p-i}_j \\ b^p_i b^{p-i}_j \dfrac{\mathrm{d}}{\mathrm{d}\gamma} b^{p-i-j}_k \end{bmatrix}\,. \qquad (6.62)$$

The Duffy transformation results in the optimal order of traversal of the base functions depicted in Fig. 6.12. Note that the traversal order agrees with the definitions introduced in Section 5.5.2 and each oriented face has the same order of traversal as the triangle Fig. 6.5. We relate the base functions to their respective polytopes using the index triplets.

Observation 6.2 (Tetrahedron base functions)
The polytope of each base function $b^p_{ijk}(\xi,\eta,\zeta)$ is determined as follows.

- *The indices $(0,0,0),(0,0,p),(0,p,0)$ and $(p,0,0)$ represent the respective vertex base functions.*
- *The first edge is associated with the triplet $(0,0,k)$ where $0<k<p$, the second with $(0,j,0)$ where $0<j<p$ and the third with $(i,0,0)$ where $0<i<p$. The slated edges are given by $(0,j,p-j)$ with $0<j<p$, $(i,0,p-i)$ with $0<i<p$ and $(i,p-i,0)$ with $0<i<p$, respectively.*

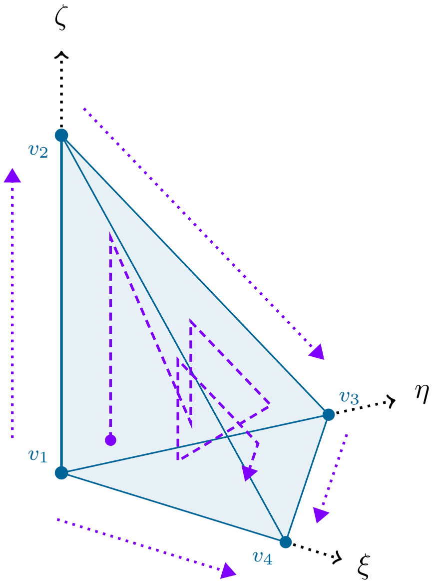

Figure 6.12: Order of traversal of tetrahedral Bézier base functions on the unit tetrahedron. The traversal order on each face agrees with an orientation of the vertices $f_{ijk} = \{v_i, v_j, v_k\}$ such that $i < j < k$. The traversal order on each edge is from the lower index vertex to the higher index vertex.

- *The base functions of the first face are given by* $(0, j, k)$ *with* $0 < j < p$ *and* $0 < k < p - j$. *The second face is associated with the base functions given by the triplets* $(i, 0, k)$ *with* $0 < i < p$ *and* $0 < k < p - i$. *The base functions of the third face are related to the indices* $(i, j, 0)$ *with* $0 < i < p$ *and* $0 < j < p - i$. *Lastly, the base functions of the slated face are given by* $(i, j, p - i - j)$ *with* $0 < i < p$ *and* $0 < j < p - i$.
- *The remaining indices correspond to the cell base functions.*

The Bézier base functions are depicted in Fig. 6.13 on their respective polytopes.

6.3.2 Nédélec elements of the second type

We proceed analogously to the definition of the Nédélec element of the second type for triangles by constructing a polytopal template on the unit tetrahedron. The template is then used in conjunction with an H^1-conforming polynomial basis to span the $\mathcal{N}_{II}$-space on the unit tetrahedron.

We define the vertex-edge tangent vector $\mathbf{e}_3$ for v_1-e_{12} such that its tangential projection is one on e_{12} and zero on all other neighbouring edges. The same vector is the tangent vector associated with edge e_{12}. Next we define the edge-face vector $-\mathbf{e}_2$ for the edge e_{12} and face f_{123}. On the face f_{123} we employ the base vectors $\mathbf{e}_3$ and $\mathbf{e}_2$ which span the plane on the face. Lastly, we employ the full set of the Cartesian base vectors for the cell, namely $\mathbf{e}_3$, $\mathbf{e}_2$ and $\mathbf{e}_1$. The template vectors of the remaining polytopes are derived by covariant Piola transformations of the unit tetrahedron c_{1234} to equivalent permutations c_{ijkl} and adjusting the sign of the vector to ensure a positive projection on the tangent vector, compare with Fig. 6.6. The resulting template is given by the sum of the following polytopal

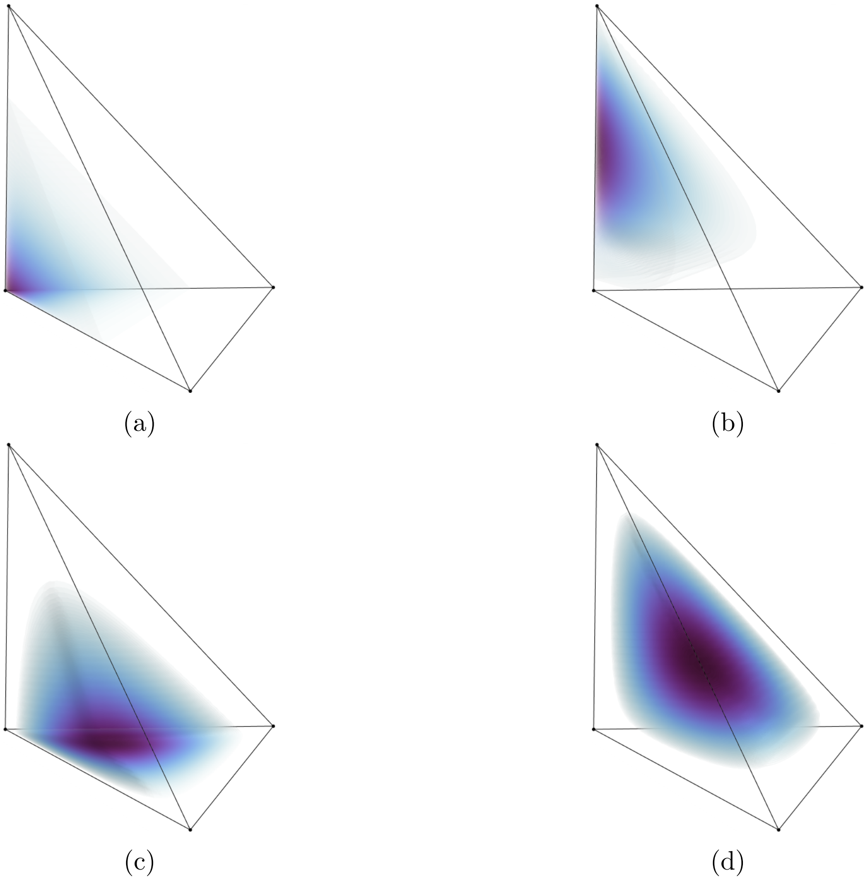
(a)

(b)

(c)

(d)

Figure 6.13: Quartic Bézier vertex (a), edge (b), face (c), and cell (c) base functions on the reference tetrahedron.

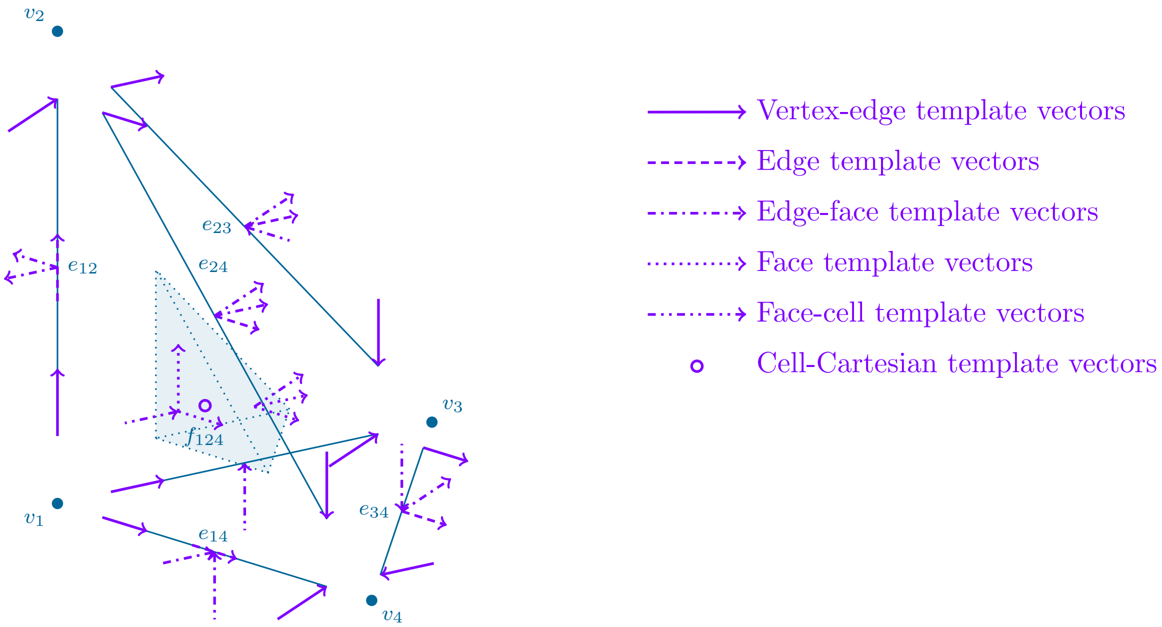

Figure 6.14: Template vectors for the reference tetrahedron on their corresponding polytopes. Only vectors on the visible sides of the tetrahedron are depicted.

sets depicted in Fig. 6.14

$$\begin{aligned}
&\mathcal{T}_1 = \{\mathbf{e}_3, \mathbf{e}_2, \mathbf{e}_1\}\,, && \mathcal{T}_2 = \{\mathbf{e}_1 + \mathbf{e}_2 + \mathbf{e}_3, \mathbf{e}_2, \mathbf{e}_1\}\,, && \mathcal{T}_3 = \{\mathbf{e}_1 + \mathbf{e}_2 + \mathbf{e}_3, -\mathbf{e}_3, \mathbf{e}_1\}\,, \\
&\mathcal{T}_4 = \{\mathbf{e}_1 + \mathbf{e}_2 + \mathbf{e}_3, -\mathbf{e}_3, -\mathbf{e}_2\}\,, && \mathcal{T}_{12} = \{\mathbf{e}_3, -\mathbf{e}_2, -\mathbf{e}_1\}\,, && \mathcal{T}_{13} = \{\mathbf{e}_2, \mathbf{e}_3, -\mathbf{e}_1\}\,, \\
&\mathcal{T}_{14} = \{\mathbf{e}_1, \mathbf{e}_3, \mathbf{e}_2\}\,, && \mathcal{T}_{23} = \{\mathbf{e}_2, \mathbf{e}_1 + \mathbf{e}_2 + \mathbf{e}_3, -\mathbf{e}_1\}\,, && \mathcal{T}_{24} = \{\mathbf{e}_1, \mathbf{e}_1 + \mathbf{e}_2 + \mathbf{e}_3, \mathbf{e}_2\}\,, \\
&\mathcal{T}_{34} = \{\mathbf{e}_1, \mathbf{e}_1 + \mathbf{e}_2 + \mathbf{e}_3, -\mathbf{e}_3\}\,, && \mathcal{T}_{123} = \{\mathbf{e}_3, \mathbf{e}_2, -\mathbf{e}_1\}\,, && \mathcal{T}_{124} = \{\mathbf{e}_3, \mathbf{e}_1, \mathbf{e}_2\}\,, \\
&\mathcal{T}_{134} = \{\mathbf{e}_2, \mathbf{e}_1, -\mathbf{e}_3\}\,, && \mathcal{T}_{234} = \{\mathbf{e}_2, \mathbf{e}_1, \mathbf{e}_1 + \mathbf{e}_2 + \mathbf{e}_3\}\,, && \mathcal{T}_{1234} = \{\mathbf{e}_3, \mathbf{e}_2, \mathbf{e}_1\}\,,
\end{aligned} \tag{6.63}$$

and reads

$$\mathcal{T} = \{\mathcal{T}_1, \mathcal{T}_2, \mathcal{T}_3, \mathcal{T}_4, \mathcal{T}_{12}, \mathcal{T}_{13}, \mathcal{T}_{14}, \mathcal{T}_{23}, \mathcal{T}_{24}, \mathcal{T}_{34}, \mathcal{T}_{123}, \mathcal{T}_{124}, \mathcal{T}_{134}, \mathcal{T}_{234}, \mathcal{T}_{1234}\}\,. \tag{6.64}$$

Theorem 6.6 (Linear independence)
Let U^p be an H^1-conforming basis on the unit tetrahedron, then its tensor product with the polytopal template yields a unisolvent Nédélec element of the second type

$$\begin{aligned}
&\mathcal{N}_{II}^p = \left\{\bigoplus_{i=1}^{4} \mathcal{V}_i^p \otimes \mathcal{T}_i\right\} \oplus \left\{\bigoplus_{j\in\mathcal{J}} \mathcal{E}_j^p \otimes \mathcal{T}_j\right\} \oplus \left\{\bigoplus_{k\in\mathcal{K}} \mathcal{F}_k^p \otimes \mathcal{T}_k\right\} \oplus \{\mathcal{C}_{1234}^p \otimes \mathcal{T}_{1234}\}\,, \\
&\mathcal{J} = \{(1,2),(1,3),(1,4),(2,3),(2,4),(3,4)\}\,, \qquad \mathcal{K} = \{(1,2,3),(1,2,4),(1,3,4),(2,3,4)\}\,,
\end{aligned} \tag{6.65}$$

where $\mathcal{V}_i^p$ are the sets of vertex base functions, $\mathcal{E}_j^p$ are the sets of edge base functions, $\mathcal{F}_k^p$ are the sets of face base functions and $\mathcal{C}_{1234}^p$ is the set of cell base functions.

Proof. Linear independence of the vectorial base functions is inherited from the linear independence of the underlying H^1-conforming basis since each base function is multiplied with three linearly independent template vectors. Further, the dimension of the basis

$$\dim[U^p(\Omega)]^3 = \dim[P^p(\Omega)]^3 = \dim \mathcal{N}_{II}^p(\Omega)\,, \tag{6.66}$$

agrees with the dimension of the Nédélec element of the second type. ☐

Theorem 6.7 ($H(\mathrm{curl}, V)$-conformity)
Under the corresponding Piola transformations, the basis spans an $H(\mathrm{curl})$-conforming subspace.

Proof. The conformity of a grid composed solely of unit tetrahedrons is $H(\mathrm{curl})$-conforming due to the methodology used to construct the polytopal template, namely by an initial definition of a minimal set of template vectors and permutations of the unit tetrahedron. This is the case since the template reduces the interface condition from $[\![\mathrm{tr}^{\mathrm{t}}_{\partial \mathrm{V}}\, \mathbf{p}]\!] = 0$ to $[\![\mathrm{tr}_{\partial \mathrm{V}} \langle \mathbf{t}, \mathbf{p} \rangle]\!] = 0$ for the non-cell base functions, which is upheld by the underlying U^p-space. Conformity of a general grid is consequently achieved by employing consistent Piola transformations. ☐

We can now use the polytopal template to define the Bézier-Nédélec element of the second type for arbitrary powers while inheriting optimal complexity.

Definition 6.9 (Bézier-Nédélec II tetrahedral basis)
We define the base functions on the reference tetrahedron.

- *On the edges the base functions read*

$$
\begin{aligned}
&e_{12}: && \boldsymbol{\vartheta}(\xi,\eta,\zeta) = b^p_{000}\mathbf{e}_3\,, && \boldsymbol{\vartheta}(\xi,\eta,\zeta) = b^p_{00p}(\mathbf{e}_1+\mathbf{e}_2+\mathbf{e}_3)\,,\\
& && \boldsymbol{\vartheta}(\xi,\eta,\zeta) = b^p_{00k}\mathbf{e}_3\,, \quad 0<k<p\,, && \\
&e_{13}: && \boldsymbol{\vartheta}(\xi,\eta,\zeta) = b^p_{000}\mathbf{e}_2\,, && \boldsymbol{\vartheta}(\xi,\eta,\zeta) = b^p_{0p0}(\mathbf{e}_1+\mathbf{e}_2+\mathbf{e}_3)\,,\\
& && \boldsymbol{\vartheta}(\xi,\eta,\zeta) = b^p_{0j0}\mathbf{e}_2\,, \quad 0<j<p\,, && \\
&e_{14}: && \boldsymbol{\vartheta}(\xi,\eta,\zeta) = b^p_{000}\mathbf{e}_1\,, && \boldsymbol{\vartheta}(\xi,\eta,\zeta) = b^p_{p00}(\mathbf{e}_1+\mathbf{e}_2+\mathbf{e}_3)\,,\\
& && \boldsymbol{\vartheta}(\xi,\eta,\zeta) = b^p_{i00}\mathbf{e}_1\,, \quad 0<i<p\,, && \\
&e_{23}: && \boldsymbol{\vartheta}(\xi,\eta,\zeta) = b^p_{00p}\mathbf{e}_2\,, && \boldsymbol{\vartheta}(\xi,\eta,\zeta) = -b^p_{0p0}\mathbf{e}_3\,,\\
& && \boldsymbol{\vartheta}(\xi,\eta,\zeta) = b^p_{0j,p-j}\mathbf{e}_2\,, \quad 0<j<p\,, && \\
&e_{24}: && \boldsymbol{\vartheta}(\xi,\eta,\zeta) = b^p_{00p}\mathbf{e}_1\,, && \boldsymbol{\vartheta}(\xi,\eta,\zeta) = -b^p_{p00}\mathbf{e}_3\,,\\
& && \boldsymbol{\vartheta}(\xi,\eta,\zeta) = b^p_{i0,p-i}\mathbf{e}_1\,, \quad 0<i<p\,, && \\
&e_{34}: && \boldsymbol{\vartheta}(\xi,\eta,\zeta) = b^p_{0p0}\mathbf{e}_1\,, && \boldsymbol{\vartheta}(\xi,\eta,\zeta) = -b^p_{p00}\mathbf{e}_2\,,\\
& && \boldsymbol{\vartheta}(\xi,\eta,\zeta) = b^p_{i,p-i,0}\mathbf{e}_1\,, \quad 0<i<p\,, &&
\end{aligned}
\tag{6.67}
$$

  where the first two base functions on each edge are the vertex-edge base functions.

- *The face base functions are given by*

$$
\begin{aligned}
&f_{123}: && \boldsymbol{\vartheta}(\xi,\eta,\zeta) = -b^p_{00k}\mathbf{e}_2\,, && 0<k<p\,,\\
& && \boldsymbol{\vartheta}(\xi,\eta,\zeta) = b^p_{0j0}\mathbf{e}_3\,, && 0<j<p\,,\\
& && \boldsymbol{\vartheta}(\xi,\eta,\zeta) = b^p_{0j,p-j}(\mathbf{e}_1+\mathbf{e}_2+\mathbf{e}_3)\,, && 0<j<p\,,\\
& && \boldsymbol{\vartheta}(\xi,\eta,\zeta) = b^p_{0jk}\mathbf{e}_3\,, && 0<j<p\,, \quad 0<k<p-j\,,\\
& && \boldsymbol{\vartheta}(\xi,\eta,\zeta) = b^p_{0jk}\mathbf{e}_2\,, && 0<j<p\,, \quad 0<k<p-j\,,\\
&f_{124}: && \boldsymbol{\vartheta}(\xi,\eta,\zeta) = -b^p_{00k}\mathbf{e}_1\,, && 0<k<p\,,\\
& && \boldsymbol{\vartheta}(\xi,\eta,\zeta) = b^p_{i00}\mathbf{e}_3\,, && 0<i<p\,,\\
& && \boldsymbol{\vartheta}(\xi,\eta,\zeta) = b^p_{i0,p-i}(\mathbf{e}_1+\mathbf{e}_2+\mathbf{e}_3)\,, && 0<i<p\,,\\
& && \boldsymbol{\vartheta}(\xi,\eta,\zeta) = b^p_{i0k}\mathbf{e}_3\,, && 0<i<p\,, \quad 0<k<p-i\,,\\
& && \boldsymbol{\vartheta}(\xi,\eta,\zeta) = b^p_{i0k}\mathbf{e}_1\,, && 0<i<p\,, \quad 0<k<p-i\,,\\
&f_{134}: && \boldsymbol{\vartheta}(\xi,\eta,\zeta) = -b^p_{0j0}\mathbf{e}_1\,, && 0<j<p\,,\\
& && \boldsymbol{\vartheta}(\xi,\eta,\zeta) = b^p_{i00}\mathbf{e}_2\,, && 0<i<p\,,\\
& && \boldsymbol{\vartheta}(\xi,\eta,\zeta) = b^p_{i,p-i,0}(\mathbf{e}_1+\mathbf{e}_2+\mathbf{e}_3)\,, && 0<i<p\,,\\
& && \boldsymbol{\vartheta}(\xi,\eta,\zeta) = b^p_{ij0}\mathbf{e}_2\,, && 0<i<p\,, \quad 0<j<p-i\,,
\end{aligned}
$$

$$
\begin{aligned}
& && \boldsymbol{\vartheta}(\xi,\eta,\zeta) = b^p_{ij0}\mathbf{e}_1\,, && 0<i<p\,, \quad 0<j<p-i\,, \\
& f_{234}: && \boldsymbol{\vartheta}(\xi,\eta,\zeta) = -b^p_{0j,p-j}\mathbf{e}_1\,, && 0<j<p\,, \\
& && \boldsymbol{\vartheta}(\xi,\eta,\zeta) = b^p_{i0,p-i}\mathbf{e}_2\,, && 0<i<p\,, \\
& && \boldsymbol{\vartheta}(\xi,\eta,\zeta) = -b^p_{i,p-i,0}\mathbf{e}_3\,, && 0<i<p\,, \\
& && \boldsymbol{\vartheta}(\xi,\eta,\zeta) = b^p_{ij,p-i-j}\mathbf{e}_2\,, && 0<i<p\,, \quad 0<j<p-i\,, \\
& && \boldsymbol{\vartheta}(\xi,\eta,\zeta) = b^p_{ij,p-i-j}\mathbf{e}_1\,, && 0<i<p\,, \quad 0<j<p-i\,,
\end{aligned}
\tag{6.68}
$$

where the first three formulas for each face are the edge-face base functions.

- *Finally, the cell base functions read*

$$
\begin{aligned}
& c_{1234}: && \boldsymbol{\vartheta}(\xi,\eta,\zeta) = -b^p_{0jk}\mathbf{e}_1\,, && 0<j<p\,, \quad 0<k<p-j\,, \\
& && \boldsymbol{\vartheta}(\xi,\eta,\zeta) = b^p_{i0k}\mathbf{e}_2\,, && 0<i<p\,, \quad 0<k<p-i\,, \\
& && \boldsymbol{\vartheta}(\xi,\eta,\zeta) = -b^p_{ij0}\mathbf{e}_3\,, && 0<i<p\,, \quad 0<j<p-i\,, \\
& && \boldsymbol{\vartheta}(\xi,\eta,\zeta) = b^p_{ij,p-i-j}(\mathbf{e}_1+\mathbf{e}_2+\mathbf{e}_3)\,, && 0<i<p\,, \quad 0<j<p-i\,, \\
& && \boldsymbol{\vartheta}(\xi,\eta,\zeta) = b^p_{ijk}\mathbf{e}_3\,, && \begin{matrix} 0<i<p\,, \\ 0<j<p-i\,, \\ 0<k<p-i-j \end{matrix}\,, \\
& && \boldsymbol{\vartheta}(\xi,\eta,\zeta) = b^p_{ijk}\mathbf{e}_2\,, && \begin{matrix} 0<i<p\,, \\ 0<j<p-i\,, \\ 0<k<p-i-j \end{matrix}\,, \\
& && \boldsymbol{\vartheta}(\xi,\eta,\zeta) = b^p_{ijk}\mathbf{e}_1\,, && \begin{matrix} 0<i<p\,, \\ 0<j<p-i\,, \\ 0<k<p-i-j \end{matrix}\,,
\end{aligned}
\tag{6.69}
$$

where the first four formulas are the face-cell base functions.

A depiction of quartic base functions on their respective polytopes is given in Fig. 6.15.

6.3.3 Nédélec elements of the first type

In order to improve the convergence rates and recover lost precision over curl terms we consider the Nédélec space of the first type, where the polynomial space is augmented with a minimal set of curl-type base functions, such that the kernel of the next polynomial space in the exact sequence is complete and of degree p instead of degree $p-1$. The construction is achieved by an explicit split of the higher order base functions between the kernel and the part orthogonal to the kernel $\mathcal{N}_I^p \setminus \mathcal{N}_I^0 = ([\ker(\mathrm{curl}) \cap \mathcal{N}_I^p] \oplus [\ker^\perp(\mathrm{curl}) \cap \mathcal{N}_I^p]) \setminus \mathcal{N}_I^0$. We start by taking the gradients of the base functions of an H^1-conforming polynomial space U^{p+1} while excluding vertex base functions

$$
\boldsymbol{\vartheta}_i(\xi,\eta,\zeta) = \nabla_\xi n_i^{p+1}\,. \tag{6.70}
$$

The latter results in $(p+3)(p+2)(p+1)/6-4$ base functions. We complete the space of constants with the six lowest order Nédélec base functions of the first type ($\mathcal{N}_I^0$) from Eq. (5.61). Next we need

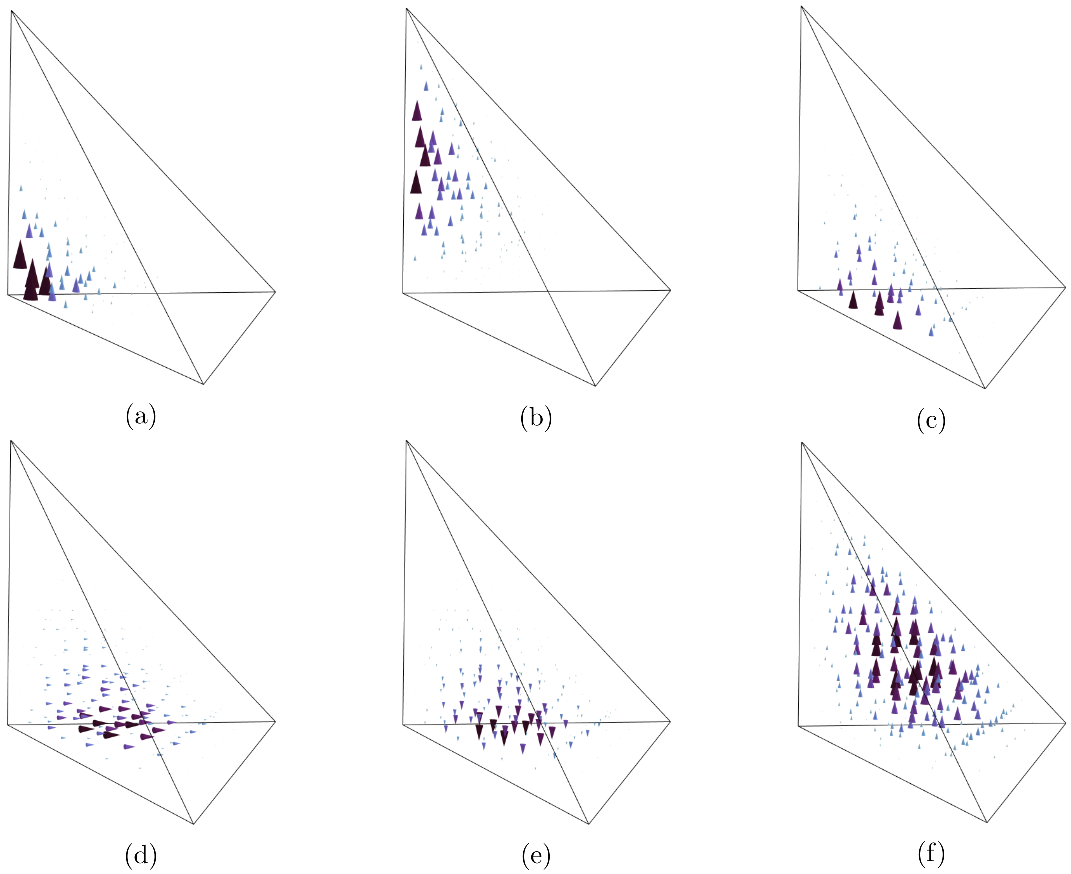

(a) (b) (c)

(d) (e) (f)

Figure 6.15: Quartic vertex-edge (a), edge (b), edge-face (c), face (d), face-cell (e) and pure cell (f) base functions of the Nédélec element of the second type on the reference tetrahedron.

to augment the space, such that the curl of the space has the same polynomial degree as its kernel. We complete the face base functions using the polytopal template (see Fig. 6.16) of the triangle with the lowest tetrahedral Nédélec base functions (see Eq. (5.61)),

$$\begin{aligned}
&\mathcal{T}_1 = \{\boldsymbol{\vartheta}_4^I, \boldsymbol{\vartheta}_5^I, \boldsymbol{\vartheta}_6^I\}\,, && \mathcal{T}_2 = \{-\boldsymbol{\vartheta}_2^I, -\boldsymbol{\vartheta}_3^I, \boldsymbol{\vartheta}_6^I\}\,, && \mathcal{T}_3 = \{-\boldsymbol{\vartheta}_3^I, -\boldsymbol{\vartheta}_5^I\}\,, \\
&\mathcal{T}_{12} = \{\boldsymbol{\vartheta}_4^I - \boldsymbol{\vartheta}_2^I, \boldsymbol{\vartheta}_5^I - \boldsymbol{\vartheta}_3^I\}\,, && \mathcal{T}_{13} = \{\boldsymbol{\vartheta}_1^I + \boldsymbol{\vartheta}_4^I, \boldsymbol{\vartheta}_6^I - \boldsymbol{\vartheta}_3^I\}\,, && \mathcal{T}_{14} = \{\boldsymbol{\vartheta}_1^I + \boldsymbol{\vartheta}_5^I, \boldsymbol{\vartheta}_2^I + \boldsymbol{\vartheta}_6^I\}\,, \\
&\mathcal{T}_{23} = \{\boldsymbol{\vartheta}_1^I - \boldsymbol{\vartheta}_2^I, \boldsymbol{\vartheta}_6^I - \boldsymbol{\vartheta}_5^I\}\,, && \mathcal{T}_{24} = \{\boldsymbol{\vartheta}_1^I - \boldsymbol{\vartheta}_3^I, \boldsymbol{\vartheta}_4^I + \boldsymbol{\vartheta}_6^I\}\,, && \mathcal{T}_{34} = \{\boldsymbol{\vartheta}_2^I - \boldsymbol{\vartheta}_3^I, \boldsymbol{\vartheta}_4^I - \boldsymbol{\vartheta}_5^I\}\,, \\
&\mathcal{T}_{123} = \{\boldsymbol{\vartheta}_1^I - \boldsymbol{\vartheta}_2^I + \boldsymbol{\vartheta}_4^I\}\,, && \mathcal{T}_{124} = \{\boldsymbol{\vartheta}_1^I - \boldsymbol{\vartheta}_3^I + \boldsymbol{\vartheta}_5^I\}\,, && \mathcal{T}_{134} = \{\boldsymbol{\vartheta}_2^I - \boldsymbol{\vartheta}_3^I + \boldsymbol{\vartheta}_6^I\}\,, \\
&\mathcal{T}_{234} = \{\boldsymbol{\vartheta}_4^I - \boldsymbol{\vartheta}_5^I + \boldsymbol{\vartheta}_6^I\}\,,
\end{aligned} \tag{6.71}$$

such that the full polytopal template is given by

$$\mathcal{T} = \{\mathcal{T}_1, \mathcal{T}_2, \mathcal{T}_3, \mathcal{T}_{12}, \mathcal{T}_{13}, \mathcal{T}_{14}, \mathcal{T}_{23}, \mathcal{T}_{24}, \mathcal{T}_{34}, \mathcal{T}_{123}, \mathcal{T}_{124}, \mathcal{T}_{134}, \mathcal{T}_{234}\}\,. \tag{6.72}$$

For the non-gradient cell functions we use the construction introduced in [5]

$$\mathcal{R}^p = \left\{ (p+1) b_{i-e_j}^p \nabla \lambda_j - \frac{i_j}{p+1} \nabla_\xi b_i^{p+1} \mid i \in \mathcal{I}_o \right\}\,, \tag{6.73}$$

where $\mathcal{I}_o$ is the set of multi-indices of cell functions, e_j is the unit multi-index with the value one at position j and i_j is the value of the i-multi-index at position j. Note that only the first term in the cell functions is required to span the next space in the sequence due to

$$\operatorname{curl} \left([p+1] b_{i-e_j}^p \nabla_\xi \lambda_j - \frac{i_j}{p+1} \nabla_\xi b_i^{p+1} \right) = \operatorname{curl}([p+1] b_{i-e_j}^p \nabla_\xi \lambda_j)\,. \tag{6.74}$$

The term is defined using the surface normals and as such, can be viewed as a combination of surface and cell templates. However, without the added gradient the function would not belong to $[P^p]^3 \oplus \boldsymbol{\xi} \times [\widetilde{P}]^3$ and consequently, would not be part of the Nédélec space. Therefore, a general methodology would be to use the template and modify it to fit in $[P^p]^3 \oplus \boldsymbol{\xi} \times [\widetilde{P}]^3$. By limiting $\mathcal{R}^p$ to $\mathcal{R}_*^p$ such that $\mathcal{R}_*^p$ contains only the surface permutations with $\nabla \lambda_j = \mathbf{e}_j$ and the cell permutations with $j \in \{1, 2\}$, one retrieves the necessary base functions. The sum of the lowest order Nédélec base functions, the template base functions, the gradient base functions, and the non-gradient cell base functions yields exactly $(p+4)(p+3)(p+1)/2$, thus satisfying the required dimensionality of the Nédélec space. The complete space reads

$$\begin{aligned}
\mathcal{N}_I^p = &\mathcal{N}_I^0 \oplus \left\{ \bigoplus_{i \in \mathcal{I}} \nabla \mathcal{E}_i^{p+1} \right\} \oplus \left\{ \bigoplus_{j \in \mathcal{J}} \nabla \mathcal{F}_j^{p+1} \right\} \oplus \nabla \mathcal{C}_{1234}^{p+1} \oplus \left\{ \bigoplus_{k=1}^{3} \mathcal{V}_k^p \otimes \mathcal{T}_k \right\} \oplus \left\{ \bigoplus_{i \in \mathcal{I}} \mathcal{E}_i^p \otimes \mathcal{T}_i \right\} \\
&\oplus \left\{ \bigoplus_{j \in \mathcal{J}} \mathcal{F}_j^p \otimes \mathcal{T}_j \right\} \oplus \mathcal{R}_*^{p+1}\,, \qquad \begin{aligned} &\mathcal{I} = \{(1,2), (1,3), (1,4), (2,3), (2,4), (3,4)\}\,, \\ &\mathcal{J} = \{(1,2,3), (1,2,4), (1,3,4), (2,3,4)\} \end{aligned} \;.
\end{aligned} \tag{6.75}$$

Theorem 6.8 (Linear independence)
The set of base functions given by the lowest order Nédélec element of the first type, the gradients of the H^1-conforming base functions in U^{p+1} (without vertex base functions), the tensor product between U^p and the polytopal template vectors and the non-gradient cell basis $\mathcal{R}_*^{p+1}$ yields a linearly independent basis for $\mathcal{N}_I^p$.

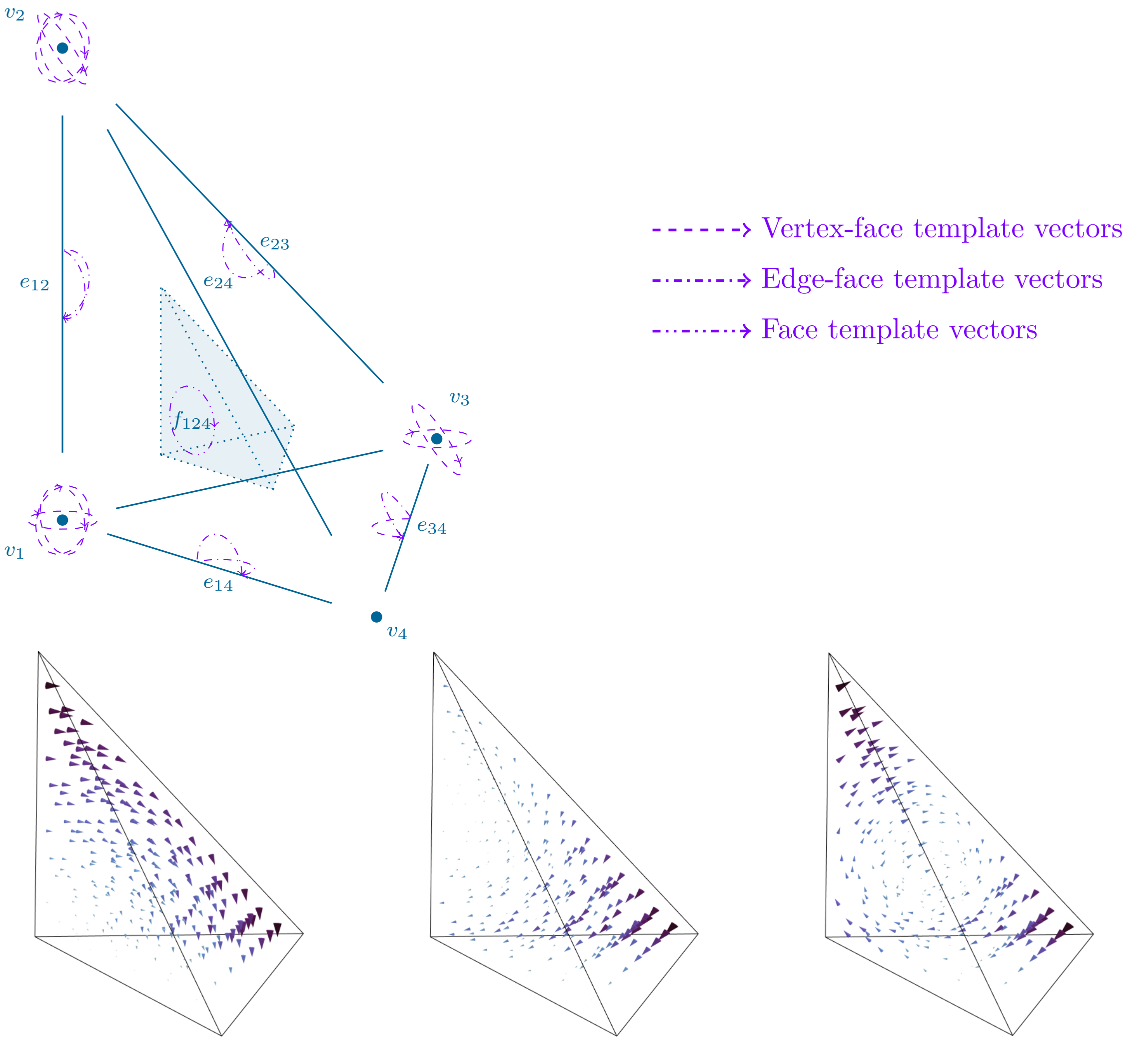

(a) (b) (c)

Figure 6.16: Template vectors on the reference tetrahedron for base functions orthogonal to the kernel of the curl operator (a). Only part of the template is depicted. Visualization of the vertex (b), edge (c) and face (d) template vectors for the first face.

Proof. The partition of unity property of both Bézier and Lagrange base functions guarantees the linear independence of the gradients between themselves since

$$\sum_i c_i \nabla_\xi n_i = \nabla_\xi \sum c_i \, n_i \neq 0 \,, \tag{6.76}$$

if not all constants c_i are equal to zero. The gradients are linearly independent of the lowest order Nédélec base functions since their tangential traces on edges are at least linear, whereas the tangential traces of the lowest order base functions are constant on each edge. The template base functions are linearly independent of the edge base functions since they have zero tangential traces on edges. The linear independence of the face functions follows analogously to the proof for triangles, since their traces are non-vanishing only on their respective faces and vanish for all other faces. The construction and proof of linear independence of the non-gradient cell base functions is found in [5]. □

Theorem 6.9 ($H(\mathrm{curl}, V)$-conformity)
The constructed element on the reference domain is conforming under covariant Piola mappings to the physical domain of the base functions and contravariant Piola mappings of their respective curls.

Proof. The lowest order Nédélec base functions are $H(\mathrm{curl})$-conforming by their respective degrees of freedom. The gradients of U^{p+1} are conforming by the exact sequence property, see Fig. 4.1. The polytopal template of the face functions is built using the lowest order Nédélec base functions, thus ensuring its conformity under covariant Piola mappings onto the physical domain when a consistent H^1-conforming subspace U^{p+1} basis is used to construct the underlying tensor products. The non-gradient cells are composed of cell gradients and the scaling of a surface vector on its respective surface and as such, are traceless. □

Here, the Bézier basis is used to construct the higher order Nédélec base functions of the first type.

Definition 6.10 (Bézier-Nédélec I tetrahedral basis)
The base functions are defined on the reference tetrahedron.

- *For the edges we use the lowest order base functions from Eq.* (5.61)*. The remaining edge base functions are given by the gradients*

$$\begin{aligned}
&e_{12}: && \boldsymbol{\vartheta}(\xi,\eta,\zeta) = \boldsymbol{\vartheta}^I_1 \,, && \\
& && \boldsymbol{\vartheta}(\xi,\eta,\zeta) = \nabla_\xi b^{p+1}_{00k} \,, && 0 < k < p+1 \,, \\
&e_{13}: && \boldsymbol{\vartheta}(\xi,\eta,\zeta) = \boldsymbol{\vartheta}^I_2 \,, && \\
& && \boldsymbol{\vartheta}(\xi,\eta,\zeta) = \nabla_\xi b^{p+1}_{0j0} \,, && 0 < j < p+1 \,, \\
&e_{14}: && \boldsymbol{\vartheta}(\xi,\eta,\zeta) = \boldsymbol{\vartheta}^I_3 \,, && \\
& && \boldsymbol{\vartheta}(\xi,\eta,\zeta) = \nabla_\xi b^{p+1}_{i00} \,, && 0 < i < p+1 \,, \\
&e_{23}: && \boldsymbol{\vartheta}(\xi,\eta,\zeta) = \boldsymbol{\vartheta}^I_4 \,, && \\
& && \boldsymbol{\vartheta}(\xi,\eta,\zeta) = \nabla_\xi b^{p+1}_{0j,p+1-j} \,, && 0 < j < p+1 \,, \\
&e_{24}: && \boldsymbol{\vartheta}(\xi,\eta,\zeta) = \boldsymbol{\vartheta}^I_5 \,, && \\
& && \boldsymbol{\vartheta}(\xi,\eta,\zeta) = \nabla_\xi b^{p+1}_{i0,p+1-i} \,, && 0 < i < p+1 \,,
\end{aligned}$$

$$e_{34}: \qquad \boldsymbol{\vartheta}(\xi,\eta,\zeta) = \boldsymbol{\vartheta}_6^I\,,$$

$$\boldsymbol{\vartheta}(\xi,\eta,\zeta) = \nabla_\xi b_{00k}^{p+1}\,, \qquad 0 < i < p+1\,. \tag{6.77}$$

- *On faces we employ both template base functions and gradients*

$$\begin{aligned}
f_{123}: \quad & \boldsymbol{\vartheta}(\xi,\eta,\zeta) = b_{000}^p \boldsymbol{\vartheta}_4^I\,, \\
& \boldsymbol{\vartheta}(\xi,\eta,\zeta) = -b_{00p}^p \boldsymbol{\vartheta}_2^I\,, \\
& \boldsymbol{\vartheta}(\xi,\eta,\zeta) = b_{00k}^p (\boldsymbol{\vartheta}_4^I - \boldsymbol{\vartheta}_2^I)\,, && 0 < k < p\,, \\
& \boldsymbol{\vartheta}(\xi,\eta,\zeta) = b_{0j0}^p (\boldsymbol{\vartheta}_1^I + \boldsymbol{\vartheta}_4^I)\,, && 0 < j < p\,, \\
& \boldsymbol{\vartheta}(\xi,\eta,\zeta) = b_{0j,p-j}^p (\boldsymbol{\vartheta}_1^I - \boldsymbol{\vartheta}_2^I)\,, && 0 < j < p\,, \\
& \boldsymbol{\vartheta}(\xi,\eta,\zeta) = b_{0jk}^p (\boldsymbol{\vartheta}_1^I - \boldsymbol{\vartheta}_2^I + \boldsymbol{\vartheta}_4^I)\,, && 0 < j < p\,, \quad 0 < k < p-j\,, \\
& \boldsymbol{\vartheta}(\xi,\eta,\zeta) = \nabla_\xi b_{0jk}^{p+1}\,, && 0 < j < p+1\,, \quad 0 < k < p+1-j\,, \\
f_{124}: \quad & \boldsymbol{\vartheta}(\xi,\eta,\zeta) = b_{000}^p \boldsymbol{\vartheta}_5^I\,, \\
& \boldsymbol{\vartheta}(\xi,\eta,\zeta) = -b_{00p}^p \boldsymbol{\vartheta}_3^I\,, \\
& \boldsymbol{\vartheta}(\xi,\eta,\zeta) = b_{00k}^p (\boldsymbol{\vartheta}_5^I - \boldsymbol{\vartheta}_3^I)\,, && 0 < k < p\,, \\
& \boldsymbol{\vartheta}(\xi,\eta,\zeta) = b_{i00}^p (\boldsymbol{\vartheta}_1^I + \boldsymbol{\vartheta}_5^I)\,, && 0 < i < p\,, \\
& \boldsymbol{\vartheta}(\xi,\eta,\zeta) = b_{i0,p-i}^p (\boldsymbol{\vartheta}_1^I - \boldsymbol{\vartheta}_3^I)\,, && 0 < i < p\,, \\
& \boldsymbol{\vartheta}(\xi,\eta,\zeta) = b_{i0k}^p (\boldsymbol{\vartheta}_1^I - \boldsymbol{\vartheta}_3^I + \boldsymbol{\vartheta}_5^I)\,, && 0 < i < p\,, \quad 0 < k < p-i\,, \\
& \boldsymbol{\vartheta}(\xi,\eta,\zeta) = \nabla_\xi b_{i0k}^{p+1}\,, && 0 < i < p+1\,, \quad 0 < k < p+1-i\,, \\
f_{134}: \quad & \boldsymbol{\vartheta}(\xi,\eta,\zeta) = b_{000}^p \boldsymbol{\vartheta}_6^I\,, \\
& \boldsymbol{\vartheta}(\xi,\eta,\zeta) = -b_{0p0}^p \boldsymbol{\vartheta}_3^I\,, \\
& \boldsymbol{\vartheta}(\xi,\eta,\zeta) = b_{0j0}^p (\boldsymbol{\vartheta}_6^I - \boldsymbol{\vartheta}_3^I)\,, && 0 < j < p\,, \\
& \boldsymbol{\vartheta}(\xi,\eta,\zeta) = b_{i00}^p (\boldsymbol{\vartheta}_2^I + \boldsymbol{\vartheta}_6^I)\,, && 0 < i < p\,, \\
& \boldsymbol{\vartheta}(\xi,\eta,\zeta) = b_{i,p-i,0}^p (\boldsymbol{\vartheta}_2^I - \boldsymbol{\vartheta}_3^I)\,, && 0 < i < p\,, \\
& \boldsymbol{\vartheta}(\xi,\eta,\zeta) = b_{ij0}^p (\boldsymbol{\vartheta}_2^I - \boldsymbol{\vartheta}_3^I + \boldsymbol{\vartheta}_6^I)\,, && 0 < i < p\,, \quad 0 < j < p-i\,, \\
& \boldsymbol{\vartheta}(\xi,\eta,\zeta) = \nabla_\xi b_{ij0}^{p+1}\,, && 0 < i < p+1\,, \quad 0 < j < p+1-i\,, \\
f_{234}: \quad & \boldsymbol{\vartheta}(\xi,\eta,\zeta) = b_{00p}^p \boldsymbol{\vartheta}_6^I\,, \\
& \boldsymbol{\vartheta}(\xi,\eta,\zeta) = -b_{0p0}^p \boldsymbol{\vartheta}_5^I\,, \\
& \boldsymbol{\vartheta}(\xi,\eta,\zeta) = b_{0j,p-j}^p (\boldsymbol{\vartheta}_6^I - \boldsymbol{\vartheta}_5^I)\,, && 0 < j < p\,, \\
& \boldsymbol{\vartheta}(\xi,\eta,\zeta) = b_{i0,p-i}^p (\boldsymbol{\vartheta}_4^I + \boldsymbol{\vartheta}_6^I)\,, && 0 < i < p\,,
\end{aligned}$$

$$
\begin{aligned}
\boldsymbol{\vartheta}(\xi,\eta,\zeta) &= b^{p}_{i,p-i,0}(\boldsymbol{\vartheta}^{I}_{4} - \boldsymbol{\vartheta}^{I}_{5})\,, && 0 < i < p\,, \\
\boldsymbol{\vartheta}(\xi,\eta,\zeta) &= b^{p}_{ij,p-i-j}(\boldsymbol{\vartheta}^{I}_{4} - \boldsymbol{\vartheta}^{I}_{5} + \boldsymbol{\vartheta}^{I}_{6})\,, && 0 < i < p\,, \quad 0 < j < p - i\,, \\
\boldsymbol{\vartheta}(\xi,\eta,\zeta) &= \nabla_{\xi} b^{p+1}_{ij,p-i.j}\,, && 0 < i < p+1\,, \quad 0 < j < p+1-i\,. \qquad (6.78)
\end{aligned}
$$

- *The cell base functions read*

$$
\begin{aligned}
c_{1234}: \quad \boldsymbol{\vartheta}(\xi,\eta,\zeta) &= (p+2) b^{p+1}_{i-1,jk}\mathbf{e}_1 - \frac{i}{p+2}\nabla_{\xi} b^{p+2}_{ijk}\,, && \begin{array}{l} 0 < i < p+2\,, \\ 0 < j < p+2-i\,, \quad , \\ 0 < k < p+2-i-j \end{array} \\
\boldsymbol{\vartheta}(\xi,\eta,\zeta) &= (p+2) b^{p+1}_{i,j-1,k}\mathbf{e}_2 - \frac{j}{p+2}\nabla_{\xi} b^{p+2}_{ijk}\,, && \begin{array}{l} 0 < i < p+2\,, \\ 0 < j < p+2-i\,, \quad , \\ 0 < k < p+2-i-j \end{array} \\
\boldsymbol{\vartheta}(\xi,\eta,\zeta) &= (p+2) b^{p+1}_{ij0}\mathbf{e}_3 - \frac{1}{p+2}\nabla_{\xi} b^{p+2}_{ij1}\,, && \begin{array}{l} 0 < i < p+2\,, \\ 0 < j < p+2-i \end{array}, \\
\boldsymbol{\vartheta}(\xi,\eta,\zeta) &= \nabla_{\xi} b^{p+1}_{ijk}\,, && \begin{array}{l} 0 < i < p+1\,, \\ 0 < j < p+1-i\,, \quad . \\ 0 < k < p+1-i-j \end{array} \qquad (6.79)
\end{aligned}
$$

A depiction of the higher order base functions on the reference tetrahedron is given in Fig. 6.17. The lowest order base functions are visualized in Fig. 5.11.

Remark 6.5
Unlike in all previous constructions, the non-gradient cells functions employed here do not allow for a straight-forward algorithm with optimal complexity as they combine two independent Bernstein base functions.

6.4 Embedding of boundary conditions

The degrees of freedom in [30] commute between the continuous and discrete spaces. As such, they allow to exactly satisfy the consistent coupling condition [27]. We note that the functionals can be viewed as a hierarchical system of Dirichlet boundary problems. In the case of hierarchical base functions [110], they can be solved independently. However, here the boundary value of each polytope is required in advance. In other words, one must first solve the problem for vertices, then for edges, afterwards for faces, and finally for the cell. In our case the degrees of freedom for the cell are irrelevant since a cell is never part of the boundary.

Remark 6.6
In the hp-FEA software Rayse, vertices, edges and faces represent finite elements on their own. Their respective Dirichlet boundary problems are solved hierarchically and independently of the actual finite elements (being triangles in two dimensions and tetrahedra in three dimensions).

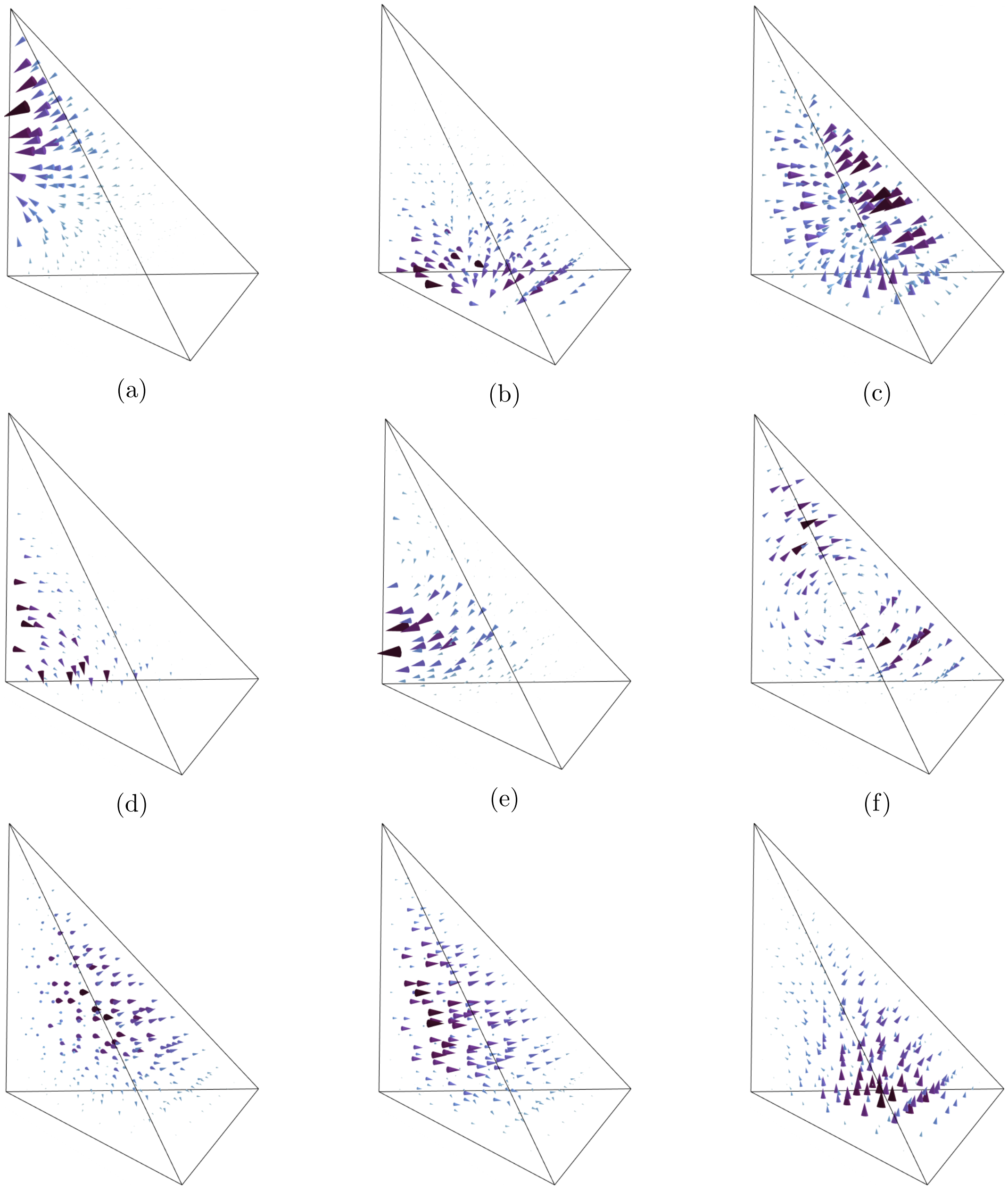

(a) (b) (c)

(d) (e) (f)

(g) (h) (i)

Figure 6.17: Gradients of quartic Bézier edge (a), face (b) and cell (c) base functions on the reference tetrahedron. Cubic non-gradient vertex-face (d), edge-face (e) and face (f) base functions. The first three cell base functions (g-i) for the quadratic element.

6.4.1 Boundary vertices

We start with the vertices. The finite element mesh identifies each vertex with a tuple of coordinates. It suffices to evaluate the displacement field at the vertex

$$u_i^d = \widetilde{u}\bigg|_{\mathbf{x}_i} \, . \tag{6.80}$$

If the field is vectorial, each component is evaluated at the designated vertex. The boundary conditions of the microdistortion field are associated with tangential projections and as such do not have vertex-type degrees of freedom. This is the case since a vertex does not define a unique tangential plane.

6.4.2 Boundary edges

The edge functional for the H^1-conforming subspace Eq. (6.21) can be reformulated for a reference edge on a unit domain $\alpha \in [0,1]$. We parametrize the edge via

$$\mathbf{x}(\alpha) = (1-\alpha)\mathbf{x}_1 + \alpha\mathbf{x}_2 \, . \tag{6.81}$$

As such, the following relation exists between the unit parameter and the arc-length parameter

$$\mathbf{t} = \frac{\mathrm{d}}{\mathrm{d}\alpha}\mathbf{x} = \mathbf{x}_2 - \mathbf{x}_1 \, , \qquad \mathrm{d}s = \|\mathrm{d}\mathbf{x}\| = \|\mathbf{x}_2 - \mathbf{x}_1\|\mathrm{d}\alpha = \|\mathbf{t}\|\mathrm{d}\alpha \, . \tag{6.82}$$

By the chain rule we find

$$\frac{\mathrm{d}u}{\mathrm{d}s} = \frac{\mathrm{d}u}{\mathrm{d}\alpha}\frac{\mathrm{d}\alpha}{\mathrm{d}s} = \|\mathbf{t}\|^{-1}\frac{\mathrm{d}u}{\mathrm{d}\alpha} \, , \tag{6.83}$$

for some function u. On edges, the test and trial functions are Bernstein polynomials parametrized by the unit domain. The function representing the boundary condition $\widetilde{u}(\mathbf{x})$ however, is parametrized by the Cartesian coordinates of the physical space. We find its derivative with respect to the arc-length parameter by observing

$$\frac{\mathrm{d}}{\mathrm{d}s}\widetilde{u} = \langle \frac{\mathrm{d}}{\mathrm{d}s}\mathbf{x}, \, \nabla_x \widetilde{u} \rangle \, . \tag{6.84}$$

The derivative of the coordinates with respect to the arc-length is simply the normed tangent vector

$$\frac{\mathrm{d}}{\mathrm{d}s}\mathbf{x} = \frac{\mathrm{d}\mathbf{x}}{\mathrm{d}\alpha}\frac{\mathrm{d}\alpha}{\mathrm{d}s} = \|\mathbf{t}\|^{-1}\mathbf{t} \, . \tag{6.85}$$

Consequently, the edge boundary condition is given by

$$\begin{aligned} \int_{s_i} \frac{\partial q_j}{\partial s}\frac{\partial u}{\partial s} \, \mathrm{d}s &= \int_0^1 \left(\|\mathbf{t}\|^{-1}\frac{\mathrm{d}q_j}{\mathrm{d}\alpha} \right) \left(\|\mathbf{t}\|^{-1}\frac{\mathrm{d}u}{\mathrm{d}\alpha} \right) \|\mathbf{t}\| \, \mathrm{d}\alpha \\ &= \int_0^1 \left(\|\mathbf{t}\|^{-1}\frac{\mathrm{d}q_j}{\mathrm{d}\alpha} \right) \langle \|\mathbf{t}\|^{-1}\mathbf{t}, \, \nabla_x \widetilde{u} \rangle \|\mathbf{t}\| \, \mathrm{d}\alpha = \int_{s_i} \frac{\partial q_j}{\partial s}\frac{\partial \widetilde{u}}{\partial s} \, \mathrm{d}s \qquad \forall \, q_j \in P^p(\alpha) \, , \end{aligned} \tag{6.86}$$

and can be solved by assembling the stiffness matrix of the edge and the load vector induced by the prescribed displacement field $\widetilde{u}$, representing volume forces

$$k_{ij} = \int_0^1 \left(\|\mathbf{t}\|^{-1}\frac{\mathrm{d}n_i}{\mathrm{d}\alpha} \right) \left(\|\mathbf{t}\|^{-1}\frac{\mathrm{d}n_j}{\mathrm{d}\alpha} \right) \|\mathbf{t}\| \, \mathrm{d}\alpha \, , \quad f_i = \int_0^1 \langle \|\mathbf{t}\|^{-1}\mathbf{t}, \, \nabla_x \widetilde{u} \rangle \left(\|\mathbf{t}\|^{-1}\frac{\mathrm{d}n_i}{\mathrm{d}\alpha} \right) \|\mathbf{t}\| \, \mathrm{d}\alpha \, . \tag{6.87}$$

Next we consider the Dirichlet boundary conditions for the microdistortion with the Nédélec space of the second type $\mathcal{N}_{II}$. The problem reads

$$\int_{s_i} q_j \langle \mathbf{t},\, \mathbf{p} \rangle \, \mathrm{d}s = \int_{s_i} q_j \langle \mathbf{t},\, \nabla_x \widetilde{u} \rangle \, \mathrm{d}s \qquad \forall \, q_j \in P^p(s_i) \, . \tag{6.88}$$

Observe that on the edge the test functions q_j are chosen to be the Bernstein polynomials. Further, by the polytopal template construction of the $\mathcal{N}_{II}$-space there holds $\langle \mathbf{t},\, \boldsymbol{\theta}_i \rangle |_s = n_i(\alpha)$. As such, the components of the corresponding stiffness matrix and load vectors read

$$k_{ij} = \int_0^1 n_i \, n_j \|\mathbf{t}\| \, \mathrm{d}\alpha \, , \qquad\qquad f_i = \int_0^1 n_i \langle \mathbf{t},\, \nabla_x \widetilde{u} \rangle \|\mathbf{t}\| \, \mathrm{d}\alpha \, . \tag{6.89}$$

Note that in order to maintain the exactness property, the degree of the Nédélec spaces $\mathcal{N}_I^p, \mathcal{N}_{II}^p$ is always one less than the degree of the subspace U^{p+1}.

Lastly, we consider the Nédélec element of the first type. The problem is given by

$$\int_{s_i} q_j \langle \mathbf{t},\, \mathbf{p} \rangle \, \mathrm{d}s = \int_{s_i} q_j \langle \mathbf{t},\, \nabla_x \widetilde{u} \rangle \, \mathrm{d}s \qquad \forall \, q_j \in P^p(s_i) \, . \tag{6.90}$$

We define

$$q_i = \dfrac{\mathrm{d}}{\mathrm{d}\alpha} n_i^{p+1} \, , \tag{6.91}$$

and observe that on the edges the Nédélec base functions yield

$$\langle \mathbf{t},\, \boldsymbol{\theta}_j \rangle = \langle \mathbf{t},\, \nabla_x n_j^{p+1} \rangle = \dfrac{\mathrm{d}}{\mathrm{d}\alpha} n_j^{p+1} \, . \tag{6.92}$$

Therefore, the components of the stiffness matrix and the load vector result in

$$k_{ij} = \int_0^1 \dfrac{\mathrm{d}n_i^{p+1}}{\mathrm{d}\alpha} \dfrac{\mathrm{d}n_j^{p+1}}{\mathrm{d}\alpha} \|\mathbf{t}\| \, \mathrm{d}\alpha \, , \qquad\qquad f_i = \int_0^1 \dfrac{\mathrm{d}n_i^{p+1}}{\mathrm{d}\alpha} \langle \mathbf{t},\, \nabla_x \widetilde{u} \rangle \|\mathbf{t}\| \, \mathrm{d}\alpha \, . \tag{6.93}$$

6.4.3 Boundary faces

We start with the face boundary condition for the H^1-conforming subspace. The problem reads

$$\int_{A_i} \langle \nabla_f q_j,\, \nabla_f u \rangle \, \mathrm{d}A = \int_{A_i} \langle \nabla_f q_j,\, \nabla_f \widetilde{u} \rangle \, \mathrm{d}A \qquad \forall \, q_j \in P^p(A_i) \, . \tag{6.94}$$

The surface is parametrized by the barycentric mapping from the unit triangle $\Gamma = \{(\xi, \eta) \in [0,1]^2 \mid \xi + \eta \leq 1\}$. The surface gradient is given by

$$\nabla_f \widetilde{u} = \nabla_x \widetilde{u} - \dfrac{1}{\|\mathbf{n}\|^2} \langle \nabla_x \widetilde{u},\, \mathbf{n} \rangle \mathbf{n} \, , \tag{6.95}$$

where $\mathbf{n}$ is the surface normal. The surface gradient can also be expressed via

$$\nabla_f u = \mathbf{e}^i \partial_i^x u = \mathbf{g}^\beta \partial_\beta^\xi u \, , \qquad\qquad \beta \in \{1, 2\} \, , \tag{6.96}$$

where ∂^x_β are partial derivates with respect to the physical coordinates, ∂^ξ_β are partial derivatives with respect to the reference domain and $\mathbf{g}^\beta$ are the contravariant base vectors. Further, the Einstein summation convention over corresponding indices is implied. The covariant base vectors are given by

$$\mathbf{g}_\beta = \frac{\partial \mathbf{x}}{\partial \xi^\beta} \,. \tag{6.97}$$

One can find the contravariant vector orthogonal to the surface by

$$\mathbf{g}^3 = \mathbf{n} = \mathbf{g}_1 \times \mathbf{g}_2 \,. \tag{6.98}$$

We define the mixed transformation matrix

$$\boldsymbol{T} = \begin{bmatrix} \mathbf{g}_1 & \mathbf{g}_2 & \mathbf{g}^3 \end{bmatrix} \,. \tag{6.99}$$

Due to the orthogonality relation $\langle \mathbf{g}_i, \, \mathbf{g}^j \rangle = \delta_i^j$ the transposed inverse of $\boldsymbol{T}$ is clearly

$$\boldsymbol{T}^{-T} = \begin{bmatrix} \mathbf{g}^1 & \mathbf{g}^2 & \mathbf{g}_3 \end{bmatrix} \,. \tag{6.100}$$

Thus, we can compute the surface gradient of functions parametrized by the reference triangle via

$$\nabla_f u = \begin{bmatrix} \mathbf{g}^1 & \mathbf{g}^2 \end{bmatrix} \nabla_\xi u = \boldsymbol{T}_*^{-T} \nabla_\xi u \,, \qquad \boldsymbol{T}_*^{-T} = \begin{bmatrix} \mathbf{g}^1 & \mathbf{g}^2 \end{bmatrix} \,. \tag{6.101}$$

Further, there holds the following relation between the physical surface and the reference surface

$$\mathrm{d}A = \|\mathbf{n}\| \mathrm{d}\Gamma = \|\mathbf{g}^3\| \mathrm{d}\Gamma = \sqrt{\langle \mathbf{g}_1 \times \mathbf{g}_2, \, \mathbf{g}^3 \rangle} \, \mathrm{d}\Gamma = \sqrt{\det \boldsymbol{T}} \, \mathrm{d}\Gamma \,. \tag{6.102}$$

Consequently, we can write the components of the stiffness matrix and load vector as

$$\begin{aligned} k_{ij} &= \int_\Gamma \langle \boldsymbol{T}_*^{-T} \nabla_\xi n_i, \, \boldsymbol{T}_*^{-T} \nabla_\xi n_j \rangle \sqrt{\det \boldsymbol{T}} \, \mathrm{d}\Gamma \,, \\ f_i &= \int_\Gamma \langle \boldsymbol{T}_*^{-T} \nabla_\xi n_i, \, \nabla_x \widetilde{u} - (\det \boldsymbol{T})^{-1} \langle \nabla_x \widetilde{u}, \, \mathbf{n} \rangle \mathbf{n} \rangle \sqrt{\det \boldsymbol{T}} \, \mathrm{d}\Gamma = \int_\Gamma \langle \boldsymbol{T}_*^{-T} \nabla_\xi n_i, \, \nabla_x \widetilde{u} \rangle \sqrt{\det \boldsymbol{T}} \, \mathrm{d}\Gamma \,, \end{aligned} \tag{6.103}$$

with the orthogonality $\langle \mathbf{g}^\beta, \, \mathbf{n} \rangle = 0$ for $\beta \in \{1, 2\}$.

In order to embed the consistent coupling boundary condition to the microdistortion we deviate from the degrees of freedom defined in Section 6.1.4 and apply the simpler $H(\mathrm{div}\boldsymbol{R})$-projection

$$\langle \mathbf{q}_i, \, \mathbf{p}, \rangle_{H(\mathrm{div}\boldsymbol{R})} = \langle \mathbf{q}_i, \, \nabla_f \widetilde{u} \rangle_{H(\mathrm{div}\boldsymbol{R})} \qquad \forall \, \mathbf{q}_i \in \mathcal{N}_I^p(A) \quad \text{or} \quad \forall \, \mathbf{q}_i \in \mathcal{N}_{II}^p(A) \,. \tag{6.104}$$

Due to $\ker(\mathrm{curl}) = \nabla H^1$ the problem reduces to

$$\int_{A_i} \langle \mathbf{q}_j, \, \mathbf{p} \rangle + \langle \mathrm{div}(\boldsymbol{R}\mathbf{q}_j), \, \mathrm{div}(\boldsymbol{R}\mathbf{p}) \rangle \, \mathrm{d}A = \int_{A_i} \langle \mathbf{q}_j, \, \nabla_f \widetilde{u} \rangle \, \mathrm{d}A \qquad \forall \, \mathbf{q}_j \in \mathcal{N}_I^p(A) \quad \text{or} \quad \forall \, \mathbf{q}_j \in \mathcal{N}_{II}^p(A) \,. \tag{6.105}$$

We express the co- and contravariant Piola transformation from the two-dimensional reference domain to the three-dimensional physical domain using

$$\boldsymbol{\theta}_i = \boldsymbol{T}_*^{-T} \boldsymbol{\vartheta}_i \,, \qquad \mathrm{div}_x \, \boldsymbol{R} \boldsymbol{\theta}_i = \frac{1}{\sqrt{\det \boldsymbol{T}}} \mathrm{div}_\xi \, \boldsymbol{R} \boldsymbol{\vartheta}_i \,. \tag{6.106}$$

Thus, the stiffness matrix components and load vector components read

$$\begin{aligned} k_{ij} &= \int_\Gamma \langle \boldsymbol{T}_*^{-T} \boldsymbol{\vartheta}_i, \, \boldsymbol{T}_*^{-T} \boldsymbol{\vartheta}_j \rangle + \langle (\det \boldsymbol{T})^{-1/2} \, \mathrm{div}_\xi \, \boldsymbol{R} \boldsymbol{\vartheta}_i, \, (\det \boldsymbol{T})^{-1/2} \, \mathrm{div}_\xi \, \boldsymbol{R} \boldsymbol{\vartheta}_j \rangle \sqrt{\det \boldsymbol{T}} \, \mathrm{d}\Gamma \,, \\ f_i &= \int_\Gamma \langle \boldsymbol{T}_*^{-T} \boldsymbol{\vartheta}_i, \, \nabla_x \widetilde{u} - (\det \boldsymbol{T})^{-1} \langle \nabla_x \widetilde{u}, \, \mathbf{n} \rangle \mathbf{n} \rangle \sqrt{\det \boldsymbol{T}} \, \mathrm{d}\Gamma = \int_\Gamma \langle \boldsymbol{T}_*^{-T} \boldsymbol{\vartheta}_i, \, \nabla_x \widetilde{u} \rangle \sqrt{\det \boldsymbol{T}} \, \mathrm{d}\Gamma \,, \end{aligned} \tag{6.107}$$

where we again make use of the orthogonality between the surface tangent vectors and its normal vector.

6.5 Assembly of element matrices

6.5.1 Numerical quadrature

Although the base functions are expressed using (α, β, γ) the domain is either the reference triangle or the reference tetrahedron, which require fewer quadrature points than their counterparts given by the Duffy transformation (quad or hexahedron). As such, we employ a mixture of the efficient quadrature points introduced in [34, 51, 84, 108, 109] for triangles and tetrahedra, where we avoid quadrature schemes with points on the edges or faces of the reference domain due to the recursion formula of the Bernstein polynomials Eq. (6.11). The quadrature points are mapped to their equivalent expression in (α, β, γ). Consequently, the integration over the reference triangle or tetrahedron reads

$$\begin{aligned} \int_{A_e} f(x,y)\,\mathrm{d}A &= \int_\Gamma (f \circ (\xi, \eta))(\alpha, \beta) |\det \boldsymbol{J}|\,\mathrm{d}\Gamma\,, \\ \int_{V_e} f(x,y,z)\,\mathrm{d}V &= \int_\Omega (f \circ (\xi, \eta, \zeta))(\alpha, \beta, \gamma) |\det \boldsymbol{J}|\,\mathrm{d}\Omega\,. \end{aligned} \tag{6.108}$$

6.5.2 Schur complement

Unlike in standard finite elements, higher order finite elements often entail cell base functions, also known as bubble functions. The latter are not directly connected to neighbouring elements and as such, can be statically condensed using the Schur complement method. We proceed by partitioning the field into boundary values $\mathbf{u}_b$ and cell values $\mathbf{u}_c$, thus resulting in the discrete vectors and stiffness matrix

$$\mathbf{u}_e^d = \begin{bmatrix} \mathbf{u}_b \\ \mathbf{u}_c \end{bmatrix}, \qquad \mathbf{f}_e^d = \begin{bmatrix} \mathbf{f}_b \\ \mathbf{f}_c \end{bmatrix}, \qquad \boldsymbol{K}_e = \begin{bmatrix} \boldsymbol{K}_{bb} & \boldsymbol{K}_{bc} \\ \boldsymbol{K}_{cb} & \boldsymbol{K}_{cc} \end{bmatrix}. \tag{6.109}$$

Consequently, we can express the discrete values of the cell base functions via

$$\mathbf{u}_c = \boldsymbol{K}_{cc}^{-1}(\mathbf{f}_c - \boldsymbol{K}_{cb}\mathbf{u}_b)\,. \tag{6.110}$$

Inserting the latter in the upper row of the system of equations yields

$$\boldsymbol{K}_{bb}\mathbf{u}_b + \boldsymbol{K}_{bc}\boldsymbol{K}_{cc}^{-1}(\mathbf{f}_c - \boldsymbol{K}_{cb}\mathbf{u}_b) = \mathbf{f}_b \quad \iff \quad (\boldsymbol{K}_{bb} - \boldsymbol{K}_{bc}\boldsymbol{K}_{cc}^{-1}\boldsymbol{K}_{cb})\mathbf{u}_b = \mathbf{f}_b - \boldsymbol{K}_{bc}\boldsymbol{K}_{cc}^{-1}\mathbf{f}_c\,. \tag{6.111}$$

Thus, the condensed stiffness matrix and load vector read

$$\boldsymbol{K}_e^* = \boldsymbol{K}_{bb} - \boldsymbol{K}_{bc}\boldsymbol{K}_{cc}^{-1}\boldsymbol{K}_{cb}\,, \qquad \mathbf{f}_e^* = \mathbf{f}_b - \boldsymbol{K}_{bc}\boldsymbol{K}_{cc}^{-1}\mathbf{f}_c\,. \tag{6.112}$$

Two main advantages of the procedure are discussed in [110]. Firstly, the global matrix has a much smaller dimension. Secondly, the condensed matrix is usually better conditioned. Both combined lead to faster and more accurate solutions. The discrete values of the cell base functions can be recovered after the global solution step via Eq. (6.110) and used for internal interpolation.

Remark 6.7

In case of both linear elasticity and the relaxed micromorphic continuum the bilinear forms are symmetric positive definite. Consequently, the computation of $\boldsymbol{K}_{cc}^{-1}$ in the hp-FEA software Rayse is achieved using the in-place Cholesky decomposition ($\boldsymbol{L}\boldsymbol{L}^T$).

7 Numerical examples

A common method for testing the efficiency of finite elements is by constructing artificial analytical solutions. We define the analytical displacement field $\widetilde{\mathbf{u}}$ and analytical microdistortion field $\widetilde{\boldsymbol{P}}$ and compute the resulting residuum by inserting them into the corresponding strong forms. Thus, the corresponding volume forces $\mathbf{f}$ and micro-moments $\boldsymbol{M}$ are retrieved. Prescribing the entire boundary with the appropriate Dirichlet boundary conditions $\partial V = A_D$ and applying the extracted volume forces and micro-moments guarantees the defined fields to be the analytical solutions. This is clearly the case since they equilibrate the problem and by the Lax-Milgram theorem, the solution is unique.

In the following we test the finite element formulations with both artificial analytical solutions and analytical solutions derived for infinite domains. Specifically the behaviour of the approximations in comparison to the analytical solutions for infinite domains is an indicator for appropriate choices of finite elements, as these solutions represent the intrinsic behaviour of the model. In addition, we test the ability of the finite element formulations to correctly iterate between micro $\mathbb{C}_{\text{micro}}$ and macro $\mathbb{C}_{\text{macro}}$ stiffnesses as described by the characteristic length parameter L_c. A fitting of the L_c parameter for an homogenized body with an underlying discrete microstructure is presented in the plane strain model.

The majority of convergence results are presented by measuring the error in the Lebesgue norm over the domain

$$\|\widetilde{\mathbf{u}} - \mathbf{u}^h\|_{L^2} = \sqrt{\int_V \|\widetilde{\mathbf{u}} - \mathbf{u}^h\|^2 \,\mathrm{d}V} \,, \qquad \|\widetilde{\boldsymbol{P}} - \boldsymbol{P}^h\|_{L^2} = \sqrt{\int_V \|\widetilde{\boldsymbol{P}} - \boldsymbol{P}^h\|^2 \,\mathrm{d}V} \,, \tag{7.1}$$

in which context $\{\widetilde{\mathbf{u}}, \widetilde{\boldsymbol{P}}\}$ and $\{\mathbf{u}^h, \boldsymbol{P}^h\}$ are the analytical and approximate subspace solutions, respectively.

7.1 Antiplane shear

7.1.1 Exponential convergence for trigonometric solutions

We start testing the convergence rates by constructing an artificial analytical solution for antiplane shear. The domain is defined to be the axis-symmetric square $\overline{A} = [-10, 10]^2$ with a complete Dirichlet boundary $s_D = \partial A$. The displacement and microdistortion fields are chosen to be

$$\widetilde{u} = \sin(x) + \cos(y) \,, \qquad \widetilde{\mathbf{p}} = \nabla \widetilde{u} = \begin{bmatrix} \cos(x) \\ -\sin(y) \end{bmatrix} \,, \tag{7.2}$$

and are embedded into the Dirichlet boundary. By inserting the latter into the strong forms in Problem. 3.2.2 we extract the corresponding force and micro-moment fields

$$f = 0 \,, \qquad \mathbf{m} = \mu_{\text{micro}} \begin{bmatrix} \cos(x) \\ -\sin(y) \end{bmatrix} \,, \tag{7.3}$$

where for simplicity, we set all material constants to one $\mu_\text{e} = \mu_{\text{micro}} = \mu_{\text{macro}} = L_\text{c} = 1$. The behaviour of the displacement u and the microdistortion $\mathbf{p}$ is depicted in Fig. 7.2. We note that a reasonable visual approximation is first achieved with 940 linear elements or 66 cubic elements. The convergence results of the respective fields are given in Fig. 7.1. We note that both Nédélec element formulations yield the same convergence rates. This is to be expected as $\mathcal{N}_I$ is enriched in its solenoidal part (in comparison to $\mathcal{N}_{II}$) and the solution is completely irrotational. As such, the added base functions do not improve the solution and yield zero. The main advantage of higher order finite elements becomes

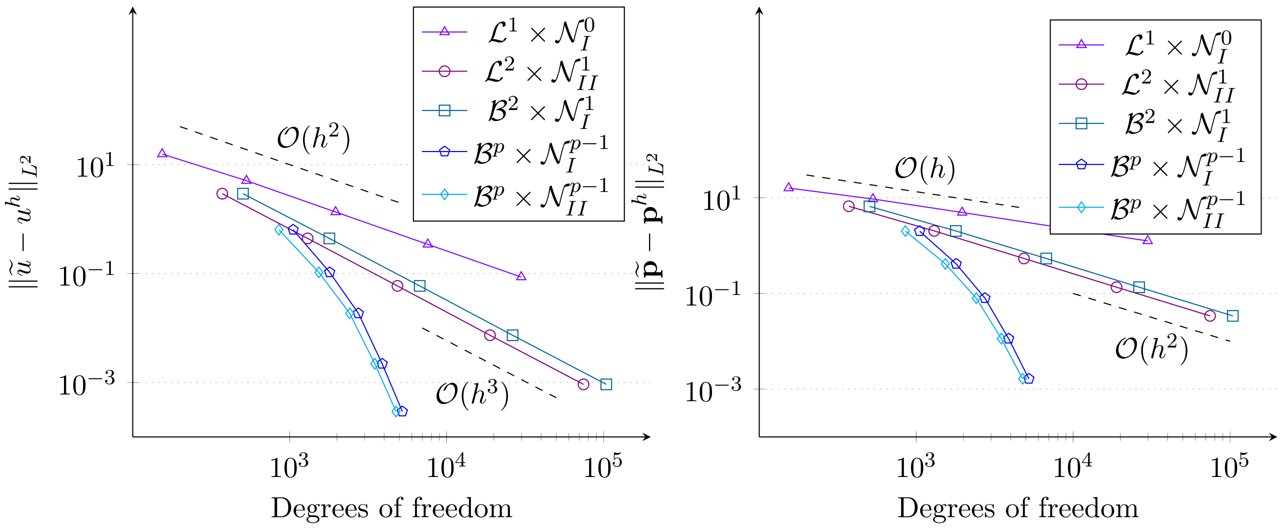

(a) (b)

Figure 7.1: Convergence of the lower order elements under h-refinement and of the higher order elements under p-refinement over $p \in \{3, 4, 5, 6, 7\}$ with 66 elements. The error in the displacement is given in (a) and the error in the microdistortion in (b).

apparent when considering the exponential convergence of $\mathcal{B}^p \times \mathcal{N}_I^{p-1}$ and $\mathcal{B}^p \times \mathcal{N}_{II}^{p-1}$. In terms of amount of degrees of freedom, the refinement of the order of an element, known as p-refinement or p-adaption, allows to more efficiently approximate the exact solution. In comparison, decreasing the element size (h-refinement) is bound to an algebraic rate.

In order to observe the difference in convergence between the Nédélec element of the first type and Nédélec element of the second type we require a solenoidal field in the microdistortion. We define the domain $\overline{A} = [-2, 2]^2$. The prescribed displacement and microdistortion fields read

$$\widetilde{u} = \frac{(x^2-4)(y^2-4)}{4}\,, \qquad\qquad \widetilde{\mathbf{p}} = \sin([x^2-4][y^2-4]) \begin{bmatrix} y \\ -x \end{bmatrix}, \tag{7.4}$$

and are embedded on the Dirichlet boundary $s_D = \partial A$. Clearly, $\widetilde{\mathbf{p}}$ cannot be given by some gradient of a scalar potential. The corresponding force and micro-moment are derived for the same material constants as in the previous example (all set to one)

$$f = \frac{1}{2}(4xy(y^2-4)\cos([x^2-4][y^2-4]) - 4xy(x^2-4)\cos([x^2-4][y^2-4]) - x^2 - y^2 + 8)\,,$$

$$\mathbf{m} = \frac{1}{2}\left[\begin{matrix} 8x^2y\left(x^2-4\right)\left(y^2-4\right)\sin\left(\left(x^2-4\right)\left(y^2-4\right)\right) - 8x^2y\cos\left(\left(x^2-4\right)\left(y^2-4\right)\right) - x\left(y^2-4\right) \\ -8x^3\left(y^2-4\right)^2\sin\left(\left(x^2-4\right)\left(y^2-4\right)\right) - 8xy^2\left(x^2-4\right)\left(y^2-4\right)\sin\left(\left(x^2-4\right)\left(y^2-4\right)\right) \end{matrix}\right. \dots$$

$$\begin{matrix} +8y^3\left(x^2-4\right)^2\sin\left(\left(x^2-4\right)\left(y^2-4\right)\right) - 16y\left(x^2-4\right)\cos\left(\left(x^2-4\right)\left(y^2-4\right)\right) \\ +8xy^2\cos\left(\left(x^2-4\right)\left(y^2-4\right)\right) + 16x\left(y^2-4\right)\cos\left(\left(x^2-4\right)\left(y^2-4\right)\right) \end{matrix} \dots$$

$$\left.\begin{matrix} +4y\sin\left(\left(x^2-4\right)\left(y^2-4\right)\right) \\ -4x\sin\left(\left(x^2-4\right)\left(y^2-4\right)\right) - y\left(x^2-4\right) \end{matrix}\right]. \tag{7.5}$$

The displacement and microdistortion fields are depicted in Fig. 7.3. Considering the left edge of the domain, it is apparent that only the quadratic $\mathcal{B}^2 \times \mathcal{N}_I^1$-formulation deals with boundary conditions

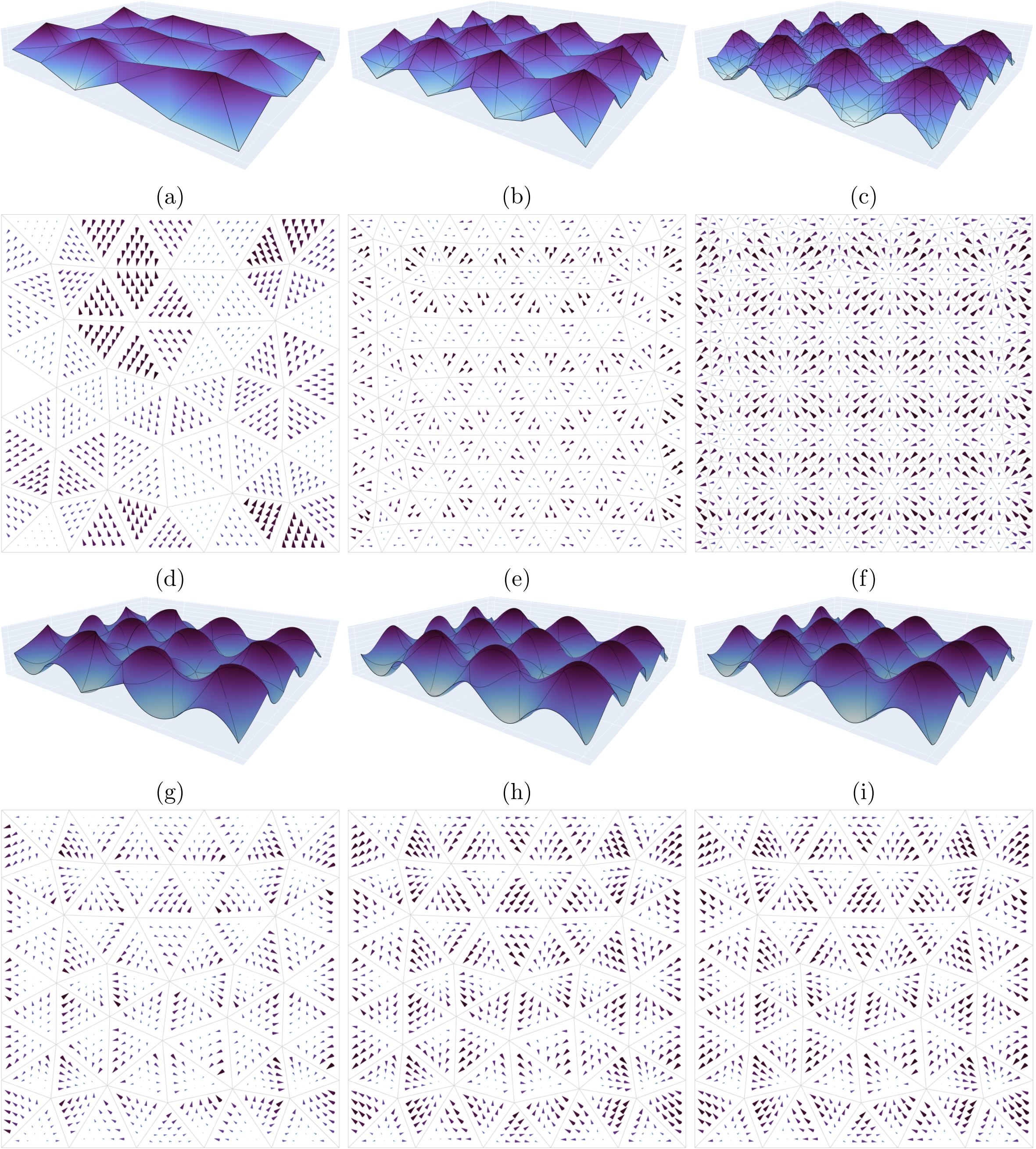
(a) (b) (c)
(d) (e) (f)
(g) (h) (i)
(j) (k) (l)

Figure 7.2: Depiction of the displacement field (a)-(c) and the microdistortion field (d)-(f) for the linear element under h-refinement with 66, 244 and 940 elements, corresponding to 154, 530 and 1962 degrees of freedom. The p-refinement of the displacement field on the coarsest mesh of 66 elements is visualized in (g)-(l) with $p \in \{2, 3, 4\}$, corresponding to 372, 845 and 1534 degrees of freedom.

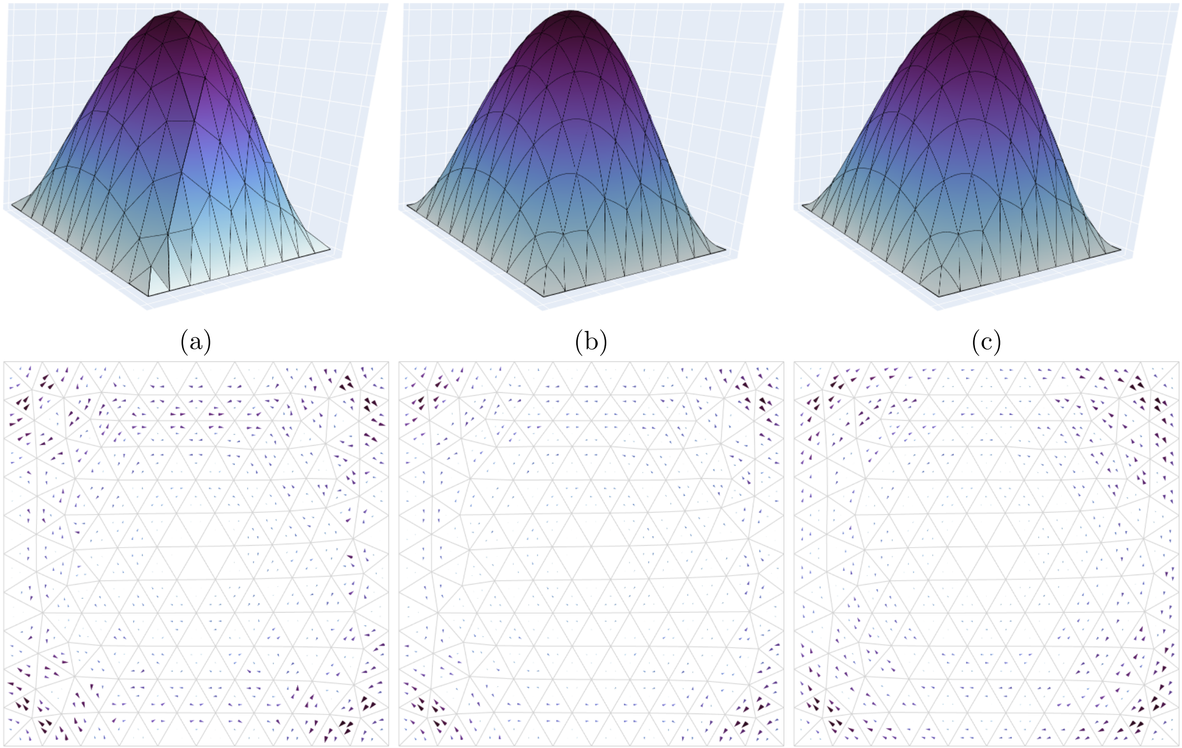

(a) (b) (c)

(d) (e) (f)

Figure 7.3: Depiction of the displacement field (a)-(c) and the microdistortion field (d)-(f) using 246 elements of the $\mathcal{L}^1 \times \mathcal{N}_I^0$-, $\mathcal{L}^2 \times \mathcal{N}_{II}^1$- and $\mathcal{B}^2 \times \mathcal{N}_I^1$-formulations.

correctly. This is the case due to $\mathcal{B}^2 \times \mathcal{N}_I^1$ being the lowest order formulation that introduces cell base functions for the microdistortion, thus allowing to better separate the behaviour of its tangential and normal components on the boundary. Despite introducing a non-gradient solution for the microdistortion $\mathbf{p}$ the convergence rates given in Fig. 7.4 do not improve when moving from the $\mathcal{N}_{II}$- to the $\mathcal{N}_I$-formulation. Recalling Lemma 5.8 and Remark 5.5 it is clear that the s-regularity of the current problem is $s = 1$.

7.1.2 Normal-discontinuous microdistortion

Nédélec elements are tangentially continuous and as such, allow for a discontinuous normal component at an interface between elements. This feature is a characteristic of the larger space $H(\text{curl}) \supset H^1$ and must be captured correctly by the approximating discrete subspace. Consequently, we test the validity of the proposed finite elements by constructing an artificial analytical solution with a jump in the normal component of the microdistortion and measure the resulting convergence rates. The analytical solution is defined as

$$\widetilde{u} = \begin{cases} (1-y^2)(e^{x+1}-1) & \text{for} \quad x \leq 0 \\ (1-y^2)(e^{1-x}-1) & \text{for} \quad x > 0 \end{cases} , \qquad \widetilde{\mathbf{p}} = \nabla \widetilde{u} = \begin{cases} \begin{bmatrix} \left(1-y^2\right) e^{x+1} \\ 2y\left(1-e^{x+1}\right) \end{bmatrix} & \text{for} \quad x \leq 0 \\ \begin{bmatrix} \left(y^2-1\right) e^{1-x} \\ 2y\left(1-e^{1-x}\right) \end{bmatrix} & \text{for} \quad x > 0 \end{cases} . \tag{7.6}$$

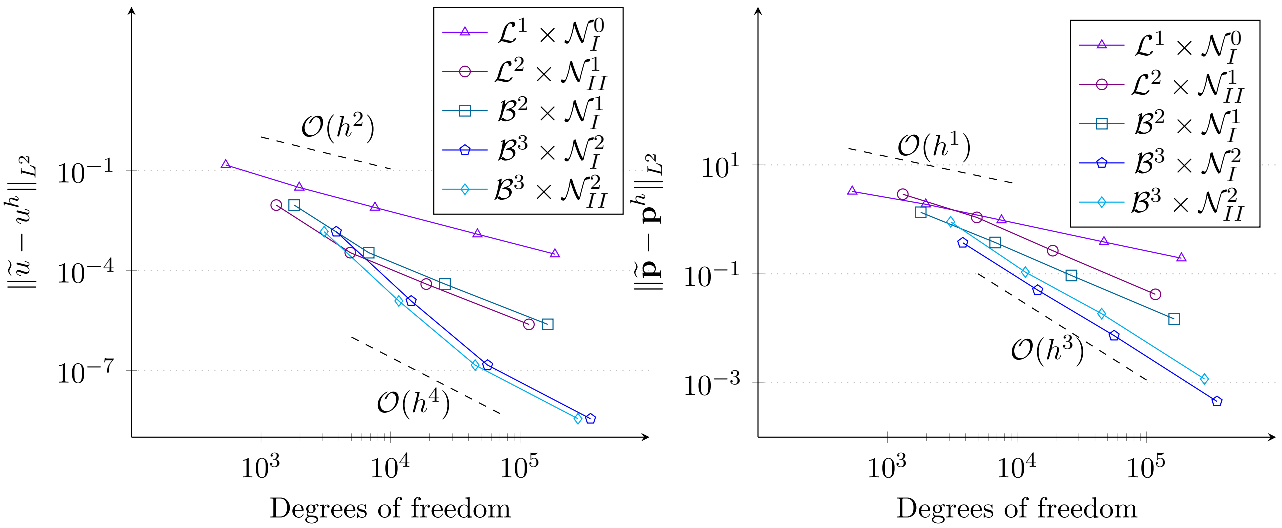

(a) (b)

Figure 7.4: Convergence of the displacement (a) and the microdistortion (b) under h-refinement.

The fields are embedded on the Dirichlet boundary $\overline{s}_D = \partial A$ of the axis-symmetric domain $\overline{A} = [-1, 1]^2$. The jump of the normal component is clearly at the interface $x = 0$. The corresponding micro-moment vector induced by the strong form reads

$$\mathbf{m} = \begin{cases} \begin{bmatrix} \left(1 - y^2\right) e^{x+1} \\ 2y \left(1 - e^{x+1}\right) \end{bmatrix} & \text{for} \quad x \leq 0 \\ \begin{bmatrix} \left(y^2 - 1\right) e^{1-x} \\ 2y \left(e^x - e\right) e^{-x} \end{bmatrix} & \text{for} \quad x > 0 \end{cases} , \tag{7.7}$$

where all the material constants are set to one. Due to $\widetilde{\mathbf{p}} = \nabla \widetilde{u}$ no body forces occur, compare with Eq. (3.47a). The jump in the normal component is depicted in Fig. 7.5. The linear formulation captures the solution well for a fine enough discretization. On the coarsest mesh, first the cubic formulation yields a satisfactory approximation of the displacement yield. This can be observed when comparing the top of the displacement fields at $(x, y) = (0, 0)$ where quadratic formulation yields a faulty sharp edge. The convergence rates are given in Fig. 7.6. Clearly, the optimal convergence rate is maintained across the various polynomial formulations and even exponential convergence is observed for pure p-refinement. In comparison, a formulation with $\mathbf{p} \in [H^1(A)]^2$ would impose the higher regularity C^0 on the microdistortion. This can be done using H^1-conforming finite elements for the formulation of the microdistortion $\mathbf{p}$ and leads to suboptimal convergence rates, see [101].

7.1.3 Motz's problem

The application of p-refinement leads to exponential convergence when the analytical solution is smooth enough. However, in practice, many geometries and load cases induce singularities in the behaviour of the solution, such that exponential convergence is lost. The hp-finite element method can regain exponential convergence by applying simultaneous h- and p-refinements. The h-refinement is applied to the area of the domain where the singularity arises, thus localizing it further. At the same time, p-refinement is applied to areas of the domain where highly smooth solutions are expected.

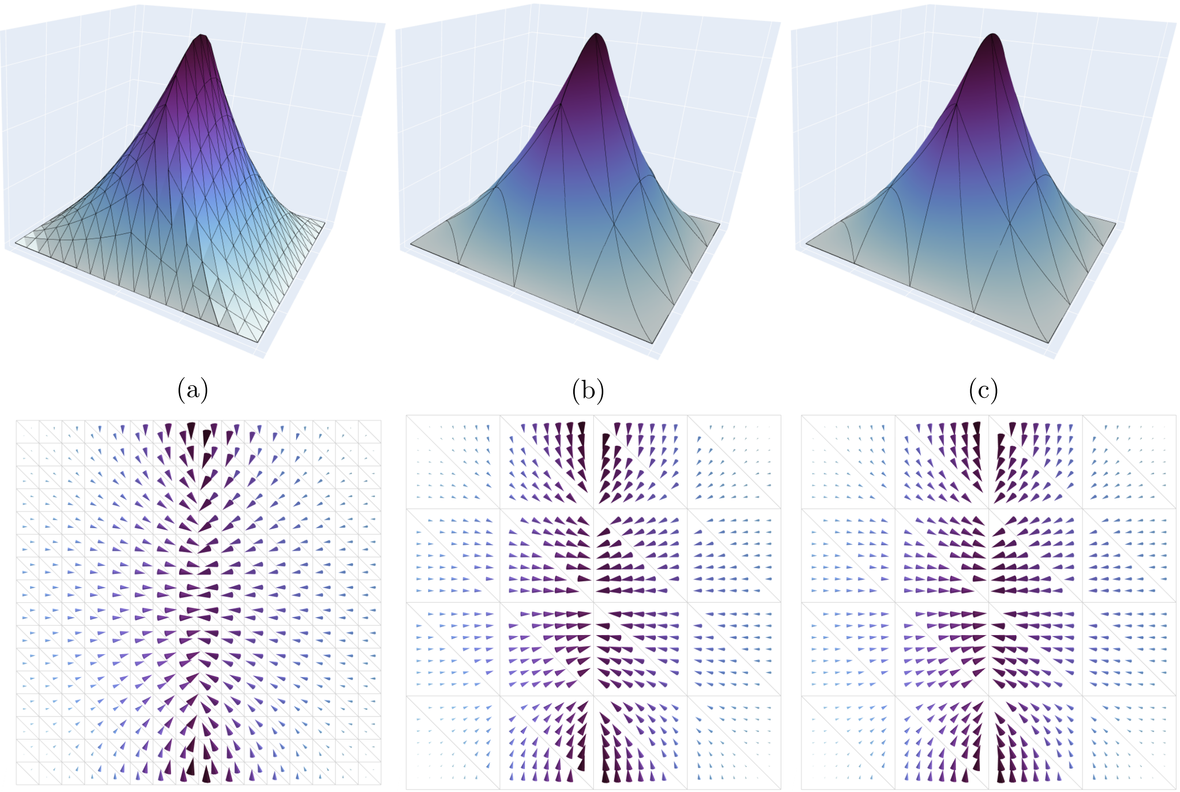

(a) (b) (c)

(d) (e) (f)

Figure 7.5: Displacement field using 1090 linear elements (a), 32 quadratic elements (b) and 32 cubic elements (c), corresponding to 1090, 258 and 530 degrees of freedom, respectively. The related microdistortion fields are depicted in (d)-(f).

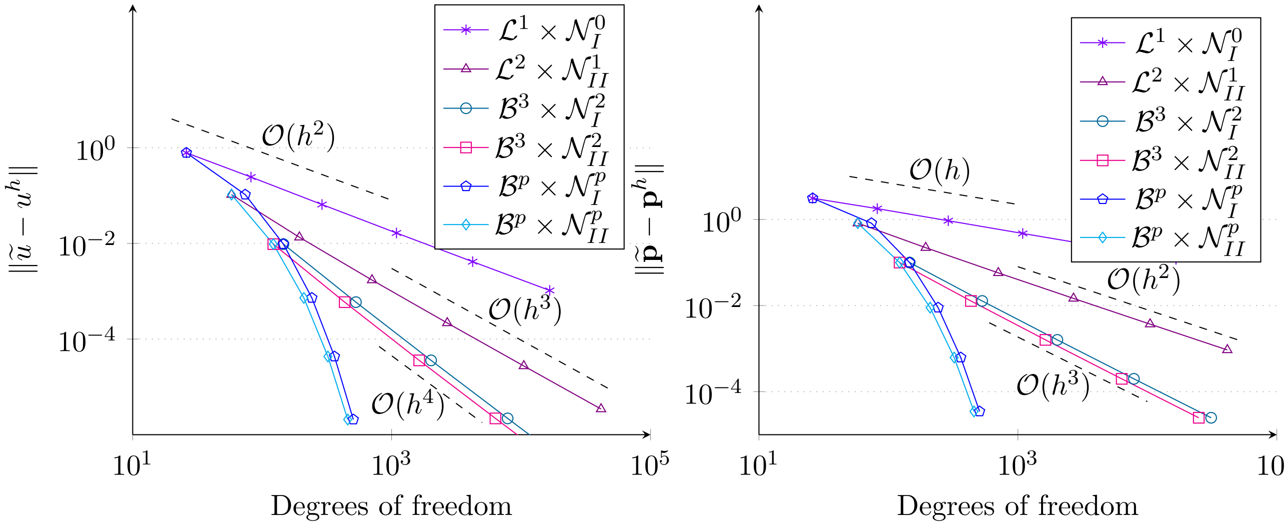

(a) (b)

Figure 7.6: Displacement (a) and microdistortion (b) fields of the discontinuous-normal problem and convergence rates under h-, p-, and hp-refinements (b).

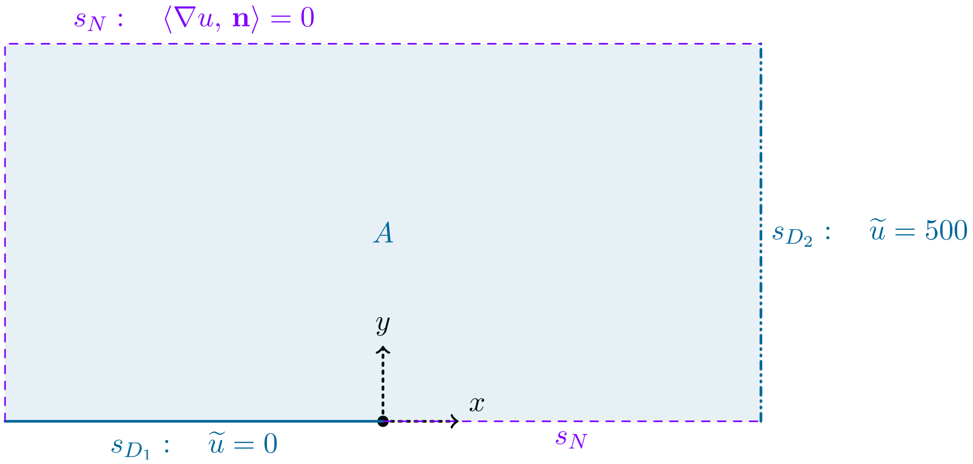

Figure 7.7: Domain and boundary conditions of Motz's problem.

In the following we consider Motz's problem, which is a common benchmark for hp-refinement techniques. The domain is defined to be $\overline{A} = [-1, 1] \times [0, 1]$ and the boundary is split as follows

$$\overline{s}_{D_1} = [-1, 0] \times \{0\} \, , \qquad \overline{s}_{D_2} = \{1\} \times [0, 1] \, , \qquad s_N = \partial A \setminus (\overline{s}_{D_1} \oplus \overline{s}_{D_1}) \, , \tag{7.8}$$

such that on the Dirichlet boundary the displacement reads

$$\widetilde{u} \bigg|_{s_{D_1}} = 0 \, , \qquad \widetilde{u} \bigg|_{s_{D_2}} = 500 \, . \tag{7.9}$$

A depiction of the problem is given in Fig. 7.7. The displacement field provokes a singularity at $(x, y) = (0, 0)$ where the gradient of u approaches infinity [63]. The analytical solution of Motz's problem is given by the infinite series

$$u(r, \varphi) = \sum_{j=0}^{\infty} d_j r^{j+1/2} \cos([j + 1/2]\varphi) \, , \qquad r = \sqrt{x^2 + y^2} \, , \qquad \varphi = \arctan(y/x) \, , \tag{7.10}$$

where d_i are the true expansion coefficients. Here we make use of the numerically accurate expansion coefficients derived in [63] to validate our results.

Note that Motz's problem is defined for the Laplace equation $\Delta u = 0$ and not the relaxed micromorphic model. However, as shown in Section 3.2.3, it suffices to set the characteristic length to zero $L_c = 0$ in order to obtain similar behaviour.

The employed meshes are depicted im Fig. 7.8. The comparison follows by using both global h-refinement on structured meshes and local h-refinement at the point of the singularity on unstructured meshes. Due to the complex nature of the analytical solution we deviate from the Lebesgue norm and measure convergence by sampling approximatively 1500 points throughout the domain

$$e = \sqrt{\sum_{i=1}^{\approx 1500} (\widetilde{u} - u)^2 \bigg|_{\mathbf{x}_i}} \, . \tag{7.11}$$

The solutions of the displacement and microdistortion fields are depicted in Fig. 7.9 (a)-(b). The singularity is clearly illustrated by the intensity of the microdistortion. The convergence rates are given in Fig. 7.9 (c). Due to the singularity, using either linear or quadratics elements under h-refinement leads only to linear convergence. Interestingly, quadratic convergence is shown for p-refinement. Optimal exponential convergence is recovered by applying the localized h-refinement at the singularity and simultaneously increasing the polynomial order of the elements.

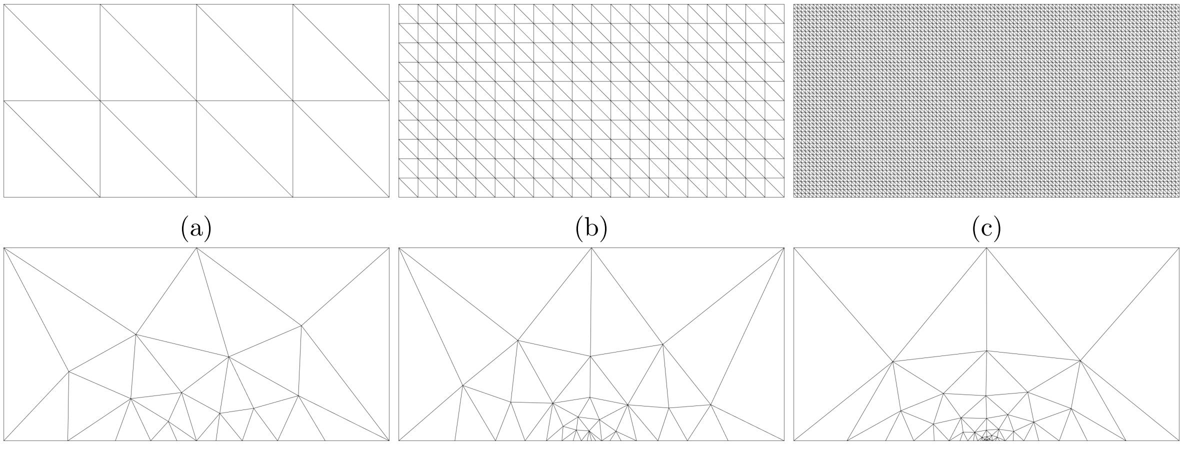

Figure 7.8: Global h-refinement of the structured mesh (16, 400 and 10000 elements) (a)-(c) and local h-refinement of the unstructured mesh (32, 52 and 80 elements) at the singularity point (d)-(f).

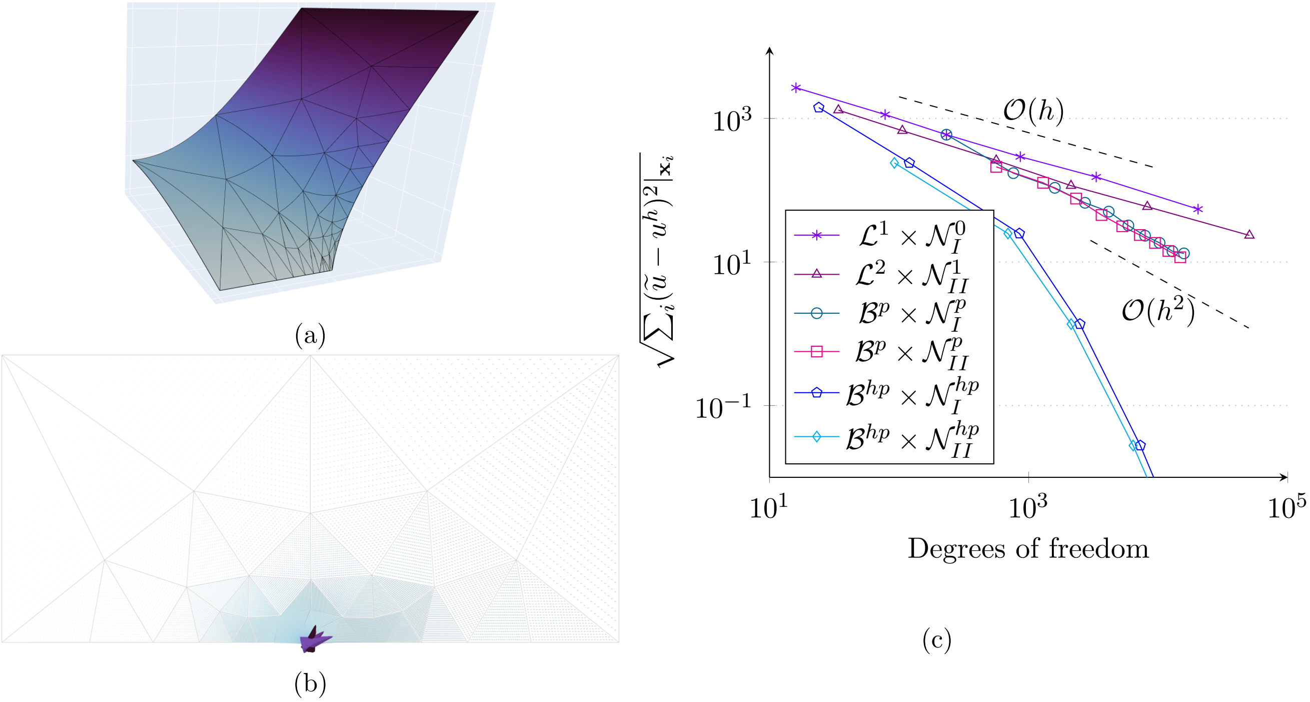

Figure 7.9: Displacement (a) and microdistortion (b) fields of the Motz problem and convergence rates under h-, p-, and hp-refinements (b).

7.1.4 Gradient microdistortion

In Theorem 4.6 we explored the conditions for which the microdistortion reduces to a gradient field. By defining the micro-moment with a scalar potential

$$\mathbf{m} = \nabla \frac{100 - x^2 - y^2}{10} = -\frac{1}{5} \begin{bmatrix} x \\ y \end{bmatrix} , \tag{7.12}$$

and constructing an analytical solution for the displacement field

$$\widetilde{u} = \sin\left(\frac{x^2 + y^2}{5}\right) , \tag{7.13}$$

we can recover the analytical solution of the microdistortion

$$\begin{aligned} \mathbf{p} = \frac{1}{\mu_{\mathrm{e}} + \mu_{\mathrm{micro}}} (\mathbf{m} + \mu_{\mathrm{e}} \nabla \widetilde{u}) &= \frac{1}{2} \left(-\frac{1}{5} \begin{bmatrix} x \\ y \end{bmatrix} + \frac{2}{5} \begin{bmatrix} x \cos([x^2 + y^2]/5) \\ y \cos([x^2 + y^2]/5) \end{bmatrix} \right) \\ &= \frac{1}{5} \begin{bmatrix} x \cos([x^2 + y^2]/5) \\ y \cos([x^2 + y^2]/5) \end{bmatrix} - \frac{1}{10} \begin{bmatrix} x \\ y \end{bmatrix} , \end{aligned} \tag{7.14}$$

where for simplicity we set all material constants to one. We note that the microdistortion is not equal to the gradient of the displacement field and as such, their tangential projections on an arbitrary boundary are not automatically the same. However, for both the gradient of the displacement field and the micro-moment is the tangential projection on the boundary of the circular domain $\overline{A} = \{\mathbf{x} \in \mathbb{R}^2 \mid \|\mathbf{x}\| \leq 10\}$ equal to zero

$$\langle \nabla \mathbf{t}, \, \widetilde{u} \rangle \bigg|_{\partial A} = \langle \mathbf{t}, \, \mathbf{m} \rangle \bigg|_{\partial A} = 0 , \tag{7.15}$$

and as such the microdistortion belongs to $\mathbf{p} \in H_0(\mathrm{curl}, A)$. Consequently, we can set $s_D = \partial A$ and the consistent coupling condition remains compatible. With the displacement and the microdistortion fields at hand we derive the corresponding forces

$$f = \frac{1}{25} \left[2x^2 \sin\left(\frac{x^2 + y^2}{5}\right) + 2y^2 \sin\left(\frac{x^2 + y^2}{5}\right) - 10 \cos\left(\frac{x^2 + y^2}{5}\right) - 5 \right] . \tag{7.16}$$

The approximation of the displacement and microdistortion fields using linear and higher order elements is depicted in Fig. 7.10. We note that even with almost 3000 finite elements and 6000 degrees of freedom the linear formulation is incapable of finding an adequate approximation. On the other side of the spectrum, the higher order approximation (degree 7) with 57 elements and 4097 degrees of freedom yields very accurate results in the interior of the domain. However, the exterior of the domain is captured rather poorly. This is the case since the geometry of the circular domain is being approximated by linear triangles. Thus, in this setting, a finer mesh captures the geometry in a more precise manner. The effects of the geometry on the approximation of the solution are also clearly visible in the convergence graphs in Fig. 7.11; only after a certain accuracy in the domain description is achieved do the finite elements retrieve their predicted convergence rates. This is clearly observable when comparing the convergence curves of the linear and seventh order elements. The linear element generates quadratic convergence $p + 1 = 1 + 1 = 2$, whereas the seventh-order element yields the convergence slope 7 (where 8 is expected). Although the seventh-order formulation encompasses more degrees of freedom, it employs a coarser mesh and as such, generates higher errors at the boundary. The errors themselves can be traced back to the consistent coupling condition since, for a non-perfect circle the gradient of the displacement field induces tangential projections on the imperfect boundary. The influence of the latter effect is even more apparent in the convergence of the microdistortion, where the higher order formulations are unable to perform optimally on coarse meshes.

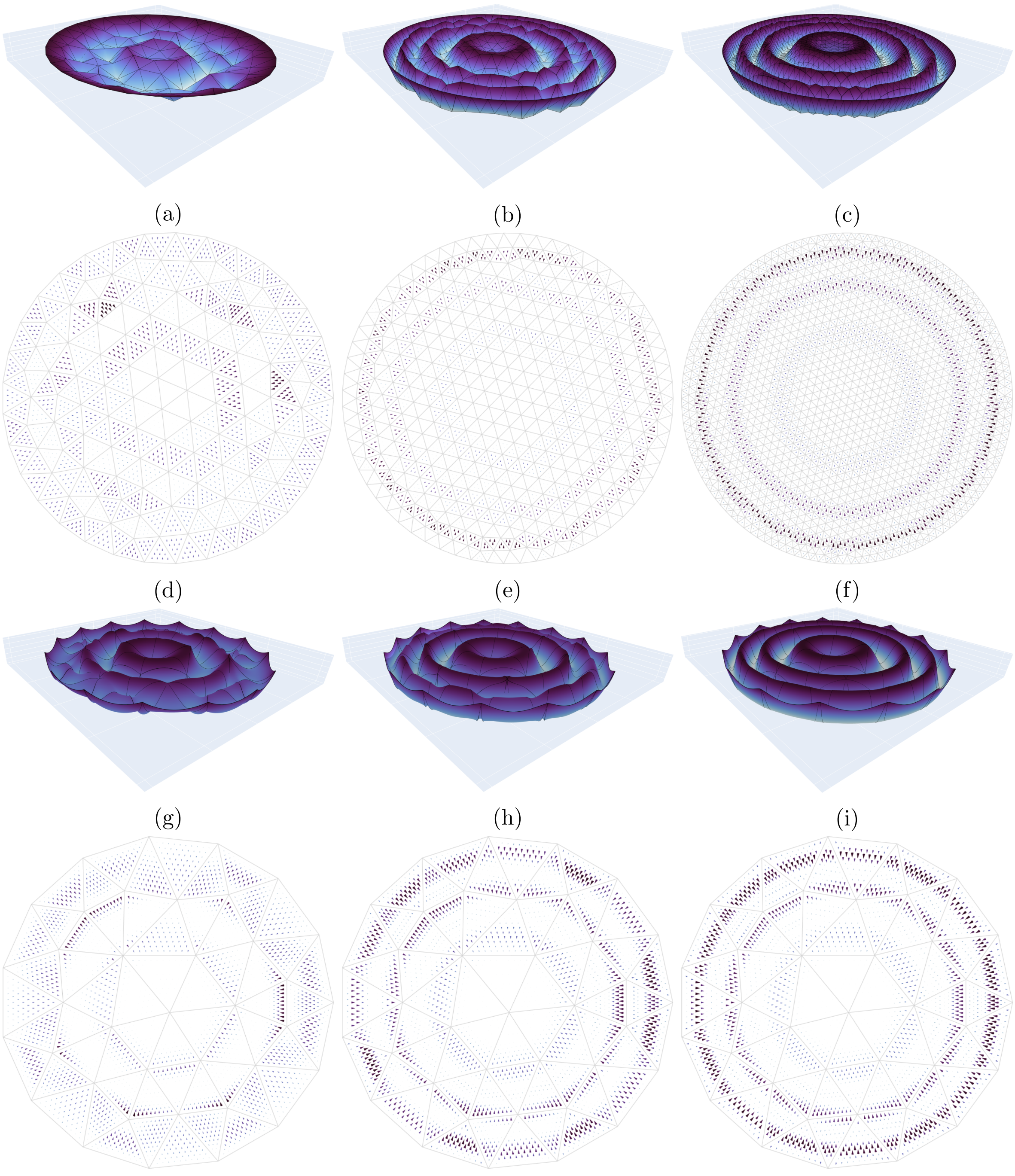

(a) (b) (c)

(d) (e) (f)

(g) (h) (i)

(j) (k) (l)

Figure 7.10: Depiction of the displacement field (a)-(c) and the microdistortion field (d)-(f) for the linear element under h-refinement with 225, 763 and 2966 elements, corresponding to 485, 1591 and 6060 degrees of freedom. The p-refinement of the displacement field on the coarsest mesh of 57 elements is visualized in (g)-(l) with $p \in \{3, 5, 7\}$, corresponding to 731, 2072 and 4097 degrees of freedom.

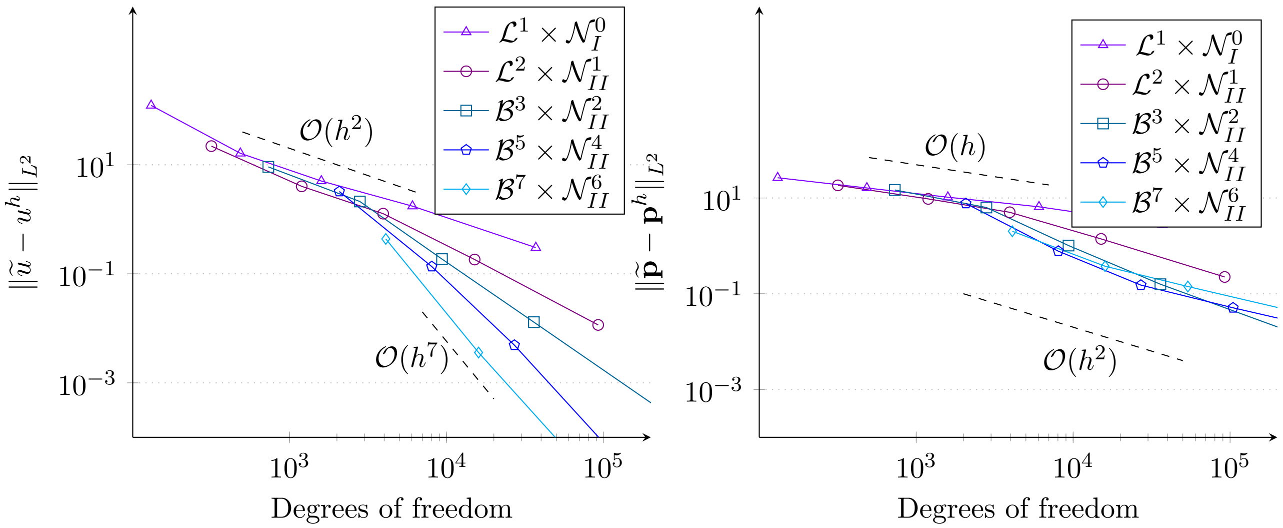

(a) (b)

Figure 7.11: Convergence of displacement (a) and the microdistortion (b) under h-refinement for multiple polynomial degrees.

7.2 Plane strain

7.2.1 Shear stiffness

The relaxed micromorphic model is able to interpolate between stiffnesses defined by the macro and micro material parameters [90]. This is achieved by varying the characteristic length parameter L_c and reflects the influence of the microstructure on the stiffness of the system consequently on the resulting deformations.

In the following we test the behaviour of the plane strain model under shear deformation and vary the characteristic length scale parameter L_c. The domain is given by $\overline{A} = [0, 10]^2$ with the Dirichlet boundaries $\overline{s}_{D_1} = [0, 10] \times \{0\}$ and $\overline{s}_{D_2} = [0, 10] \times \{10\}$ such that the Neumann boundary reads $s_D = \partial A \setminus \{\overline{s}_{D_1} \oplus \overline{s}_{D_2}\}$. On the Dirichlet boundary we embed the constant displacement fields

$$\widetilde{\mathbf{u}}\Big|_{s_{D_1}} = \begin{bmatrix} 0 \\ 0 \end{bmatrix}, \qquad \widetilde{\mathbf{u}}\Big|_{s_{D_2}} = \begin{bmatrix} 4 \\ 0 \end{bmatrix}. \tag{7.17}$$

The material constants of the micro- and macro-structure are chosen to represent the expected result of higher micro stiffness

$$\lambda_{\text{macro}} = 10, \qquad \mu_{\text{macro}} = 5, \qquad \lambda_{\text{micro}} = 50, \qquad \mu_{\text{micro}} = 25, \qquad \mu_c = 5\,. \tag{7.18}$$

The meso-parameters are retrieved by reformulating Eq. (3.20)

$$\mu_e = \frac{\mu_{\text{micro}}\mu_{\text{macro}}}{\mu_{\text{micro}} - \mu_{\text{macro}}}\,, \qquad \lambda_e = \frac{1}{3}\left(\frac{(2\mu_{\text{micro}} + 3\lambda_{\text{micro}})(2\mu_{\text{macro}} + 3\lambda_{\text{macro}})}{(2\mu_{\text{micro}} + 3\lambda_{\text{micro}}) - (2\mu_{\text{macro}} + 3\lambda_{\text{macro}})} - 2\mu_e\right)\,, \tag{7.19}$$

and read

$$\lambda_e = 12.5\,, \qquad \mu_e = 6.25\,. \tag{7.20}$$

The displacement field and the corresponding microdistortion are depicted in Fig. 7.12 for $L_c \in \{10, \sqrt{10}, 1\}$. The behaviour of the displacement follows the pattern of the analytical solution for simple shear derived in [90]. Namely, for high L_c-values it is flat, for mid-values curved and for low values it flattens again. The intensity of the microdistortion increases with a decreasing L_c-value.

We measure the energy of the model with varying L_c-values. The lower bound is given according to Eq. (3.19) by an equivalent Cauchy model. We compute the energy with tenth order finite elements for high accuracy and find $I_\mathrm{macro} \approx 15.6$. The upper bound is derived using Eq. (3.23) yielding $I_\mathrm{micro} \approx 78.03$. The progression of the energy in illustrated in Fig. 7.13. Clearly, the exactness of the subspace greatly influences the resulting energy and as such may distort the expected relation to an underlying micro-structure. Using linear elements requires very fine meshes to find valid results, as the stiffness is otherwise overestimated. Although quadratic elements already offer a major improvement, it is first with cubic elements that satisfactory results are achieved even on coarse meshes. This may be due to the intrinsic behaviour of the relaxed micromorphic model, seeing as the analytical solution predicts an hyperbolic function (incorporating sinh and tanh), for which power series expansions first become relevant when third order terms are included. On a very coarse mesh of 2 elements, accurate descriptions can be achieved by using higher order elements. We note that the change in the energy only occurs for $\mu_\mathrm{c} \neq 0$, which is also consistent with the results of [90]. If the coupling modulus is set to zero $\mu_\mathrm{c} = 0$, the relaxed micromorphic model always finds the energy of a Cauchy model with macro material parameters. The highest energy produced by the relaxed micromorphic model is $\lim_{L_\mathrm{c}\to\infty} I_\mathrm{Relaxed} \approx 35.1$. An equivalent Cauchy model produces the latter energy for the material constants $\lambda \approx 22.5$ and $\mu \approx 11.25$, where the assumption of a constant ratio between the Lamé parameters is used (implying a constant Poisson ratio).

7.2.2 Correspondence with micro-structured materials

The relaxed micromorphic model aspires to correctly capture the behaviour of materials with a pronounced microstructure. To that end, the characteristic length parameter L_c is applied to govern the influence of the microstructure. Essentially, the characteristic length parameter allows the relaxed micromorphic model to iterate between materials representing a discrete structure and those that are highly homogeneous and behave like standard continua. In [7] and [73] the authors derive the micro and macro stiffnesses of a metamaterial using homogenization

$$\begin{aligned} &\lambda_\mathrm{macro} = 1.74\,, && \mu_\mathrm{macro} = 5.89\,, && \mu^*_\mathrm{macro} = 0.62\,, && \lambda_\mathrm{micro} = 5.27\,, \\ &\mu_\mathrm{micro} = 12.8\,, && \mu^*_\mathrm{micro} = 8.33\,, && \mu_\mathrm{c} = 2.28 \cdot 10^{-3}\,, \end{aligned} \tag{7.21}$$

and the matrices of the material constants take the form

$$\mathbb{C} = \begin{bmatrix} 2\mu+\lambda & \lambda & 0 \\ \lambda & 2\mu+\lambda & 0 \\ 0 & 0 & 2\mu^* \end{bmatrix}, \qquad \boldsymbol{\varepsilon} = \begin{bmatrix} \varepsilon_{11} \\ \varepsilon_{22} \\ \varepsilon_{12} \end{bmatrix}, \tag{7.22}$$

in Voigt notation. The underlying geometry of the micro structure is depicted in Fig. 7.14. The material employed is aluminium with the following Lamé constants

$$\lambda = 51.08\,, \qquad \mu = 26.32\,. \tag{7.23}$$

An open question of the above works is the relation of the characteristic length to materials derived by a periodic embedding of the microstructure. In order to derive a relation, we compute a large set of Cauchy continua with fully resolved micro-structures, where the size of the underlying unit cell decreases. A depiction of the cells and their discretization is given in Fig. 7.15. We compute the energy of structures containing between 1×1 and up to 20×20 unit cells, for which the materials constants are those of aluminium. The fitting of the characteristic length L_c is then achieved by comparing

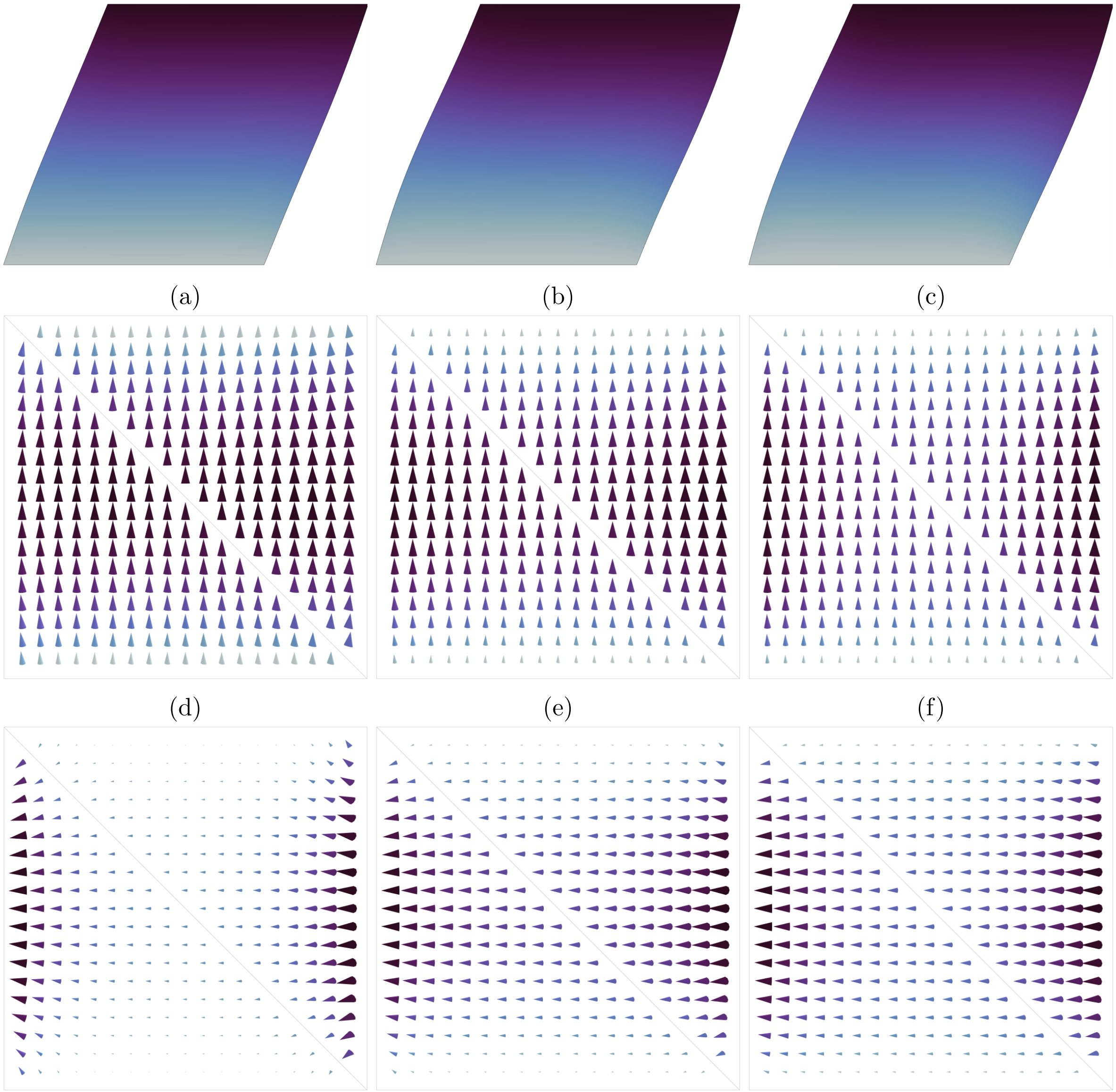

(a) (b) (c)

(d) (e) (f)

(g) (h) (i)

Figure 7.12: Displacement field with $L_c \in \{10, \sqrt{10}, 1\}$ (a)-(c), respectively. Depiction of the corresponding first row (d)-(f) and last row (h)-(g) of the microdistortion fields.

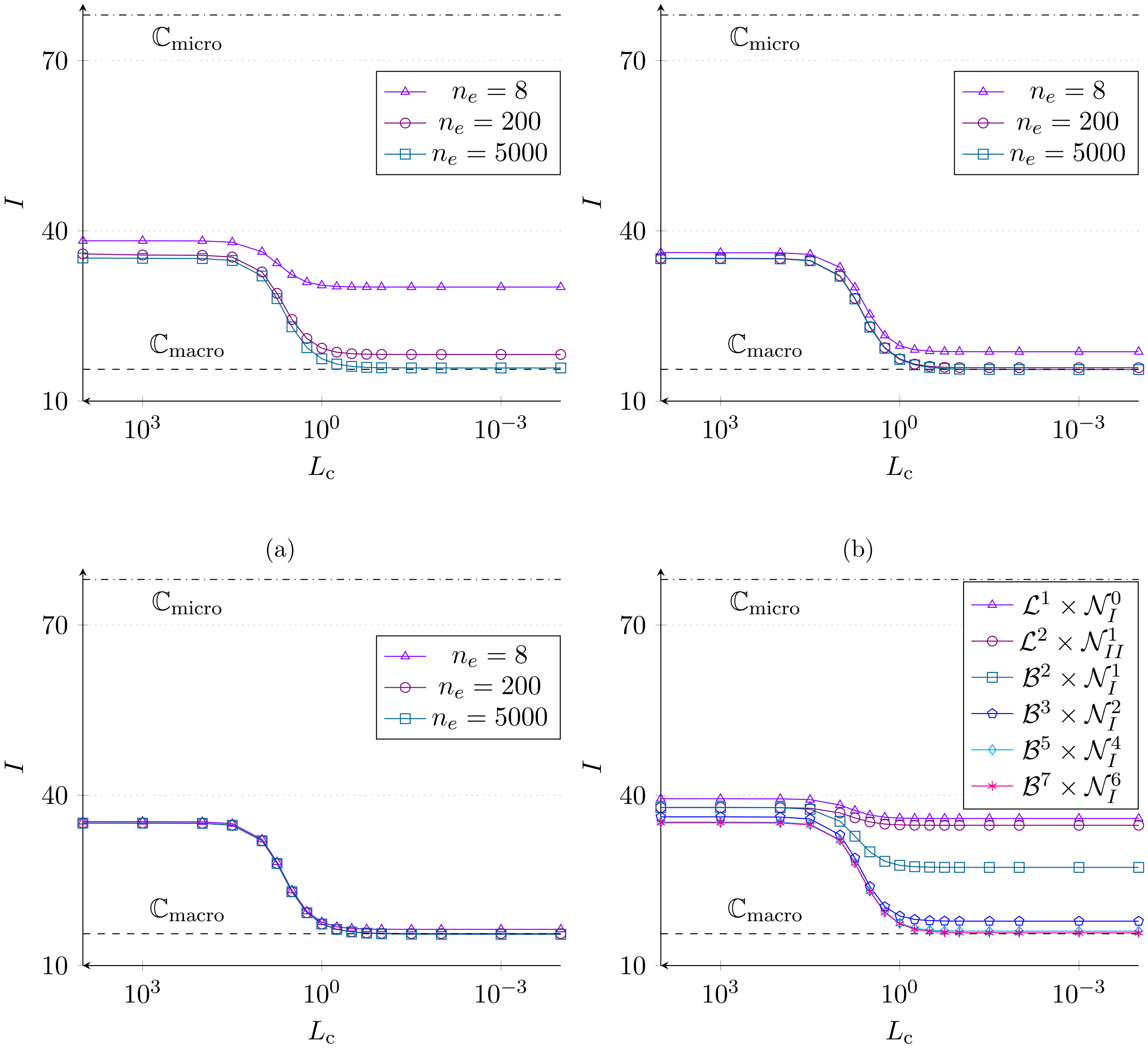

(a) (b)

(c) (d)

Figure 7.13: Energy progression of the relaxed micromorphic model with respect to L_{c} using the linear (a), quadratic (b) and cubic (c) finite element formulations. The energy computed with the coarsest mesh of 2 elements is depicted in (d) for various polynomial powers.

to the energy of the relaxed micromorphic model. The upper and lower bounds on the energy are computed using homogenized material parameters with a standard Cauchy model. The domain of the relaxed micromorphic model is defined as $\overline{A} = [0, 10]^2$ with the total Dirichlet boundary $\overline{s}_D = \partial A$. We impose the periodic conditions on the Dirichlet boundary

$$\widetilde{u}\Big|_{s_D} = \frac{1}{10}\begin{bmatrix}\sin(\pi y/5)\\ \sin(\pi x/5)\end{bmatrix} . \tag{7.24}$$

The resolved geometry computed with the Cauchy model is of the same dimensions as the domain of the relaxed micromorphic model and the same boundary conditions apply. The resulting deformation maps are depicted in Fig. 7.16. Clearly, the displacement homogenizes with an increasing number of cells towards the continuous solutions depicted in Fig. 7.18 (c), given by the Cauchy model for the macro parameters. In Fig. 7.17 we give the resulting displacement and microdistortion fields for the fitted characteristic length such that the energy for the 4×4, 7×7 and 20×20 periodic grids matches. The limits of the relaxed micromorphic model are shown in Fig. 7.18 with $L_\mathrm{c} \to \infty$ and $L_\mathrm{c} \to 0$. We observe that the intensity of the displacement field increases in the interior of the domain for $L_\mathrm{c} \to 0$ while at the same time the microdistortion field shifts to the edges of the domain without changing its general intensity.

The changes in energy for an increasing number of cells as well as the fitting in L_c are illustrated in Fig. 7.19. For the range of $n \times n$ unit cells such that $n \geq 3$ we can find a corresponding characteristic length in the relaxed micromorphic model, such that the same energy is produced. If the amount of cells is under three ($n < 3$) the micro-structure is so pronounced that the structure cannot be computed with an analogous continuum. This is because the upper bound of the relaxed micromorphic model is given by an equivalent Cauchy model with micro stiffness parameters, which do not allow to reach the energy of the discrete structure. This is clearly illustrated in Fig. 7.19 (b) where the energy points outside the bound were extrapolated.

We can interpolate the relation between the amount of unit cells and the characteristic length parameter using cubic splines. For the first point we use $n = 3$ and the corresponding L_c-value. For the last point we choose a limit with a high amount of cells, for example $n = 1000$, implying a million cells, and set $L_\mathrm{c} = 0$ thus emulating $\lim_{n\to\infty} L_\mathrm{c} = 0$. The fitting of L_c with a varying amount of data points is depicted in Fig. 7.20. Using eight points and higher where the first five are taken at the beginning, one point in the middle, and the remainder at the end (including the limit) we are able to find highly accurate approximations in the range. However, the accuracy of the extrapolation diminishes at around $n > 20$ for the eight-point approximation. The ten-point fitting remains viable up to $n \leq 26$ and the full approximation up to $n \leq 27$. The criterium for viability is the continuous stagnation of the L_c-value with an increasing number of cells. However, due to the minimal change in L_c with respect to larger values of n we can approximate the remainder of the curve ($n > 20$) by fitting the plateau function

$$L_\mathrm{c}^j(n) = L_\mathrm{c}^j \, e^{c(j-n)} , \tag{7.25}$$

where j is the starting n-value such that $n \in [j, \infty)$ and L_c^j is the value of L_c fitted for j (not L_c to the power of j). In our case we find $L_\mathrm{c}^{14} \approx L_\mathrm{c}^{15}(1 - e^{0.0235(14-n)})$.

We note that the same procure cannot be trivially applied to other deformation modes without first finding the associated homogenized material parameters. For example, in an equivalent bending test the $n \times n$ structures with $n \geq 4$ produced energies of $I \leq 8.437$. Since the relaxed micromorphic model is bound from below by the equivalent Cauchy model with macro stiffness we are not able to fit the characteristic length as $\lim_{L_\mathrm{c}\to 0} I \approx 8.874$ being larger than the energy produced by the discrete structure. The same problematic arises for shear tests.

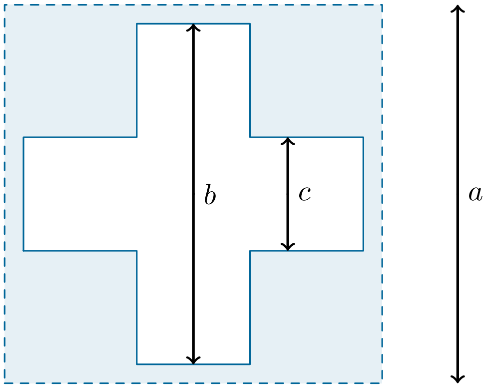

$a = 1$

$b = 0.9$

$c = 0.3$

$E = 70$

$\nu = 0.33$

Figure 7.14: The underlying microstructure of the investigated metamaterial and its material parameters.

7.3 Three-dimensional model

7.3.1 Convergence test

We start our confirmation of the three-dimensional formulation by constructing artificial solutions with high regularity and measuring convergence rates. Let the domain be given by a beam structure such that $\overline{V} = [0,10] \times [-1,1]^2$ where Dirichlet boundary reads $A_D = \partial V$, we define the analytical solution

$$\widetilde{\mathbf{u}} = \begin{bmatrix} 0 \\ 0 \\ \sin(\pi x) \end{bmatrix} , \qquad \widetilde{\boldsymbol{P}} = \mathrm{D}\widetilde{\mathbf{u}} + 10(1-y^2)(1-z^2)\sin(\pi x) \begin{bmatrix} 0 & 0 & 0 \\ 0 & 0 & 0 \\ 0 & -z & y \end{bmatrix} , \tag{7.26}$$

and imposed it on the Dirichlet boundary. The corresponding forces and micro-moments for the material parameters

$$\lambda_{\mathrm{e}}, \mu_{\mathrm{e}}, \lambda_{\mathrm{micro}}, \mu_{\mathrm{micro}}, \mu_{\mathrm{macro}}, L_{\mathrm{c}} = 1 , \qquad \mu_{\mathrm{c}} = 0, \tag{7.27}$$

result in

$$\mathbf{f} = \begin{bmatrix} 10\pi y(y^2-1)(z^2-1)\cos(\pi x) \\ 20(-y^2+z^2)\sin(\pi x) \\ yz(60y^2 - 20z^2 - 40)\sin(\pi x) \end{bmatrix} ,$$

$$\boldsymbol{M} = \left[\begin{matrix} 20y\left(y^2-1\right)\left(z^2-1\right)\sin\left(\pi x\right) & 0 \\ 0 & 20y\left(y^2-1\right)\left(z^2-1\right)\sin\left(\pi x\right) \\ \pi\left(20y^3z - 20yz^3 + 1\right)\cos\left(\pi x\right) & z\left(120y^2 - 10\pi^2\left(y^2-1\right)\left(z^2-1\right) - 20\left(y^2-1\right)\left(z^2-1\right) - 80\right)\sin\left(\pi x\right) \end{matrix}\right. \cdots$$

$$\cdots \left.\begin{matrix} \pi\cos\left(\pi x\right) \\ -20z\left(y^2-1\right)\left(z^2-1\right)\sin\left(\pi x\right) \\ y\left(-120z^2 + 60\left(y^2-1\right)\left(z^2-1\right) + 10\pi^2\left(y^2-1\right)\left(z^2-1\right) + 80\right)\sin\left(\pi x\right) \end{matrix}\right] . \tag{7.28}$$

The behaviour of the displacement and microdistortion fields under h- and p-refinement is depicted in Fig. 7.21. The necessity of a large amount of lower order elements in order to capture the high frequency solution is apparent. Even with 141900 elements and 597820 degrees of the freedom the

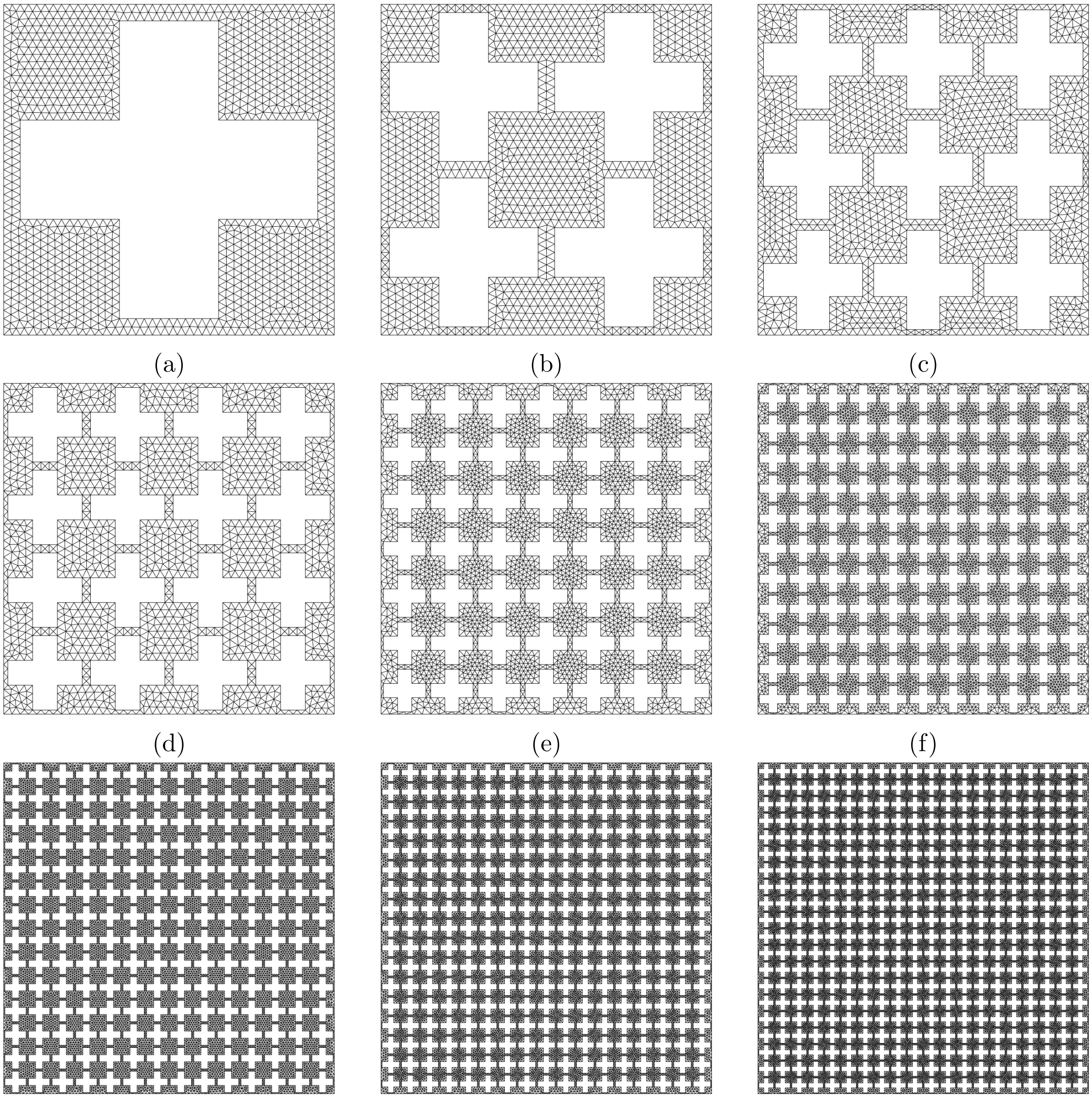
(a) (b) (c)

(d) (e) (f)

(g) (h) (i)

Figure 7.15: Depiction of $n \times n$ unit cells and their discretization in the domain with $n \in \{1, 2, 3, 4, 7, 11, 14, 17, 20\}$ presented over (a)-(i), respectively.

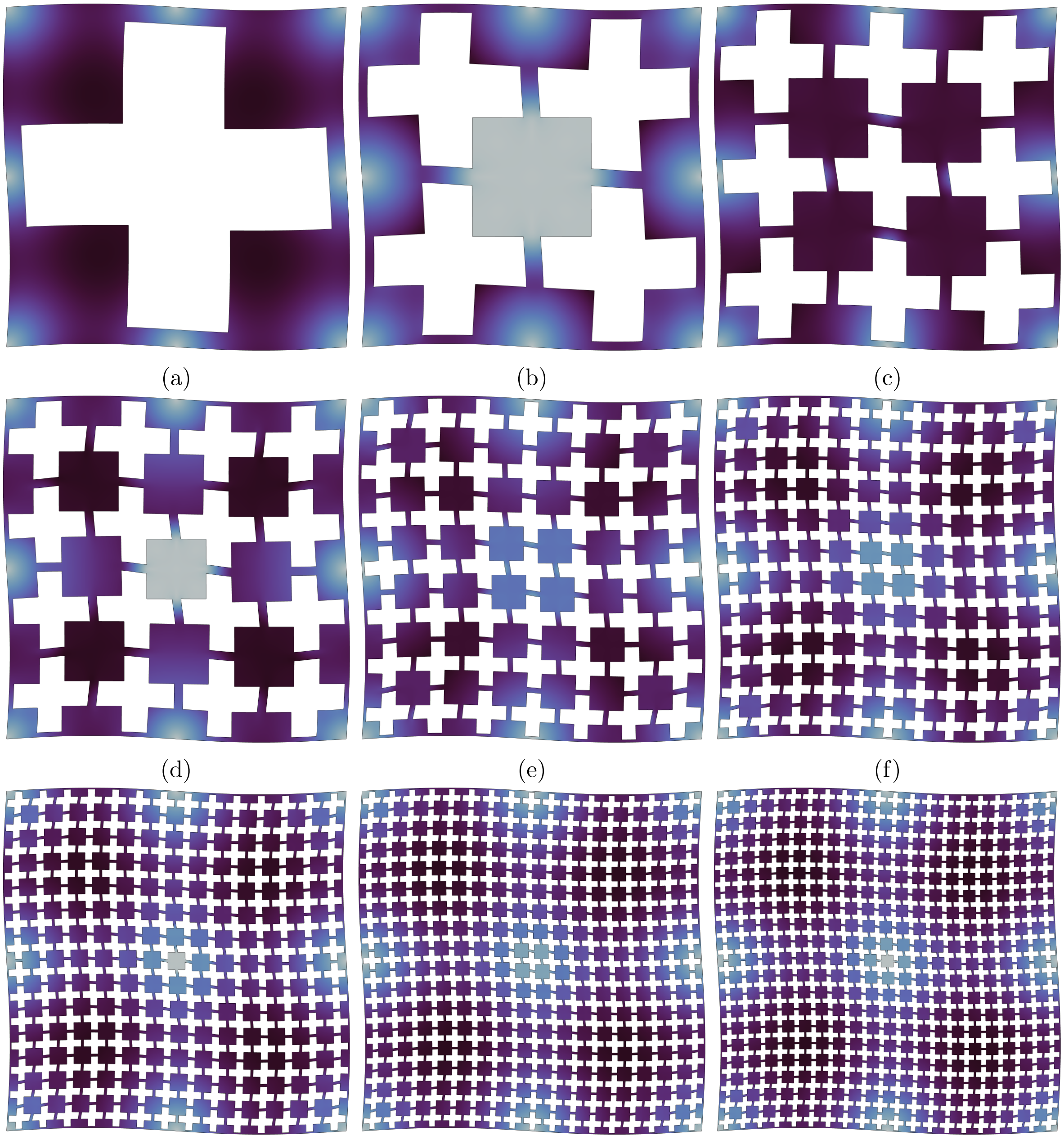

Figure 7.16: Intensity of the displacement for the fully resolved model with the number of cells $n \times n$ such that $n \in \{1, 2, 3, 4, 7, 11, 14, 17, 20\}$ presented over (a)-(i), respectively.

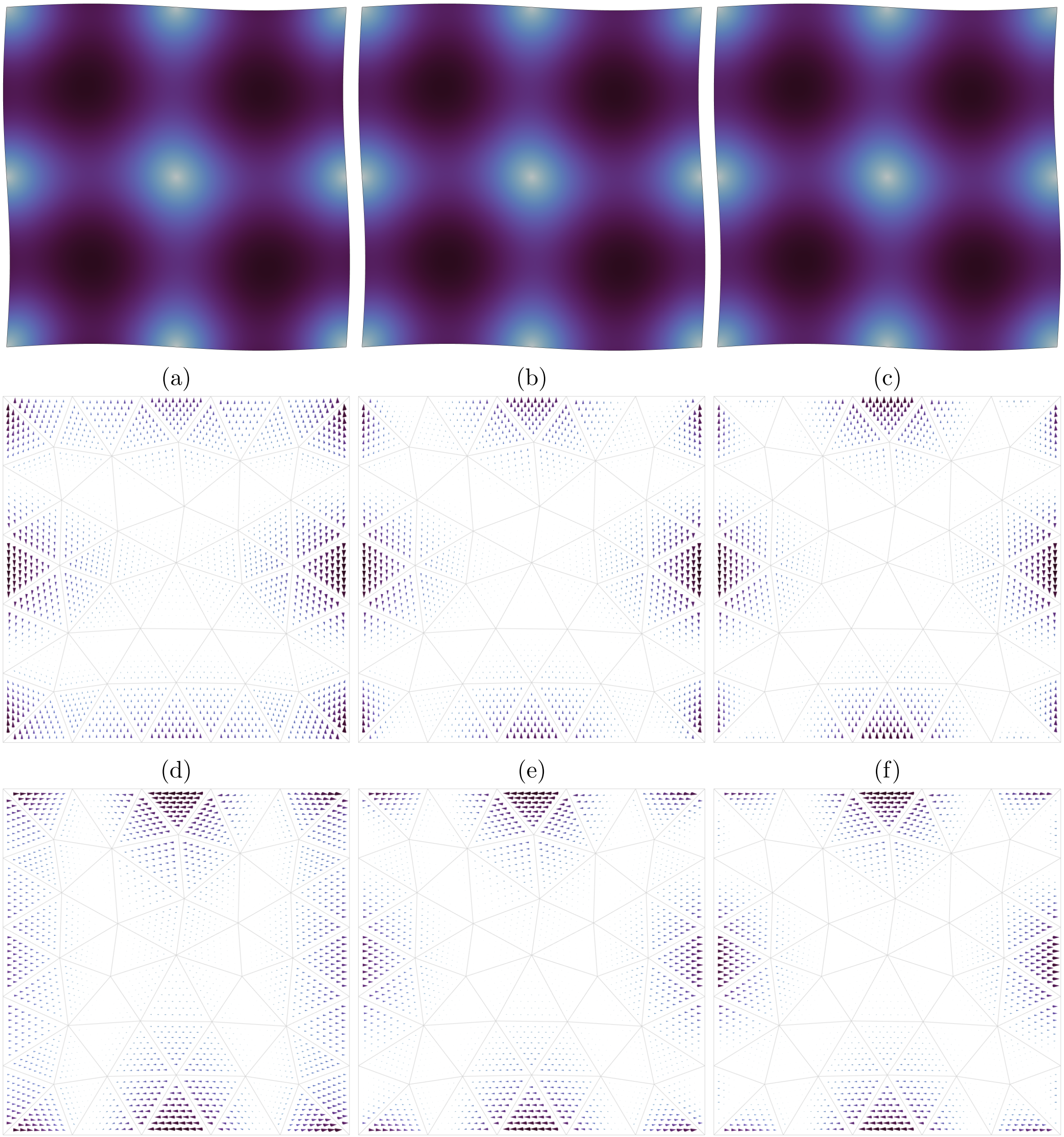

(a) (b) (c)

(d) (e) (f)

(g) (h) (i)

Figure 7.17: Displacement fields (a)-(c) and corresponding microdistortion fields in x (d)-(f) and y (g)-(i) for the solutions $L_\mathrm{c} \in \{1.704384479, 0.8179682, 0.42446779\}$ yielding the equivalent energy for the fully resolved models with 4×4, 7×7 and 20×20 unit cells, respectively.

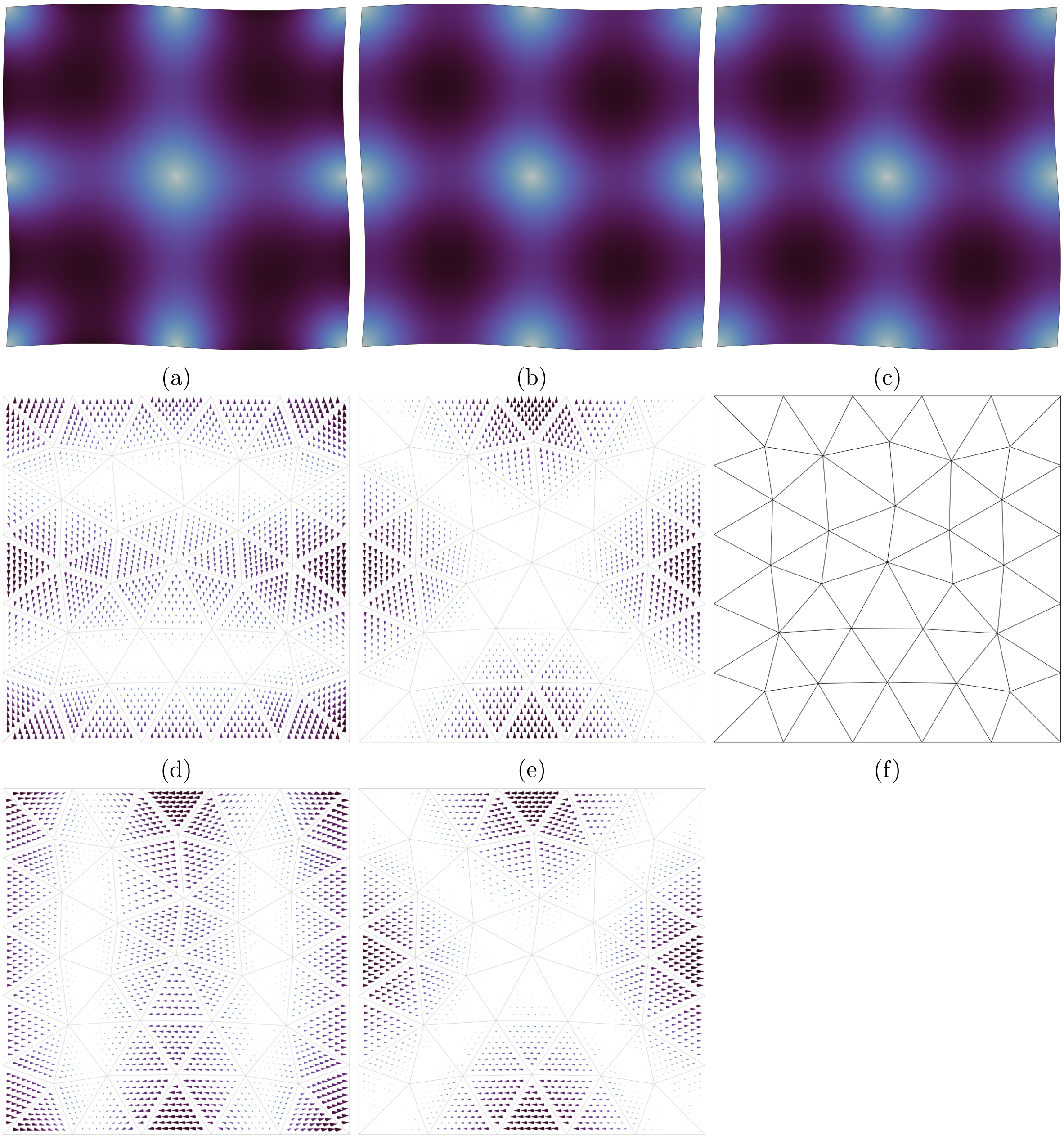

(a) (b) (c)

(d) (e) (f)

(g) (h)

Figure 7.18: Limit displacement fields for $L_{\mathrm{c}} \to \infty$ (a) and $L_{\mathrm{c}} \to 0$ (b) and their corresponding microdistortion fields in x (d)-(e) and y (g)-(h), respectively. The equivalent lower bound given by the Cauchy model (c). In (f) we depict the mesh used in computation of the continua models, where the finite element order is set to ten for accuracy.

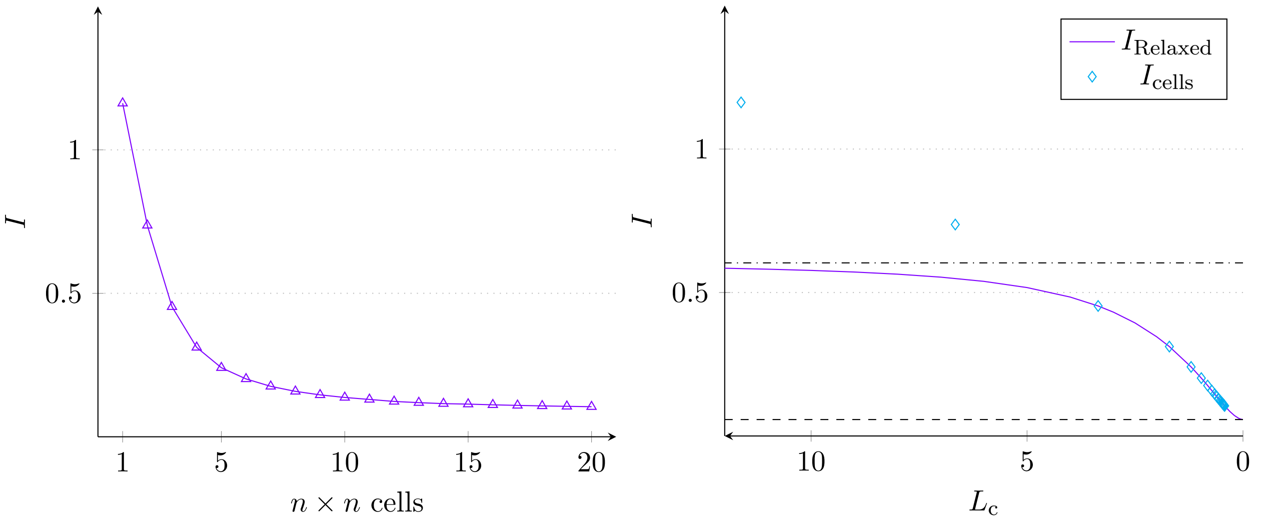

(a) (b)

Figure 7.19: Energy progression of the fully resolved geometry for an increasing number of cells (a) and corresponding L_c-values for in the relaxed micromorphic model (b) with the bounds of $\mathbb{C}_{\text{micro}}$ and $\mathbb{C}_{\text{macro}}$. The points above the upper bound in (b) are estimated via extrapolation an cannot be captured by the relaxed micromorphic model.

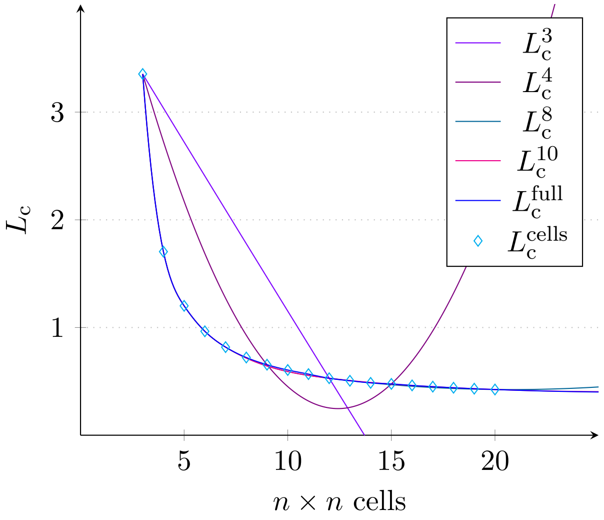

Figure 7.20: Fitting of L_c with respect to the number of unit cells $n \times n$ for various collections of discrete energy points.

solution still generates plateaus at the peaks. Although the solution of the quadratic element seems well enough, it is simply due to the fortunate placing of element interfaces at the peaks and cannot be expected in general discretizations. A truly stable solution scheme is achieved by using cubic finite elements, as these can account for internal oscillations. We observe that the cubic formulation with 1260 elements and 96538 degrees of freedom offers a far better approximation of the displacement and microdistortion fields.

The respective convergence rates under h- and p-refinement are given in Fig. 7.22. The elements yield the predicted optimal convergence rate. We note that no better convergence rates are observed for the Nédélec elements of the first type over the elements of the second type. Clearly, the problem exhibits full s-regularity. The influence of the placement of element interfaces is evident as the quadratic formulations generate lower errors at first and later stabilize at a steady convergence rate.

7.3.2 Cylindrical bending

In order to test the ability of the finite element formulations to capture the intrinsic behaviour of the relaxed micromorphic model we compare with analytical solutions of boundary-value problems. The first example considers the displacement and microdistortion fields under cylindrical bending [89] for infinite planes. Let the infinite plane be defined as $V = (-\infty, \infty)^2 \times [-1/2, 1/2]$ the analytical solution for cylindrical bending reads

$$\mathbf{u} = \kappa \begin{bmatrix} -xz \\ 0 \\ x^2/2 \end{bmatrix} , \qquad \boldsymbol{P} = -\kappa \begin{bmatrix} [41z + 20\sqrt{82}\,\mathrm{sech}(\sqrt{41/2})\sinh(\sqrt{82}z)]/1681 & 0 & x \\ 0 & 0 & 0 \\ -x & 0 & 0 \end{bmatrix} , \tag{7.29}$$

where the material constants are set to

$$\lambda_{\mathrm{e}} = \lambda_{\mathrm{micro}} = 0 \, , \qquad \mu_{\mathrm{e}} = \mu_{\mathrm{macro}} = 1/2 \, , \qquad \mu_{\mathrm{c}} = 0 \, , \qquad L_{\mathrm{c}} = 1 \, , \qquad \mu_{\mathrm{micro}} = 20 \, . \tag{7.30}$$

The intensity parameter κ is chosen to be $\kappa = 14/200$.

Obviously, we cannot compute on infinite plains. However, it suffices to compare the solutions at a sufficient distance from the boundary, as per the principle of Saint-Venant the embedded fields homogenize the further they are from their source and the intrinsic solution resurfaces. As such, we define the finite domain $\overline{V} = [-10, 10]^2 \times [-1/2, 1/2]$ and the boundaries

$$\begin{aligned} &\overline{A}_{D_1} = \{-10\} \times [-10, 10] \times [-1/2, 1/2] \, , \qquad && \overline{A}_{D_2} = \{10\} \times [-10, 10] \times [-1/2, 1/2] \, , \\ &A_N = \partial V \setminus \{\overline{A}_{D_1} \oplus \overline{A}_{D_2}\} \, . \end{aligned} \tag{7.31}$$

On the Dirichlet boundary we impose the translated analytical solution $\widetilde{\mathbf{u}} = \mathbf{u} - \begin{bmatrix} 0 & 0 & 3.5 \end{bmatrix}^T$.

The displacement field and the last row of the microdistortion are depicted in Fig. 7.23. The displacement field is dominated by its quadratic term and captured very correctly. The last row of the microdistortion is a linear function and easily approximated even with linear elements. In contrary, the P_{11} component of the microdistortion is a hyperbolic function of the z-axis. The results of its approximation at $x = y = 0$ (the centre of the plane) are given in Fig. 7.24. We observe that even increasing the number of linear finite elements to the extreme only results in better oscillations around the analytical solution. In comparison, higher order formulations converge towards the hyperbolic behaviour. Unlike in many of the previous examples we notice a measurable difference between the quadratic Nédélec elements of the first and second type. In fact, the approximation of the quadratic Nédélec element of the first type is nearly perfect, whereas its second type counterpart clearly deviates from the analytical solution at $z \approx -0.25$. Taking the cubic second type element yields the desired

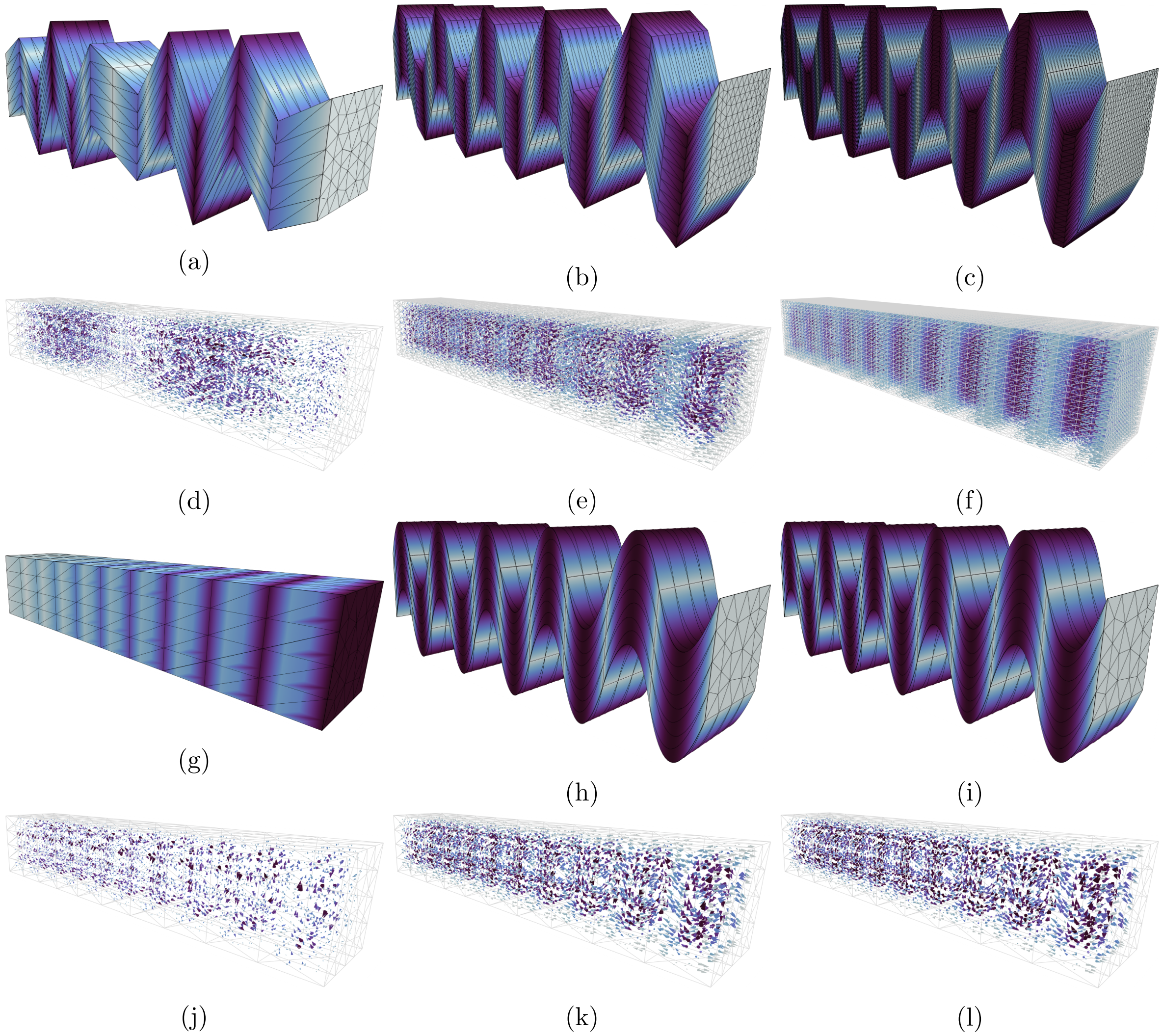

Figure 7.21: Depiction of the displacement field (a)-(c) and the last row of the microdistortion field (d)-(f) for the linear element under h-refinement with 2376, 18450 and 141900 elements, corresponding to 11476, 81550 and 597820 degrees of freedom. The p-refinement of the displacement field on a coarse mesh of 1260 elements is visualized in (g)-(l) with $p \in \{1, 2, 3\}$, corresponding to 6364, 33442 and 96358 degrees of freedom.

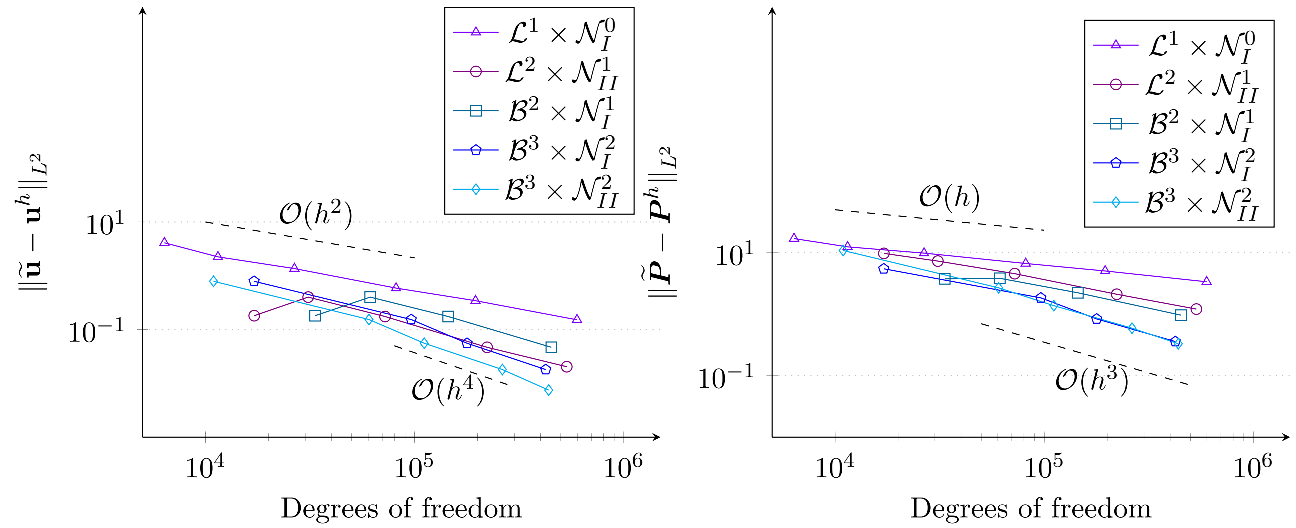

(a) (b)

Figure 7.22: Convergence under h-adaption for various polynomial orders.

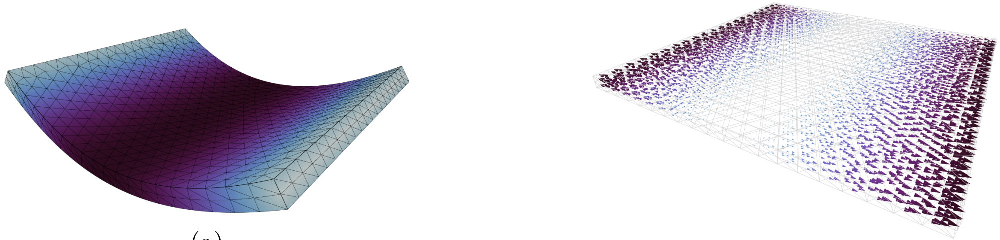

(a) (b)

Figure 7.23: Displacement (a) and last row of the microdistortion (b) for the quadratic formulation using the Nédélec element of the first type.

result. This phenomenon is an evident indicator of the prominent role of the Curl of the microdistortion in this type of problems. Firstly, the microdistortion is a non-gradient field. Secondly, the Curl of the analytical solution induces an hyperbolic sine term. Such functions are often approximated using cubic terms in power series, thus explaining the necessity of such high order elements for correct computations.

7.3.3 Torsion test

In the following we consider the intrinsic behaviour of the relaxed micromorphic model under torsion. In [88] the authors introduce the analytical solution for the infinite domain $V = (-\infty, \infty) \times \{\mathbf{r} \in \mathbb{R}^2 \mid \|\mathbf{r}\| \leq r\}$. For choice of material parameters

$$\mu_{\mathrm{e}} = 1/14\,, \qquad \mu_{\mathrm{micro}} = 1\,, \qquad \mu_{\mathrm{c}} = \mu_{\mathrm{macro}} = 1/2\,, \qquad L_{\mathrm{c}} = 1\,, \qquad \lambda_{\mathrm{e}} = \lambda_{\mathrm{micro}} = 0\,, \tag{7.32}$$

we find the analytical solution on the mantel surfaces of the cylinder

$$\mathbf{u}\Big|_{\mathbf{r}=3} = 3\theta x \begin{bmatrix} 0 \\ -\sin(\phi) \\ \cos(\phi) \end{bmatrix},$$

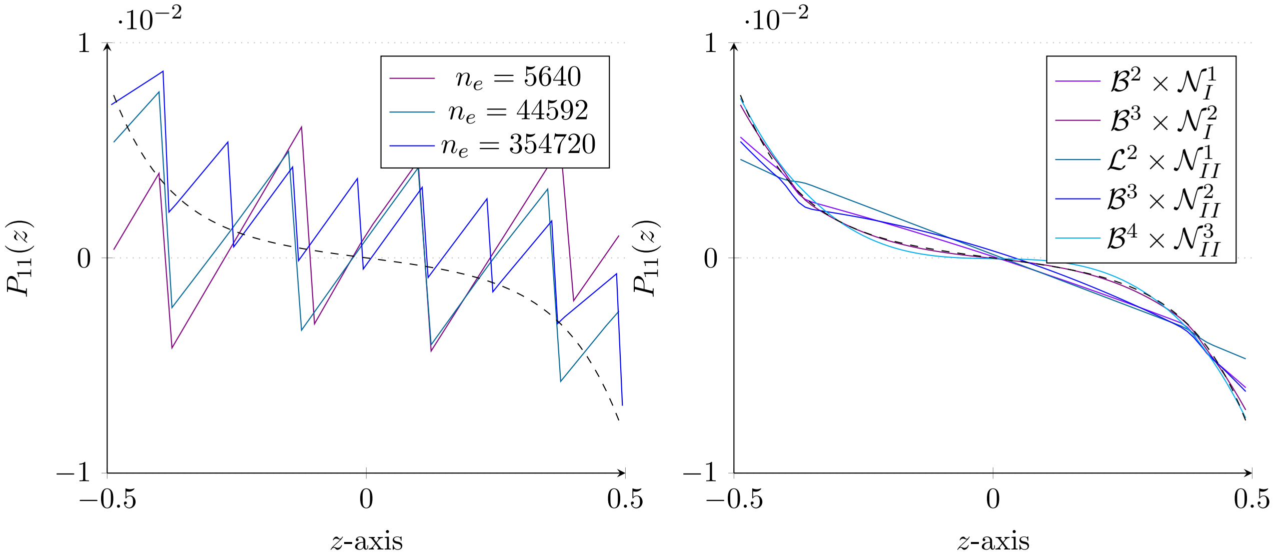

(a)

(b)

Figure 7.24: Convergence of the lowest order formulation under h-refinement with 732, 5640 and 44592 elements (a) and of the higher order formulations under p-refinement using 732 elements(b) towards the analytical solution (dashed curve) of the $P_{11}(z)$ component at $x = y = 0$.

$$\boldsymbol{P}\Big|_{\mathbf{r}=3} = \theta \begin{bmatrix} 0 & 0.952374\sin(\phi) & -0.952374\cos(\phi) \\ -1.80116\sin(\phi) & 0 & -x \\ 1.80116\cos(\phi) & x & 0 \end{bmatrix}, \tag{7.33}$$

where $r = 3$ and the rotational intensity is $\theta = 1/30$. Due to the complexity (long expression) of the general analytical solution and its dependency on Bessel functions (being solutions to the Bessel partial differential equation) we only give the formula for our specific case. In order to compare with subspace solutions we define the finite domain $\overline{V} = \{\mathbf{r} \in \mathbb{R}^2 \mid \|\mathbf{r}\| \leq 3\} \times [0, 30]$ with Dirichlet boundaries at $x = 0$ and $x = 1$. While the analytical solution assumes a constant rotation of the cross-section of the beam, we use the simplified linear rotation field

$$\mathbf{u}\Big|_{x=0} = 0\,, \qquad \mathbf{u}\Big|_{x=30} = \begin{bmatrix} 0 \\ -z \\ y \end{bmatrix}, \tag{7.34}$$

and embed it in the Dirichlet boundary. Due to the principal of Saint-Venant, the analytical solution is retrieved at a sufficient distance from the Dirichlet boundary.

The discretized geometry as well as the solutions for the displacement field and the first row of the microdistortion are depicted in Fig. 7.25. Clearly, the linear progression of the torque of the displacement is captured correctly. Further, with the expectation of the vicinity of the Dirichlet boundary, the satisfactory approximation of the first row of the microdistortion field is apparent. The progression of the P_{21} and P_{23} components at $z \approx 3$ over the x-axis for h- and p-refinement is given in Fig. 7.26. We note that the analytical solution (dashed lines) is retrieved for fine enough meshes. Although the employment of higher order elements does improve the approximation notably. Without the accompanying h-refinement the analytical solution is not retrieved. This is due to the high dependency on the geometry of the mesh. As illustrated in Fig. 7.25, only very fine meshes approximate

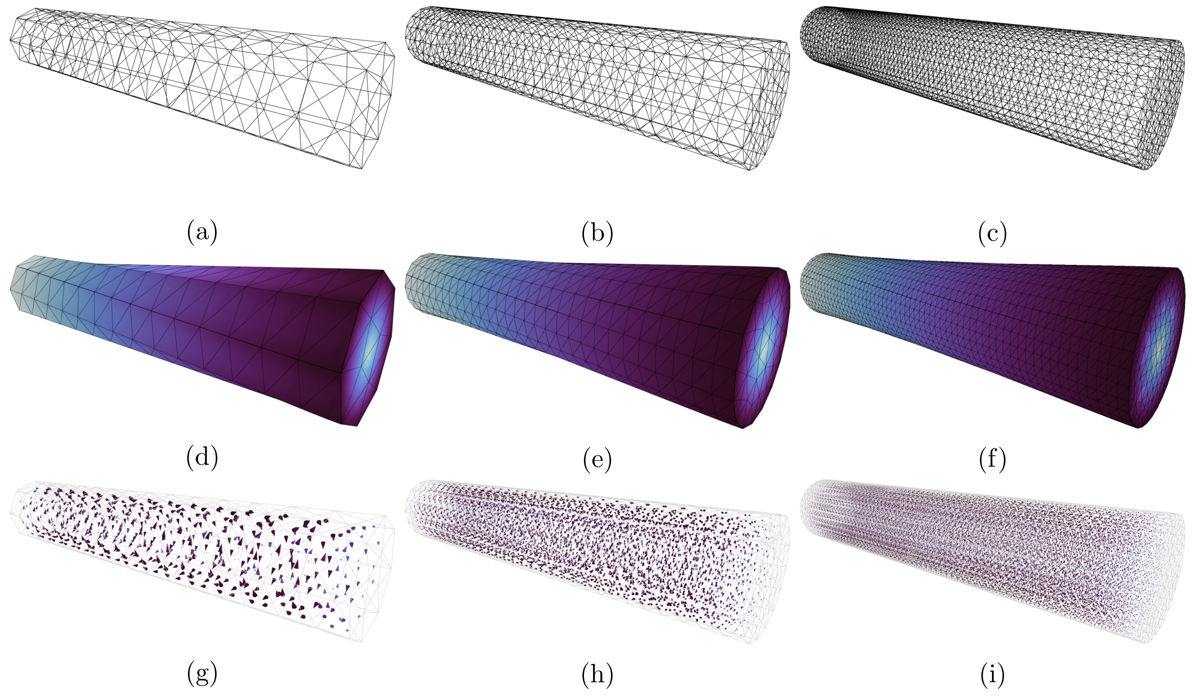
(a) (b) (c) (d) (e) (f) (g) (h) (i)

Figure 7.25: Depiction of the meshes with 630, 5760 and 38160 elements (a)-(c) and the corresponding solutions for the displacement (d)-(f) and the first row of the microdistortion (g)-(l) using the lowest order elements.

the circular shape of the beam well enough to allow for accurate solutions. This is apparent when considering the progression of the cubic formulation, where only the finest discretization is able to retrieve the predicted result.

7.3.4 Bounded stiffness property

In a previous example in two dimensions we explored the stiffness of the relaxed micromorphic model with respect to varying L_c-values. The fitting procedure showcased the ability to find a corresponding characteristic length value to describe an equivalent discrete structure using a relaxed micromorphic continuum model. The same can be done in three dimensions. The principal requirement for such fitting procedures is the pre-computation of lower and upper bounds on the elasticity parameters for an homogenized continuum model of an underlying unit cell structure. Since the parameters of such geometries are an active topic of research and not currently available we consider an artificial example.

Let the domain be given by the axis-symmetric cube $\overline{V} = [-1,1]^3$ with a total Dirichlet boundary

$$\overline{A}_{D_1} = \{(x,y,z) \in [-1,1]^3 \mid x = \pm 1\} \, , \qquad \overline{A}_{D_2} = \{(x,y,z) \in [-1,1]^3 \mid y = \pm 1\} \, ,$$
$$\overline{A}_{D_3} = \{(x,y,z) \in [-1,1]^3 \mid z = \pm 1\} \, , \tag{7.35}$$

we embed the periodic boundary conditions

$$\widetilde{u}\Big|_{A_{D_1}} = \begin{bmatrix} (1-y^2)\sin(\pi[1-z^2])/10 \\ 0 \\ 0 \end{bmatrix} \, , \qquad \widetilde{u}\Big|_{A_{D_2}} = \begin{bmatrix} 0 \\ (1-x^2)\sin(\pi[1-z^2])/10 \\ 0 \end{bmatrix} \, ,$$

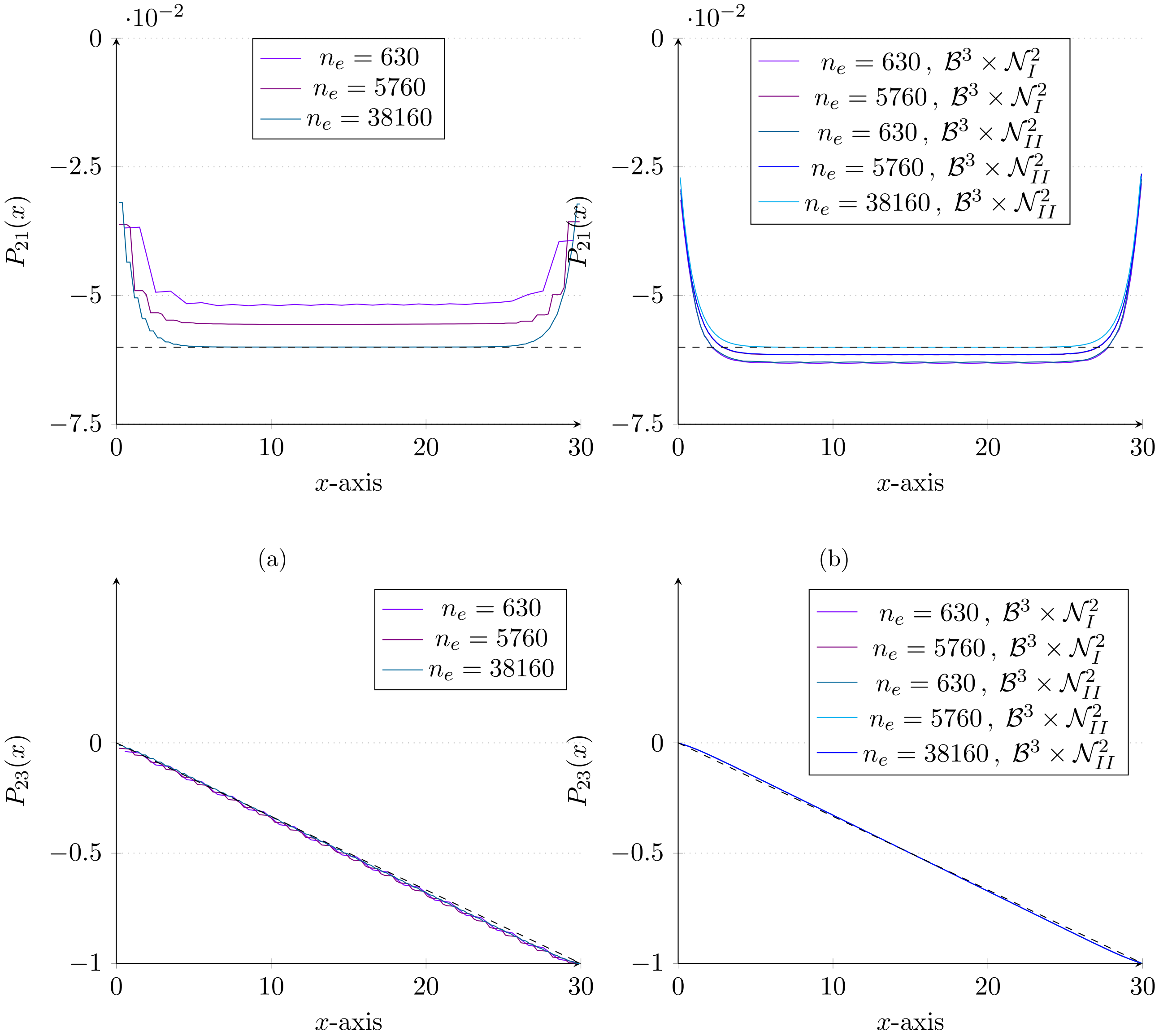

(a)

(b)

(c)

(d)

Figure 7.26: Convergence of the lowest order formulation under h-refinement with 630, 5760 and 38160 elements (a) and of the cubic order formulations under h-refinement using 630 and 5760 elements (b) towards the analytical solution (dashed curve) of the $P_{23}(x)$ component at $y = 3$, $z = 0$.

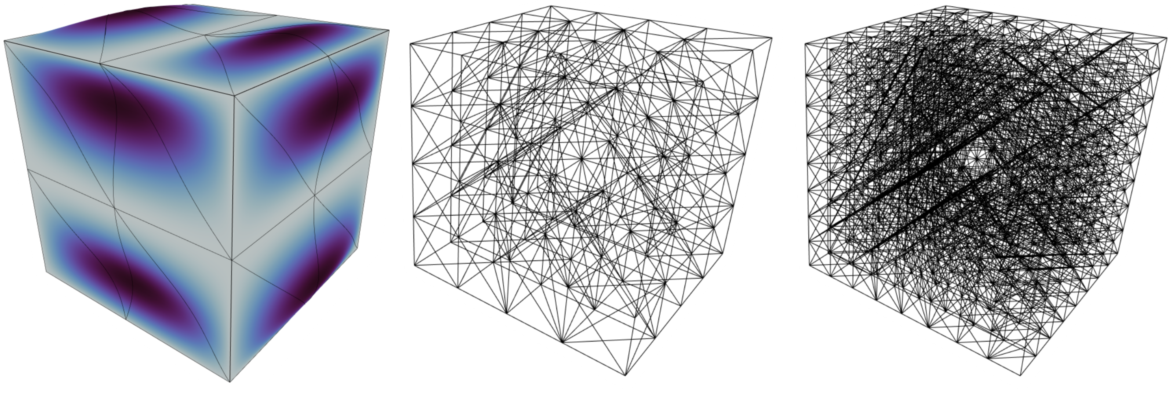
(a) (b) (c)

Figure 7.27: Displacement field of the Cauchy model on the coarsest mesh of 48 finite elements of the tenth order (a) and depictions of the meshes with 384 (b) and 3072 (c) elements, respectively.

$$\widetilde{u}\Big|_{A_{D_3}} = \begin{bmatrix} 0 \\ 0 \\ (1-y^2)\sin(\pi[1-x^2])/10 \end{bmatrix} . \tag{7.36}$$

The material parameters are chosen as

$$\lambda_{\text{macro}} = 2 \, , \qquad \mu_{\text{macro}} = 1 \, , \qquad \lambda_{\text{micro}} = 10 \, , \qquad \mu_{\text{micro}} = 5 \, , \qquad \mu_{\text{c}} = 1 \, , \tag{7.37}$$

thus giving rise to the following meso-parameters

$$\lambda_{\text{e}} = 2.5 \, , \qquad \mu_{\text{e}} = 1.25 \, . \tag{7.38}$$

The displacement field as well as some examples of the employed meshes are depicted in Fig. 7.27. In order to compute the upper and lower bound on the energy we utilize the equivalent Cauchy model formulation with the micro- and macro elasticity parameters. In order to assert the high accuracy of the solution of the bounds we employ tenth order finite elements. The progression of the energy in dependence of the characteristic length parameter L_{c} is given in Fig. 7.28. We observe the high mesh dependency of the lower order formulations, where the energy is clearly overestimated. The higher order formulations all capture the upper bound correctly but diverge with respect to the result of the lower bound. Notably, the approximation using the Nédélec element of the first type is more accurate than the equivalent formulation with the Nédélec element of the second type, thus indicating the non-negligible involvement of the micro-dislocation in the energy. Using standard mesh coarseness the cubic element formulation with Nédélec elements of the first type yields satisfactory results. In order to achieve the same on highly coarse meshes, one needs to employ seventh order elements.

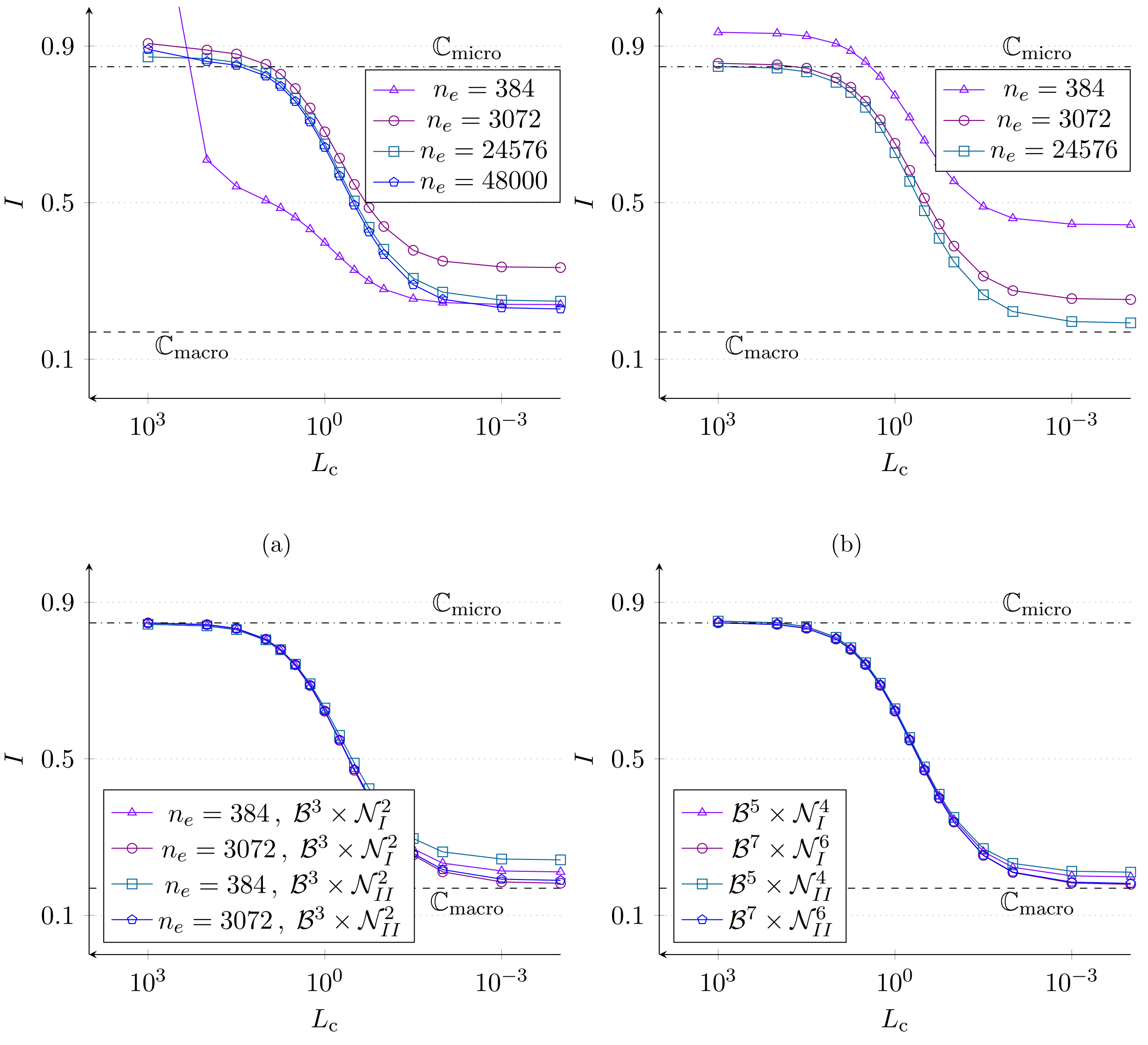

(a)

(b)

(c)

(d)

Figure 7.28: Energy progression of the relaxed micromorphic model with respect to L_c using the linear (a), quadratic (b) and cubic (c) finite element formulations. The energy computed with the coarsest mesh of 48 elements is depicted in (d) for various polynomial powers.

8 Conclusions and outlook

The relaxed micromorphic model is shown to be well-posed in the space $X = [H^1]^3 \times H(\mathrm{Curl})$ by the Lax-Milgram theorem, where the case of a positive semi-definite rotational coupling tensor $\mathbb{C}_\mathrm{c}$, well-posedness of the model is maintained by the consistent coupling condition due to the generalized Korn's inequality. As such, Cea's lemma can be applied and subsequently utilized for the derivation of a priori error estimates based on commuting interpolations on the de Rham complex. In this work, error estimates are introduced for the Nédélec elements of first and second types, and later improved for s-regularity. The convergence rates are confirmed in numerical examples.

In Section 5, the construction of low order conforming finite elements for the relaxed micromorphic model is demonstrated. This encompasses solutions to the orientation problem by vertex-sequencing and methods of applying the discrete consistent coupling condition, where Lagrangian elements are employed in the approximation of the displacement field.

The intrinsic behaviour of the relaxed micromorphic model is revealed by the analytical solutions to boundary value problems. Clearly, the continuum exhibits hyperbolic and trigonometric solutions, which are not easily approximated by low order finite elements. The examples provided in Section 7 demonstrate that cubic and higher order finite elements yield excellent results in approximate solutions of the model.

The polytopal template methodology introduced in Section 6 allows to easily and flexibly construct $H(\mathrm{curl})$-conforming vectorial finite elements that inherit many of the characteristics of an underlying H^1-conforming basis, which can be chosen independently. This is achieved by equipping each polytope of the reference element with a template of vector fields. The multiplication of an H^1 base function with a template vector on the corresponding polytope yields an $H(\mathrm{curl})$-conforming base function. The template allows to readily distinguish between cell and non-cell base functions based on the trace operators $\mathrm{tr}^{\mathrm{t}}_{\partial \mathrm{A}}$ and $\mathrm{tr}^{\mathrm{t}}_{\partial \mathrm{V}}$. Further, the definition of a template for non-gradient base functions allows to split the space between gradients and non-gradients, with the exclusion of the lowest order base functions. Consequently, it allows to formulate the enriched Nédélec element of the first type, which enables an improved order of convergence. The split is also useful for applications not discussed in this work. For example, it allows to employ base functions according to the nature of the approximated field, i.e., irrotational or solenoidal, thus reducing unnecessary degrees of freedom. Further, the curl of the non-gradient base functions can be used to span the solenoidal polynomial basis of $H(\mathrm{div})$-conforming elements. The correctness of the polytopal template method and its production of a unisolvent $H(\mathrm{curl})$-conforming basis is shown via linear independence and conformity theorems. The method can be used to produce arbitrary order Nédélec elements of the first and second type.

In this work, we made use of Bernstein polynomials. The latter boast optimal complexity properties manifesting in the form of sum factorization. The natural decomposition of their multi-variate versions into multiplications of univariate Bernstein base functions via the Duffy transformation allows to construct optimal iterators for their evaluation using recursion formulas. Further, this characteristic makes the use of dual numbers in the computation of their derivatives idle. Finally, the intrinsic order of traversal induced by the factorization is exploited optimally by the choice of clock-wise orientation of the reference element. The consequence of these combined features is demonstrated in the resulting high-performance hp-finite element program Rayse.

The ability of the relaxed micromorphic model to iterate between the energies of homogeneous materials and materials with an underlying micro-structure using the characteristic length scale parameter L_c is demonstrated in several examples. Primarily, it is shown that the relaxed micromorphic model can be used to compute the energies of an equivalent periodic metamaterial with a hollowed plus-shaped unit cell by fitting the L_c-parameter. However, it is also shown that correct iterations with respect to L_c require either fine-discretizations or higher order elements. The excellent performance of the proposed higher order finite elements in the linear static case is proven by both examples with varying L_c-values and comparisons with analytical solutions. This is a precursor for their application in the dynamic setting, which is important since the relaxed micromorphic model is often employed in the computation of elastic waves (e.g., for acoustic metamaterials), where high frequency solutions are common.

The proposed computational schemes are lacking in their description of curved geometries. Due to the consistent coupling condition, this can easily lead to errors emanating from the boundary. Consequently, a topic for future works would be the investigation of curved finite elements [54, 55] and their behaviour with respect to the model. Another major issue is the conditioning of the global matrix with respect to the material parameters and specifically the characteristic length scale L_c, where large values lead to rapidly increasing computation times. The problem could be alleviated if proper pre-conditioners are designed.

9 References

[1] Abdulle, A.: Analysis of a heterogeneous multiscale FEM for problems in elasticity. Mathematical Models and Methods in Applied Sciences **16**(04), 615–635 (2006)

[2] Ainsworth, M., Andriamaro, G., Davydov, O.: Bernstein–Bézier finite elements of arbitrary order and optimal assembly procedures. SIAM Journal on Scientific Computing **33**(6), 3087–3109 (2011)

[3] Ainsworth, M., Andriamaro, G., Davydov, O.: A Bernstein–Bézier basis for arbitrary order Raviart–Thomas finite elements. Constructive Approximation **41**(1), 1–22 (2015)

[4] Ainsworth, M., Coyle, J.: Hierarchic finite element bases on unstructured tetrahedral meshes. International Journal for Numerical Methods in Engineering **58**(14), 2103–2130 (2003)

[5] Ainsworth, M., Fu, G.: Bernstein–Bézier bases for tetrahedral finite elements. Computer Methods in Applied Mechanics and Engineering **340**, 178–201 (2018)

[6] Aivaliotis, A., Daouadji, A., Barbagallo, G., Tallarico, D., Neff, P., Madeo, A.: Low-and high-frequency stoneley waves, reflection and transmission at a Cauchy/relaxed micromorphic interface (2018). URL `https://arxiv.org/abs/1810.12578`

[7] Aivaliotis, A., Tallarico, D., d'Agostino, M.V., Daouadji, A., Neff, P., Madeo, A.: Frequency- and angle-dependent scattering of a finite-sized meta-structure via the relaxed micromorphic model. Archive of Applied Mechanics **90**(5), 1073–1096 (2020)

[8] Altenbach, H.: Kontinuumsmechanik: Einführung in die materialunabhängigen und materialabhängigen Gleichungen. Springer Berlin Heidelberg (2015)

[9] Anjam, I., Valdman, J.: Fast MATLAB assembly of FEM matrices in 2d and 3d: Edge elements. Applied Mathematics and Computation **267**, 252–263 (2015)

[10] Arnold, D.N., Guzmán, J.: Local L^2-bounded commuting projections in FEEC (2021). URL `https://arxiv.org/abs/2104.00184`

[11] Askes, H., Aifantis, E.: Gradient elasticity in statics and dynamics: An overview of formulations, length scale identification procedures, finite element implementations and new results. International Journal of Solids and Structures **48**, 1962–1990 (2011)

[12] Babuška, I., Suri, M.: The p and h-p versions of the finite element method, basic principles and properties. SIAM Review **36**(4), 578–632 (1994)

[13] Babuška, I., Guo, B.: Approximation properties of the h-p version of the finite element method. Computer Methods in Applied Mechanics and Engineering **133**(3), 319–346 (1996)

[14] Barbagallo, G., Madeo, A., d'Agostino, M.V., Abreu, R., Ghiba, I.D., Neff, P.: Transparent anisotropy for the relaxed micromorphic model: Macroscopic consistency conditions and long wave length asymptotics. International Journal of Solids and Structures **120**, 7–30 (2017)

[15] Barbagallo, G., Tallarico, D., D'Agostino, M.V., Aivaliotis, A., Neff, P., Madeo, A.: Relaxed micromorphic model of transient wave propagation in anisotropic band-gap metastructures. International Journal of Solids and Structures **162**, 148–163 (2019)

[16] Bathe, K.: Finite Element Procedures. Prentice Hall International editions. Prentice Hall (1996)

[17] Baydin, A.G., Pearlmutter, B.A., Radul, A.A., Siskind, J.M.: Automatic differentiation in machine learning: a survey. Journal of Marchine Learning Research **18**, 1–43 (2018)

[18] Bochev, P.B., Gunzburger, M.D.: Least-Squares Finite Element Methods, vol. 166. Springer Science & Business Media (2009)

[19] Braess, D.: Finite Elemente - Theorie, schnelle Löser und Anwendungen in der Elastizitätstheorie, 5 edn. Springer-Verlag, Berlin (2013)

[20] Brezzi, F., Douglas, J., Marini, L.D.: Two families of mixed finite elements for second order elliptic problems. Numerische Mathematik **47**(2), 217–235 (1985)

[21] Carneiro, V.H., Meireles, J., Puga, H.: Auxetic materials — a review. Materials Science-Poland **31**(4), 561–571 (2013)

[22] Chasapi, M., Mester, L., Simeon, B., Klinkel, S.: Isogeometric analysis of 3d solids in boundary representation for problems in nonlinear solid mechanics and structural dynamics. International Journal for Numerical Methods in Engineering **123**(5), 1228–1252 (2022)

[23] Ciarlet, P.: The Finite Element Method for Elliptic Problems. ISSN. Elsevier Science (1978)

[24] Cordero, N.M., Gaubert, A., Forest, S., Busso, E.P., Gallerneau, F., Kruch, S.: Size effects in generalised continuum crystal plasticity for two-phase laminates. Journal of the Mechanics and Physics of Solids **58**(11), 1963–1994 (2010)

[25] Cosserat, E., Cosserat, F.: Sur la théorie de l'élasticité. premier mémoire. In: Annales de la Faculté des sciences de Toulouse: Mathématiques, vol. 10, pp. I1–I116 (1896)

[26] d'Agostino, M.V., Barbagallo, G., Ghiba, I.D., Eidel, B., Neff, P., Madeo, A.: Effective description of anisotropic wave dispersion in mechanical band-gap metamaterials via the relaxed micromorphic model. Journal of Elasticity **139**(2), 299–329 (2020)

[27] d'Agostino, M.V., Rizzi, G., Khan, H., Lewintan, P., Madeo, A., Neff, P.: The consistent coupling boundary condition for the classical micromorphic model: existence, uniqueness and interpretation of parameters. Continuum Mechanics and Thermodynamics (2022)

[28] D'Alessandro, L., Krushynska, A.O., Ardito, R., Pugno, N.M., Corigliano, A.: A design strategy to match the band gap of periodic and aperiodic metamaterials. Scientific Reports **10**(1), 16403 (2020)

[29] Demkowicz, L.: Computing with hp-Adaptive Finite Elements. Vol. 1: One- and Two-Dimensional Elliptic and Maxwell Problems. Chapman and Hall/CRC (2006)

[30] Demkowicz, L., Buffa, A.: H^1, $H(\text{curl})$ and $H(\text{div})$-conforming projection-based interpolation in three dimensions: Quasi-optimal p-interpolation estimates. Computer Methods in Applied Mechanics and Engineering **194**(2), 267–296 (2005). Selected papers from the 11th Conference on The Mathematics of Finite Elements and Applications

[31] Demkowicz, L., Kurtz, J., Pardo, D., Paszynski, M., Rachowicz, W., Zdunek, A.: Computing with hp-Adaptive Finite Elements. Vol. II: Frontiers: Three-Dimensional Elliptic and Maxwell Problems with Applications. Chapman and Hall/CRC (2007)

[32] Demkowicz, L., Monk, P., Vardapetyan, L., Rachowicz, W.: De Rham diagram for hp-finite element spaces. Computers and Mathematics with Applications **39**(7), 29–38 (2000)

[33] Di Nezza, E., Palatucci, G., Valdinoci, E.: Hitchhiker's guide to the fractional Sobolev spaces. Bulletin des Sciences Mathématiques **136**(5), 521–573 (2012)

[34] Dunavant, D.A.: High degree efficient symmetrical Gaussian quadrature rules for the triangle. International Journal for Numerical Methods in Engineering **21**(6), 1129–1148 (1985)

[35] Ebobisse, F., Neff, P., Forest, S.: Well-posedness for the microcurl model in both single and polycrystal gradient plasticity. International Journal of Plasticity **107**, 1–26 (2018)

[36] Efendiev, Y., Hou, T.: Multiscale Finite Element Methods. Springer-Verlag New York (2009)

[37] Eidel, B., Fischer, A.: The heterogeneous multiscale finite element method for the homogenization of linear elastic solids and a comparison with the FE^2 method. Computer Methods in Applied Mechanics and Engineering **329**, 332–368 (2018)

[38] Eremeyev, V.A., Lebedev, L.P., Altenbach, H.: Foundations of Micropolar Mechanics. Springer Science & Business Media (2012)

[39] Eringen, A.: Microcontinuum Field Theories. I. Foundations and Solids. Springer-Verlag New York (1999)

[40] Fike, J.A., Alonso, J.J.: Automatic differentiation through the use of hyper-dual numbers for second derivatives. In: S. Forth, P. Hovland, E. Phipps, J. Utke, A. Walther (eds.) Recent Advances in Algorithmic Differentiation, pp. 163–173. Springer Berlin Heidelberg, Berlin, Heidelberg (2012)

[41] Forest, S., Sievert, R.: Nonlinear microstrain theories. International Journal of Solids and Structures **43**(24), 7224–7245 (2006)

[42] Fuentes, F., Keith, B., Demkowicz, L., Nagaraj, S.: Orientation embedded high order shape functions for the exact sequence elements of all shapes. Computers & Mathematics with Applications **70**(4), 353–458 (2015)

[43] Geers, M., Kouznetsova, V., Brekelmans, W.: Multi-scale computational homogenization: Trends and challenges. Journal of Computational and Applied Mathematics **234**(7), 2175–2182 (2010). Fourth International Conference on Advanced COmputational Methods in ENgineering (ACOMEN 2008)

[44] Geuzaine, C., Remacle, J.F.: Gmsh: A 3-D finite element mesh generator with built-in pre- and post-processing facilities. International Journal for Numerical Methods in Engineering **79**(11), 1309–1331 (2009)

[45] Ghiba, I.D., Neff, P., Madeo, A., Placidi, L., Rosi, G.: The relaxed linear micromorphic continuum: Existence, uniqueness and continuous dependence in dynamics. Mathematics and Mechanics of Solids **20**(10), 1171–1197 (2015)

[46] Ghiba, I.D., Neff, P., Owczarek, S.: Existence results for non-homogeneous boundary conditions in the relaxed micromorphic model. Mathematical Methods in the Applied Sciences **44**(2), 2040–2049 (2021)

[47] Hiptmair, R., Pauly, D., Schulz, E.: Traces for Hilbert complexes (2022). URL `https://arxiv.org/abs/2203.00630`

[48] Hu, Q., Xia, Y., Natarajan, S., Zilian, A., Hu, P., Bordas, S.P.A.: Isogeometric analysis of thin Reissner–Mindlin shells: locking phenomena and B-bar method. Computational Mechanics **65**(5), 1323–1341 (2020)

[49] Hughes, T., Cottrell, J., Bazilevs, Y.: Isogeometric analysis: CAD, finite elements, NURBS, exact geometry and mesh refinement. Computer Methods in Applied Mechanics and Engineering **194**(39), 4135–4195 (2005)

[50] Hütter, G.: Application of a microstrain continuum to size effects in bending and torsion of foams. International Journal of Engineering Science **101**, 81–91 (2016)

[51] Jaśkowiec, J., Sukumar, N.: High-order cubature rules for tetrahedra. International Journal for Numerical Methods in Engineering **121**(11), 2418–2436 (2020)

[52] Jeong, J., Neff, P.: Existence, uniqueness and stability in linear Cosserat elasticity for weakest curvature conditions. Mathematics and Mechanics of Solids **15**(1), 78–95 (2010)

[53] Jeong, J., Ramézani, H., Münch, I., Neff, P.: A numerical study for linear isotropic Cosserat elasticity with conformally invariant curvature. ZAMM - Journal of Applied Mathematics and Mechanics / Zeitschrift für Angewandte Mathematik und Mechanik **89**(7), 552–569 (2009)

[54] Johnen, A., Remacle, J.F., Geuzaine, C.: Geometrical validity of curvilinear finite elements. Journal of Computational Physics **233**, 359–372 (2013)

[55] Johnen, A., Remacle, J.F., Geuzaine, C.: Geometrical validity of high-order triangular finite elements. Engineering with Computers **30**(3), 375–382 (2014)

[56] Jönsson, J.: Continuum Mechanics of Beam and Plate Flexure. U : Institut for Bygningsteknik, Aalborg Universitet. Department of Mechanical Engineering, Aalborg University, Aalborg (1995). Pdf. for print 232 pp.

[57] Kirchner, N., Steinmann, P.: Mechanics of extended continua: modeling and simulation of elastic microstretch materials. Computational Mechanics **40**(4), 651 (2006)

[58] Knees, D., Owczarek, S., Neff, P.: A local regularity result for the relaxed micromorphic model based on inner variations (2022). URL `https://arxiv.org/abs/2208.04821`

[59] Lai, M.J., Schumaker, L.L.: Spline Functions on Triangulations. Cambridge University Press (2007)

[60] Lewintan, P., Müller, S., Neff, P.: Korn inequalities for incompatible tensor fields in three space dimensions with conformally invariant dislocation energy. Calculus of Variations and Partial Differential Equations **60**(4), 150 (2021)

[61] Lewintan, P., Neff, P.: L^p-versions of generalized Korn inequalities for incompatible tensor fields in arbitrary dimensions with p-integrable exterior derivative. Comptes Rendus. Mathématique **359**(6), 749–755 (2021)

[62] Lewintan, P., Neff, P.: Nečas–Lions lemma revisited: An L^p-version of the generalized Korn inequality for incompatible tensor fields. Mathematical Methods in the Applied Sciences **44**(14), 11392–11403 (2021)

[63] Lu, T.T., Hu, H.Y., Li, Z.C.: Highly accurate solutions of Motz's and the cracked beam problems. Engineering Analysis with Boundary Elements **28**(11), 1387–1403 (2004)

[64] Madeo, A., Barbagallo, G., Collet, M., d'Agostino, M.V., Miniaci, M., Neff, P.: Relaxed micromorphic modeling of the interface between a homogeneous solid and a band-gap metamaterial: New perspectives towards metastructural design. Mathematics and Mechanics of Solids **23**(12), 1485–1506 (2018)

[65] Madeo, A., Neff, P., Ghiba, I.D., Rosi, G.: Reflection and transmission of elastic waves in non-local band-gap metamaterials: A comprehensive study via the relaxed micromorphic model. Journal of the Mechanics and Physics of Solids **95**, 441–479 (2016)

[66] Marchandise, E., Remacle, J.F., Geuzaine, C.: Optimal parametrizations for surface remeshing. Engineering with Computers **30**(3), 383–402 (2014)

[67] Mindlin, R.: Micro-structure in linear elasticity. Archive for Rational Mechanics and Analysis **16**, 51–78 (1964)

[68] Mindlin, R.D., Eshel, N.N.: On first strain-gradient theories in linear elasticity. International Journal of Solids and Structures **4**(1), 109–124 (1968)

[69] Monk, P.: Finite Element Methods for Maxwell's Equations. Numerical Mathematics and Scientific Computation. Oxford University Press, New York (2003)

[70] Nedelec, J.C.: Mixed finite elements in $\mathbb{R}^3$. Numerische Mathematik **35**(3), 315–341 (1980)

[71] Nédélec, J.C.: A new family of mixed finite elements in $\mathbb{R}^3$. Numerische Mathematik **50**(1), 57–81 (1986)

[72] Neff, P., Bîrsan, M., Osterbrink, F.: Existence theorem for geometrically nonlinear Cosserat micropolar model under uniform convexity requirements. Journal of Elasticity **121**(1), 119–141 (2015)

[73] Neff, P., Eidel, B., d'Agostino, M.V., Madeo, A.: Identification of scale-independent material parameters in the relaxed micromorphic model through model-adapted first order homogenization. Journal of Elasticity **139**(2), 269–298 (2020)

[74] Neff, P., Ghiba, I.D., Lazar, M., Madeo, A.: The relaxed linear micromorphic continuum: well-posedness of the static problem and relations to the gauge theory of dislocations. The Quarterly Journal of Mechanics and Applied Mathematics **68**(1), 53–84 (2015)

[75] Neff, P., Ghiba, I.D., Madeo, A., Placidi, L., Rosi, G.: A unifying perspective: the relaxed linear micromorphic continuum. Continuum Mechanics and Thermodynamics **26**(5), 639–681 (2014)

[76] Neff, P., Jeong, J., Ramézani, H.: Subgrid interaction and micro-randomness – novel invariance requirements in infinitesimal gradient elasticity. International Journal of Solids and Structures **46**(25), 4261–4276 (2009)

[77] Neff, P., Madeo, A., Barbagallo, G., D'Agostino, M.V., Abreu, R., Ghiba, I.D.: Real wave propagation in the isotropic-relaxed micromorphic model. Proceedings of the Royal Society A: Mathematical, Physical and Engineering Sciences **473**, 2197 (2017)

[78] Neff, P., Münch, I.: Simple shear in nonlinear cosserat elasticity: bifurcation and induced microstructure. Continuum Mechanics and Thermodynamics **21**(3), 195–221 (2009)

[79] Neff, P., Pauly, D., Witsch, K.J.: Maxwell meets Korn: A new coercive inequality for tensor fields with square-integrable exterior derivative. Mathematical Methods in the Applied Sciences **35**(1), 65–71 (2012)

[80] Neidinger, R.D.: Introduction to automatic differentiation and matlab object-oriented programming. SIAM Review **52**(3), 545–563 (2010)

[81] Neunteufel, M.: Mixed finite element methods for nonlinear continuum mechanics and shells. Ph.D. thesis, Wien (2021). URL `http://hdl.handle.net/20.500.12708/17043`

[82] Neunteufel, M., Pechstein, A.S., Schöberl, J.: Three-field mixed finite element methods for nonlinear elasticity. Computer Methods in Applied Mechanics and Engineering **382**, 113857 (2021)

[83] Owczarek, S., Ghiba, I.D., Neff, P.: A note on local higher regularity in the dynamic linear relaxed micromorphic model. Mathematical Methods in the Applied Sciences **44**(18), 13855–13865 (2021)

[84] Papanicolopulos, S.A.: Efficient computation of cubature rules with application to new asymmetric rules on the triangle. J. Comput. Appl. Math. **304**, 73–83 (2016)

[85] Pauly, D., Schomburg, M.: Hilbert complexes with mixed boundary conditions part 1: de Rham complex. Mathematical Methods in the Applied Sciences **45**(5), 2465–2507 (2022)

[86] Pechstein, A.S., Schöberl, J.: An analysis of the TDNNS method using natural norms. Numerische Mathematik **139**(1), 93–120 (2018)

[87] Raviart, P.A., Thomas, J.M.: A mixed finite element method for 2-nd order elliptic problems. In: I. Galligani, E. Magenes (eds.) Mathematical Aspects of Finite Element Methods, pp. 292–315. Springer Berlin Heidelberg, Berlin, Heidelberg (1977)

[88] Rizzi, G., Hütter, G., Khan, H., Ghiba, I.D., Madeo, A., Neff, P.: Analytical solution of the cylindrical torsion problem for the relaxed micromorphic continuum and other generalized continua (including full derivations). Mathematics and Mechanics of Solids p. 10812865211023530 (2021)

[89] Rizzi, G., Hütter, G., Madeo, A., Neff, P.: Analytical solutions of the cylindrical bending problem for the relaxed micromorphic continuum and other generalized continua. Continuum Mechanics and Thermodynamics **33**(4), 1505–1539 (2021)

[90] Rizzi, G., Hütter, G., Madeo, A., Neff, P.: Analytical solutions of the simple shear problem for micromorphic models and other generalized continua. Archive of Applied Mechanics **91**(5), 2237–2254 (2021)

[91] Rizzi, G., Khan, H., Ghiba, I.D., Madeo, A., Neff, P.: Analytical solution of the uniaxial extension problem for the relaxed micromorphic continuum and other generalized continua (including full derivations). Archive of Applied Mechanics (2021)

[92] Rizzi, G., Neff, P., Madeo, A.: Metamaterial shields for inner protection and outer tuning through a relaxed micromorphic approach. arXiv (2021). URL `https://arxiv.org/abs/2111.12001`

[93] Romeo, M.: A microstretch continuum approach to model dielectric elastomers. Zeitschrift für angewandte Mathematik und Physik **71**(2), 44 (2020)

[94] Schittny, R., Bückmann, T., Kadic, M., Wegener, M.: Elastic measurements on macroscopic three-dimensional pentamode metamaterials. Applied Physics Letters **103**(23), 231905 (2013)

[95] Schöberl, J.: NETGEN an advancing front 2D/3D-mesh generator based on abstract rules. Computing and Visualization in Science **1**(1), 41–52 (1997)

[96] Schöberl, J., Zaglmayr, S.: High order Nédélec elements with local complete sequence properties. COMPEL - The international Journal for Computation and Mathematics in Electrical and Electronic Engineering **24**(2), 374–384 (2005)

[97] Schröder, J., Sarhil, M., Scheunemann, L., Neff, P.: Lagrange and $H(\mathrm{curl}, \mathcal{B})$ based finite element formulations for the relaxed micromorphic model. Computational Mechanics (2022)

[98] Sky, A., Muench, I., Neff, P.: A finite element formulation for a simplified, relaxed micromorphic continuum model. PAMM **20**(1), e202000336 (2021)

[99] Sky, A., Muench, I., Neff, P.: On $[H^1]^{3\times 3}$, $[H(\mathrm{curl})]^3$ and $H(\mathrm{symCurl})$ finite elements for matrix-valued Curl problems. Journal of Engineering Mathematics **136**(1), 5 (2022)

[100] Sky, A., Neunteufel, M., Muench, I., Schöberl, J., Neff, P.: Primal and mixed finite element formulations for the relaxed micromorphic model. Computer Methods in Applied Mechanics and Engineering **399**, 115298 (2022)

[101] Sky, A., Neunteufel, M., Münch, I., Schöberl, J., Neff, P.: A hybrid $H^1 \times H(\mathrm{curl})$ finite element formulation for a relaxed micromorphic continuum model of antiplane shear. Computational Mechanics **68**(1), 1–24 (2021)

[102] Sky, A., Polindara, C., Muench, I., Birk, C.: A flexible sparse matrix data format and parallel algorithms for the assembly of sparse matrices in general finite element applications using atomic synchronisation primitives (2020). URL `https://arxiv.org/abs/2012.00585`

[103] Solin, P., Segeth, K., Dolezel, I.: Higher-Order Finite Element Methods (1st ed.). Chapman and Hall/CRC (2003)

[104] Stavric, M., Wiltsche, A.: Geometrical elaboration of auxetic structures. Nexus Network Journal **21**(1), 79–90 (2019)

[105] Szabó, B., Babuška, I.: Finite Element Analysis. A Wiley-Interscience publication. Wiley (1991)

[106] Voss, J., Baaser, H., Martin, R.J., Neff, P.: More on anti-plane shear. Journal of Optimization Theory and Applications **184**(1), 226–249 (2020)

[107] Walsh, S., Tordesillas, A.: Finite element methods for micropolar models of granular materials. Applied Mathematical Modelling **30**(10), 1043–1055 (2006). Special issue of the 12th Biennial Computational Techniques and Applications Conference and Workshops (CTAC-2004) held at The University of Melbourne, Australia, from 27th September to 1st October 2004

[108] Witherden, F., Vincent, P.: On the identification of symmetric quadrature rules for finite element methods. Computers & Mathematics with Applications **69**(10), 1232–1241 (2015)

[109] Xiao, H., Gimbutas, Z.: A numerical algorithm for the construction of efficient quadrature rules in two and higher dimensions. Computers & Mathematics with Applications **59**(2), 663–676 (2010)

[110] Zaglmayr, S.: High order finite element methods for electromagnetic field computation. Ph.D. thesis, Johannes Kepler Universität Linz (2006). URL `https://www.numerik.math.tugraz.at/~zaglmayr/pub/szthesis.pdf`

[111] Zienkiewicz, O.C., Taylor, R.L., Zhu, J.Z.: The Finite Element Method: Its Basis and Fundamentals, Sixth Edition. Butterworth-Heinemann (2005)

A Symmetry and anti-symmetry tensors

The symmetry and anti-symmetry operators can be represented using fourth order tensors. Let $\mathbb{J}$ be the fourth order identity tensor

$$\mathbb{J}\boldsymbol{P} = \boldsymbol{P}\,, \qquad \mathbb{J} = \mathbf{e}_i \otimes \mathbf{e}_j \otimes \mathbf{e}_i \otimes \mathbf{e}_j\,, \tag{A.1}$$

and let $\mathbb{T}$ be the fourth order transposition tensor

$$\mathbb{T}\boldsymbol{P} = \boldsymbol{P}^T\,, \qquad \mathbb{T} = \mathbf{e}_i \otimes \mathbf{e}_j \otimes \mathbf{e}_j \otimes \mathbf{e}_i\,, \tag{A.2}$$

then there follows

$$\operatorname{sym}\boldsymbol{P} = \frac{1}{2}(\boldsymbol{P} + \boldsymbol{P}^T) = \frac{1}{2}(\mathbb{J} + \mathbb{T})\boldsymbol{P} = \mathbb{S}\boldsymbol{P}\,, \quad \operatorname{skew}\boldsymbol{P} = \frac{1}{2}(\boldsymbol{P} - \boldsymbol{P}^T) = \frac{1}{2}(\mathbb{J} - \mathbb{T})\boldsymbol{P} = \mathbb{A}\boldsymbol{P}\,. \tag{A.3}$$

We can derive an equivalent matrix notation by redefining $\boldsymbol{P}$ as a nine-dimensional vector

$$\widehat{\boldsymbol{P}} = \begin{bmatrix} P_{11} & P_{12} & P_{13} & P_{21} & P_{22} & P_{23} & P_{31} & P_{32} & P_{33} \end{bmatrix}^T\,. \tag{A.4}$$

Consequently, we find

$$\widehat{\mathbb{S}} = \begin{bmatrix} 1 & 0 & 0 & 0 & 0 & 0 & 0 & 0 & 0 \\ 0 & 0.5 & 0 & 0.5 & 0 & 0 & 0 & 0 & 0 \\ 0 & 0 & 0.5 & 0 & 0 & 0 & 0.5 & 0 & 0 \\ 0 & 0.5 & 0 & 0.5 & 0 & 0 & 0 & 0 & 0 \\ 0 & 0 & 0 & 0 & 1 & 0 & 0 & 0 & 0 \\ 0 & 0 & 0 & 0 & 0 & 0.5 & 0 & 0.5 & 0 \\ 0 & 0 & 0.5 & 0 & 0 & 0 & 0.5 & 0 & 0 \\ 0 & 0 & 0 & 0 & 0 & 0.5 & 0 & 0.5 & 0 \\ 0 & 0 & 0 & 0 & 0 & 0 & 0 & 0 & 1 \end{bmatrix}, \quad \widehat{\mathbb{A}} = \begin{bmatrix} 0 & 0 & 0 & 0 & 0 & 0 & 0 & 0 & 0 \\ 0 & 0.5 & 0 & -0.5 & 0 & 0 & 0 & 0 & 0 \\ 0 & 0 & 0.5 & 0 & 0 & 0 & -0.5 & 0 & 0 \\ 0 & -0.5 & 0 & 0.5 & 0 & 0 & 0 & 0 & 0 \\ 0 & 0 & 0 & 0 & 0 & 0 & 0 & 0 & 0 \\ 0 & 0 & 0 & 0 & 0 & 0.5 & 0 & -0.5 & 0 \\ 0 & 0 & -0.5 & 0 & 0 & 0 & 0.5 & 0 & 0 \\ 0 & 0 & 0 & 0 & 0 & -0.5 & 0 & 0.5 & 0 \\ 0 & 0 & 0 & 0 & 0 & 0 & 0 & 0 & 0 \end{bmatrix}. \tag{A.5}$$

Similarly, by redefining $\boldsymbol{P}$ as a four-dimensional vector for the plane strain problem

$$\widehat{\boldsymbol{P}} = \begin{bmatrix} P_{11} & P_{12} & P_{21} & P_{22} \end{bmatrix}^T\,, \tag{A.6}$$

we find the corresponding symmetry and anti-symmetry matrices

$$\widehat{\mathbb{S}} = \begin{bmatrix} 1 & 0 & 0 & 0 \\ 0 & 0.5 & 0.5 & 0 \\ 0 & 0.5 & 0.5 & 0 \\ 0 & 0 & 0 & 1 \end{bmatrix}, \qquad \widehat{\mathbb{A}} = \begin{bmatrix} 0 & 0 & 0 & 0 \\ 0 & 0.5 & -0.5 & 0 \\ 0 & -0.5 & 0.5 & 0 \\ 0 & 0 & 0 & 0 \end{bmatrix}. \tag{A.7}$$